

TIDAL BAND CURRENT VARIABILITY
OVER THE NORTHERN CALIFORNIA CONTINENTAL SHELF

by

Leslie Karen Rosenfeld

B.S. University of Washington, Seattle, Washington
(1978)

SUBMITTED IN PARTIAL FULFILLMENT OF THE
REQUIREMENTS FOR THE DEGREE OF

DOCTOR OF PHILOSOPHY

at the

MASSACHUSETTS INSTITUTE OF TECHNOLOGY

and the

WOODS HOLE OCEANOGRAPHIC INSTITUTION

December 1986

© Leslie K. Rosenfeld 1986

The author hereby grants to MIT and WHOI permission to reproduce
and distribute copies of this thesis document in whole or in part.

Signature of Author

Joint Program in Oceanography, Massachusetts
Institute of Technology/Woods Hole Oceanographic
Institution

Certified by

Robert C. Beardsley
Thesis Supervisor

Accepted by

Joseph Pedlosky
Chairman, Joint Committee for Physical
Oceanography, Massachusetts Institute of
Technology/Woods Hole Oceanographic Institution

ACKNOWLEDGMENTS

My interest in oceanography started long before graduate school, and I have been fortunate to meet along the way a number of people who taught me, encouraged me, and offered me the opportunities that have enabled me to get to this point in my career. My thanks to Bob Graunke, Nikos Orphanoudakis, Mike Rawson, John Thompson, Hal Mofjeld, Bill Boicourt, Dick Whaley, and Bill Ryan for believing in me and for showing me that oceanography could be fun.

I would like to express my appreciation to the scientists of the Physical Oceanography Departments at WHOI and MIT, most of whom I have called upon for assistance, at one time or another, during my years as a graduate student in the Joint Program. In particular, I would like to thank my advisor: Bob Beardsley; my thesis committee members: Ken Brink, Jim Price, Paola Rizzoli, and Bob Weller; and Dave Chapman, Harry Bryden, and Mel Briscoe, with whom I have had many helpful discussions. My thanks also to Carol Alessi and Dick Limeburner, without whom the data collection and processing would never have been achieved. Thanks to Anne-Marie Michael and Veta Green for assistance with the typing, and to all the other support staff who helped me.

Dave Aubrey of the Geology Department provided the computer program for the tidal analysis; Brad Butman, John Moody, and Marlene Noble of USGS shared their computer programs, their time and their ideas with me; and John Farrington of the Chemistry Department was a constant source of encouragement.

CODE was a multi-institutional experiment involving too many people for me to thank individually each person who contributed to its success and to my dissertation work, so I thank the CODE Group collectively for allowing me to use this data set.

Bill Grant fit into many of the categories above. He was a member of my thesis committee, a CODE participant, and someone who helped and encouraged me. Most importantly, he was not afraid or embarrassed to be openly supportive, and his enthusiasm was unflagging. I am sorry I did not finish this dissertation in time for him to see the completed version.

Without the constant support of my fellow Joint Program students (and their spouses), I could not have completed this undertaking. They were there in the good times and the bad. Thanks guys. And to my many friends around the country who 'phoned in their moral support long-distance - I really appreciated it.

Finally, thanks go to my parents who, although they thought I was crazy, didn't try to stop me, and to my sister, Alison, who stepped in at the eleventh hour and kept me from falling apart.

While in graduate school, I received financial support from the WHOI Education Office, a NASA traineeship, and NSF grants OCE 80-14941 and OCE 84-17769.

TABLE OF CONTENTS

	<u>Page</u>
ABSTRACT	2
ACKNOWLEDGMENTS	3
CHAPTER I. INTRODUCTION	7
References	13
CHAPTER II. DIURNAL PERIOD WIND STRESS AND CURRENT FLUCTUATIONS OVER THE CONTINENTAL SHELF OFF NORTHERN CALIFORNIA	15
Abstract	16
1. Introduction	17
2. Historical Review	18
3. Data	21
4. Description of Diurnal Wind Stress and Heating Cycles	27
A. Wind Stress	27
i. Frequency Domain	28
ii. Time Domain	34
B. Heat Flux	38
5. Description of Diurnal Period Currents	40
6. Correlation Between Wind Stress and Currents	51
7. Diurnal Tidal Currents	54
8. Forced Response	59
A. Interior Forced Response	64
B. Frictional Forced Response	67
9. Conclusions	85
Appendix A: Complex Demodulation	87
Appendix B: High-Pass Filter	90
Appendix C: Time-Dependent Ekman Layer	91
Appendix D: Mixed Layer Parameters	97
Acknowledgments	99
References	100
CHAPTER III. BAROTROPIC SEMIDIURNAL TIDAL CURRENTS OFF NORTHERN CALIFORNIA DURING THE COASTAL OCEAN DYNAMICS EXPERIMENT (CODE)	105
Abstract	106
1. Introduction	107
2. Data	109
3. Method of Analysis	113
4. Observations	118
5. Discussion	122

6.	Theory for a Kelvin Wave Along a Bumpy Boundary	136
7.	Conclusions	145
	Appendix	147
	Acknowledgments	148
	References	149
CHAPTER IV.	BAROCLINIC SEMIDIURNAL TIDAL CURRENTS OVER THE CONTINENTAL SHELF OFF NORTHERN CALIFORNIA	151
	Abstract	152
	List of Symbols	153
1.	Introduction	156
2.	Observations of Internal Tides on Continental Shelves	157
3.	Data	165
4.	Methods of Analysis	169
5.	Observations	173
6.	Comparison with Internal Wave Theory	191
7.	Generation	210
8.	Effects of Shear in the Low Frequency Flow	220
9.	Conclusions	223
	Appendix: Application of Baine's Theory of Internal Tide Generation	225
	Acknowledgments	227
	References	228
CHAPTER V.	CONCLUSIONS	233
	BIOGRAPHICAL NOTE	237

CHAPTER I

INTRODUCTION

The rise and fall of sea level with fixed periodicity, known as the tide, is probably one of the earliest physical oceanographic phenomena observed by man. The tidal currents associated with this process have also received man's attention for centuries, particularly in coastal areas. Newton (1687) provided an explanation for the astronomical tide-generating force (ATGF), but systematic study of the dynamics of tidal currents awaited the work of Laplace (1776) who formulated the fundamental equations governing long waves in a barotropic ocean. Since that time, an enormous body of literature dealing with both barotropic and baroclinic tides has accumulated. Nearly every physical oceanography textbook includes a discussion of tides, and there have been numerous review articles written on the subject. While some of these references are cited in the succeeding chapters, the lists given there are by no means comprehensive. More references were consulted as background reading during the preparation of this dissertation than are cited in the text. Two of these which I have found to be particularly useful, and which deserve specific mention, are LeBlond and Mysak (1978) and Hendershott (1981).

In spite of all the effort spent on the study of tides and tidal currents, not everything about them is clearly understood. Although the equilibrium tide that would result if the earth were covered with a homogeneous fluid of uniform depth that could respond instantaneously to the ATGF is well known for every point on the earth, local geometric, bathymetric, hydrographic, and meteorological conditions cause the observed tide to deviate substantially from this. Global numerical models can predict fairly well sea level variations on a coarse grid. Finer resolution local models have been applied to some

coastal areas, again with good results for sea level. Tidal current predictions are usually not as accurate.

The focus of this dissertation is on the description and dynamical interpretation of the tidal band current fluctuations over the continental shelf off northern California. The term "tidal band" is used here to denote fluctuations with periods from about one-half to one day, including all the major diurnal and semidiurnal tidal constituents. The semidiurnal frequency is super-inertial, and the diurnal frequency sub-inertial, at this mid-latitude location. Kinetic and potential energy are strongly peaked at the diurnal and semidiurnal frequencies. Although inertial currents are occasionally observed, particularly during the winter when internal wave energy in general is elevated in this locale, they do not contribute significantly to the current variance. Consequently, the treatment here is divided into discussion of the diurnal and semidiurnal variability. Each chapter emphasizes a process which can cause the tidal currents to deviate from what would be anticipated based solely on observations of sea level. In Chapter II, the diurnal current variability is discussed, and the role played by atmospheric forcing is examined in detail. In Chapter III, the barotropic semidiurnal tidal currents over the shelf are described, and the effect of small-scale bumps in the coastline is evaluated. The baroclinic semidiurnal tidal currents, which are dependent upon the local time-varying hydrographic conditions, are examined in Chapter IV.

The term barotropic means that pressure is constant on constant density surfaces, while baroclinic means that pressure is not constant on constant density surfaces. In a homogeneous fluid, all flow is

barotropic. In a stratified fluid, the flow may be considered to be made up of two components, one of which is independent of stratification and, in an inviscid fluid, is constant throughout the water column, and another which varies with depth due to the influence of the stratified density field on the pressure gradient. The first component, which is due to the deflection of the sea surface, is commonly referred to as the barotropic component of flow, and the second component is referred to as the baroclinic.

There is no practical way to completely separate the barotropic and baroclinic components of flow in the data. In regard to the tidal currents analyzed here, two approaches were used together to estimate the barotropic component. First, the currents were vertically integrated over the depth of the water column, to take advantage of the fact that the baroclinic horizontal currents can be expressed as a sum of modes, each of which, in an inviscid fluid, integrates to zero under the assumptions of a flat bottom and a rigid lid. The effect on the baroclinic modes of a free surface is minimal. In the case of two-dimensional flow over a uniformly sloping bottom, the cross-slope velocity also integrates to zero over the depth of the fluid (Wunsch, 1969), and in the case of three-dimensional flow over slowly varying topography, it is a good approximation. Since the ocean is not inviscid, the bottom is not flat, and the vertical resolution used in the integration is limited by the number of points where measurements are available, integration over depth gives only an approximation to the barotropic component.

The second approach uses the fact that, at a given location, the sea level variations associated with the ATGF repeat in a predictable

fashion. The barotropic currents, which are due to the gradients in sea level, also should be deterministic and periodic. The baroclinic currents, on the other hand, are not strictly repeatable in time, due to non-periodic variations in the density field. The use of long time series to calculate the amplitudes and phases of the currents at tidal frequencies helps to isolate the deterministic part of the signal. This method can not completely remove the baroclinic part however, because the barotropic and baroclinic components may be at least partially phase-locked in time.

All of the data used in this thesis were collected as part of the Coastal Ocean Dynamics Experiment (CODE), which was conceived and designed to study the synoptic band (2 - 10 day) wind-driven flow over the continental shelf. The spatial and temporal resolution of the measurements, however, make it an excellent data set for studying the energetic tidal band motions as well. A brief overview of the experiment is given by the CODE Group (1983). Although the emphasis here is on the current data, use is made of the available wind, bottom pressure, sea level, and temperature measurements, as necessary, to aid in explaining the response of the coastal ocean at tidal frequencies. The moored data collected during the summers of 1981 and 1982 are described in Rosenfeld (1983a) and Limeburner (1985), respectively. In addition, each chapter of this work includes a data section outlining what measurements were used in that particular chapter. Although the primary interest here is on the variability at tidal frequencies, the relationship to, and influence of, the mean and low frequency motions is pointed out where appropriate. The CODE region is in an area characterized by strong upwelling-favorable winds

during the spring and summer, with equatorward mean flow near the surface, and weaker equatorward or poleward flow beneath. During the winter, the wind stress is equally strong as in summer, but the direction is variable. Mean currents are poleward at all depths (Rosenfeld, 1983b). The non-tidal flow in the CODE region, as well as a variety of other topics relating to CODE, have been studied by a number of investigators. Beardsley and Lentz (1987) list the work published to date.

The major results of this thesis clearly illustrate that many factors influence the tidal frequency current variability over the northern California continental shelf. The nearshore barotropic semidiurnal currents may vary by as much as several hundred percent over alongshore distances of only tens of kilometers, partially due to small bumps in the coastline. The time variability of the semidiurnal currents is a strong function of density structure, with the baroclinic component of flow at times overwhelming the barotropic component. The diurnal currents are seasonally dependent, with strong surface-intensification during the summer due primarily to the diurnal signal in the wind stress, which is intensified during periods of upwelling-favorable winds.

These results demonstrate that, despite our basic understanding of tidal phenomena, accurate prediction of the temporal and spatial variability of tidal band currents can be very difficult without a detailed knowledge of the local geometry, stratification, and atmospheric forcing.

References

- Beardsley, R. C. and S. J. Lentz, The Coastal Ocean Dynamics Experiment (CODE) collection: An introduction. Journal of Geophysical Research, 92, 1987, in press.
- CODE Group, Coastal Ocean Dynamics Experiment (CODE): A preliminary program description. Oceanography Report, EOS, 64, 538-540, 1983.
- Hendershott, M. C., Long waves and ocean tides. In: Evolution of Physical Oceanography. B. A. Warren and C. Wunsch, eds., M.I.T. Press, 292-341, 1981.
- Laplace, P. S., Recherches sur plusieurs points du systeme du monde. Memoires de l'Academie Royale des Sciences de Paris, 89, 177-264, 1776.
- LeBlond, P. H. and L. A. Mysak, Waves in the Ocean. Elsevier Scientific Publishing Company, 602 pp., 1978.
- Limeburner, R., ed., CODE-2 Moored Array and Large-Scale Data Report. Woods Hole Oceanographic Institution Technical Report WHOI-85-35, CODE Technical Report No. 38, 234 pp., 1985.
- Newton, I., Philosophiae Naturalis Principia Mathematica, 1687. See Newton's Principia, Cajori's 1946 version of Motte's 1729 translation, University of California Press, 680 pp.
- Rosenfeld, L. K., ed., CODE-2 Moored Array and Large-Scale Data Report. Woods Hole Oceanographic Institution Technical Report WHOI-83-23, CODE Technical Report No. 21, 186 pp., 1983a.
- Rosenfeld, L. K., Seasonal characteristics of the mean and low-frequency currents during CODE. EOS, 64, 717, Abstract, 1983b.
- Wunsch, C., Progressive internal waves on slopes. Journal of Fluid Mechanics, 35, 131-144, 1969.

CHAPTER II

DIURNAL PERIOD WIND STRESS AND CURRENT FLUCTUATIONS
OVER THE CONTINENTAL SHELF OFF NORTHERN CALIFORNIA

ABSTRACT

Diurnal period wind stress and current fluctuations measured over the continental shelf off northern California during the Coastal Ocean Dynamics Experiment in the summers of 1981 and 1982 are examined. The diurnal currents are strongly surface-intensified, with amplitudes of up to 20 cm s^{-1} . At depths less than 35 m, the diurnal currents are non-stationary and their amplitude is well correlated with the amplitude modulation of the local diurnal wind stress. Beneath the surface layer, the diurnal current ellipses rotate clockwise with semi-major axes of 1 to 3 cm s^{-1} . A mixed layer model driven with diurnal wind stress and surface heat flux produces currents similar to those observed in the upper water column. The deeper currents are consistent with a combination of freely propagating Kelvin and first mode coastal-trapped waves and an interior flow forced by the diurnal wind stress in the presence of a coast.

1. INTRODUCTION

Measurements made over the continental shelf off northern California during the Coastal Ocean Dynamics Experiment (CODE), in the summers of 1981 and 1982, show intermittent surface-intensified clockwise-rotating diurnal period currents with amplitudes of up to 20 cm s^{-1} . A strong diurnal signal in the along-shelf component of wind stress is observed during time periods when the low frequency wind stress is equatorward. Direct forcing by the local diurnal wind stress, in combination with the diurnal heating cycle, can account for much of the diurnal period energy observed in the upper ocean currents over the inner and mid-shelf. Below the surface mixed layer, the diurnal currents are clockwise-rotating and of order $1 \text{ to } 3 \text{ cm s}^{-1}$. These deep currents can be accounted for by the combination of a Kelvin wave, first mode coastal-trapped wave, and interior flow forced by the diurnal wind stress in the presence of a coast.

The purpose of this paper is to describe the diurnal period current fluctuations observed in CODE, and evaluate the contributions made by both tidal and atmospheric forcing in driving these. Previous studies of diurnal period variability in other regions of coastal upwelling are reviewed in Section 2. Although a seabreeze circulation is common to many of these areas and the meteorology of this phenomenon has been well described, this work represents the first integrated analysis of diurnal period wind stress and currents. The CODE data used in this study are outlined in Section 3. The diurnal period wind stress and heating cycles are described in Section 4 and the diurnal period current variability in Section 5. In Section 6, evidence for the correlation between the diurnal period wind stress

and currents is presented. The diurnal tidal currents are estimated in Section 7. In Section 8, models for both the inviscid (Part A) and frictional (Part B) components of the flow forced by a diurnally varying wind stress are discussed. Conclusions are given in Section 9.

2. HISTORICAL REVIEW

As part of the Coastal Upwelling Ecosystems Analysis (CUEA) program, oceanographic experiments were conducted off the coasts of Oregon, northwest Africa, and Peru in the 1970s. Meteorological measurements were made in conjunction with these, and in all cases the presence of a significant diurnal signal in the wind field was noted. In an effort to place the CODE measurements in historical and geographic perspective, observations of the diurnal winds, currents, and temperature fluctuations from these three upwelling regions are reviewed here.

The seabreeze circulation off the coast of Oregon has been discussed by Burt et al. (1974) using 13 days of wind observations made 50 km offshore during August, 1970, and by a number of authors using data from CUE-I and CUE-II which were conducted in the summers of 1972 and 1973. The following picture emerges. The diurnal period winds rotate clockwise (CW) and have amplitude in the along-shelf direction two to three times that in the cross-shelf direction. Halpern (1974) attributes this to the presence of coastal mountains. Burt et al. (1974) found that the along-shelf component of wind exhibited a diurnal signal of amplitude 2 m s^{-1} , peaking in the equatorward direction at 1930 PDT. O'Brien and Pillsbury (1974) reported seeing no seabreeze signal 30 km offshore in 1972. In 1973

however, the diurnal winds 13 km from shore, as described in Halpern (1974), bore marked resemblance to the winds 50 km from shore reported by Burt et al. (1974). Averaged over a period of 52 days, the along-shelf wind showed a 2 m s^{-1} daily variation on top of a 3 m s^{-1} equatorward mean. Maximum equatorward speeds occurred at about 2000 PDT. Burt et al. (1974) noted that the amplitude of the diurnal variations 50 km from shore changed over the 13 day period they examined, and saw that it was linearly related to the daily mean along-shelf wind velocity with the diurnal amplitude decreasing as mean equatorward winds increased. O'Brien and Pillsbury (1974), however, noted the opposite tendency in winds nearer to shore. They found that the seabreeze was best developed during times of upwelling-favorable winds, which is in agreement with the observations from the CODE area.

Halpern (1974) states that there is no evidence for forcing of the low-frequency upwelling circulation by the diurnal winds, and does not comment on the forcing of diurnal currents by diurnal winds. Hayes and Halpern (1976) state that the diurnal band near-surface horizontal kinetic energy may be related to the diurnal variations in the wind. O'Brien and Pillsbury (1974) surmise that the persistent seabreeze forcing should induce a CW-rotating response in the ocean currents at the diurnal period, but they made no attempt to look for it. Denbo and Allen (1984) examined the CUE-II current data using rotary empirical orthogonal function analysis in three frequency bands, one of which was the diurnal. They noted surface-intensified CW-rotating flow, coherent with the wind stress, in the upper 15 m, below which the diurnal currents were nearly depth-independent.

Halpern (1977) analyzed measurements of winds and near-surface temperature and currents made during March and April, 1974 off the coast of northwest Africa, as part of the JOINT-I experiment of CUEA. He found that the diurnal wind vector rotated CW, and that the cross-shelf diurnal kinetic energy was five times that of the along-shelf. The amplitude of the diurnal cross-shelf wind was 3.5 m s^{-1} , 32 km from shore. Diurnal period fluctuations in the temperature and current were observed in the upper 15 m of the water column. Because the diurnal currents rotated CW, were limited to the upper part of the water column, and had a ratio of 0.01 to the wind fluctuations, Halpern concluded that they might be generated by the diurnal period wind, but went no further.

Burt et al. (1973) examined 11.5 days of wind measurements made in April, 1969, 20 km offshore Peru, near 15°S latitude. After removal of the mean, they found the cross-shelf component of wind to have an amplitude of 0.5 m s^{-1} with maximum onshore velocity at 1400 hours local time. The along-shelf component was found to have an amplitude of 0.7 m s^{-1} with maximum equatorward velocity at 2100 hours. Brink (1979) examined CUEA JOINT-II wind and near-surface temperature data from the same area collected for 69 days during March - May, 1977, and also noted that the along-shelf diurnal wind exceeded the cross-shelf wind, and that the wind stress peaked near sunset. Brink noted the strong diurnal cycle in mixed layer depth and commented that it is governed by the interplay of mechanical and thermal forcing. Johnson (1981) examined the diurnal period currents for a 10 day period in March of 1977, and noted that they were largest in the surface layer (less than 15 m) over the inner shelf, consistent with forcing by the

seabreeze. He did a complex demodulation of the currents at the diurnal, semidiurnal, and inertial frequencies, and found a relationship between the amplitude of inertial motions and wind forcing, but not so for the diurnal motions.

3. DATA

The CODE data offer a unique opportunity to explore the effects of a diurnally oscillating wind on the coastal oceanographic environment. Atmospheric and oceanographic parameters were measured concurrently over the northern California shelf for roughly three month periods in two consecutive summers, 1981 and 1982. Winds were measured at offshore buoys as well as at coastal stations. Numerous current measurements allow examination of the three-dimensional spatial structure of the flow. Figures 1 and 2 show the location of all instruments providing data analyzed here. Table 1 gives the positions, depths and dates for these time series. For a more complete description of the moored data acquired during CODE, the reader is referred to the CODE moored array data reports (Rosenfeld, 1983 and Limeburner, 1985).

Within the small-scale CODE array, coastal winds were measured at Bodega Bay, Sea Ranch, and Pt. Arena during CODE-1 and -2. Data were also available for part of the winter in between from Bodega Bay and Sea Ranch. Winds over the ocean were measured on buoys deployed at R3, C3, and C5 during the summer of 1981 (CODE-1) and at N3, C2¹,

¹ The wind stress record from C2 in CODE-2 has not been used here because it shows irregularities in both amplitude and phase which cause low coherence at the diurnal frequency between this record and all the other CODE-2 stress records.

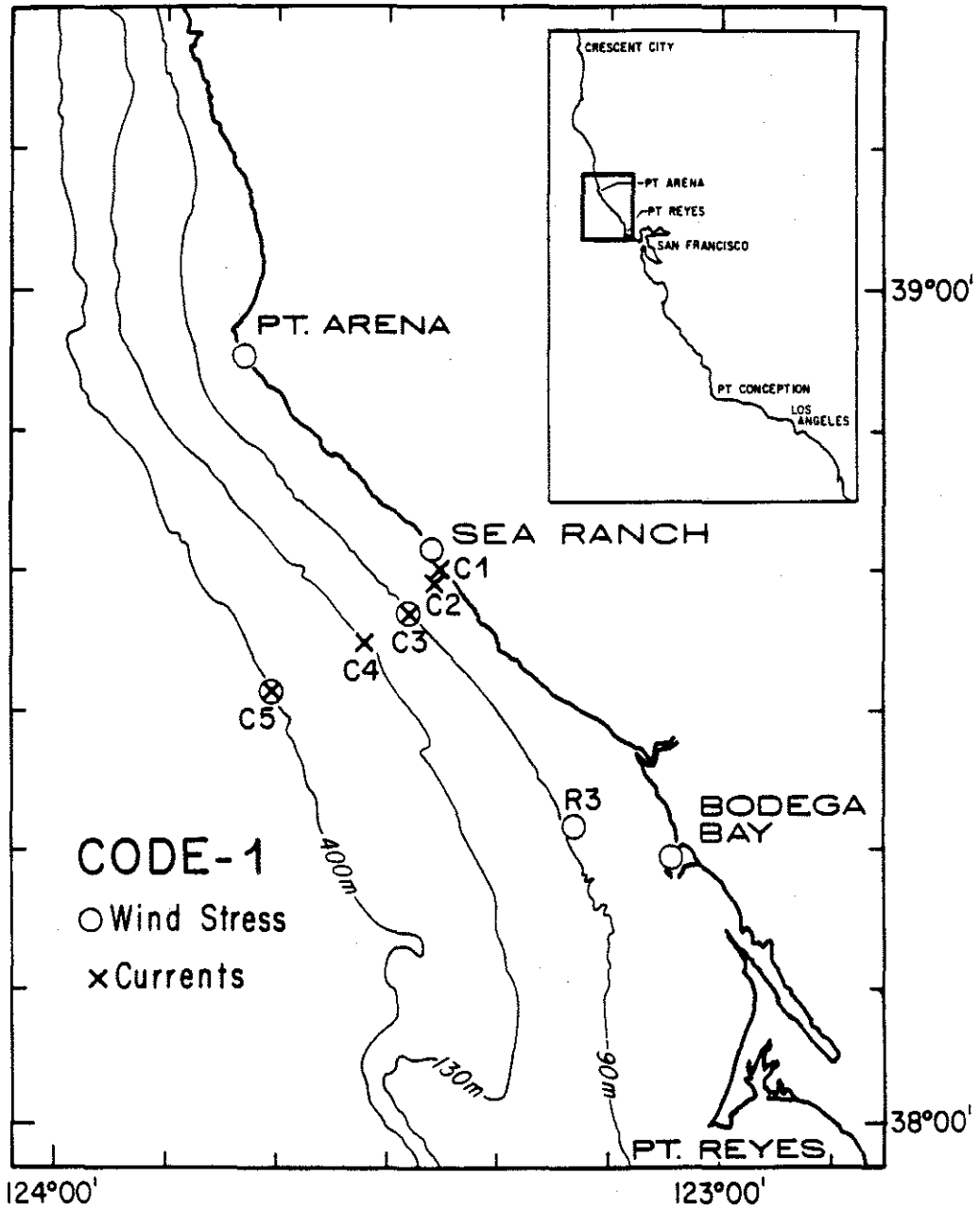


Figure 1. Location of CODE-1 wind stress measurements and C-line current meter moorings are shown.

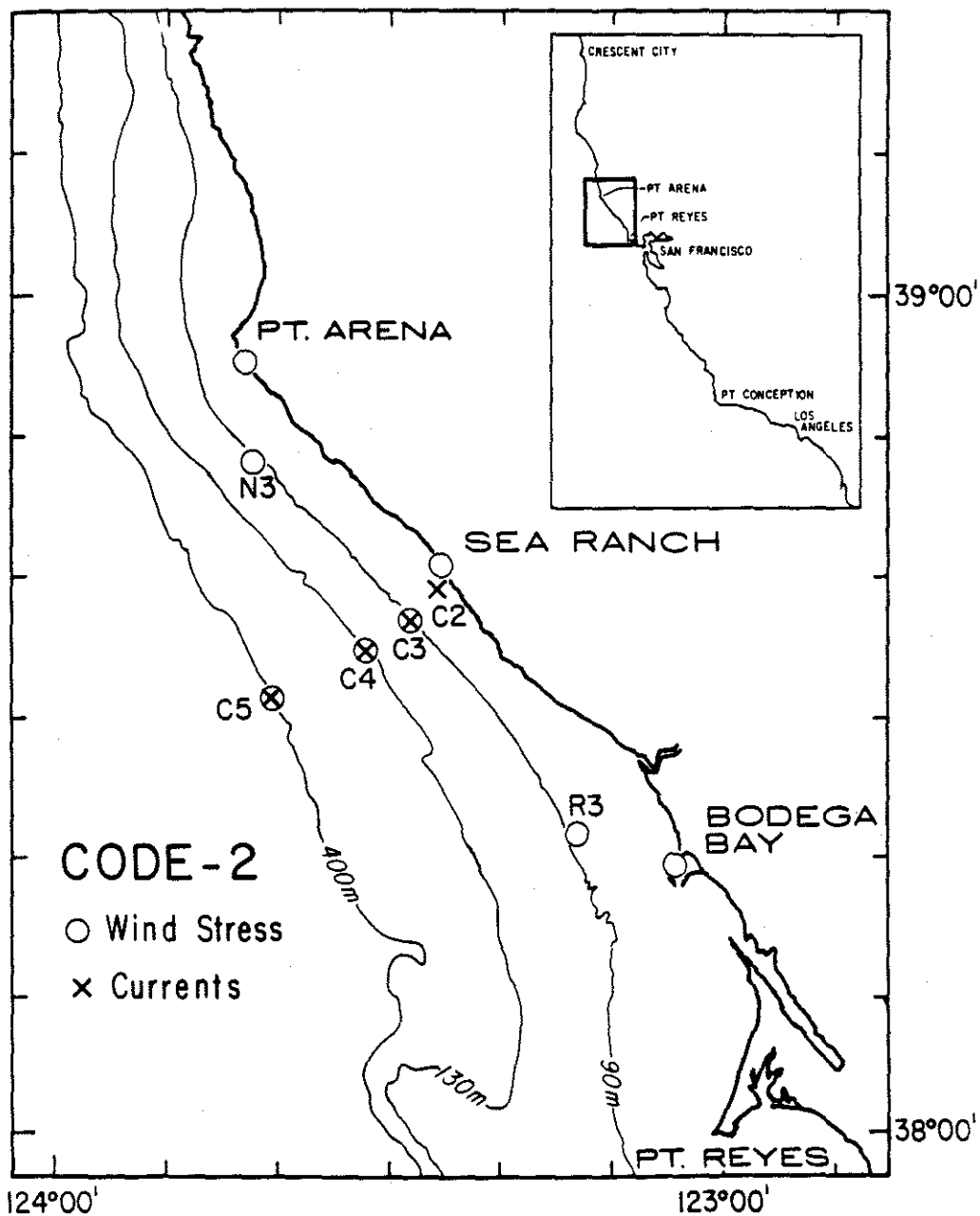


Figure 2. Location of CODE-2 wind stress measurements and C-line current meter moorings are shown.

CODE-1

Station	Water Depth (m)	Latitude North	Longitude West	Start	Stop	Instrument	Depth (m)
WIND STRESS							
Pt. Arena	Coastal	38°57.0'	123°44.4'	4/01/81	8/01/81	WR	-6.1
C5	402	38°31.2'	123°40.5'	4/12/81	8/01/81	VAWR	-3.5
C3	94	38°36.5'	123°28.1'	4/12/81	7/31/81	VAWR, I	-3.5
Sea Ranch	Coastal	38°41.0'	123°25.5'	3/11/81	8/03/81	WR	-10.0
R3	90	38°21.6'	123°13.0'	4/13/81	8/03/81	VAWR	-3.5
Bodega Bay	Coastal	38°19.0'	123°04.0'	3/11/81	8/03/81	WR	-10.0
CURRENTS							
C1	30	38°39.8'	123°25.1'	3/25/81	7/23/81	VMCM	4.0
	30	38°39.8'	123°25.1'	3/25/81	7/23/81	VMCM	7.0
	30	38°39.8'	123°25.1'	3/25/81	7/23/81	VMCM	11.0
	33	38°39.6'	123°24.8'	4/01/81	7/23/81	VMCM	23.0
	33	38°39.6'	123°24.8'	4/01/81	7/23/81	VMCM	27.0
C2	63	38°39.3'	123°25.6'	4/14/81	8/01/81	VMCM	4.0
	63	38°39.3'	123°25.6'	4/13/81	7/13/81	VMCM	14.0
C3	90	38°37.2'	123°28.3'	4/08/81	7/14/81	VMCM	9.0
	90	38°37.2'	123°28.3'	4/07/81	7/23/81	VMCM	14.0
	90	38°37.2'	123°28.3'	4/08/81	7/14/81	VMCM	29.0
	90	38°36.7'	123°28.0'	4/08/81	7/14/81	VMCM	35.0
	90	38°36.7'	123°28.0'	4/08/81	7/13/81	VMCM	83.0
C4	133	38°34.5'	123°32.6'	4/09/81	7/13/81	VMCM	19.0
	133	38°34.5'	123°32.6'	4/09/81	7/14/81	VMCM	29.0
	133	38°34.3'	123°32.7'	4/09/81	7/14/81	VMCM	45.0
	133	38°34.3'	123°32.7'	4/09/81	7/13/81	VMCM	65.0
	133	38°34.3'	123°32.7'	4/09/81	7/23/81	VMCM	75.0
	133	38°34.3'	123°32.7'	4/09/81	7/23/81	VMCM	95.0
	133	38°34.3'	123°32.7'	4/09/81	7/14/81	VMCM	123.0
C5	402	38°31.2'	123°40.5'	4/12/81	8/01/81	VACM	9.0

Abbreviations: WR - wind recorder, VAWR - vector averaging wind recorder, VMCM - vector measuring current meter, VACM - vector averaging current meter, I - insolation

Table 1a. Location, instrument type, and depth are listed for all data used in this paper. Start and stop dates (GMT) are for the full record length available, although the entire time series was not necessarily used in the analysis here.

CODE-2

Station	Water Depth (m)	Latitude North	Longitude West	Start	Stop	Instrument	Depth (m)
WIND STRESS							
Pt. Arena	Coastal	38°57.0'	123°44.4'	3/01/82	8/31/82	WR	-6.1
N3	93	38°48.1'	123°41.8'	4/08/82	8/17/82	VAWR	-3.5
C5	400	38°30.8'	123°40.3'	3/30/82	8/19/82	VAWR	-3.5
C4	130	38°33.4'	123°31.7'	4/01/82	8/17/82	VAWR	-3.5
C3	93	38°36.4'	123°27.7'	3/24/82	7/28/82	VAWR, I	-3.5
Sea Ranch	Coastal	38°41.0'	123°25.5'	3/01/82	8/16/82	WR	-10.0
R3	90	38°25.4'	123°16.4'	3/23/82	8/17/82	VAWR	-3.5
Bodega Bay	Coastal	38°19.0'	123°04.0'	3/01/82	8/31/82	WR	-10.0
CURRENTS							
C2	60	38°38.2'	123°25.3'	3/12/82	8/05/82	VMCM	10.0
	60	38°38.2'	123°25.3'	3/12/82	8/13/82	VMCM	20.0
	60	38°38.2'	123°25.3'	3/12/82	8/05/82	VMCM	35.0
	60	38°38.2'	123°25.3'	3/12/82	8/05/82	VMCM	53.0
C3	93	38°36.4'	123°27.7'	3/24/82	7/28/82	VMCM	5.0
	93	38°36.4'	123°27.7'	3/24/82	7/28/82	VACM	10.0
	93	38°36.4'	123°27.7'	3/24/82	7/28/82	VMCM	15.0
	90	38°36.4'	123°27.7'	3/12/82	8/09/82	VMCM	20.0
	90	38°36.4'	123°27.7'	3/12/82	8/05/82	VMCM	35.0
	90	38°36.4'	123°27.7'	3/12/82	8/09/82	VMCM	53.0
	90	38°36.4'	123°27.7'	3/12/82	8/05/82	VMCM	70.0
	90	38°36.4'	123°27.7'	3/12/82	8/09/82	VMCM	83.0
C4	130	38°33.3'	123°31.6'	4/01/82	8/17/82	VACM	10.0
	130	38°33.3'	123°31.6'	4/01/82	8/17/82	VMCM	20.0
	130	38°33.3'	123°31.6'	4/01/82	8/17/82	VMCM	35.0
	130	38°33.3'	123°31.6'	4/01/82	8/17/82	VMCM	55.0
	130	38°33.3'	123°31.6'	4/01/82	8/17/82	VMCM	70.0
	130	38°33.3'	123°31.6'	4/01/82	8/17/82	VMCM	90.0
	130	38°33.3'	123°31.6'	4/01/82	8/17/82	VACM	121.0
C5	400	38°30.8'	123°40.3'	3/30/82	8/19/82	VMCM	20.0
	400	38°30.8'	123°40.3'	3/30/82	8/19/82	VMCM	35.0
	400	38°30.8'	123°40.3'	3/30/82	8/19/82	VMCM	55.0
	400	38°30.8'	123°40.3'	3/30/82	8/19/82	VACM	70.0
	400	38°30.8'	123°40.3'	3/30/82	8/19/82	VMCM	90.0
	400	38°30.8'	123°40.3'	3/30/82	8/19/82	VACM	110.0
	400	38°30.8'	123°40.3'	3/30/82	8/19/82	VACM	150.0

Abbreviations: WR - wind recorder, VAWR - vector averaging wind recorder, VMCM - vector measuring current meter, VACM - vector averaging current meter, I - insolation

Table 1b. Location, instrument type, and depth are listed for all data used in this paper. Start and stop dates (GMT) are for the full record length available, although the entire time series was not necessarily used in the analysis here.

C3, C4, C5, and R3 during the summer of 1982 (CODE-2). Complete accountings of the meteorological measurements made in the CODE-1 and CODE-2 small-scale experiments are given in Mills and Beardsley (1983) and Beardsley, Alessi, and Limeburner (1985), respectively, and are discussed in more detail in Beardsley et al. (1987). Wind records were converted into wind stress using the method developed by Large and Pond (1981) for neutral stability and discussed in Mills and Beardsley (1983). This method was developed for use with steady winds measured over open water, but is applied here to these coastal measurements for lack of a more appropriate formulation.

Air temperature, water temperature at one meter depth, and insolation measured on the meteorological buoy at C3 during CODE-1 and -2 are used in calculating surface heat flux. The instrumentation used in acquiring these data is described in Mills and Beardsley (1983) and Beardsley et al. (1985).

Current meter moorings were arranged in a T-shaped array during CODE-1 and along four cross-shelf transects during CODE-2. In general, current meters at depths less than 30 m were deployed on slack moorings with surface flotation, those at depths greater than that were on taut subsurface moorings. The exceptions to this are that the instruments below 20 m at C1 during CODE-1 were on a subsurface mooring, and the 35 and 55 m instruments at C5 during CODE-2 were on a surface mooring. The surface moorings had scopes ranging from 2.0 (for the C1 mooring in 30 m depth) to 1.1 for the C5 moorings in 400 m depth. Twenty meters of the 1.5-inch chain and 30 to 50 m of 0.75-inch chain were used at the bottom of the slack moorings to decrease mooring motion. Computer simulations of the

behavior of the surface moorings using realistic current profiles based on the mean, low frequency, diurnal, and semidiurnal current components, individually and in combination with each other, show that the inclination of the current meters from the vertical is generally less than 5° . The horizontal excursion is less than 10 m, which corresponds to a velocity of 0.05 cm s^{-1} at the diurnal frequency. For the subsurface moorings, the inclinations are less than 0.5° and the horizontal excursions less than 0.5 m. For these reasons, contamination of the current and temperature measurements due to mooring motion is considered minimal.

Current data from the central, or C, line will be presented here. Hourly-averaged time series of currents and winds were decomposed into along- and cross-shelf components, directed along 317°T and 47°T respectively. A common time period of 90 days for CODE-1 (4/14/81 1300 - 7/13/81 1200 GMT) and 105 days for CODE-2 (4/14/82 1300 - 7/28/82 1200 GMT) was used as a starting point for many of the analyses presented here.

4. DESCRIPTION OF THE DIURNAL WIND STRESS AND HEATING CYCLES

A. WIND STRESS

Beardsley et al. (1987) explain why the diurnal variability in the wind field at the CODE site is more prominent in the along-shelf component of wind as opposed to the cross-shelf component as in a classic seabreeze circulation. The major effect of the daytime coastal heating is to drive a circulation cell in the cross-shelf, vertical plane which advects a jet of high along-shelf momentum air from offshore to over the coast. The jet is strengthened by nearshore

subsidence of the marine inversion layer which has its minimum elevation in the late afternoon, close to the time of the greatest equatorward wind stress. As discussed in Beardsley et al. (1987), strengthening of the synoptic scale pressure gradient results in increased daily averaged equatorward winds, as well as larger diurnal variations.

Figures 3 and 4 show the hourly time series of along-shelf wind stress for CODE-1 and -2, respectively. The cross-shelf wind stress is much weaker, as shown in Mills and Beardsley (1983) and Beardsley et al. (1985). The outstanding features to be noted here are: (1) the mean along-shelf wind stress is equatorward and large enough such that the diurnal variations do not cross zero; (2) the diurnal variations are intermittent in time; (3) the diurnal variations are largest at C3, and decrease in the along-shelf as well as cross-shelf directions from that site. In an effort to quantify the above statements, two approaches have been taken. First, a statistical description in the frequency domain of the diurnal period variability and its relationship to the total wind stress field is presented. This, of course, has the disadvantage of lumping together times when the diurnal variability is large with times when it is weak, so a second approach emphasizing the time variability of the diurnal signal is used. This employs results of a complex demodulation technique described in Appendix A.

i. FREQUENCY DOMAIN

Figure 5 shows total variance spectra for wind stress at Sea Ranch, C3 and C5 for CODE-1 and -2. Diurnal and semidiurnal peaks are

ALONG-SHELF WIND STRESS

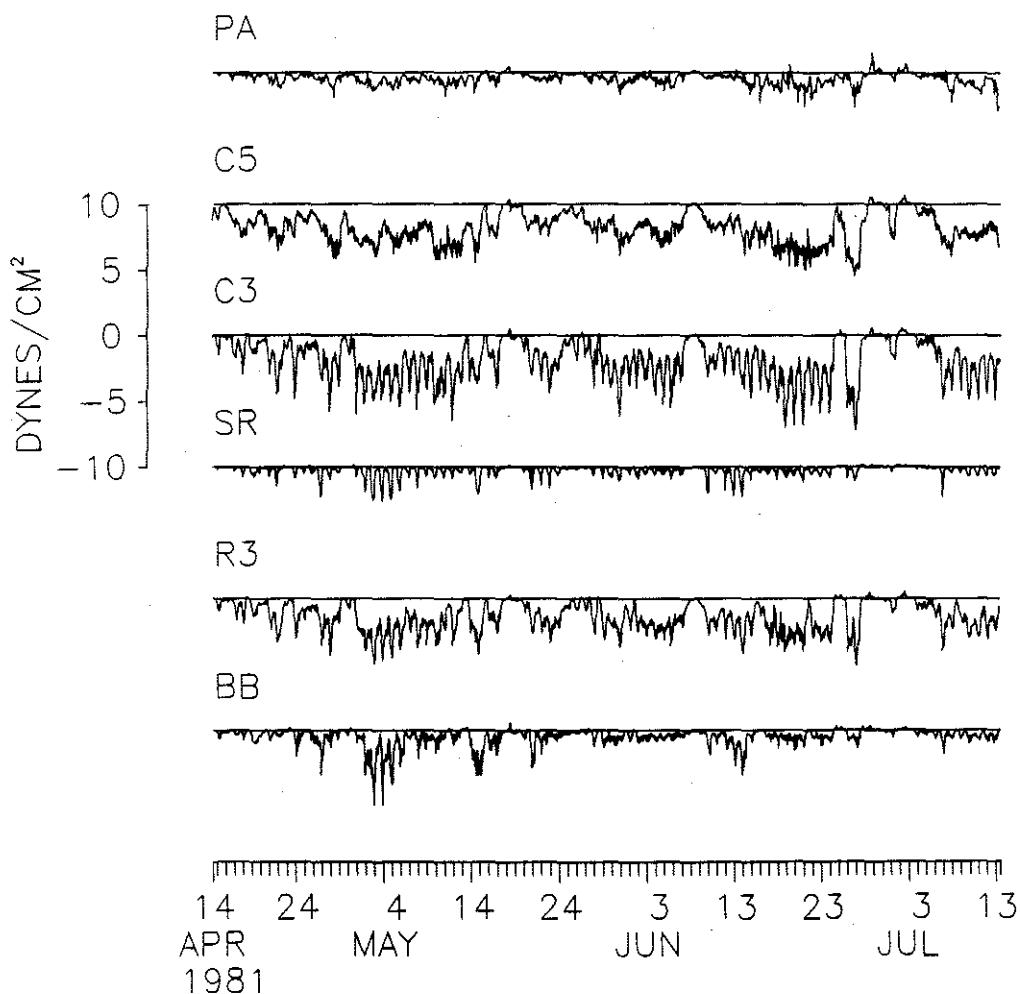


Figure 3. CODE-1 along-shelf wind stress time series are shown. Positive values are toward 317°T. The Sea Ranch wind record used to derive the wind stress time series shown here, and used throughout this paper, is a factor of 2 smaller than that shown in Mills and Beardsley (1983). The reason for this is discussed in Beardsley et al. (1987).

ALONG-SHELF WIND STRESS

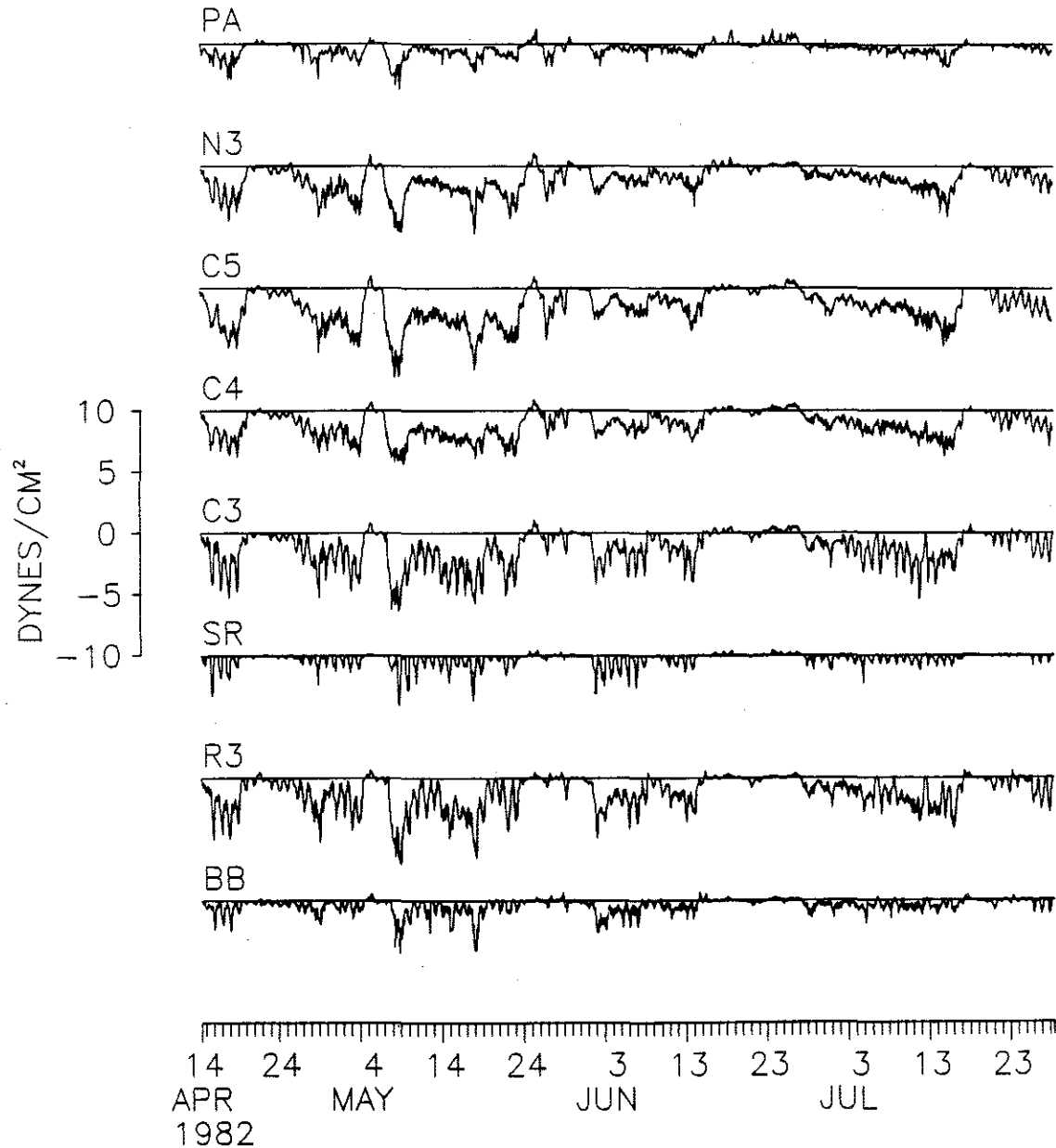


Figure 4. CODE-2 along-shelf wind stress time series are shown. Positive values are toward 317°T.

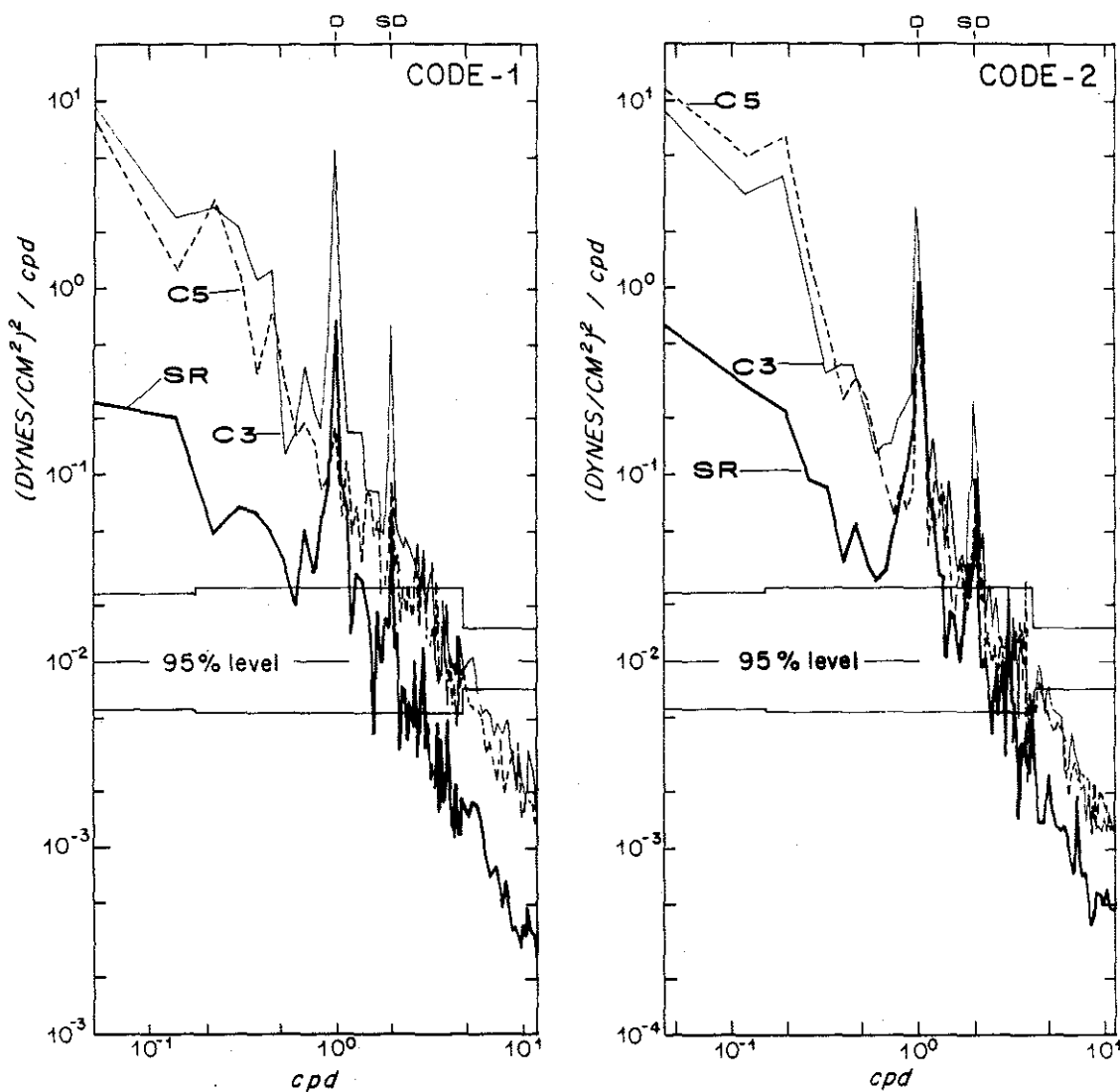


Figure 5. Variance density spectra for wind stress at Sea Ranch, C3, and C5 are shown. 90 day time series from CODE-1 (4/14/81 - 7/13/81) and 105 day time series from CODE-2 (4/14/82 - 7/28/82) were used after removal of the mean and a least squares fit linear trend. The diurnal (D) and semidiurnal (SD) frequencies are marked.

significant for all series, except at C5 during CODE-1. Statistics for the mean and diurnal band wind stress for all the records are reported in Table 2. The information in this table and these figures can be summarized as follows: (1) during the summer, the diurnal band ellipse is oriented within 20° of the along-shelf direction (317°T) everywhere except at Pt. Arena; (2) the direction of rotation of the diurnal stress vector is CW everywhere; (3) the largest diurnal stress variations are found at C3, while the largest mean stress is found at C5 during CODE-2 and is nearly equal at C3 and C5 during CODE-1; and (4) during the summer, diurnal band variability accounts for over 20% of the total variance at Sea Ranch, 10 to 20% at C3, R3 and Bodega Bay and less than 5% everywhere else. During the winter, only 5 to 10% of the total variance is in the diurnal band at Sea Ranch and Bodega Bay.

The phase of the diurnal wind stress is strongly keyed to the daily heating cycle (Beardsley et al., 1987). This is reflected in the high coherence in the diurnal band among most of the measurement sites. Of the six stations in CODE-1, the along-shelf component at four (Sea Ranch, C3, R3, and Bodega Bay) are highly coherent (> 0.9) with each other. The coherence between C5 and these four stations is lower (0.6 - 0.8), but still significant at the 95% confidence level. During CODE-2, all stations were coherent with each other at the 95% confidence level. In both years, Pt. Arena, which has very little energy in the diurnal band, is least coherent with the rest of the array.

1	2	3			4			5			6			7			8			9			10			11		
		Station	Total	U	V	U	V	CCW	Diurnal Band Ellipse Orientation (deg)	Mean	U	V	Total Variance $(\frac{\text{dynes}^2}{\text{cm}^2})$	% Variance in Diurnal Band														
		Code-1											4/14/81 - 7/13/81															
		Pt. Arena	4.0	2.1	1.9	2.6	1.4	47	-0.38	-0.45	0.38	3.4																
		C5	4.2	1.0	3.3	3.2	1.0	174	-0.40	-1.83	1.45	0.9																
		C3	131.6	12.2	119.4	81.4	50.1	164	0.14	-1.92	2.45	17.4																
		Sea Ranch	15.7	0.2	15.5	8.3	7.3	177	-0.03	-0.26	0.18	28.6																
		R3	46.1	3.8	42.2	26.4	19.6	164	0.31	-1.40	1.31	11.4																
		Bodega Bay	15.2	1.0	14.2	8.9	6.2	10	-0.09	-0.49	0.48	10.3																
		Code-2											4/14/82 - 7/28/82															
		Pt. Arena	7.1	3.8	3.3	5.1	2.0	48	-0.26	-0.38	0.50	4.0																
		N3	13.8	1.1	12.7	9.1	4.7	13	-0.36	-1.09	1.24	3.2																
		C5	16.9	2.6	14.3	11.9	5.0	17	-0.56	-1.52	2.28	2.1																
		C4	12.7	1.2	11.5	9.2	3.5	172	-0.05	-1.13	1.08	3.3																
		C3	70.4	8.0	62.4	45.8	24.7	163	0.12	-1.24	1.92	10.6																
		Sea Ranch	21.7	0.9	20.8	12.7	9.0	173	-0.01	-0.26	0.28	24.1																
		R3	64.7	2.6	62.1	38.4	26.3	170	0.13	-1.16	1.74	10.5																
		Bodega Bay	17.0	2.6	14.4	11.2	5.8	160	0.16	-0.40	0.41	12.1																
		Code - Winter											12/23/81 - 3/22/82															
		Sea Ranch	4.1	0.7	3.4	2.6	1.5	159	-0.01	-0.01	0.16	8.5																
		Bodega Bay	6.5	2.6	3.9	4.2	2.2	142	0.07	-0.07	0.37	5.6																

Table 2. Total variance density and variance density divided into cross-shelf (U), along-shelf (V), clockwise (CW), and counter-clockwise (CCW) rotating components of the diurnal band ($1.00 \pm .07$ cpd) wind stress are listed in columns 2-6. Column 7 gives the average ellipse orientation of the diurnal band fluctuations, measured clockwise from the along-shelf direction (317°). The mean cross- and along-shelf wind stress are given in columns 8 and 9, the total variance in each wind stress record in column 10, and the percent variance accounted for by the diurnal band is in column 11.

ii. TIME DOMAIN

The variation in time of the amplitude of the diurnal wind stress is evident in the complex demodulation time series (see Appendix A) shown in Figures 6 and 7 for Sea Ranch, C3 and C5. Although both 24 and 12 hour periods were included in the analysis carried out for both along-shelf and cross-shelf wind stress components, only the amplitude and phase of the diurnal period along-shelf stress is shown. A constant value for phase indicates that a true 24-hour signal has been isolated and is phase-locked to the day-night cycle. A phase of -90° corresponds to maximum equatorward wind stress at 1600 PST. The equatorward stress peaks at about 1400 to 1500 PST at Sea Ranch, and an hour or two later at C3.

The diurnal stress is usually largest at C3 during both CODE-1 and -2. Amplitude modulations in the along-shelf diurnal wind stress are significantly correlated at the 95% confidence level at Sea Ranch, C3, R3 and Bodega Bay during CODE-1 (Table 3). C5 is uncorrelated in time with the other locations and its phase (not shown) is erratic. Point Arena was not included in the calculation, since the diurnal wind stress there was not highly coherent with the rest of the array. During CODE-2, all the amplitude modulations are correlated with each other except for Sea Ranch with C4, C5, and N3. As with the coherence in the diurnal band, the correlations seem to show groupings among Sea Ranch, C3, R3, and Bodega Bay and N3, C4, and C5 (Table 3). This is suggestive that most of the time the first group of sites falls within the nearshore zone defined in Beardsley et al. (1987) (see Figures 16 and 17 in that paper), while the second group of stations lies in the intermediate zone. These boundaries are of course not fixed, which

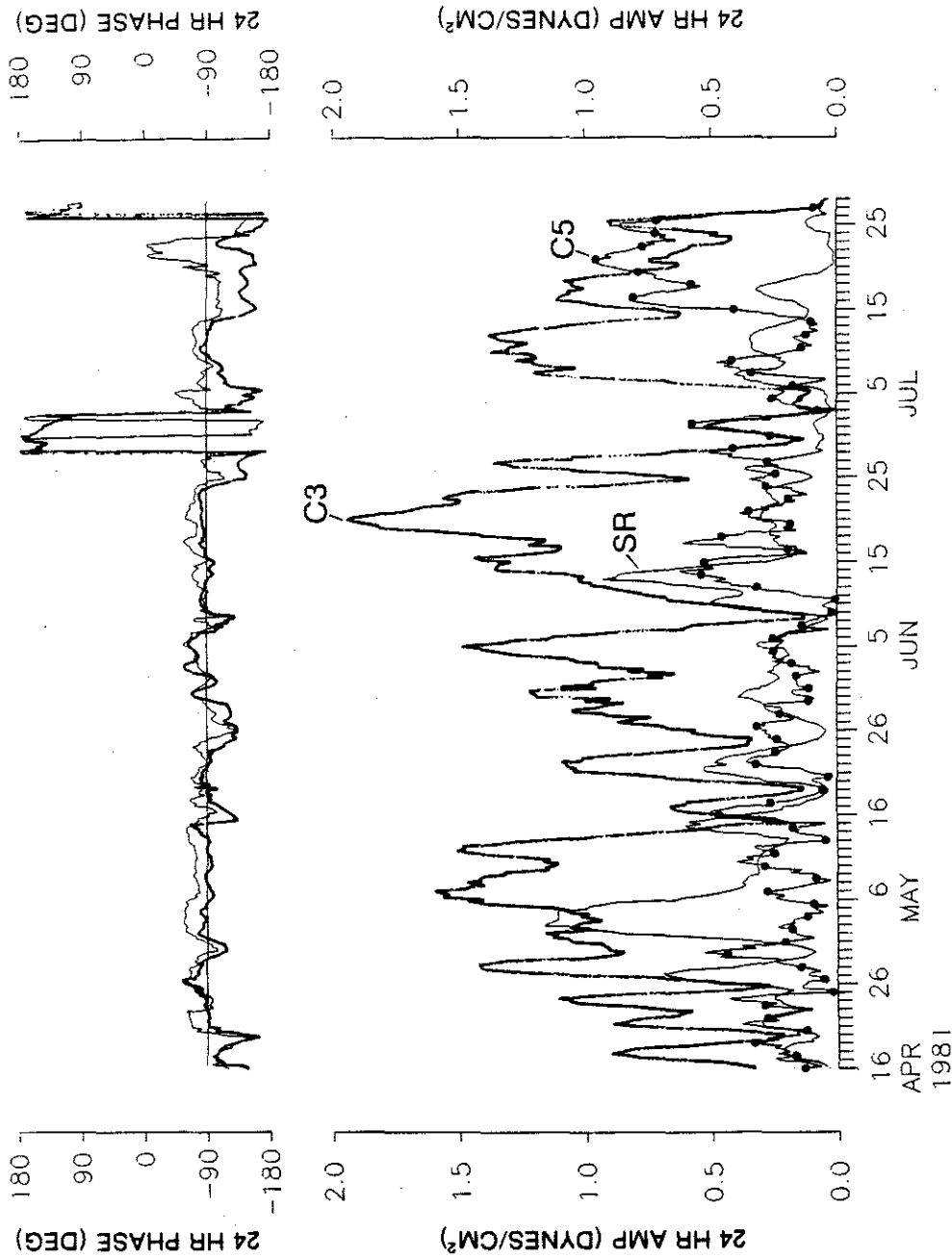


Figure 6. Amplitude and phase of the diurnal along-shelf wind stress during CODE-1 at Sea Ranch and C3 are shown. Amplitude only is shown for C5 because the phase is erratic. There are amplitude and phase estimates every six hours, each representing a least squares fit done over a 48 hour period. A phase of -90° corresponds to peak equatorward wind stress at 1600 PST.

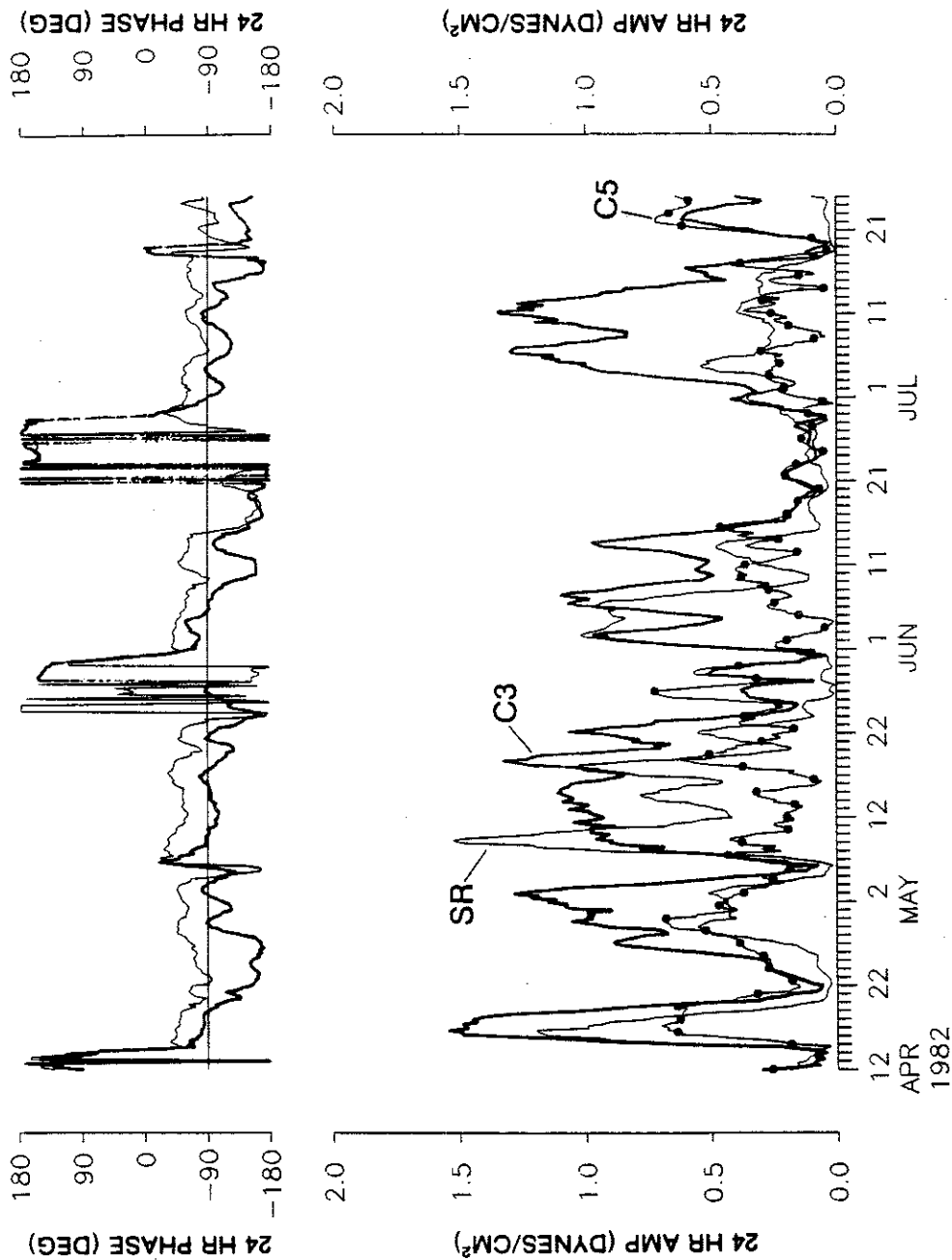


Figure 7. Amplitude and phase of the diurnal along-shelf wind stress during CODE-2 at Sea Ranch and C3 are shown. Amplitude only is shown for C5 because the phase is erratic. There are amplitude and phase estimates every six hours, each representing a least squares fit done over a 48 hour period. A phase of -90° corresponds to peak equatorward wind stress at 1600 PST.

CODE-1

Based on 408 6-hourly points (4/17/81 0000 - 7/27/81 1800 GMT)

	<u>SR</u>	<u>C3</u>	<u>C5</u>	<u>R3</u>
SR	1.00			
C3	0.39	1.00		
C5	-0.26	0.02	1.00	
R3	0.61	0.62	0.13	1.00
BB	0.87	0.30	-0.11	0.70

CODE-2

Based on 416 6-hourly points (4/12/82 0000 - 7/25/82 0000 GMT)

	<u>N3</u>	<u>SR</u>	<u>C3</u>	<u>C4</u>	<u>C5</u>	<u>R3</u>
N3	1.00					
SR	0.23	1.00				
C3	0.43	0.68	1.00			
C4	0.80	0.20	0.61	1.00		
C5	0.75	0.10	0.38	0.80	1.00	
R3	0.47	0.68	0.82	0.53	0.35	1.00
BB	0.44	0.83	0.78	0.36	0.28	0.84

Table 3. Correlation coefficients for zero time lag between amplitude modulation of diurnal along-shelf wind stress at various measurement sites. Correlation is not significantly higher at any other time lag. Based on both the autocorrelation time scales of the amplitude modulations, and the fact that each amplitude estimate is calculated for a 48-hour period, every eighth point is taken to represent an independent estimate. The number of degrees of freedom, found by dividing the number of 6-hourly points by 8, equals 51 for CODE-1 and 52 for CODE-2. Correlation coefficients greater than 0.28 are significant at the 95% confidence level.

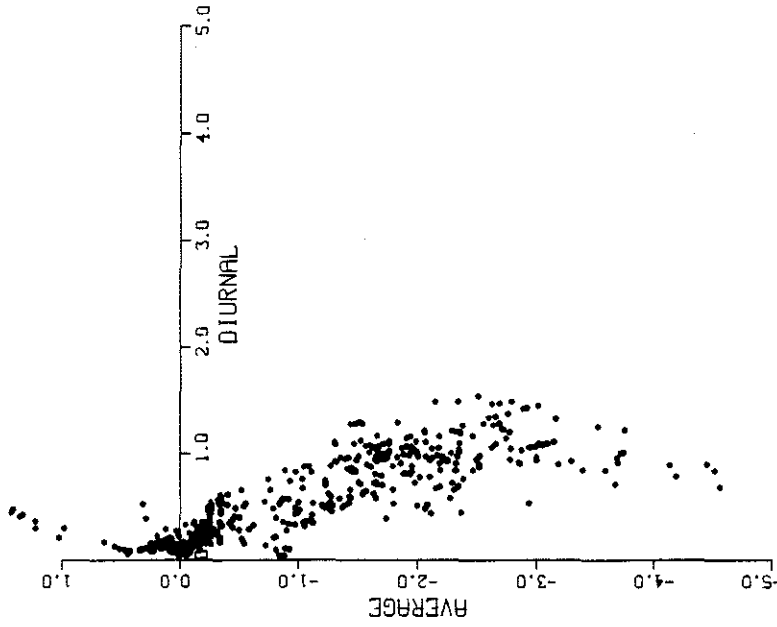
may account for why C3 and C4 appear to sometimes correspond more closely to Sea Ranch and sometimes to C5.

The diurnal variations in wind stress are largest during periods of strong equatorward wind stress. This is clearly seen in scatter plots of diurnal versus mean wind stress at C3 for CODE-1 and -2 shown in Figure 8. A similar relationship between average and diurnal components in the wind records (see Figure 7 of Beardsley et al., 1987) demonstrates that the increase in diurnal wind stress with increasing mean stress is only partially a result of the fact that stress is not a linear function of wind, so that changes in the mean wind affect the diurnal period wind stress. A positive correlation between low frequency and diurnal winds was also seen by O'Brien and Pillsbury (1974) for the nearshore winds off Oregon, but farther offshore, Burt et al. (1974) observed a negative correlation.

B. HEAT FLUX

All of the meteorological buoys deployed in CODE-1 and CODE-2 measured air and water (at 1 m depth) temperature, and most measured insolation as well. Based on shipboard measurements, the relative humidity was seen to vary very little, and a constant value of 85% at 3.5 m above sea level was assumed. Using these data in the bulk aerodynamic formulas, hourly values of sensible and latent heat flux were obtained. A daily estimate for cloud cover, obtained as a function of the ratio between the measured insolation and the predicted cloud-free insolation, was used to obtain daily values of back-scattered long-wave radiation. A complete discussion of these derived variables is given in Beardsley et al. (in prep.). Since insolation is the major con-

C3 CODE-2



C3 CODE-1

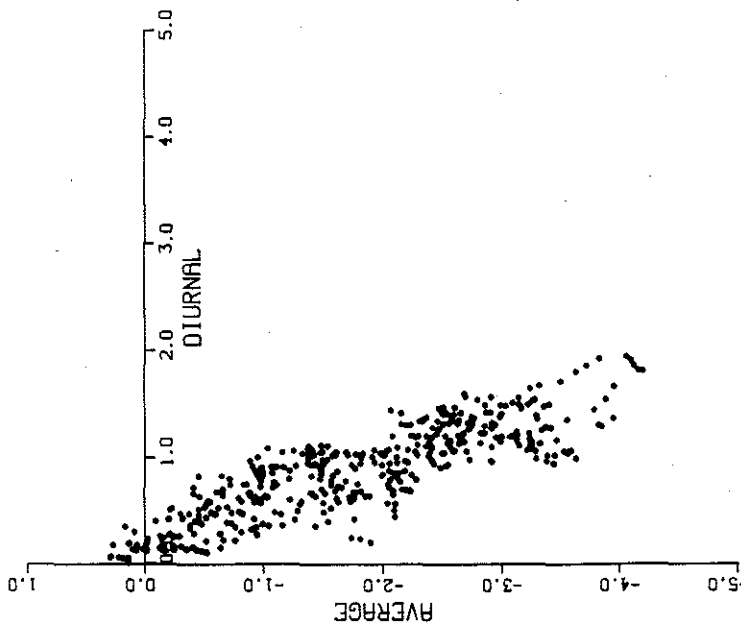


Figure 8. Scatter plots of mean versus diurnal wind stress at C3 are shown for CODE-1 and -2. Values are calculated over 48 hour periods starting every six hours. Units are dynes cm^{-2} .

tributor to the net heat flux and most of the time it varies little over the array, the surface heat flux at C3, the center of the array, was taken as representative of the area. Figure 9 shows the average daily surface heat flux for CODE-1 and -2. For CODE-1 (-2), net incoming solar radiation reaches a maximum of 73 (77) mw cm^{-2} at about 1200 PST. Sensible and latent heat flux are approximately constant over the day, and together with long-wave radiation (assumed to be constant over the day for lack of information on its diurnal variability) cause a heat loss of about 6 (4) mw cm^{-2} . The slight irregularity in the CODE-1 insolation data shown in Figure 9 was caused by a shadow from a support on the C3 buoy tower.

5. DESCRIPTION OF THE DIURNAL PERIOD CURRENTS

Time series plots of high-passed (the filter is described in Appendix B; its half-power point is at 0.028 cph) hourly-averaged currents reveal discernible bursts of diurnal period variability ranging in duration from one to several days. The 10 m current records from C3 are shown in Figure 10 as an example. The largest event, with currents over 40 cm s^{-1} , occurs during May 12-14, 1982. Comparison of kinetic energy spectra (Figure 11) from different depths shows that diurnal energy is surface-intensified during the summer. At C3 and R3, comparison of spectra calculated from the winter with those from the summer shows that the diurnal is the only frequency at which kinetic energy is larger during the summer. Figure 11 shows the tidal band total kinetic energy spectra at C3 for the 10 and 70 m currents for CODE-2 and the 10 m currents during the winter. There is no evidence of significant inertial energy during the summer in any

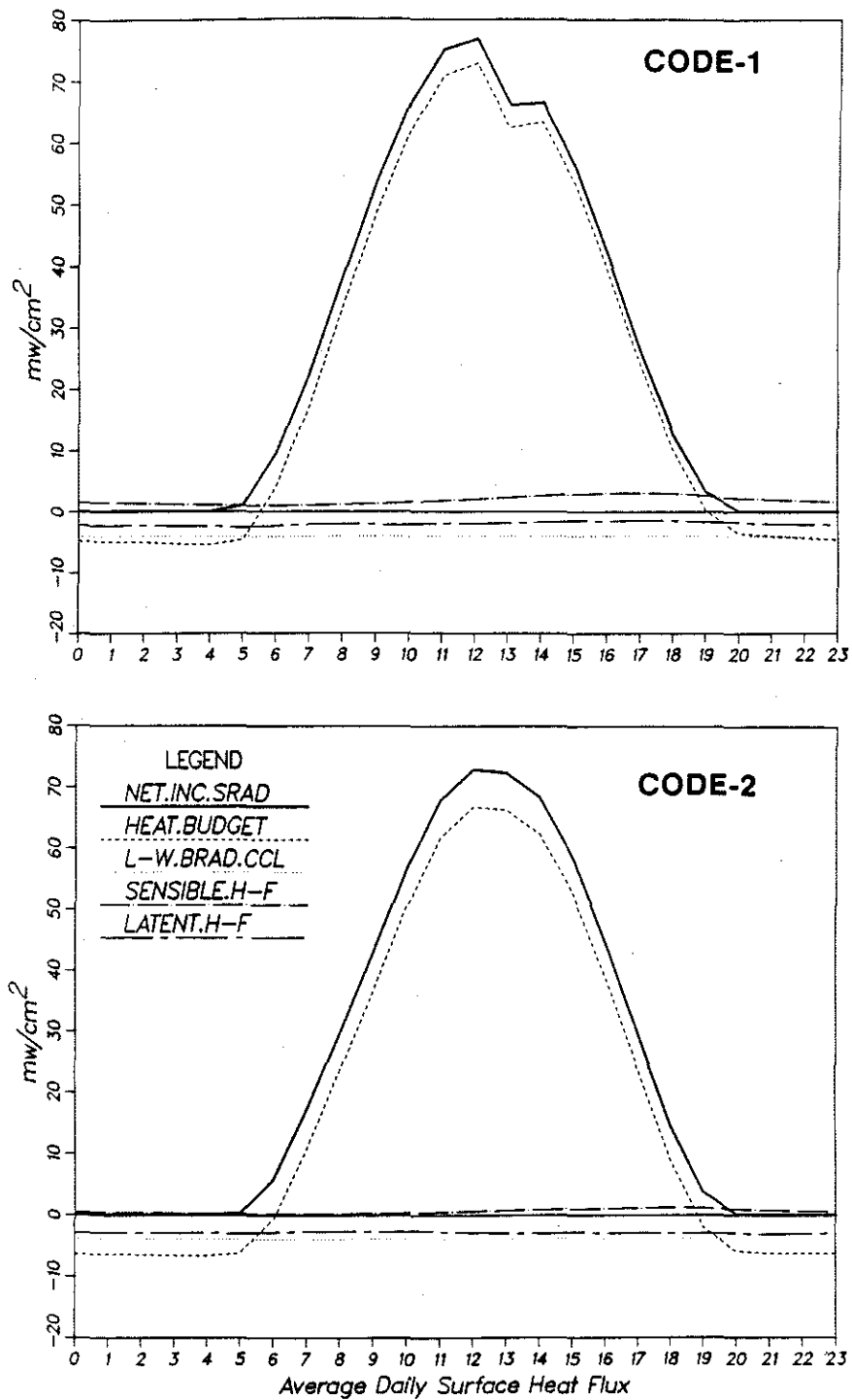


Figure 9. The average daily surface heat flux cycle is shown for the CODE-1 (4/14/81 - 7/13/81) and -2 (4/14/82 - 7/27/82) experiments. Positive values mean the heat flux is directed into the ocean. HEAT.BUDGET = net heat flux, NET.INC.SRAD = net incoming solar radiation, L-W.BRAD.CCL = long-wave radiation backscattered by cloud cover, SENSIBLE.H-F = sensible heat flux, LATENT.H-F = latent heat flux. Time in hours PST is given on the x-axis.

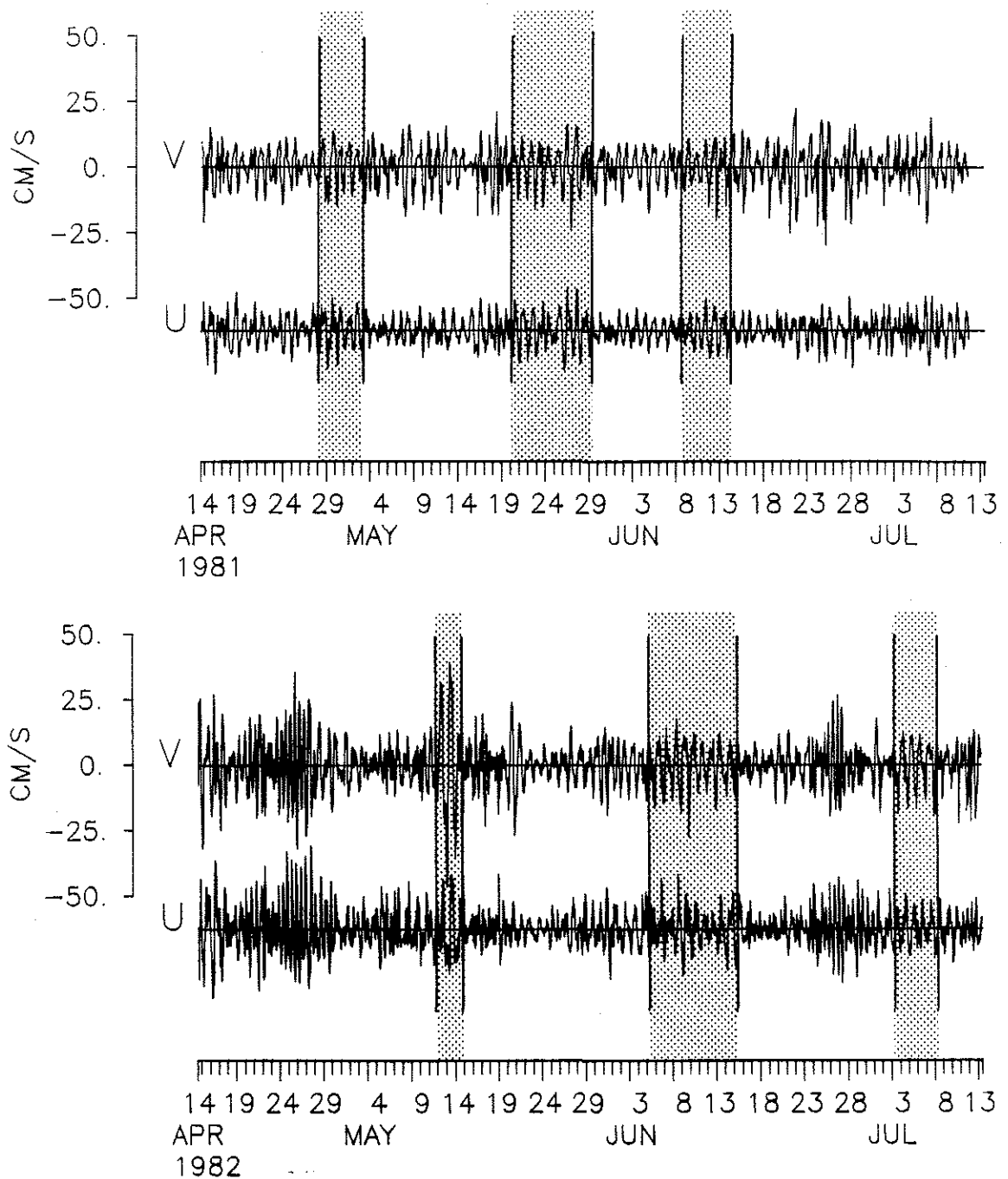


Figure 10. Time series of high-passed along-shelf (V) and cross-shelf (U) currents measured at 10 m depth at mooring C3 are shown for CODE-1 and -2. Time periods with especially large amplitude diurnal period currents are stippled. The high-pass filter used is described in Appendix B.

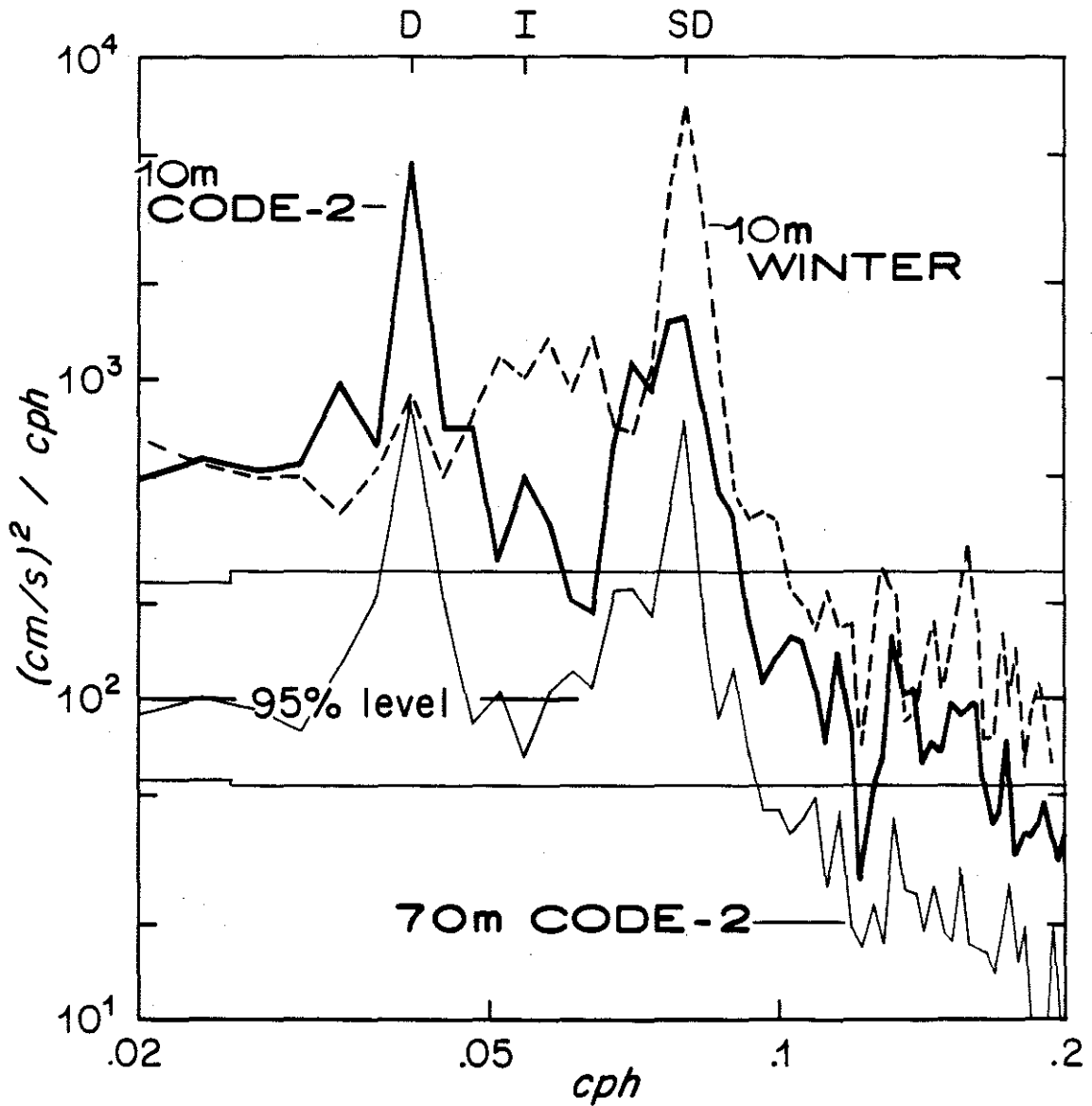


Figure 11. Kinetic energy density spectra for the tidal band currents measured at C3 at 10 and 70 m depths for a 90-day period starting 4/14/82, and at 10 m depth for 90 days starting 12/12/81. Time series were demeaned and detrended before Fourier transforming. The diurnal (D), inertial (I), and semidiurnal (SD) frequencies are marked.

shelf current spectra, whereas the winter current spectra show generally elevated energy between the diurnal and semi-diurnal frequencies, and some exhibit a distinct inertial peak.

Empirical orthogonal function (EOF) analysis in the frequency domain has been employed here to describe the spatial structure of the diurnal band variability. Amplitude and phase, relative to an arbitrary reference, of the coherent part of each input time series is obtained for each mode. This method of analysis is discussed further in Wallace and Dickinson (1972). The specifics of the calculations used here are as follows. For each EOF analysis, a cross-spectral matrix including along- and cross-shelf components of wind stress and currents was formed. Horizontal wind stress and current ellipses were constructed from the amplitudes and phases of these two orthogonal horizontal components. The objective was to determine the spatial structure of the diurnal band current field and its relationship to the wind stress fluctuations coherent with it. The currents in cm s^{-1} were weighted by 1.0, and the wind stress in dynes cm^{-2} by 0.1, so that the modal structures were largely determined by the currents. A frequency band width of 0.92 to 1.08 cpd (periods between 26.1 and 22.2 hours) was used. This includes all of the diurnal tidal constituents, and excludes the inertial frequency.

Figures 12 and 13 show the first mode at each mooring along the C-line in CODE-1 and -2, respectively. The EOF calculation was done separately for each mooring, and phases are referred to a value of zero for the along-shelf component of velocity at the uppermost instrument. The coherent diurnal wind stress from the closest wind measurement site is shown above each mooring site, as well as a vector

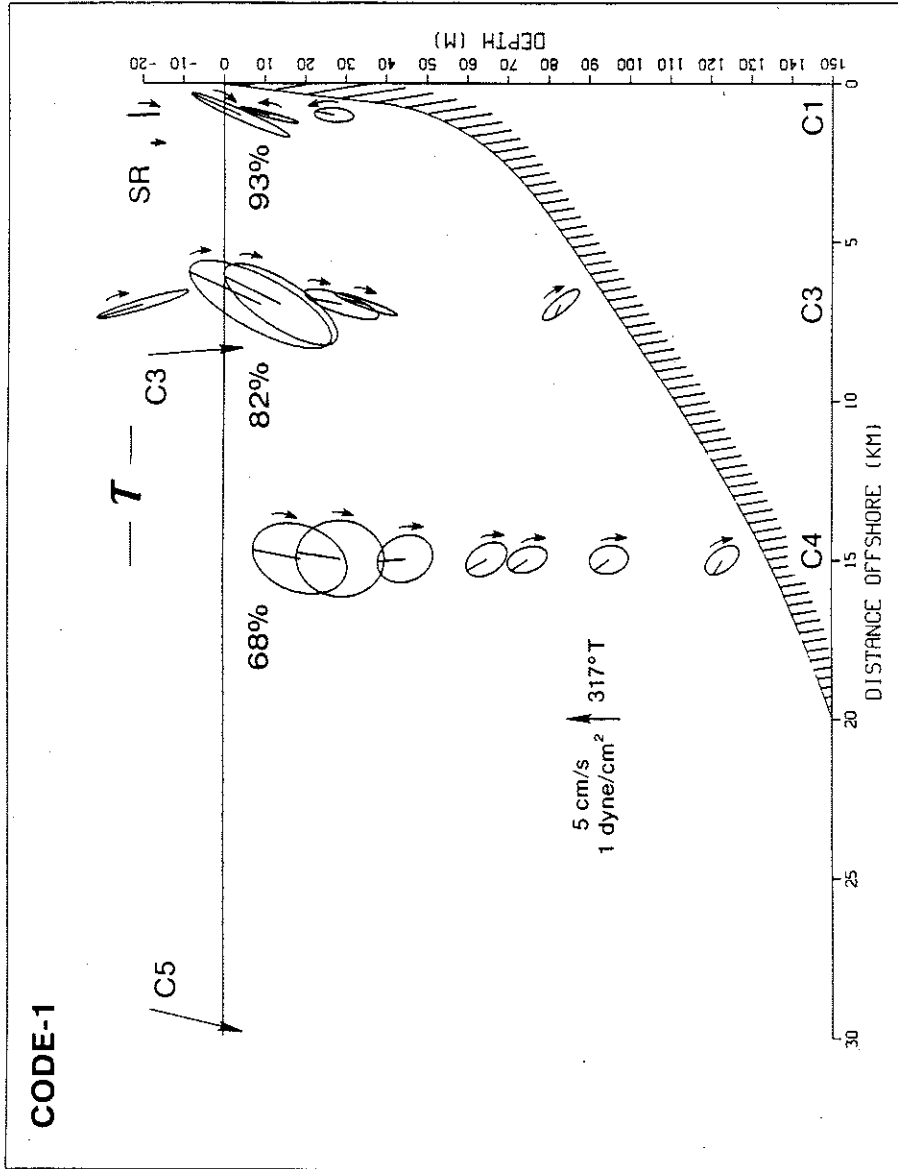


Figure 12. The first mode diurnal band horizontal current and wind stress ellipses calculated at the CODE-1 C1, C3, and C4 moorings are shown. Sea Ranch stress was included with C1 currents, and C3 stress with C3 currents. The percent variance accounted for by the first mode at each mooring is given. The lines extending from the ellipse centers indicate the direction of the vector at a common time. Phases are referenced to a value of zero for the along-shelf velocity at the uppermost current meter on each mooring. The mean wind stress vectors at Sea Ranch, C3, and C5 are also shown.

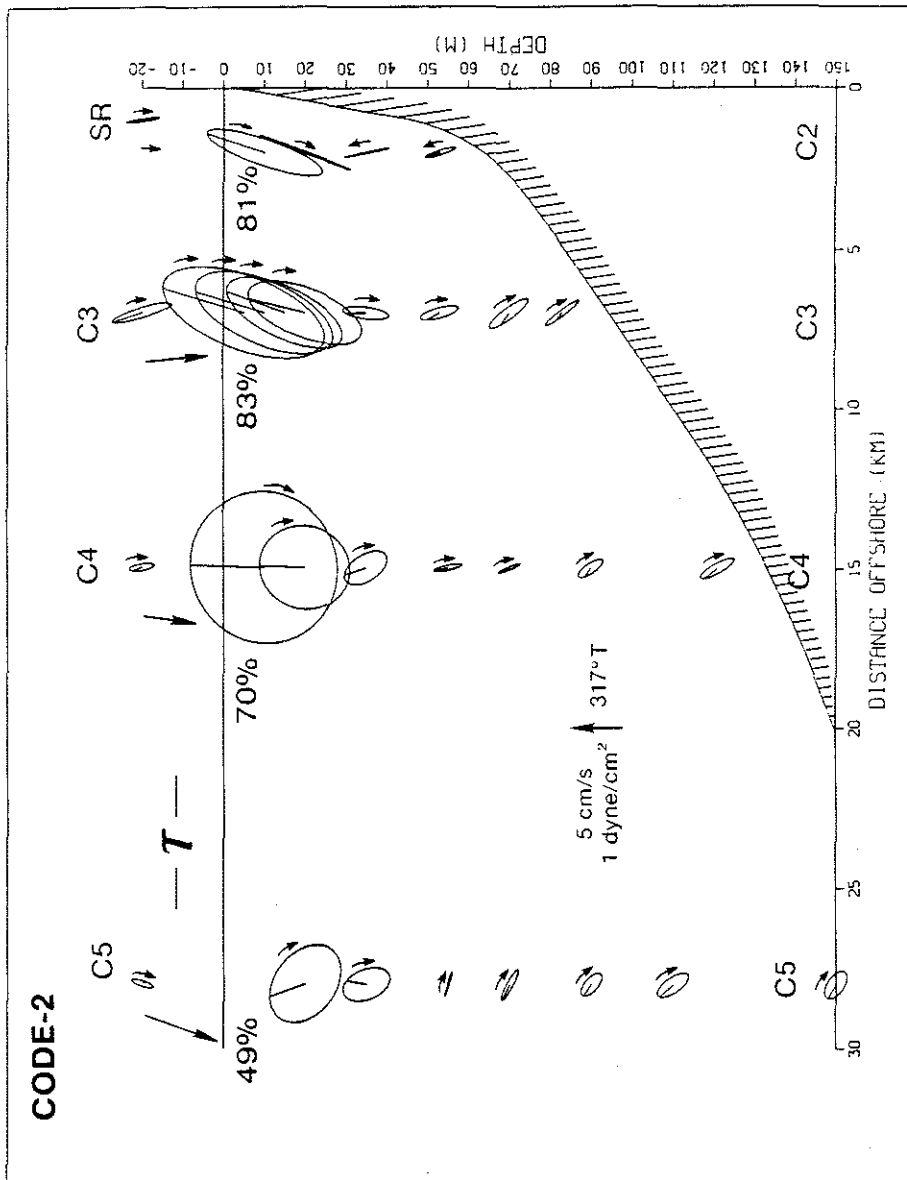


Figure 13. The first mode diurnal band horizontal current and wind stress ellipses calculated at the CODE-2 C2, C3, C4, and C5 moorings are shown. Sea Ranch wind stress was included with the C2 currents, C3 stress with the C3 currents, and likewise for C4 and C5. The percent variance accounted for by the first mode at each mooring is given. The lines extending from the ellipse centers indicate the direction of the vector at a common time. Phases are referenced to a value of zero for the along-shelf velocity at the uppermost current meter on each mooring. The mean wind stress vectors are also shown.

indicating the mean stress at that location. The percent of the total variance accounted for by the lowest mode is given next to each mooring. The coherence between the lowest mode and velocity components at each depth, or the wind stress, are listed in Table 4. The modes are dominated by the upper currents, as evidenced by the fact that the percent variance accounted for by the mode decreases with depth. A large percentage of the wind stress variance is coherent with these vertical modes. Much of the variance in the lower currents is in the second mode (not listed) at each site. The ellipses in these modes are oriented along-shelf, rotate CW, and have semi-major axes of one to two cm s^{-1} . No calculations were done for C2 and C5 during CODE-1 because the vertical resolution at those sites was poor. The size of the currents and wind stresses may be compared directly between moorings and deployments because all have been multiplied by the appropriate factors involving the eigenvalues. Phases may only be compared along a given mooring. To focus attention on the upper water column, results from the first mode calculated using all the current measurements above 40 m and the wind stress measurements along the C-line are presented in Figures 14 and 15 on an expanded vertical scale for the two experiments. Now, both magnitudes and phases may be directly compared within a given figure.

The following observations from Figures 12 through 15 are notable: (1) average diurnal band currents of over 6 cm s^{-1} are observed near the surface; (2) over the shelf, the first vertical mode at each site accounts for over 68% of the variance; (3) the percent of variance accounted for by a single vertical mode decreases in the offshore direction - at C5, over the slope, slightly less than half the

Station	CODE-1		Along-shelf	Station	CODE-2		Along-shelf
	Depth	Cross-shelf			Depth	Cross-shelf	
C1	4	0.84	0.98	C2	10	0.71	0.94
	7	0.87	0.99		20	0.62	0.91
	11	0.76	0.93		35	0.20	0.58
	23	0.63	0.92		53	0.21	0.49
	27	0.45	0.85		SR τ	0.30	0.56
	SR τ	0.05	0.83				
C3	9	0.75	0.96	C3	5	0.82	0.96
	14	0.80	0.95		10	0.81	0.97
	29	0.44	0.76		15	0.82	0.96
	35	0.38	0.66		20	0.77	0.94
	83	0.67	0.53		35	0.12	0.53
	C3 τ	0.79	0.80		53	0.23	0.38
					70	0.54	0.37
			83	0.62	0.44		
			C3 τ	0.68	0.65		
C4	19	0.70	0.85	C4	10	0.89	0.93
	29	0.75	0.82		20	0.83	0.83
	45	0.61	0.67		35	0.42	0.45
	65	0.41	0.62		55	0.04	0.25
	75	0.35	0.58		70	0.03	0.13
	95	0.41	0.49		90	0.16	0.14
	123	0.65	0.59		121	0.38	0.38
	C3 τ	0.55	0.51		C4 τ	0.64	0.60
			C5	20	0.78	0.80	
				35	0.34	0.63	
				55	0.17	0.03	
				70	0.42	0.16	
				90	0.32	0.25	
				110	0.38	0.43	
				150	0.51	0.29	
				250	0.47	0.43	
			350	0.28	0.50		
			C5 τ	0.35	0.39		

Table 4. The fraction of the indicated wind stress and current records accounted for by the first mode at each mooring. This is the same as the coherence between the time series and the mode.

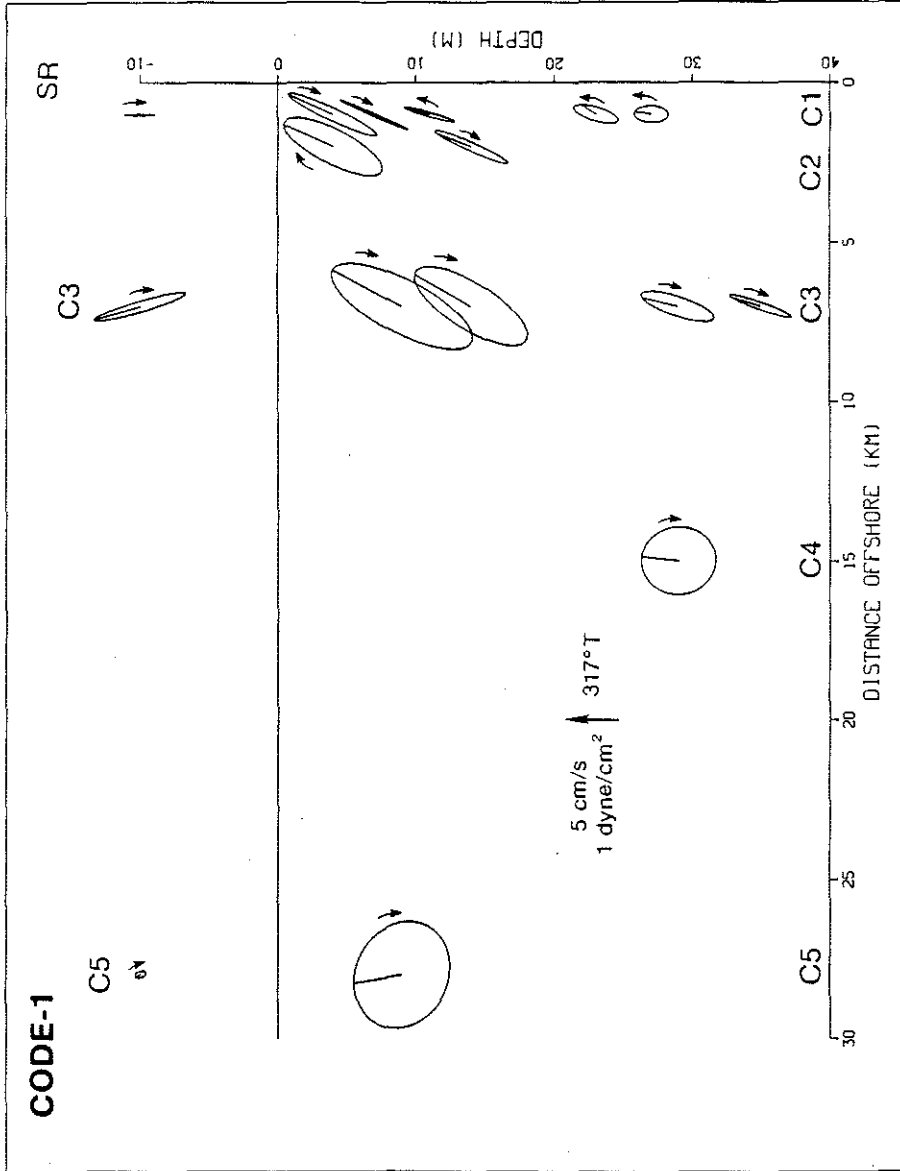


Figure 14. The first mode diurnal band upper water column horizontal current and wind stress ellipses along the C-line are shown for CODE-1. This mode accounts for 73% of the variance. Phases are referenced to a value of zero for the along-shelf current at the top current meter closest to the coast. The current record from the 19 m instrument at C4 ends one day earlier than the other records, and so is not included here.

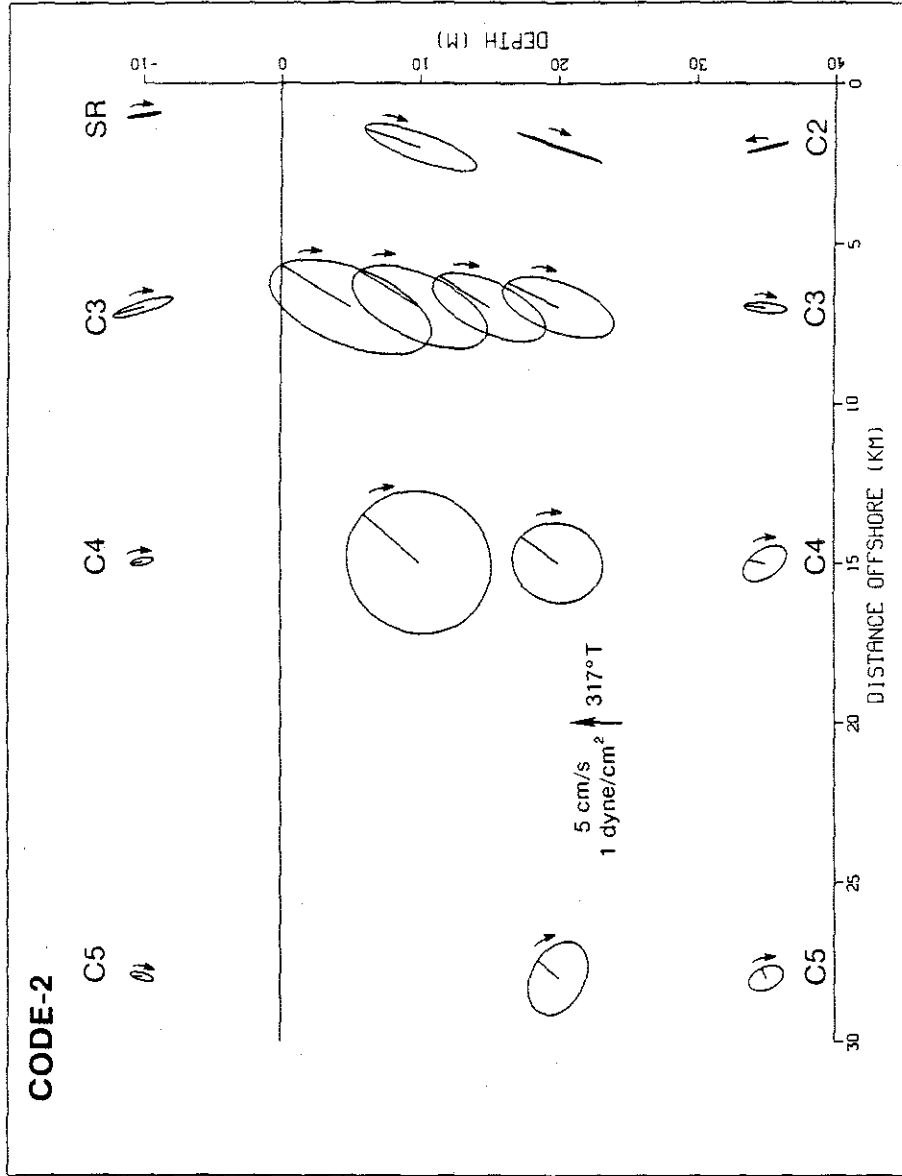


Figure 15. The first mode diurnal band upper water column horizontal current and wind stress ellipses along the C-line are shown for CODE-2. This mode accounts for 80% of the variance. Phases are referenced to a value of zero for the along-shelf current at the top current meter closest to the coast.

variance is in the first mode; (4) all current vectors rotate CW, except near the bottom at C1 during CODE-1 and C2 during CODE-2; (5) the size of the diurnal band currents decreases with depth down to about 30 to 40 m, and below that is relatively constant; (6) the near-surface ellipses are oriented to the right of the wind stress fluctuations; (7) the near-surface ellipses become less elongated in the seaward direction; (8) near-surface currents are nearly in phase with the wind stress; (9) the phase of the currents decreases with depth (i.e. the lower ones lead the upper ones); and (10) the current ellipses all across the shelf are nearly identical in size during the two summers, as are the wind stresses. Note that all of these results represent an average over the whole 90 day (CODE-1) or 105 day (CODE-2) time period.

6. CORRELATION BETWEEN WIND STRESS AND CURRENTS

The pronounced surface intensification of the diurnal currents, together with the presence of strong atmospheric forcing at the diurnal frequency, leads us to investigate the connection between these two phenomena. Three avenues have been explored in an effort to determine if the enhanced diurnal currents are consistent with direct forcing by the wind stress. The first makes use of the non-stationarity of the amplitude of the wind stress as discussed in Section 4, the second considers the horizontal structure of the diurnal wind stress and current fields, and the third approach examines the vertical structure of the currents.

These points are addressed by looking at the correlations between the diurnal amplitude modulation (determined by the complex demodu-

lation technique described in Appendix A) of the along-shelf component of wind stress and along-shelf component of currents at depths less than 35 m. These are given in Table 5. The amplitude modulation of the diurnal currents at depths to at least 20 m, but not as deep as 35 m, is strongly correlated with the amplitude modulation of the along-shelf wind stress. The correlations are greatest between the currents at a given mooring and the wind stress directly above it. Table 5 indicates that: (1) the diurnal currents at C1 in CODE-1 are highly correlated with the diurnal wind stress at Sea Ranch, and slightly less so with C3; (2) the near-surface diurnal currents at C2 are correlated with Sea Ranch and C3 wind stress, more so with Sea Ranch during CODE-1 and C3 during CODE-2; (3) C3 diurnal currents are significantly correlated with wind stress at C3, but only marginally (CODE-2) or not at all (CODE-1) with Sea Ranch and C4; and (4) C4 diurnal currents are correlated with wind stress at C4 and marginally with that at C3. There is a general pattern of highest correlations near the coast, decreasing in the offshore direction, and near the surface, decreasing with depth. The diurnal current amplitude modulations are highly coherent in the vertical at a given mooring site. The correlation drops off with cross-shelf distance more rapidly for the currents than the wind stress.

In this and previous sections, it has been established that the diurnal currents over the shelf are surface-intensified, CW-rotating, relatively depth-independent in the lower part of the water column, and correlated with the local diurnal wind stress in the upper part of the water column. Diurnal currents over the northern California shelf may be generated by two sources, tidal and atmospheric forcing. The

CODE-1				CODE-2					
Based on 334 6-hourly points (4/18 - 7/10 1981)				Based on 445 6-hourly points (4/05 - 7/25 1982)					
Wind Stress: Sea Ranch C3				Wind Stress: Sea Ranch C3	C4	C4	C5	C5	
Current				Current					
C1	4 m	0.79	0.47	C2	10 m	0.52	0.60	0.31	0.11
	7 m	0.68	0.42		20 m	0.40	0.52	0.31	0.28
	11 m	0.63	0.30		35 m	-0.05	-0.05	0.07	0.16
	23 m	0.54	0.23	C3	5 m	0.20	0.38	0.28	0.10
	27 m	0.52	0.11		10 m	0.26	0.37	0.19	0.01
C2	4 m	0.62	0.27		15 m	0.27	0.44	0.18	0.01
	14 m	0.27	0.16		20 m	0.09	0.28	0.06	-0.05
C3	9 m	-0.21	0.36	35 m	0.01	0.11	0.11	0.16	
	14 m	-0.14	0.48	C4	10 m	0.00	0.26	0.40	0.32
	29 m	-0.08	0.49		20 m	0.08	0.30	0.38	0.33
	35 m	-0.13	0.32		35 m	-0.03	0.10	0.21	0.15
C4	29 m	-0.25	-0.09	C5	20 m	-0.06	0.06	0.26	0.25
Degrees of freedom = 42				Degrees of freedom = 56					
R > 0.30 is significant at 95% level				R > 0.26 is significant at 95% level					

Table 5. Correlation coefficients between amplitude modulations of along-shelf wind stress and currents within 35 m of the sea surface for zero time lag. Correlations at time lags up to 48 hours are never significantly greater than those reported here.

foregoing analysis indicates that the diurnal currents in the nearshore upper layer of the ocean may be identified with the atmospherically forced part. In Section 7, it will be shown that the weaker currents below the surface layer are consistent with model predictions for the tidally-driven flow. In Section 8, models for the generation of diurnal currents by the diurnal wind stress will be discussed and compared with the observations.

7. DIURNAL TIDAL CURRENTS

Least squares tidal analysis (Boon and Kiley, 1978) of coastal sea level and bottom pressure measurements obtained in CODE, as well as historical data, show that the largest diurnal constituent along the northern California shelf is the luni-solar (K_1) with a period of 23.93 hours. The K_1 amplitude in the CODE region is about 37 cm. In general the S_1 constituent, with a period of 24.00 hours, is of order 1 cm on the California coast (Zetler, 1971) and Sauvel (1985) reports values of 2 cm from response analysis of pressure records from CODE-1. The S_1 tide is primarily due to radiational rather than gravitational effects and includes the action of the atmospheric tide on the sea surface, diurnal wind effects, and to a lesser extent steric changes due to thermal heating (Zetler, 1971). Based on the observed daily variations in temperature, the steric contribution to sea level change due to diurnal heating is estimated to be only about 0.1 cm in the CODE area. The next largest diurnal tidal constituent after K_1 is the principal lunar (O_1) with a period of 25.82 hours. The O_1 amplitude is approximately 23 cm in the CODE area. By contrast, the largest semi-diurnal constituent (M_2) has an

amplitude of about 55 cm in this region. Harmonic constants for the principal semidiurnal and diurnal constituents calculated from bottom pressure records in CODE-1 and CODE-2 are reported in Brown, Irish, and Erdman (1983) and Brown (1985), respectively. As reported by Munk, Snodgrass, and Wimbush (1970), both the phase and amplitude of the K_1 tide increase towards the north along the coast of California. Through fitting to pressure observations off southern California, they interpreted the K_1 tidal response as the sum of Kelvin, Poincaré and forced waves with amplitudes of 21, 24, and 9 cm, respectively, at the coast. This combination produces tidal currents of order 1 cm s^{-1} over the shelf.

The diurnal frequency is below the inertial frequency for the CODE latitude, so Poincaré and freely propagating internal waves are not permitted. One might anticipate, however, the presence of class two (vorticity) coastal-trapped waves (CTW), as have been observed off Vancouver Island to the north by Crawford and Thomson (1982), in addition to the barotropic Kelvin wave². In fact, Noble et al. (1987) have found the diurnal currents over the outer continental margin adjacent to the CODE area to be consistent with the combination of a Kelvin and first mode CTW. The tidal currents associated with these waves can be estimated from pressure measurements.

Figure 16 shows the K_1 amplitude and phase for eight coastal sea level records adjusted for atmospheric pressure (provided by J. Allen and G. Halliwell of Oregon State University) and seven bottom pressure

² The term "barotropic Kelvin wave" as used here, refers to the zeroth mode CTW. It is associated primarily with deflection of the sea surface, and has little signature in the density field. Due to the presence of topography, cross-shelf velocities may be non-zero.

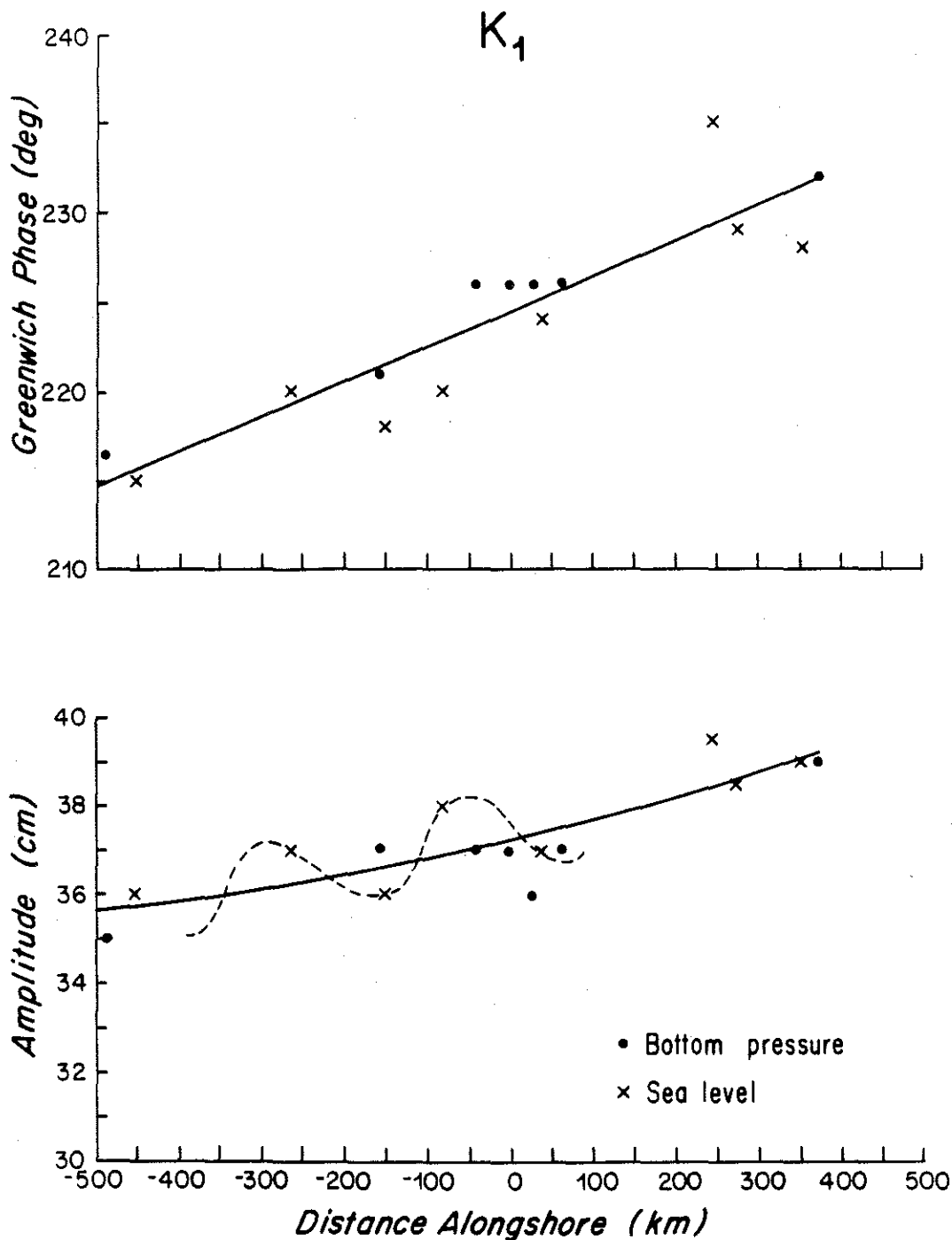


Figure 16. Amplitude and phase for the K_1 tidal constituent determined from sea level and bottom pressure measurements along the coast of California. Alongshore distances are referred to the CODE C-line. The solid line indicates the best quadratic fit. The dashed line on the amplitude plot indicates deviation from the large-scale pressure field that would be caused by a phase-locked first mode coastal-trapped wave with 1 cm amplitude and 250 km wavelength.

records from the 130 m isobath (provided by W. Brown and J. Irish of University of New Hampshire) with the solid line showing the best quadratic fit. These data, extending over 900 km of the California coastline, are representative of the large-scale pressure field. Barotropic tidal currents calculated from these data according to the method of Battisti and Clarke (1982a) are oriented along-shelf, rotate counter-clockwise (CCW) and have semi-major axes of 1 to 2 cm s^{-1} . The details of how this calculation is performed are discussed for the semidiurnal tidal currents in Rosenfeld and Beardsley (1987). Also described in that paper is a numerical scheme for calculating the wavelength and cross-shelf pressure and velocity structure for a barotropic Kelvin wave. A Kelvin wave at the K_1 period is found to have a wavelength of 16,200 km. With a coastal amplitude of 37 cm, the resultant velocities over the shelf are of amplitude 1 to 2 cm s^{-1} with CCW rotation, consistent with the predictions from the Battisti and Clarke (1982a) method. Tidal analysis of C-line currents below the surface layer show a range in amplitudes from 1 to 3 cm s^{-1} with CW rotation, so a simple Kelvin wave model can not account for them and an explanation must be sought elsewhere.

The topography in the CODE region does not permit a purely barotropic continental shelf wave at the diurnal frequency, but as pointed out by Chapman (1983), the introduction of even a slight amount of stratification can allow the dispersion curves for CTWs to go to the inertial frequency. Over the continental shelf, a mode one diurnal CTW will have CW-rotating velocity ellipses that are oriented along-shelf. A numerical model described in Brink and Chapman (1985) was used to calculate the free diurnal CTWs with realistic topography

and Brunt-Väisälä (N) frequency profile. The coastal boundary condition was applied at the 47 m isobath (a distance of one km from shore) in accordance with the theory of Mitchum and Clarke (1986). Although their theory is strictly applicable only for low frequency waves, the exact placement of the coastal wall does not change appreciably the results discussed here. Using horizontal resolution of 6.25 km, 17 grid points evenly distributed in the vertical, and bottom stress based on 0.5 m wave height³, the along-shelf wavelength for the first mode CTW ranged from 185 to 256 km, depending on the N^2 profile. Several N^2 profiles based on CODE hydrographic measurements (supplied by A. Huyer of Oregon State University) were used. The N^2 profile is imposed on the seaward edge of the domain, and the program interpolates or averages from this to 17 evenly spaced points in the vertical at each horizontal grid point. Since the distance from the coast to the 130 m isobath (about 15 km) is a large fraction of the offshore decay scale for the pressure field for this wave (about 20 km), the alongshore array of coastal sea level measurements alone was used to estimate its amplitude. The K_1 amplitudes for the coastal sea level records are marked by crosses and connected by a dashed line in Figure 16. It is seen that for the appropriate length scales, deviations from the larger scale pressure field (represented by the solid line) are of order 1 cm. A first mode CTW with this amplitude at the coast would result in velocities of 3

³ Bottom stress equal to a resistance coefficient times the bottom velocity vector is used. The resistance coefficient is a function of depth and wave height, and is calculated using a simplification of the Grant and Madsen (1979) model. The bottom stress parameterization is described in more detail in Clarke and Brink (1985).

to 4 cm s^{-1} over the shelf. Figure 17 shows the velocity ellipses (calculated from Brink's model) along the C-line for a first mode CTW with coastal amplitude 1 cm for the N^2 profile shown at the left of the figure. The velocity ellipses resulting from the sum of any two waves will depend on the phase difference between them. Although a rigorous fitting of the observed velocity ellipses to the sum of Kelvin and coastal-trapped waves is not attempted here, it is noted that the combination of a 1 cm first mode CTW and a 37 cm Kelvin wave, differing in phase by 180° , results in a CW-rotating, along-shelf oriented velocity ellipse with semi-major axis of 1.8 cm s^{-1} (at a distance of 7 km from shore). This is in reasonable agreement with the observed velocity ellipses below the surface layer as seen in the diurnal EOFs shown in Figures 12 and 13. It is important to note that over the shelf the velocity field due to the CTW is relatively depth-independent and has CW-rotating ellipses. It is also interesting that the diurnal shelf wave here is about a factor of five smaller than that observed in the current (Crawford and Thomson, 1982) and pressure fields (Battisti and Clarke, 1982b) off Vancouver Island.

8. FORCED RESPONSE

Few efforts have been made in the past to model the effects of a diurnally varying wind stress over the coastal ocean. To the author's knowledge, the only analytic model published in the open literature of the response to a seabreeze in the presence of a coast is that of Shaffer (1972), who investigated the effects on upwelling of an along-shelf trade wind and a cross-shelf seabreeze starting up from slack conditions. He used an infinitely deep homogeneous ocean

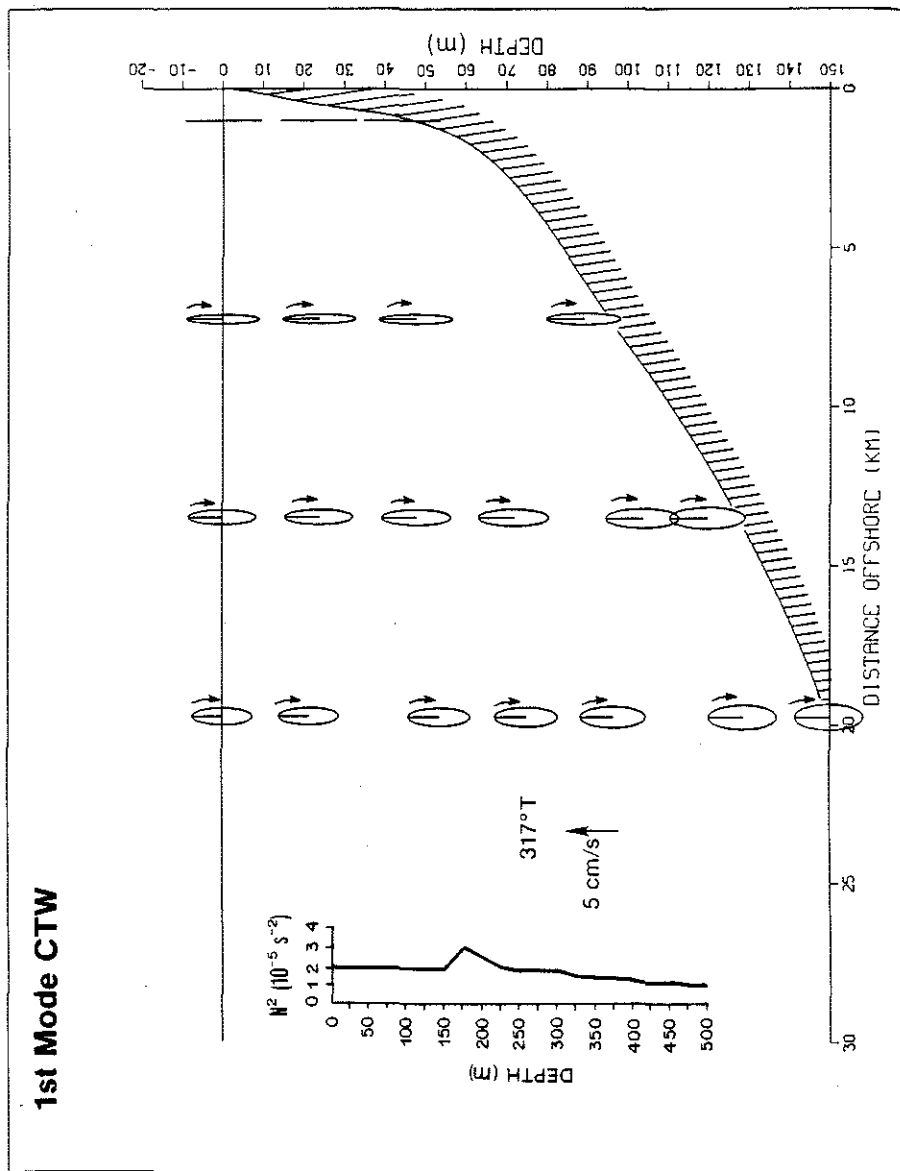


Figure 17. Horizontal current ellipses due a first mode coastal-trapped wave at diurnal frequency with pressure amplitude of 10^3 dynes cm^{-2} (equivalent to about 1 cm in sea level) at the coast. Phases at time of maximum pressure are indicated. The N^2 profile used in the computation is shown in the inset.

bounded by a vertical wall at which no slip and no normal flow conditions were imposed. Both components of the wind decayed exponentially away from the coast. No along-shelf variations were allowed, a rigid lid was imposed, and the equations were linearized. Horizontal and vertical eddy diffusivities of 10^8 and $10^2 \text{ cm}^2 \text{ s}^{-1}$, respectively, were used. This initial value problem was intended to simulate conditions on the northwest coast of Africa, but the variation of the solution with latitude was investigated, including a discussion of the resonance condition at 30° . For latitudes greater than 30° , Shaffer found that outside the coastal boundary layer, the horizontal current ellipse exhibited CW rotation, with the major axis inclined 45° to the right of the oscillating part of the wind. The vertical structure of the horizontal velocity is the same as that of the Fredholm solution presented in Ekman (1905).

Motivated by the observations off Oregon discussed in Section 2, Clancy et al. (1979) developed a time-dependent two-dimensional coupled ocean (2-layer) - atmosphere (4-layer) model and used it to explore the interactions between the seabreeze and the coastal upwelling. They found that the seabreeze caused increased upwelling and the increased upwelling altered the seabreeze, but changes in the mean along-shelf wind compensated in such a way that the air-sea feedback loop was very weak. Consistent with the findings of Burt et al. (1974), the seabreeze amplitude over the whole model ocean decreased as the mean equatorward winds increased. As has been shown here, the opposite is true in CODE, so it is unclear how applicable these model results are to northern California. The exclusion of heat flux from the atmosphere to the ocean (although heat flux in the

opposite direction is retained) makes this model unsuitable for investigating the vertical structure of the surface layer currents generated by a diurnally varying wind stress. The main results of the Clancy et al. (1979) model, as far as the ocean current response is concerned, are summarized in O'Brien et al. (1977). The seabreeze is seen to force a CW-rotating diurnal oscillation in the upper layer of the ocean near the coast.

Rather than attempt the development of a numerical model which includes all the elements at once (no low frequency assumption, the presence of a coast, diurnal heating and wind stress) necessary to examine the problem of a diurnally varying wind stress acting on the coastal ocean, the approach adopted here is to examine separately the currents generated by the stress in the upper part of the ocean, and those felt throughout the water column nearshore, due to the pressure gradient built up against the coast.

The linearized equations of motion in a stratified fluid are

$$u_t - fv = -\frac{1}{\rho_0} p_x + \frac{1}{\rho_0} F_z^x, \quad (1)$$

$$v_t - fu = -\frac{1}{\rho_0} p_y + \frac{1}{\rho_0} F_z^y, \quad (2)$$

$$p_z = -g\rho, \quad (3)$$

$$u_x + v_y + w_z = 0, \quad (4)$$

$$\rho_t + w\rho_z = 0, \quad (5)$$

where u , v , and w are the cross-shelf, along-shelf and vertical components of velocity, respectively, ρ is density, p is pressure, and f is the inertial frequency. The subscripts x , y , and z denote differentiation in the cross-shelf, along-shelf, and vertical directions. (F^X, F^Y) is the vertical turbulent flux of horizontal momentum. Horizontal diffusivity has been neglected. For the coastal ocean with wind forcing at the surface, the appropriate boundary conditions are

$$\left. \begin{aligned} F^X &= \tau^X \\ F^Y &= \tau^Y \\ w &= \eta_t \end{aligned} \right\} \text{at } z = 0, \quad (6)$$

$$\left. \begin{aligned} F^X &= B^X \\ F^Y &= B^Y \\ w &= -uH_x - vH_y \end{aligned} \right\} \text{at } z = -H, \quad (7)$$

$$\int_{-H}^0 u \, dz = 0 \quad \text{at } x = 0, \quad (8)$$

where (τ^X, τ^Y) is the wind stress vector, (B^X, B^Y) is the bottom stress vector and η denotes the sea surface elevation.

The velocity field can be separated into a pressure-induced inviscid part (u_p, v_p) and a frictional part (u_e, v_e) . The momentum equations governing the frictional part are

$$u_{e_t} - fv_e = \frac{1}{\rho_0} F_z^X, \quad (9)$$

$$v_{e_t} + fu_e = \frac{1}{\rho_0} F_z^y \quad (10)$$

The near-surface frictional part of the flow field is discussed in part B of this section.

The momentum equations governing the pressure-induced flow are

$$u_{p_t} - fv_p = -\frac{1}{\rho_0} p_x \quad (11)$$

$$v_{p_t} - fu_p = -\frac{1}{\rho_0} p_y \quad (12)$$

This component of the velocity field may be calculated independently of the details of the boundary layer flows. It is only necessary to know the surface and bottom stress vectors and their curl and divergence in order to specify the vertical velocity at the edge of the boundary layers, and the cross-shelf transport in these layers. The boundary conditions given in (6) through (8) are then modified by these terms, to give the appropriate boundary conditions for the pressure-induced flow (equations 5.4 in Brink and Chapman, 1985). A numerical solution for the pressure-induced flow, assuming all variables to have time dependence $e^{i\omega t}$, will be presented next.

A. INTERIOR FORCED RESPONSE

Due to cross-shelf transport in the surface boundary layer, diurnal wind forcing leads to a diurnal period oscillation in the pressure field that is largest at the coast. The spatial gradient of this pressure field is responsible for a pressure-driven diurnally oscillating flow that will be felt throughout the water column,

although modified with depth to some extent in a stratified fluid. Consider here a situation in which the topography and the bottom stress vary in the cross-shelf direction only. Using an N^2 profile typical of the nearshore conditions in CODE, the inviscid response was calculated using a computer program described in Brink and Chapman (1985). As in the case for free diurnal CTWs, the free surface option was used and the coastal boundary was put at the 47 m isobath. The details of the model are the same as in the unforced case (Section 7), except that the horizontal resolution is now 4 km. The interior flow is assumed to be inviscid, with all the friction confined to infinitesimally thin boundary layers at the top and bottom of the water column. The amplitude of the diurnal along-shelf wind stress at the coastal boundary ($0.40 \text{ dynes cm}^{-2}$) and at distances of 6 ($0.60 \text{ dynes cm}^{-2}$), 14 ($0.25 \text{ dynes cm}^{-2}$), and 27 km ($0.25 \text{ dynes cm}^{-2}$) offshore was specified based on the CODE-2 spectral estimates given in Table 2. The results are summarized in Table 6. The predicted current ellipses rotate CW, are oriented in the along-shelf direction, and are nearly independent of depth. Near the coast, their amplitude is similar to that of the tidal currents, but it decays rapidly offshore. The results are the same whether the wind field is specified as being independent of y , or the sum of northward and southward propagating waves with alongshore wavelength of 220 km, chosen to represent a maximum in the diurnal stress at the C-line and minima at Pt. Arena and Pt. Reyes.

Distance from 47 m isobath*	Depth	Cross-shelf Velocity		Along-shelf Velocity		Pressure	
		A	ϕ	A	ϕ	A	ϕ
(km)	(m)	(cm/s)	(deg)	(cm/s)	(deg)	(mb)	(deg)
0	0	1.9	-137	2.4	-47	123	105
	23	1.9	-137	2.4	-47	118	105
	47	1.9	-137	2.4	-47	113	104
4	0	2.0	-159	2.4	-69	92	101
	42	1.6	-157	2.0	-67	88	100
	85	1.3	-162	1.7	-72	83	96
8	0	1.6	-166	2.0	-76	60	99
	52	1.2	-165	1.5	-75	64	97
	104	1.0	-172	1.2	-82	61	92
12	0	0.7	-163	0.9	-73	41	97
	63	0.8	-168	1.0	-78	49	94
	125	0.7	-178	0.8	-88	47	89
16	0	0.2	-151	0.3	-62	36	94
	75	0.5	-171	0.6	-81	39	92
	150	0.4	+177	0.5	-93	36	88

*Add 1 km to get distance from shore.

Table 6. Interior velocities and pressures resulting from diurnal wind forcing. Phases are relative to a value of zero for the wind stress. Negative phase means current (or pressure) lags wind. Results are shown for surface, mid-depth, and bottom for the five horizontal grid points closest to shore.

stress, and to see whether a one-dimensional mixed layer model including stratification and forced by diurnal heating and wind stress can reasonably duplicate the observations, a number of experiments were run with a modified version of the PWP model. A brief description of the model, as used for this study, is given next. The model ocean is considered to be infinitely deep. The absence of a bottom boundary layer is not considered to be a problem here, since the current data indicate that the surface boundary layer flow gives way to a depth-independent interior flow before the bottom is reached.

Equations (9) and (10) for the velocity (with the addition of a damping term on the right-hand sides), together with the following equation governing temperature, are solved on an evenly spaced vertical grid ($\Delta z = 1$ m) and stepped forward in time ($\Delta t = 30$ min).

$$T_t = - \frac{1}{\rho_0 c} Q_z , \quad (13)$$

where T is temperature, Q is heat flux, $c = 3993$ joules $\text{kg}^{-1} \text{ }^\circ\text{C}^{-1}$ is the heat capacity, and $\rho_0 = 1026.1$ kg m^{-3} . Density is calculated at each time step as a linear function of temperature using $\rho = \rho_R + \alpha (T - T_R)$, with $\rho_R = 1026.1$ kg m^{-3} , $T_R = 10.3$ $^\circ\text{C}$ and $\alpha = -0.17$ $\text{kg m}^{-3} \text{ }^\circ\text{C}^{-1}$. These values were chosen in correspondence with the initial density profile shown in Figure 18. Salinity was taken to be constant in time.

The surface heat flux $Q(0)$ is modelled as the sum of a solar radiation term represented by the positive part of a sine curve, and a constant heat loss term representing the sum of the latent, sensible and long-wave radiation terms. All the heat loss is presumed to leave

B. FRICTIONAL FORCED RESPONSE

In this sub-section, the frictional part of the velocity field is considered. An eddy viscosity approach to prediction of the quasi-steady state solution for periodic wind forcing with no stratification or heating is presented in Appendix C. Such a model, however, can not be used to address questions concerning the effects of diurnal heating on the diurnal current field, which Price, Weller, and Pinkel (1986) (hereafter referred to as PWP) have shown to be important. The CODE current measurements presented in Sections 5 and 6 reveal a non-stationary surface-intensified diurnal flow that is strongly correlated with variations in the local diurnal wind stress. It has also been demonstrated (Figure 8) that the amplitude of the diurnal wind stress is linearly related to the lower frequency wind stress. PWP point out that a steady wind stress in the presence of the diurnal heating cycle will result in a current structure varying with diurnal period, which they refer to as a diurnal jet in analogy with the nocturnal jet in the atmosphere.

Although numerous one-dimensional models for the mixed layer of the ocean have been used to examine the effects of wind and buoyancy forcing on the upper ocean, only one by Dickey and Simpson (1983) has included explicitly diurnal cycles of both heating and wind stress. Several others have looked at the effects of diurnal heating in the presence of a constant wind stress (Kondo, Sasano, and Ishii, 1979; Price, Weller and Pinkel, 1986; Woods and Strass, 1986). In an effort to see whether the variations in time of the diurnal current amplitude might be due more to the changing mean wind stress combined with a diurnal cycle of surface heat flux than to the changing diurnal wind

INITIAL DENSITY PROFILE

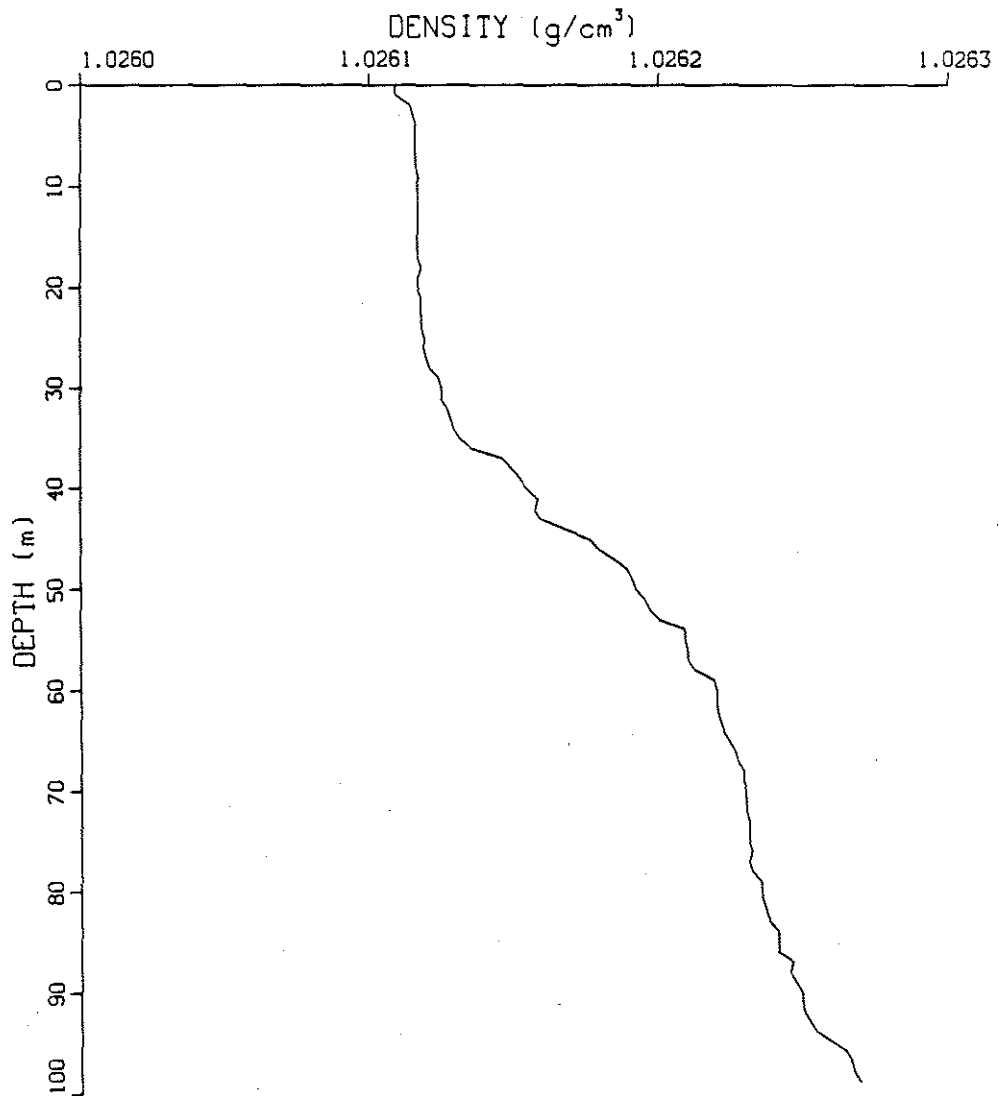


Figure 18. The initial density profile used in the one-dimensional mixed layer model calculations is shown.

from the sea surface. The net incoming solar radiation is distributed over depth according to

$$I(z) = I(0) \left[I_1 e^{-\frac{z}{\lambda_1}} + I_2 e^{-\frac{z}{\lambda_2}} \right] \quad (z \text{ positive downward}), \quad (14)$$

where the subscripts 1 and 2 refer to the long- and short-wave components of insolation. Dickey and Simpson (1983) used a level 2-1/2 turbulent closure model to investigate the influence of optical water type on the diurnal thermal response of the upper ocean for a constant wind stress. They concluded that for wind speeds greater than 6 m s^{-1} (corresponding to a stress value of about $0.6 \text{ dynes cm}^{-2}$), the diurnal amplitude of sea surface temperature is only weakly dependent on water type. The rate of increase of mean temperature and the thermal gradient at the base of the mixed layer are more affected by water type, with larger values for less clear water, again for wind speeds greater than 6 m s^{-1} . No measurements were made in CODE to allow determination of the optical water type, so it was assumed to be of the coastal Type III defined by Jerlov (1976). Paulson and Simpson's (1977) values of $I_1 = 0.78$, $I_2 = 0.22$, $\lambda_1 = 1.4 \text{ m}^{-1}$, $\lambda_2 = 7.9 \text{ m}^{-1}$ for Type III water were used. Model runs made with $I_1 = 0.6$, $I_2 = 0.4$, $\lambda_1 = 0.5 \text{ m}^{-1}$, and $\lambda_2 = 15 \text{ m}^{-1}$ give diurnal current results very similar to those shown here. In accordance with the measured surface heat flux (Figures 9 and 19a), insolation lasting over a period of 13 hours and peaking at 1230 PST is used. The amplitude is a variable input to the model. The wind stress in the along-shelf direction is modelled as the sum of a constant plus a diurnal period sinusoidal oscillation. The mean stress, and the amplitude

and phase of the diurnal stress, can be varied for each model run. The cross-shelf stress is set to zero.

At each time step, the appropriate heat flux and surface stress are applied and vertical mixing takes place between adjacent grid points until the following stability criteria are satisfied:

$$\rho_z > 0 \quad , \quad (15a)$$

$$\frac{g \Delta \rho h}{\rho_0 |\Delta \vec{V}|^2} \geq 0.65 \quad , \quad (15b)$$

$$\frac{g \rho_z}{\rho_0 |\vec{V}_z|^2} \geq 0.25 \quad , \quad (15c)$$

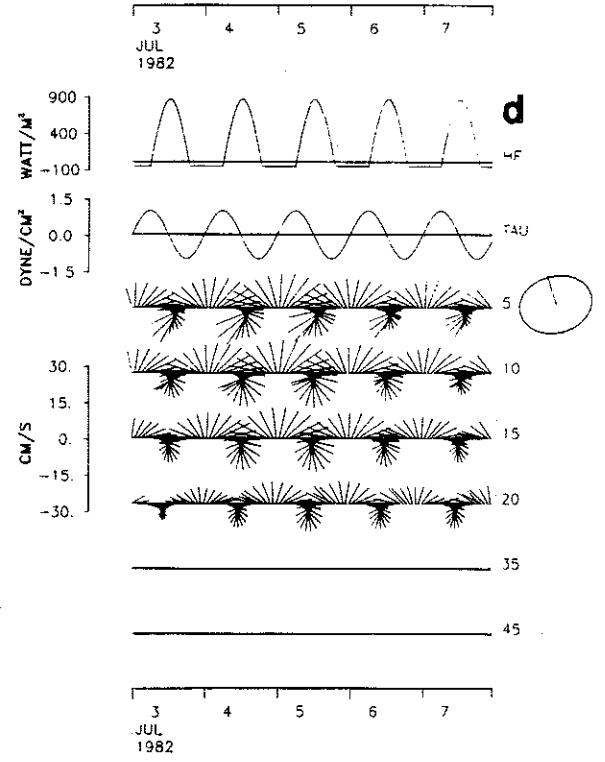
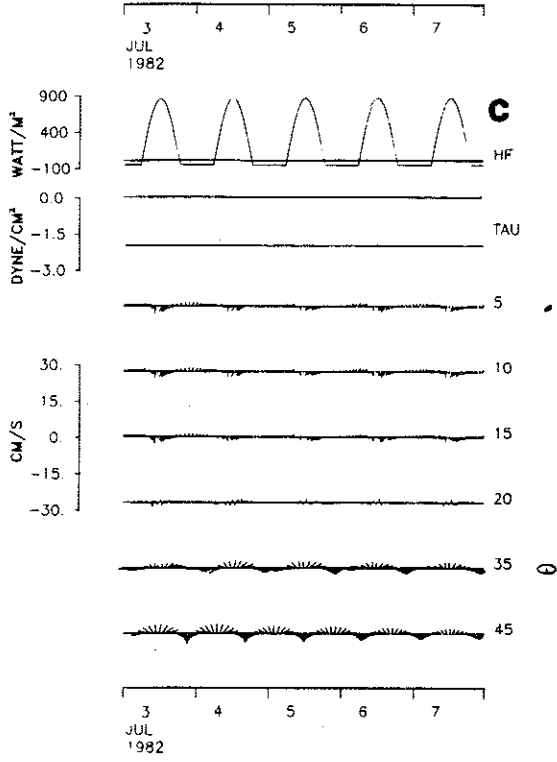
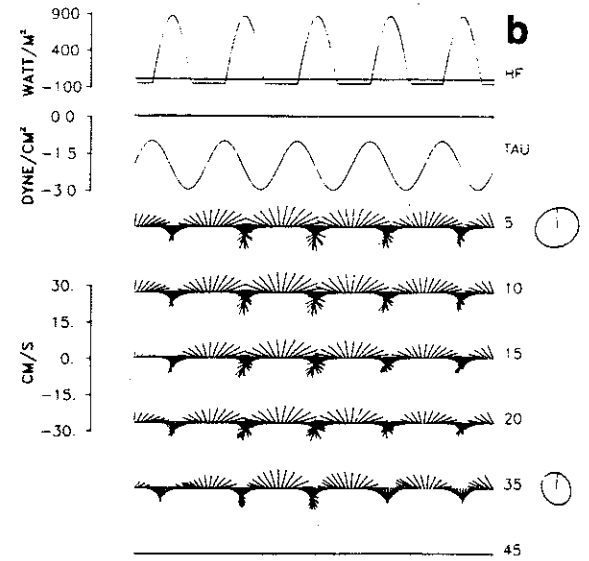
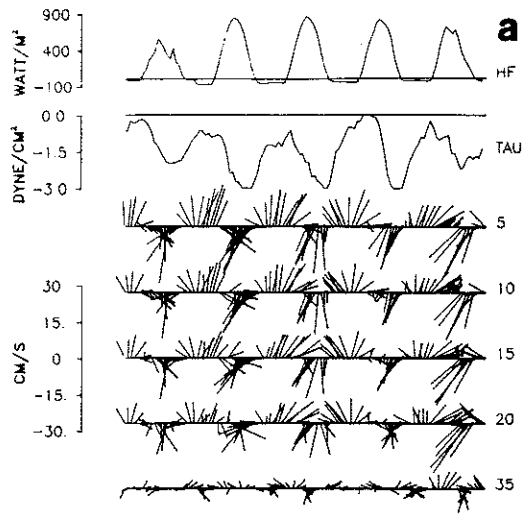
where g is gravity, \vec{V} is the velocity vector, h is the mixed layer depth, and Δ refers to the difference between the value in the mixed layer and the level just below it. Equation (15a) simulates mixing by convective overturning. Equation (15b) represents entrainment at the base of the mixed layer. Equation (15c) represents mixing by shear flow instability, and acts to smooth out the sharp jump at the base of the mixed layer. The critical values of the bulk (0.65) and gradient (0.25) Richardson numbers are based on the results of PWP.

If the forcing is turned on suddenly, and no damping is applied, strong inertial oscillations dominate the current response in the model. Both the CODE observations and theoretical considerations discussed by Kundu, Chao and McCreary (1983) and Pettigrew (1981) suggest that due to the nearby presence of the coast, there is very little inertial period energy. Because the model is one-dimensional, and there is no way to incorporate directly the effects of the coast,

two steps are taken to artificially reduce the inertial period oscillations. A ramp, linearly increasing from zero to the prescribed value of wind stress, is applied to the forcing over the first two days. In addition, a damping term of the form $-rV$ is added to the right-hand side of the momentum equations. The Rayleigh friction parameter r is set equal to $(5 \text{ days})^{-1}$, based on the results of Kundu et al. (1983). A damping term of this form and approximate magnitude was also used by Kundu (1976) in his application of the Pollard and Millard (1970) model to observations off the Oregon coast. The damping coefficient is taken to be constant with depth over the whole water column, so energy left behind in the lower water column as the mixed layer shoals is also damped. The model was run for 12.5 days.

Figure 19 shows the high-passed currents observed at C3 during the five day period July 3-7, 1982, and the high-passed current results from days 5-10 of six model runs. These results were examined in order to characterize the effects that changes in the amplitude of the diurnal heating and mean and diurnal wind stress have on the diurnal currents. In addition, the results were compared with the observations to see if the model was in agreement, in an average sense, with the observed diurnal currents during this period. This is not an attempt to duplicate the hour-by-hour or day-to-day variations in the observed forcing and currents during these 5 days, but rather to try to understand the mechanisms at work in producing the variability observed over the whole CODE-2 experiment.

Figure 19a shows the measured surface heat flux, along-shelf wind stress, and high-passed current vectors for this period. The average diurnal current ellipses at 5 and 35 m depths as determined from the



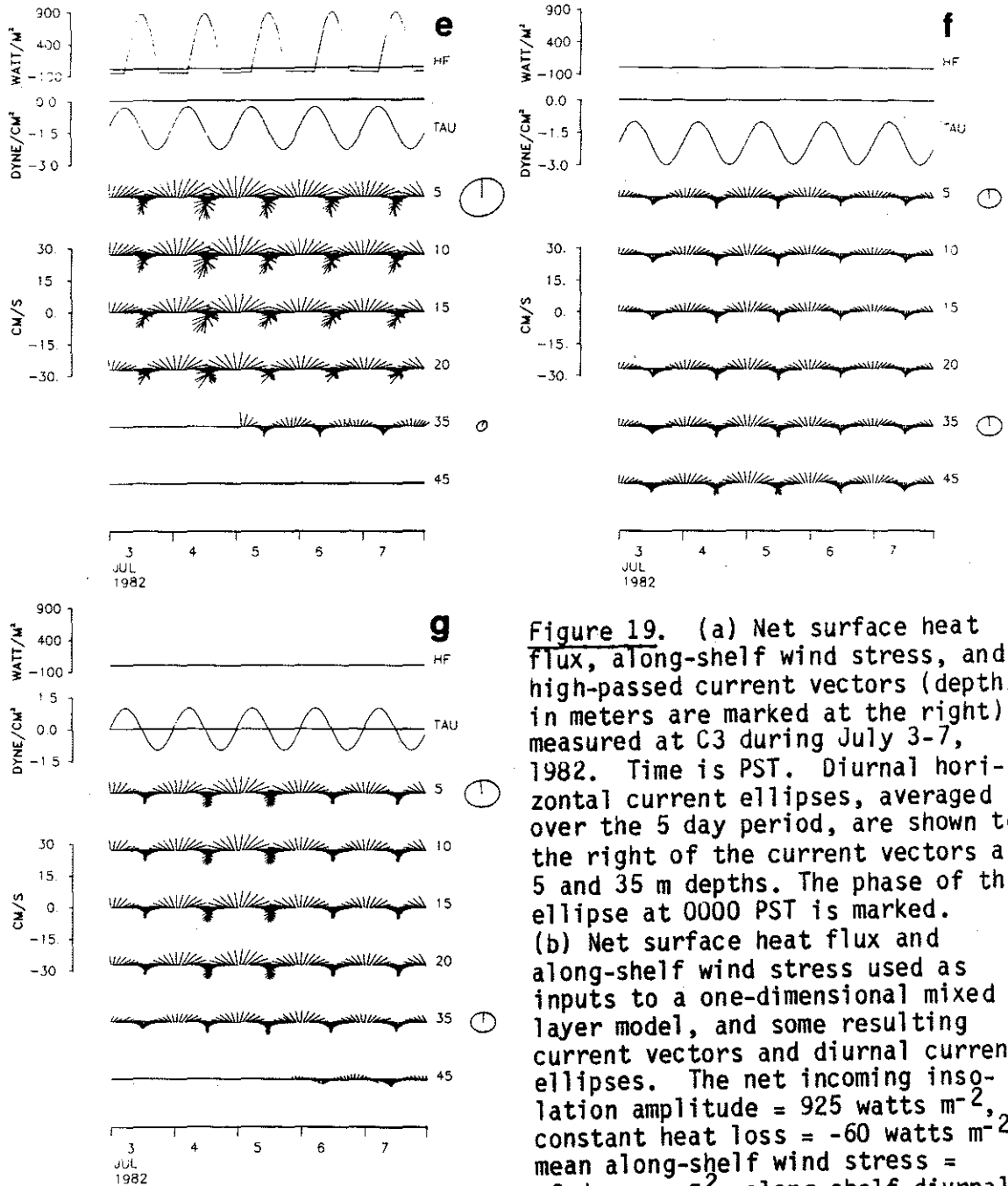


Figure 19. (a) Net surface heat flux, along-shelf wind stress, and high-passed current vectors (depths in meters are marked at the right) measured at C3 during July 3-7, 1982. Time is PST. Diurnal horizontal current ellipses, averaged over the 5 day period, are shown to the right of the current vectors at 5 and 35 m depths. The phase of the ellipse at 0000 PST is marked. (b) Net surface heat flux and along-shelf wind stress used as inputs to a one-dimensional mixed layer model, and some resulting current vectors and diurnal current ellipses. The net incoming insolation amplitude = 925 watts m^{-2} , constant heat loss = -60 watts m^{-2} , mean along-shelf wind stress = -2 dynes cm^{-2} , along-shelf diurnal wind stress amplitude = 1 dynes cm^{-2} . (c) Same as (b), but diurnal wind stress = 0. (d) Same as (b), but mean wind stress = 0. (e) Same as (b), but mean wind stress = $-1.3 \text{ dynes cm}^{-2}$. (f) Same as (b), but surface heat flux = 0. (g) Same as (b), but surface heat flux and mean wind stress = 0.

complex demodulation for this time period are shown to the right of the current vectors. It is seen that there is little variation in the amplitude or phase of the high-passed currents (which are dominated by the diurnal component during this period) between 5 and 20 m. The currents at 35 m are greatly reduced, relative to those in the upper water column. The 5 m diurnal current ellipse has a semi-major axis of 14.5 cm s^{-1} , a semi-minor axis of 5.3 cm s^{-1} , is oriented towards 339°T , and rotates in a CW manner.

Figure 19b shows the results of the model run with inputs most closely approximating the average observed forcing over this time period. The amplitude of the net solar radiation (incoming minus reflected) is set to 925 watts m^{-2} , the steady heat loss is -60 watts m^{-2} , the mean along-shelf wind stress is -2 dynes cm^{-2} , and the amplitude of the diurnal wind stress is 1 dyne cm^{-2} , with maximum equatorward stress at 1800 PST. As expected, the model currents are more circularly polarized because of the absence of coastal effects and the fact that tidal currents are not included. As seen from the 5 m ellipses, the phase of the modelled diurnal currents in the mixed layer agrees well with the observations, with the current vectors pointing almost directly upcoast (towards 317°T) at 0000 PST. The model mixed layer is slightly too deep, resulting in currents weaker than observed.

To see what effect the addition of the pressure-induced current response (Section 8A) has, the wind-forced model of Brink and Chapman (1985) was run again with wind stress values appropriate to the July 3-8 period. The sum of the resulting current ellipse at 5 m depth, 7 km from shore (corresponding to the position of the C3 mooring), and the 5 m ellipse shown in Figure 19b are shown in Figure 20. The addi-

tion of the pressure-induced flow causes the ellipse to become slightly more elongated which is more in accord with the observed 5 m current ellipse, also shown in Figure 20. The sum of the mixed-layer and pressure-induced ellipses still differs in amplitude, orientation, and eccentricity from the observed one. Addition of the tidal currents would cause more elongation and possibly turn the orientation toward the along-shelf direction, depending on the phase difference between wind-driven and tidal currents which is variable.

In successive panels of Figure 19, the effects of varying the strength of the heating, and mean and diurnal wind stress, are explored. The relative phase between the diurnal heating and wind stress is the same for all model runs. Comparison of panels c and d of Figure 19 with panel b shows that the diurnal currents in the mixed layer decrease with decreasing diurnal stress, but increase with decreasing mean stress. In the case of a 2 dynes cm^{-2} steady wind stress (Figure 19c), the mixed layer depth oscillates between 12 and 35 m (Figure 21c). The diurnal component of the current is very weak, but there is, of course, a sizeable mean current which has been removed by the high-pass filtering. The 35 m instrument is in the transition zone below the mixed layer. This is the only case explored here which resulted in an average diurnal ellipse which rotates in the CCW direction. The inertial oscillations at 45 m are the result of the deeper mixed layer that is seen to occur at the start of July 3 (see Appendix D).

The amplitude of the currents in the mixed layer is inversely proportional to the mixed layer depth, which in turn is a function of the wind stress and heating. In the model a mean stress of -2 dynes cm^{-2}

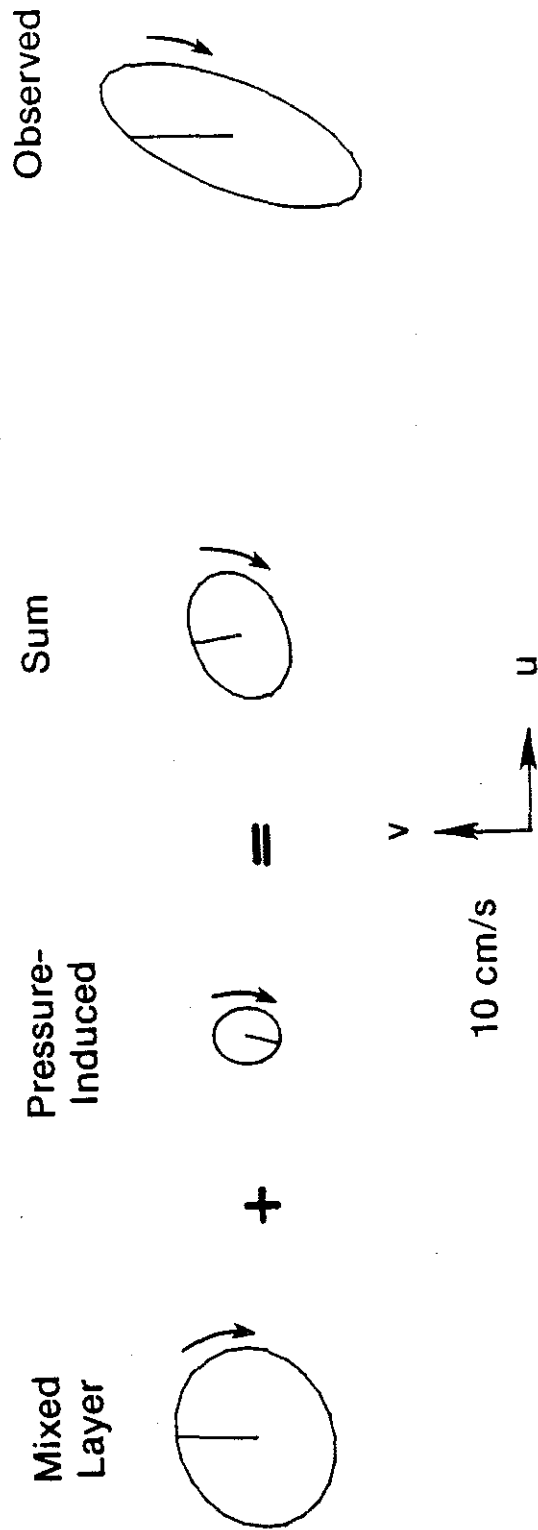


Figure 20. The 5 m horizontal current ellipses resulting from the mixed layer model with forcing as shown in Figure 19b and from the forced interior model (at 7 km from shore), and their sum, are shown along with the observed current ellipse (same as shown in Figure 19a).

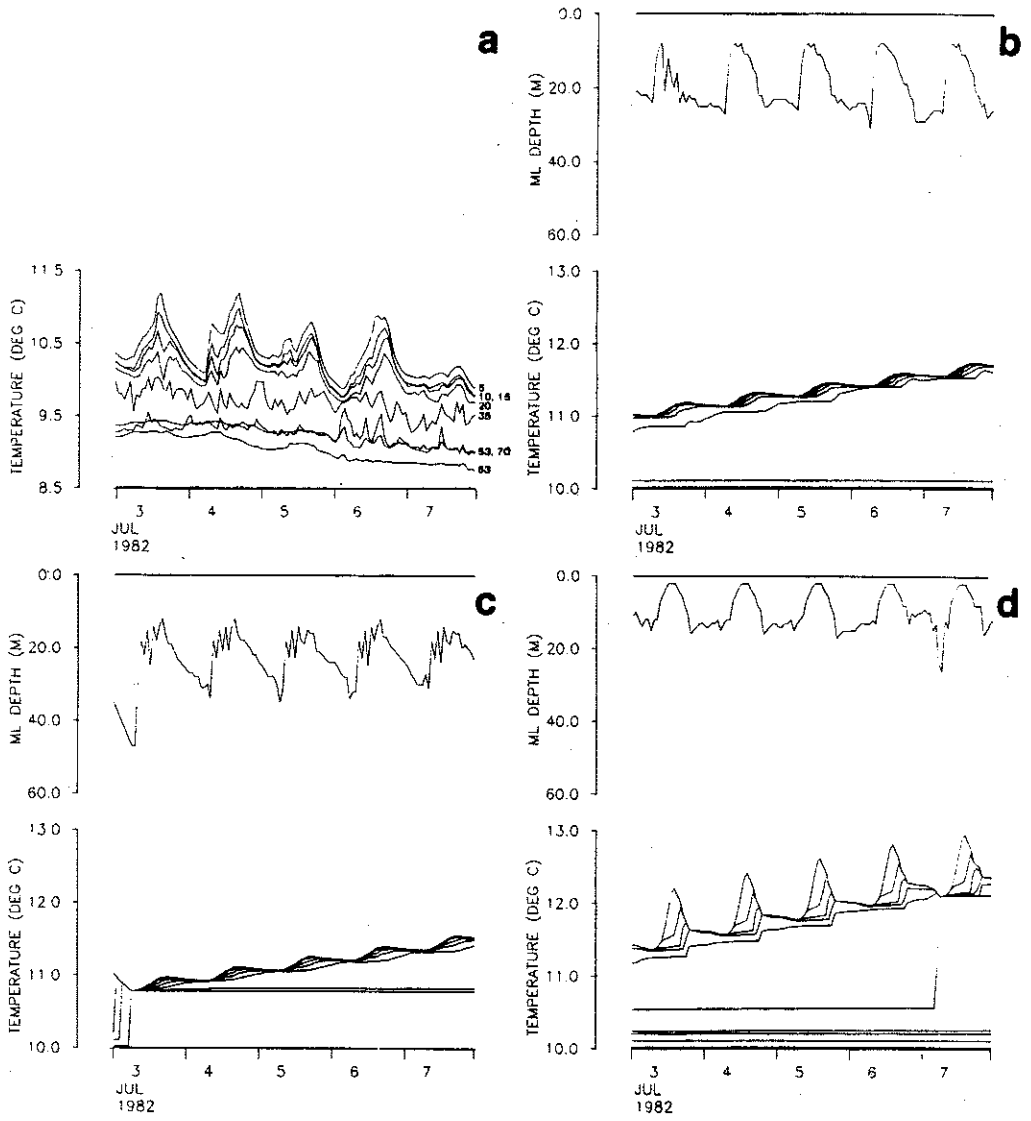
produces a mixed layer deeper than that observed, with currents that are too small. With no mean stress (Figure 19d), the mixed layer is too shallow and the currents too big. An intermediate case with a mean along-shelf wind stress of $1.3 \text{ dynes cm}^{-2}$ (Figure 19e) more nearly resembles the observations in terms of the amplitude of the mixed layer currents and the depth of penetration. Again, the 35 m level is in the transition zone between the mixed layer and the quiescent water below.

The surface heating as well as the wind stress is important in determining the structure of the diurnal current fluctuations. If the heating is turned off, but the stress is maintained as in Figure 19b, the mixed layer is observed to extend to at least 45 m (Figure 19f and 21f). The depth of the mixed layer is also a function of the initial density profile (Figure 18) to some extent, although convective overturning during the first night of the model run and subsequent restratification the next day, quickly brings the density profile into accord with the applied heating and wind stress. No CTD measurements were made in the CODE area during July 3-7, so the initial density profile was determined from one made on July 16 when, based on the current meter temperature records, the stratification was similar. The temperature from the CTD data was increased by 1.2°C throughout the water column, to bring it into approximate agreement with the temperature measured by the current meters on July 3.

As is true for the thermal response of the upper ocean (Dickey and Simpson, 1983), the phase relationship between the diurnal heating and wind forcing significantly affects the current response. For the data shown here, the wind stress peaks about 6 hours after the maximum heating, just as the evening cooling sets in. Comparison of Figure 19d

with 19g shows clearly that the presence of diurnal heating, even with a wind stress symmetric about zero, produces near-surface currents which are asymmetric, with larger equatorward than poleward velocities, as in the observations. This is due to the fact that the equatorward stress occurs during the day when heating is positive and the mixed layer is shallowest. At night, when the model stress is poleward, the mixed layer is deeper due to convective overturning caused by heat loss from the surface. The momentum flux is thus distributed over a larger column of water and the surface currents are smaller. It can be seen that there is more shear in the currents during the day than at night.

Figure 21a shows the temperatures measured by the current meters at C3 for depths from 5 to 83 m. A clear diurnal signal with a range of about 1°C is seen in the upper 20 m, whereas below 53 m, the temperature varies very little over the 5 days. The 35 m record is intermediate between these. This is consistent with the current measurements shown in Figure 20a, which also indicate a mixed layer depth of between 20 and 35 m. Due to calibration problems, absolute temperature measured by the different instruments can not be directly compared, so calculation of the mixed layer depth from the temperature data is not possible. Variations measured by an individual instrument are reliable, however. The succeeding panels of Figure 21 show the mixed layer depth and the temperature at 5 m intervals from 0 down to 45 m for the same model runs shown in Figure 19. The mixed layer depth is defined in the model as being the depth down to which the density is uniform to within 10^{-4} kg m^{-3} . Due to the excess of surface heating over cooling, there is an overall warming trend in all the model results, so that although the model was initiated with a temperature profile that approximated the



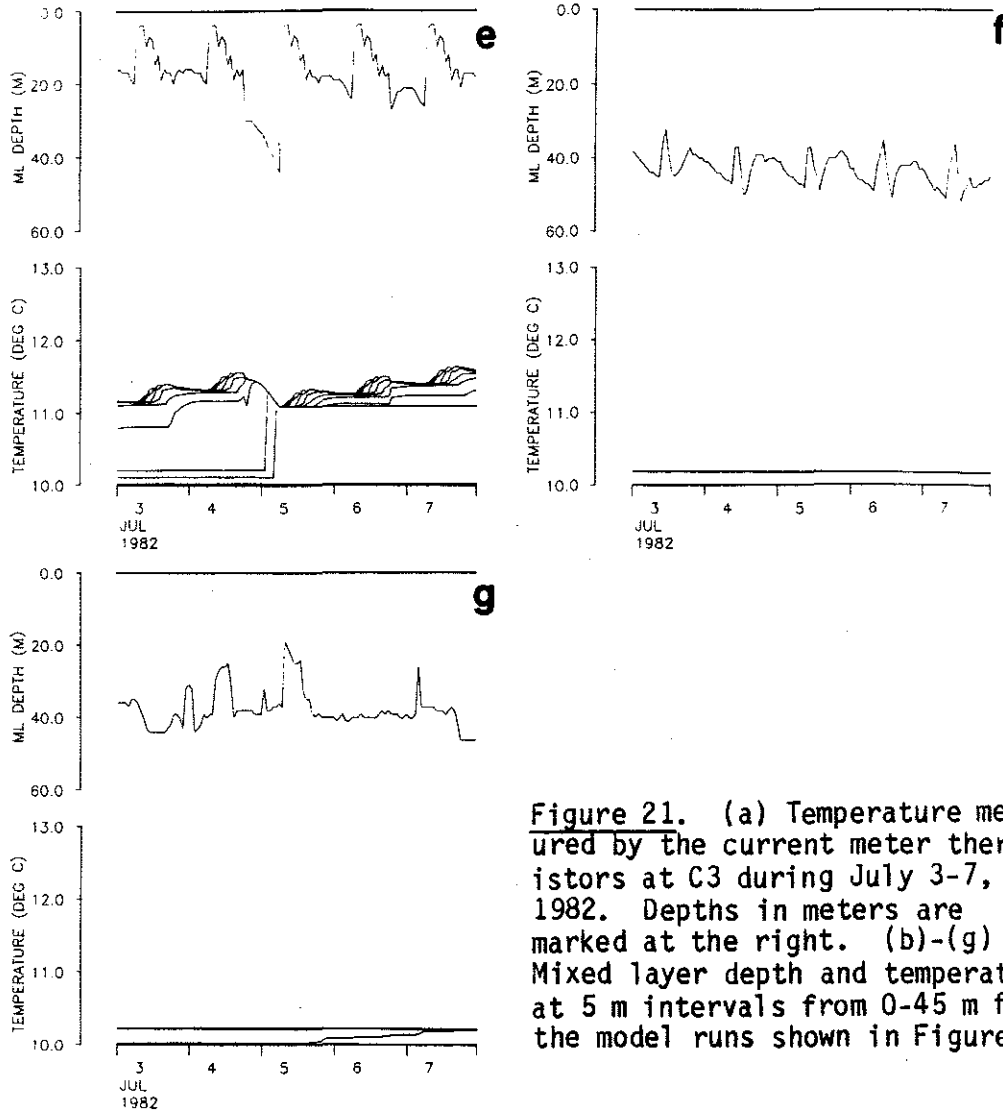


Figure 21. (a) Temperature measured by the current meter thermistors at C3 during July 3-7, 1982. Depths in meters are marked at the right. (b)-(g) Mixed layer depth and temperature at 5 m intervals from 0-45 m for the model runs shown in Figure 19.

one measured at 0000 July 3, by the fifth day of the model run (when the results shown here start), the upper water column has warmed by about 1°C. The absence of a warming trend in the data is due to the active upwelling at this site. The amplitude of the daily variations in temperature is seriously underestimated in all but case d, which is the one with a 1 dyne cm⁻² diurnal wind stress, but no mean stress. This confirms what was learned by examination of the model currents, namely that the diurnal current and temperature fluctuations are better simulated when a mean wind stress much smaller than that observed, is used to force the model. The fact that a 1°C change in temperature over the upper 20 m during the course of the day represents more heat input than the integrated daily surface heat flux, points out that part of the reason for this discrepancy is the absence of advection in the model.

From the above discussion, it is seen that the main features observed in the diurnal currents - their magnitude, vertical structure, and asymmetry in time - can best be simulated by forcing the model with the observed diurnal heating and wind stress and a reduced mean stress. The fact that the observed mean stress produces a deeper mixed layer and smaller currents than the measured ones is most likely due to the effects of upwelling which are not included in this one-dimensional model. The question as to whether changes in the diurnal current amplitude are due to changes in the mean or diurnal wind stress (which are positively correlated) is clearly answered. The correlations presented in Section 6 show that the diurnal current increases when the wind stress increases, and the model shows that the current increases when the diurnal stress increases, but decreases

when the mean stress increases. The fact that very small diurnal current amplitudes result when the model is forced by diurnal heating and only mean wind stress, also indicates that the observed diurnal currents are not primarily due to the diurnal jet mechanism. Diurnal heating is responsible for the observed asymmetry of the diurnal currents. In addition, the strength of the heating contributes to the amplitude modulation of the diurnal currents by affecting the depth of the mixed layer.

9. CONCLUSIONS

The near-surface diurnal currents over the inner and mid-shelf off northern California have an amplitude of about 6 cm s^{-1} averaged over the whole summer. During periods of strong upwelling-favorable wind, which almost always coincide with times of large diurnal wind stress, diurnal currents are typically two to three times their average value. The amplitude modulation of the diurnal period oscillations observed in the upper water column is highly correlated with the diurnal wind stress modulation in the immediate vicinity. The diurnal period fluctuations in the near-surface currents are directly forced by the local diurnal wind stress and surface heat flux. No other mechanism can account for their magnitude, temporal variability, or vertical structure.

A one-dimensional mixed layer model forced by wind stress and surface heat flux can reasonably simulate the magnitude, phase with respect to atmospheric forcing, and vertical structure of the upper ocean diurnal currents observed over the shelf in CODE, if a mean wind stress less than that observed is used. The gradual decrease in size

with increasing depth of the ellipses in the lowest EOF modes is consistent with the model, when it is considered that the mixed layer depth varies with time over the summer. The orientation and eccentricity of the observed diurnal current ellipse is not duplicated, even when the pressure-induced flow forced by the diurnal wind stress is added to the mixed layer flow. The relatively depth-independent currents below the surface layer rotate CW and have speeds of 1 to 3 cm s⁻¹. Their magnitude and sense of rotation are consistent with diurnal currents predicted from local sea level and bottom pressure measurements interpreted as the sum of a Kelvin and first mode coastal-trapped wave, and with predictions for the wind-forced interior flow, which, over the mid-shelf, has the same sense of rotation and similar magnitude as the tidal currents. Theoretically these ellipses should be oriented exactly along-shelf, but the observations show them to be oriented at a small angle to that.

The upper ocean diurnal period currents over the outer shelf and slope at C4 and C5, respectively, are larger than can be accounted for by the wind stress at those locations. In addition, the phase of the diurnal currents is erratic, particularly over the slope, and the correlation of the diurnal current amplitude modulation with that of the local diurnal stress decreases in the offshore direction. Over the slope, then, it appears that the diurnal currents are not directly forced by the local wind stress. Whether the currents there are due to leakage from other frequency bands, advection by the mean flow of diurnal currents generated nearshore farther to the north, or some other mechanism, is uncertain.

APPENDIX A: Complex Demodulation

The method of complex demodulation used in this study is described below. First, the hourly-averaged time series were high-passed with the filter described in Appendix B. It has a half-power point of 36 hours. Then, each scalar time series $S(t)$ (corresponding to the along- or cross-shelf component of wind stress or current) was separately fit by a least-squares analysis to the sum of a mean contribution \bar{S} plus two sine curves, one with frequency $\omega_1 = 1/24$ cph and one with frequency $\omega_2 = 1/12$ cph,

$$S(t) = \bar{S} + A_i \sin [\omega_i(t - t_s) + \theta_i] + \text{noise} \quad . \quad (A1)$$

The fit was done over 48 hour periods with 42 hour overlap, to yield values of amplitude A_i and phase θ_i for each harmonic every six hours. The calculated values of amplitude and phase are assigned to the time midway through the 48 hour period. The start time t_s is the beginning of the record. This was always taken to be at 0000 hours on a given day. For test purposes, some calculations were performed including higher order harmonics, but the amplitudes were so low as to be in the noise level.

Equation A1, without the noise term, may be written as

$$S'(t) = \bar{S}(t) + \sum_{i=1}^2 a_i \sin \omega_i (t - t_s) + b_i \cos \omega_i (t - t_s) \quad (A2)$$

where $A_i = \sqrt{a_i^2 + b_i^2}$ and $\theta_i = \arctan \frac{b_i}{a_i}$.

The standard errors of a_i and b_i are $\sigma \sqrt{\epsilon_{ij}}$. The variance σ^2 is

$$\sigma^2 = \frac{1}{N-M} \sum_{t=1}^{48} [S(t) - S'(t)]^2 ,$$

where $N = 48$, the number of points in the fit, and $M = 5$, the number of coefficients being fit, and

$$\epsilon_{ij}^{-1} = \sum_{t=1}^{48} (\sin \omega_i t)^2 \quad \text{or} \quad \sum_{t=1}^{48} (\cos \omega_i t)^2 .$$

Because the 48 hour time period is an exact multiple of the diurnal period and its harmonics, ϵ_{ij} is the same for all a_i 's and b_i 's. Based on a student-t distribution, the actual coefficients a_i (b_i) should fall within a_i (b_i) $\pm 2 \sigma \sqrt{\epsilon_{ij}}$, 95% of the time. Let $\delta_a = \delta_b = 2 \sigma \sqrt{\epsilon_{ij}}$, then using theory for propagation of errors, $\delta_A = \delta_a$ and δ_θ (in radians) = $(\delta_a)/A$. Figure A1 shows the amplitude and phase errors for the complex demodulation of Sea Ranch wind stress during CODE-1.

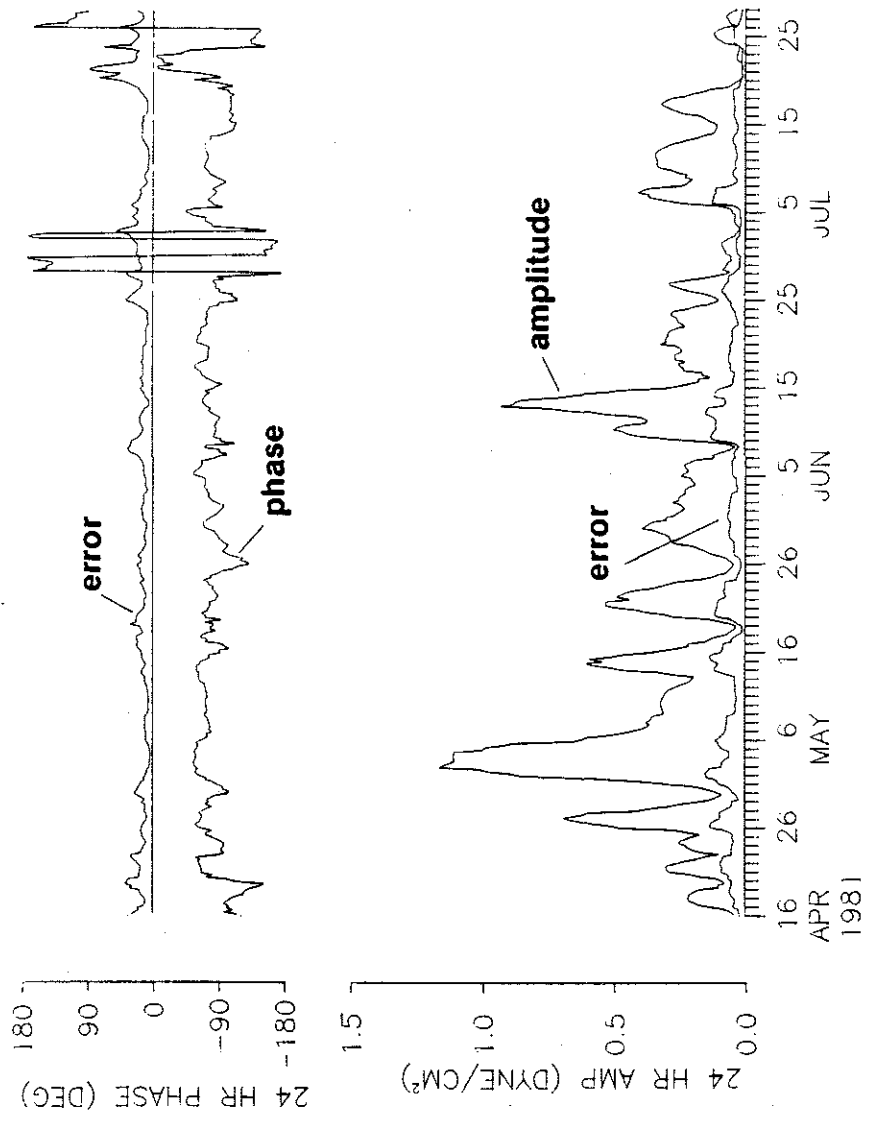


Figure A1. Diurnal amplitude and phase, and their associated expected errors, for the along-shelf wind stress at Sea Ranch during CODE-1.

APPENDIX B: High-Pass Filter

The high-pass filter employed here is symmetric, with 59 weights on each side of the central value. The weights were found by taking the negative of a complementary set of normalized low-pass filter weights, except for the central value which was set to one minus the low-pass central value. The low-pass weights were calculated according to

$$W(t) = \frac{2 \sin (.05\pi t)}{.0004 \pi^3 t^3} - \frac{[\sin (.03\pi t) + \sin (.07\pi t)]}{.0004 \pi^3 t^3}, \quad t \neq 0. \quad (B1)$$

$W(0)$ is found by use of l'Hopital's rule. This high-pass filter has a very flat response over the tidal frequency range. It passes all energy at frequencies greater than 0.035 cph, has a half-amplitude point at 0.025 cph, and at frequencies less than 0.015 cph, amplitudes are reduced to less than 3% of their original values. The half-power point is at 0.028 cph. Power at frequencies less than 0.015 cph is reduced to less than 10^{-3} of its unfiltered value.

APPENDIX C: Time-Dependent Ekman Layer

The simplest model for the time-dependent surface boundary layer is one which assumes that the time dependence of all the variables matches that of the forcing, i.e. $\partial/\partial t$ may be replaced by $i\omega$, and $1/\rho_0$ times the stress vector (F_x, F_y) equals $(A \frac{\partial u_e}{\partial z}, A \frac{\partial v_e}{\partial z})$ where A is the eddy diffusivity. If A is constant with time and depth, then this corresponds to the classic Ekman solution, with f modified by ω , and is discussed in Gonella (1972) and Faller and Kaylor (1969). The appropriate equation and boundary conditions are then

$$G_t + ifG = G_{zz} \quad , \quad (C1)$$

$$A \frac{\partial u_e}{\partial z} = 0 \quad \text{and} \quad A \frac{\partial v_e}{\partial z} = \frac{\tau_0}{\rho} \cos \omega t, \quad \omega > 0 \quad \text{at } z = 0 \quad ,$$

$$G \rightarrow 0 \quad \text{as } z \rightarrow -\infty \quad ,$$

where $G = u_e + iv_e$.

The velocity vector may be divided into CCW ($e^{+i\omega t}$) and CW ($e^{-i\omega t}$) rotating parts,

$$G = \gamma_+(z) e^{i\omega t} + \gamma_-(z) e^{-i\omega t} \quad .$$

Applying the boundary condition of $G \rightarrow 0$ as $z \rightarrow -\infty$ leads to

$$\gamma_+ = B e^{(1+i)\frac{z}{D_+}} \quad \text{and} \quad \gamma_- = C e^{(1+i)\frac{z}{D_-}} \quad ,$$

where $D_+ = \sqrt{\frac{2A}{f+\omega}}$ and $D_- = \sqrt{\frac{2A}{f-\omega}}$ are

equivalent Ekman depths for the CCW- and CW-rotating parts, respectively. Because $\omega < f$, $D_- > D_+$ so the CW part will extend deeper into the water column. Application of the surface boundary condition leads to the determination of the constants B and C.

The solution is then

$$G = \frac{\tau_0}{2\sqrt{2\rho A}} \left[D_+ e^{\frac{z}{D_+}} e^{i\left(\frac{z}{D_+} + \omega t - \frac{\pi}{4}\right)} + D_- e^{-\frac{z}{D_-}} e^{i\left(\frac{z}{D_-} - \omega t - \frac{\pi}{4}\right)} \right],$$

$$u_e = \frac{\tau_0}{2\sqrt{2\rho A}} \left[D_+ e^{\frac{z}{D_+}} \cos\left(\frac{z}{D_+} + \omega t + \frac{\pi}{4}\right) + D_- e^{-\frac{z}{D_-}} \cos\left(\frac{z}{D_-} - \omega t + \frac{\pi}{4}\right) \right], \quad (C2)$$

$$v_e = \frac{\tau_0}{2\sqrt{2\rho A}} \left[D_+ e^{\frac{z}{D_+}} \sin\left(\frac{z}{D_+} + \omega t + \frac{\pi}{4}\right) + D_- e^{-\frac{z}{D_-}} \sin\left(\frac{z}{D_-} - \omega t + \frac{\pi}{4}\right) \right].$$

At the surface, the current ellipse is oriented 45° to the right of the wind stress (as noted in Fallor and Kaylor, 1969), and the orientation turns CW with depth. The semi-major axis equals $|\gamma_+| + |\gamma_-|$, the semi-minor axis is $|\gamma_+| - |\gamma_-|$. Thus at $z = 0$, the semi-major axis equals $\sqrt{2} \tau_0 (D_+ + D_-)/4\rho A$ and the semi-minor $\sqrt{2} \tau_0 (D_+ - D_-)/4\rho A$.

Various values for A near the surface of the ocean have been calculated from data and numerical models. Generally they fall in the range of 100 to 400 $\text{cm}^2 \text{s}^{-1}$. The simplest method for estimating the vertical eddy coefficient from data is to assume that the vertical shear measured by the shallowest instruments extends to the surface. The surface boundary condition $\rho A \overline{v_z} = \overline{\tau_0^y}$ (where the overbars

indicate mean quantities) is then used to determine A. Using this method, Halpern (1976) found a value off Oregon of $55 \text{ cm}^2 \text{ s}^{-1}$ for A. Measurements at 3 and 12 m depth were used to calculate the current shear. Halpern (1977) estimated A to be equal to $125 \text{ cm}^2 \text{ s}^{-1}$ in the upper 10 m off northwest Africa. Brink et al. (1980) found a value of A between 60 and $70 \text{ cm}^2 \text{ s}^{-1}$ (depending on the time period over which the mean was calculated) off of Peru, using current records at 2.5 and 12 m to calculate the vertical shear. Using 105 day mean values of wind stress and 5 and 10 m currents measured at C3 during CODE-2, A is calculated to be $190 \text{ cm}^2 \text{ s}^{-1}$, using this method. Brink (1979) estimated the diurnal cycle of vertical eddy diffusivity off Peru from hourly values of the shear between 2.5 and 4.6 m averaged over a 69-day period. He found that the coefficient ranged from about 25 to $125 \text{ cm}^2 \text{ s}^{-1}$, with the largest value at the time of maximum wind stress. Based on results of a one-dimensional model with second order turbulence closure scheme, Kundu (1980) determined values of A from 100 to $300 \text{ cm}^2 \text{ s}^{-1}$ in the upper 20 m of the water column for an applied wind stress of $1.5 \text{ dynes cm}^{-2}$. Kondo et al. (1979) found a stability-dependent eddy diffusivity to vary between 20 and $300 \text{ cm}^2 \text{ s}^{-1}$ as a result of diurnal heating and a $0.8 \text{ dynes cm}^{-2}$ wind stress.

Theoretically, (C2) may be solved to find A if values for the amplitude of the surface wind stress τ_0 and the currents at any given depth z are known. Comparison of current ellipses calculated from (C2), using various values of A, with observed diurnal currents as estimated from the first mode frequency domain EOFs shows that the CODE-1 observations are best represented when A equals $225 \text{ cm}^2 \text{ s}^{-1}$

and the CODE-2 observations when A equals $90 \text{ cm}^2 \text{ s}^{-1}$ (Figure C1). If smaller values of A correspond to weaker wind stress and stronger stratification, as previous studies suggest, then this could help to account for the difference in the values of A between CODE-1 and -2. The average diurnal wind stress during CODE-2 is less than that during CODE-1 (Table 2) and the average stratification is greater due to the larger number of wind relaxations which lead to cessation of the upwelling (Send et al., 1987). Comparison of Figure C1 with Figures 14 and 15 shows that the diurnal current amplitude and decay scale are represented fairly well by this model. The phase of the current with respect to the wind stress is also correct. However, the CW rotation of the ellipse axes with depth in this simple model is not consistent with the observations. Of course, the assumption that A is constant with time and depth is not very realistic. Many ideas about the dependence of A on depth and with time have been proposed. From numerical model results, Kondo et al. (1979) and Kundu (1980) find that the vertical eddy diffusivity is a maximum at about 10 m depth. Madsen (1977) proposes use of an eddy coefficient that increases linearly with depth from the surface. Jordan and Baker (1980) compare the results of analytic solutions to (C1) using a number of different vertical structures for A . Although the angle between the wind stress and the surface current, and the rate of turning of the current vector with depth, will depend upon the choice of vertical structure for A , all will have current to the right of the wind with ellipse orientation turning CW with depth.

Right at the coast, the inviscid and surface and bottom Ekman ellipses must combine in such a way that the sum is oriented exactly

CODE-1

CODE-2

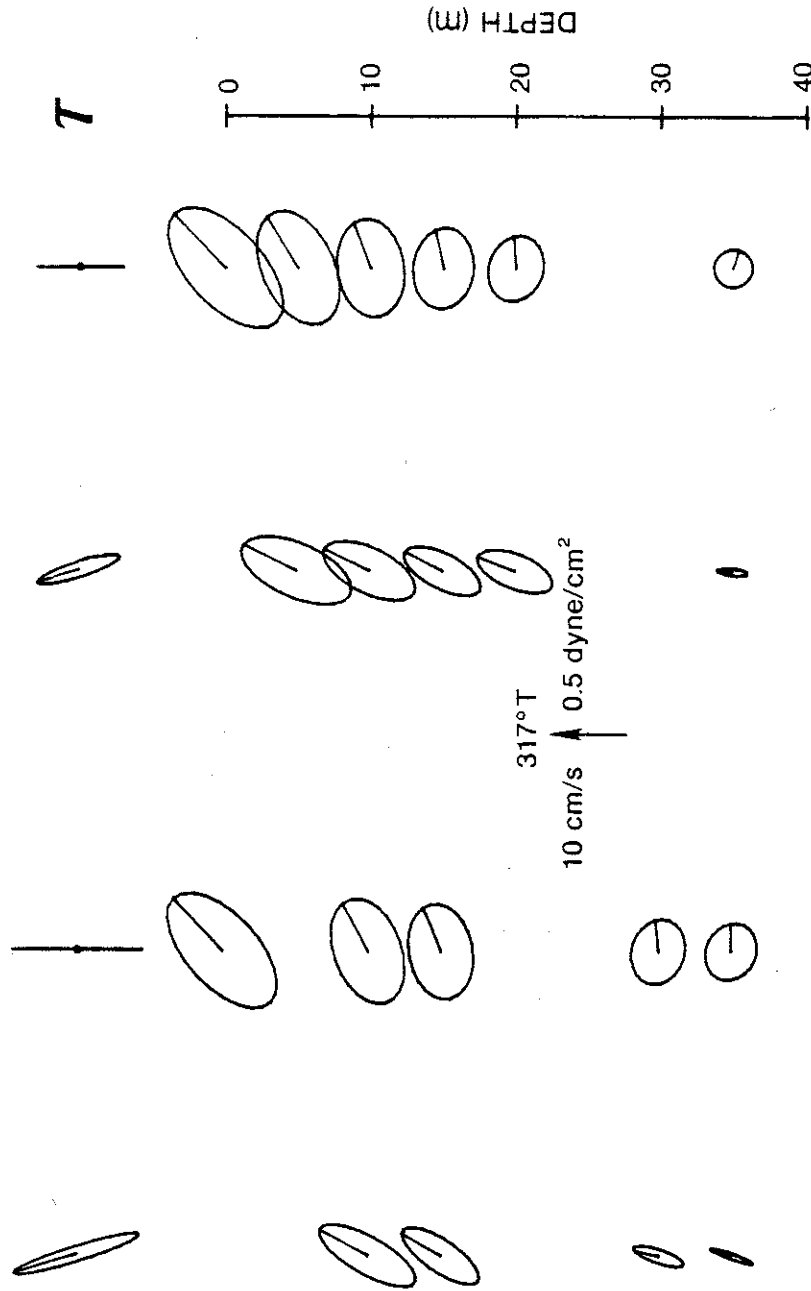


Figure C1. Current ellipses calculated with a constant eddy viscosity model (eqn. C2) are compared with the first mode diurnal currents at C3. For CODE-1, the along-shelf wind stress amplitude = $0.9 \text{ dynes cm}^{-2}$ and $A = 225 \text{ cm}^2 \text{ s}^{-1}$. For CODE-2, the along-shelf wind stress amplitude = $0.6 \text{ dynes cm}^{-2}$ and $A = 90 \text{ cm}^2 \text{ s}^{-1}$. The other model parameters are $\omega = 7.27 \times 10^{-5} \text{ s}^{-1}$, $f = 9 \times 10^{-5} \text{ s}^{-1}$, and $\rho = 1 \text{ g cm}^{-3}$. All current vectors rotate CW. Direction of current vectors at time of maximum poleward wind stress is indicated.

along-shelf. Although no attempt is made here to duplicate this balance exactly, it is noted that the inviscid forced velocity ellipses are oriented along-shelf with their cross-shelf velocity lagging the wind by about 135° , so when added to the surface Ekman ellipses, which have u leading τ by 45° , the cross-shelf components tend to cancel each other.

APPENDIX D: Mixed Layer Model Parameters

In the one-dimensional mixed layer model used here, there are, besides the variables used to describe the forcing function (i.e. amplitude and phase of the heating and wind stress), a number of other "tunable" parameters. The critical gradient and bulk Richardson numbers (R_g and R_b respectively) were chosen in accordance with the work of PWP. The numbers used seem to give reasonable thicknesses of the mixed and transition layers. The equation used to describe the depth-dependence of the absorption of solar radiation, and its effect on the model results, is discussed in the text.

There are four other parameters used in the model and two initial conditions which affect the model results, in particular the mixed layer depth. The two initial conditions are the time of day (and thus the phase of the heating cycle) at which the computation begins, and the initial density profile. If the initial density profile has a very shallow mixed layer (as the one used here did) and the model run starts at 0000 PST, there is cooling and overturning at the beginning which quickly restructures the density profile. Within a day or two, the model reaches a quasi-equilibrium state. If the model run starts at 0600, as heating begins, the succeeding night's cooling wipes out that day's stratification, plus a little bit of the deeper stratification from the initial profile. The model eventually reaches a state similar to that for the run starting at 0000, but it takes a few days longer. While this dependence on the initial conditions could be significant if trying to simulate the data exactly, it is not a problem here because the first five days of the model run are not considered when discussing the general characteristics of the results.

The last four parameters which are important in determining the mixed layer depth are the criteria by which the mixed layer depth is defined, and the way in which R_b and R_g are calculated at each time step. The mixed layer depth is defined as the depth down to which the density is uniform to within $10^{-4} \text{ kg m}^{-3}$. This is an arbitrary choice. In order to avoid a denominator of zero when calculating R_b (eqn. 15b), if $|\Delta \vec{V}|$ is less than 10^{-6} m s^{-1} , it is set to 10^{-6} . In calculating R_g (eqn. 15c), the same criteria is used for ∂V . If $\partial \rho$ is less than $10^{-4} \text{ kg m}^{-3}$, it is set to $10^{-4} \text{ kg m}^{-3}$. Varying these last three parameters can change the details of the temporal variability of the mixed layer depth shown in Figure 21, in particular the sudden sharp increases in mixed layer depth are governed by these parameter choices. Although these sudden changes in the mixed layer depth clearly have a pronounced effect on the mean temperature at the lower depths, they have only a very small effect on the diurnal cycle in temperature at all depths, because the stratification recovers within a day. The effect on the velocity field is also small, both for the reason just given and because when the mixed layer is deep the momentum input by the wind stress is spread out over a larger column of water and at any given depth there is only a small contribution.

ACKNOWLEDGMENTS

The author is greatly indebted to K. Brink for providing the computer programs to calculate the free and forced coastal-trapped waves, and to J. Price for allowing the use of his mixed-layer model. Thanks go to R. Beardsley for overseeing this work which comprises part of my doctoral dissertation. The contributions of C. Alessi, who helped with the data processing, and Veta Green and Anne-Marie Michael, who assisted with the typing, are also appreciated. This work was supported by the National Science Foundation under grant numbers OCE 80-14941 and OCE 84-17769.

References

- Battisti, D. S. and A. J. Clarke, A simple method for estimating barotropic tidal currents on continental margins with specific application to the M₂ tide off the Atlantic and Pacific coasts of the United States. Journal of Physical Oceanography, 12, 8-16, 1982a.
- Battisti, D. S. and A. J. Clarke, Estimation of nearshore tidal currents on nonsmooth continental shelves. Journal of Geophysical Research, 87, 7873-7878, 1982b.
- Beardsley, R. C., C. A. Alessi, and R. Limeburner, CODE-2: Coastal and moored meteorological observations, in CODE-2: Moored Array and Large-Scale Data Report. R. Limeburner, ed., Woods Hole Oceanographic Institution Technical Report WHOI-85-35, CODE Technical Report No. 38, 23-36, 1985.
- Beardsley, R. C., C. E. Dorman, C. A. Friehe, L. K. Rosenfeld, and C. D. Winant, Local atmospheric forcing during CODE-1 and CODE-2. Part I: A description of the marine boundary layer and atmospheric conditions over a northern California upwelling region. Journal of Geophysical Research, 92 (1987), in press.
- Beardsley, R. C., et al. Local atmospheric forcing during CODE. Part III: Local heat flux. In preparation.
- Boon, J. D., and K. P. Kiley, Harmonic analysis and tidal prediction by the method of least squares analysis. Applied Marine Science and Ocean Engineering of Virginia Institute of Marine Science, Special Report No. 186, 49 pp, 1978.
- Brink, K. H., Diurnal behavior of the mid-shelf surface mixed layer near 15°S. CUEA Newsletter, 8, 20-31, 1979.
- Brink, K. H., D. Halpern, and R. L. Smith, Circulation in the Peruvian upwelling system near 15°S. Journal of Geophysical Research, 85, 4036-4048, 1980.
- Brink, K. H. and D. C. Chapman, Programs for computing properties of coastal-trapped waves and wind-driven motions over the continental shelf and slope. Woods Hole Oceanographic Institution Technical Report WHOI-85-17, 99 pp, 1985.
- Brown, W. S., CODE-2: Bottom pressure observations, in CODE 2: Moored Array and Large-Scale Data Report, R. Limeburner, ed., Woods Hole Oceanographic Institution Technical Report WHOI-85-35, CODE Technical Report No. 38, 165-178, 1985.
- Brown, W. S., J.D. Irish, and M. R. Erdman, CODE-1: Bottom pressure observations, in CODE 1: Moored Array and Large-Scale Data Report, L. K. Rosenfeld, ed., Woods Hole Oceanographic Institution Technical Rpt WHOI-83-23, CODE Technical Rpt No. 21, 117-138, 1983.

- Burt, W. B., D. B. Enfield, R. L. Smith and H. Crew, The surface wind over an upwelling area near Pisco Peru. Boundary-Layer Meteorology, 3, 385-391, 1973.
- Burt, W., H. Crew, W. Plutchak, J. Dumon, Diurnal variations of winds over an upwelling region off Oregon. Boundary Layer Meteorology, 6, 35-45, 1974.
- Chapman, D. C., On the influence of stratification and continental shelf and slope topography on the dispersion of subinertial coastally trapped waves. Journal of Physical Oceanography, 13, 1641-1652, 1983.
- Clancy, R. M., J. D. Thompson, H. E. Hurlburt and J. D. Lee, A model of mesoscale air-sea interaction in a sea breeze-coastal upwelling regime. Monthly Weather Review, 107, 1476-1505, 1979.
- Clarke, A. J. and K. H. Brink, The response of stratified frictional flow of shelf and slope waters to fluctuating large-scale, low-frequency wind forcing. Journal of Physical Oceanography, 15, 439-453, 1985.
- Crawford, W. R. and R. E. Thomson, Continental shelf waves of diurnal period along Vancouver Island. Journal of Geophysical Research, 87, 9516-9522, 1982.
- Denbo, D. W. and J. S. Allen, Rotary empirical orthogonal function analysis of currents near the Oregon Coast. Journal of Physical Oceanography, 14, 35-46, 1984.
- Dickey, T. D. and J. J. Simpson, The influence of optical water type on the diurnal response of the upper ocean. Tellus, 35B, 142-154, 1983.
- Ekman, V. W., On the influence of the earth's rotation on ocean currents. Arkiv for Matematik, Astronomi O. Fysik, 2, 1-53, 1905.
- Faller, A. J. and R. Kaylor, Oscillatory and transitory Ekman boundary layers. Deep-Sea Research, 16, 45-58, 1969.
- Gonella, J., A rotary-component method for analyzing meteorological and oceanographic vector time series. Deep-Sea Research, 19, 833-846, 1972.
- Grant, W. D. and O. S. Madsen, Combined wave and current interaction with a rough bottom. Journal of Geophysical Research, 84, 1797-1808, 1979.
- Halpern, D., Summertime surface diurnal period winds measured over an upwelling region near the Oregon Coast. Journal of Geophysical Research, 79, 2223-2230, 1974.

- Halpern, D., Structure of a coastal upwelling event observed off Oregon during July 1973. Deep-Sea Research, 23, 495-508, 1976.
- Halpern, D., Description of wind and upper ocean current and temperature variations on the continental shelf off northwest Africa during March and April, 1974. Journal of Physical Oceanography, 7, 422-430, 1977.
- Hayes, S. P. and D. Halpern, Observations of internal waves and coastal upwelling off the Oregon coast. Journal of Marine Research, 34, 247-267, 1976.
- Jerlov, N. G., Marine Optics, Elsevier Scientific Publishing Company, 231 pp., 1976.
- Johnson, W. R., The propagation of tidal and inertial waves in the upwelling region off Peru. In Coastal Upwelling, F. A. Richards, ed., Published, American Geophysical Union, 79-86, 1981.
- Jordan, T. F. and J. R. Baker, Vertical structure of time-dependent flow dominated by friction in a well-mixed fluid. Journal of Physical Oceanography, 10, 1091-1103, 1980.
- Kondo, J. Y. Sasano, and T. Ishii, On wind-driven current and temperature profiles with diurnal period in the oceanic planetary boundary layer. Journal of Physical Oceanography, 9, 360-372, 1979.
- Kundu, P. K., An analysis of inertial oscillations observed near Oregon coast. Journal of Physical Oceanography, 6, 879-893, 1976.
- Kundu, P. K., A numerical investigation of mixed-layer dynamics. Journal of Physical Oceanography, 10, 220-236, 1980.
- Kundu, P. K., S.-Y. Chao, and J. P. McCreary, Transient coastal currents and inertio-gravity waves. Deep-Sea Research, 30, 1059-1082, 1983.
- Large, W. S. and S. Pond, Open ocean momentum flux measurements in moderate to strong winds. Journal of Physical Oceanography, 11, 324-336, 1981.
- Limeburner, R., ed., CODE-2: Moored Array and Large-Scale Data Report, Woods Hole Oceanographic Institution Technical Report WHOI-85-35, CODE Technical Report No. 38, 234 pp, 1985.
- Madsen, O. S., A realistic model of the wind-induced Ekman boundary layer. Journal of Physical Oceanography, 7, 248-255, 1977.
- Mills, C. A. and R. C. Beardsley, CODE-1: Coastal and moored meteorological observations, in CODE-1: Moored Array and Large-Scale Data Report, L. K. Rosenfeld, ed., Woods Hole Oceanographic Institution Technical Report WHOI-83-23, CODE Technical Report No. 21, 17-29, 1983.

- Mitchum, G. T. and A. J. Clarke, The frictional nearshore response to forcing by synoptic scale winds. Journal of Physical Oceanography, 16, 934-946, 1986.
- Munk, W., F. Snodgrass, and M. Wimbush, Tides off-shore: transition from California coastal to deep-sea waters. Geophysical Fluid Dynamics, 1, 161-235, 1970.
- Noble, M., L. K. Rosenfeld, R. L. Smith, J. V. Gardner, and R. C. Beardsley, Tidal currents seaward of the northern California continental shelf. Journal of Geophysical Research, 92 (1987), in press.
- O'Brien, J. J. and R. D. Pillsbury, Rotary wind spectra in a sea breeze regime. Journal of Applied Meteorology, 13, 820-825, 1974.
- O'Brien, J. J. et al., Upwelling in the ocean: two- and three-dimensional models of upper ocean dynamics and variability. In Modelling and Prediction of the Upper Layers of the Ocean, E. B. Krauss, ed., Pergamon Press, 178-192, 1977.
- Paulson, C. A. and J. J. Simpson, Irradiance measurements in the upper ocean. Journal of Physical Oceanography, 7, 952-956, 1977.
- Pettigrew, N. R., The dynamics and kinematics of the coastal boundary layer off Long Island. W.H.O.I.-M.I.T. Joint Program Doctoral Dissertation, Woods Hole Oceanographic Institution Technical Report WHOI-81-14, 262 pp, 1981.
- Pollard, R. T. and R. C. Millard, Comparison between observed and simulated wind generated inertial oscillations. Deep Sea Research, 17, 813-821, 1970.
- Price, J. F., R. A. Weller, and R. Pinkel, Diurnal cycling: observations and models of the upper ocean response to diurnal heating, cooling, and wind mixing. Journal of Geophysical Research, 91, 8411-8427, 1986.
- Rosenfeld, L. K. and R. C. Beardsley, Barotropic semi-diurnal tidal currents off northern California during the Coastal Ocean Dynamics Experiment (CODE). Journal of Geophysical Research, 92 (1987) in press.
- Rosenfeld, L. K., ed., CODE-1: Moored Array and Large-Scale Data Report, Woods Hole Oceanographic Institution Technical Report WHOI-83-23, CODE Technical Report No. 21, 186 pp, 1983.
- Sauvel, J., Some effects of the diurnal wind during CODE-1. SIO Reference Series, 85-18, 121 pp, 1985.

Shaffer, G., A theory of time-dependent upwelling induced by a spatially and temporally-varying wind with emphasis on the effects of a seabreeze-landbreeze cycle. Kieler Meeresforschung, 28, 139-161, 1972.

Wallace, J. M. and R. E. Dickinson, Empirical orthogonal representation of time series in the frequency domain. Part I: Theoretical considerations. Journal of Applied Meteorology, 11, 887-892, 1972.

Woods, J. D. and V. Strass, The response of the upper ocean to solar heating. II: The wind-driven current. Quarterly Journal of the Royal Meteorological Society, 112, 29-42, 1986.

Zetler, B. D., Radiational ocean tides along the coasts of the United States. Journal of Physical Oceanography, 1, 34-38, 1971.

CHAPTER III

BAROTROPIC SEMIDIURNAL TIDAL CURRENTS OFF NORTHERN CALIFORNIA DURING
THE COASTAL OCEAN DYNAMICS EXPERIMENT (CODE)

This chapter will appear as a paper authored by L. K. Rosenfeld
and R. C. Beardsley, under the title shown above,
in the February, 1987 issue of the
Journal of Geophysical Research

ABSTRACT

Barotropic semidiurnal tidal currents measured off the coast of northern California during the Coastal Ocean Dynamics Experiment (CODE) are examined. While the pressure field is consistent with the idea that the semidiurnal surface tide is dominated by a Kelvin wave, a high degree of variability over alongshore distances of order 25 km is observed in the velocity field. Comparison with existing models used to predict tidal velocities from sea level measurements can not account for this spatial structure. Perturbation analysis of a Kelvin wave propagating along a coastal boundary with bumps characterized by an alongshore length scale much less than the Rossby radius of deformation shows effects on the velocity and pressure field which decay offshore with the alongshore scale of the bumps. The effect on the velocity field exceeds that on the pressure field by a factor equal to the ratio of the Rossby radius to the alongshore scale of the bumps. We conclude that the alongshore structure observed in the measured barotropic semidiurnal tidal currents may be due in part to the local variations in the coastline geometry in the CODE region.

1. INTRODUCTION

The tides off the West Coast of North America are of the mixed, dominant semidiurnal type. The largest tidal constituent is the principal lunar, or M_2 . Numerous global numerical solutions of Laplace's tidal equations have been carried out and, although the location varies from model to model, most show an amphidrome in the northeast Pacific, with phase progressing from south to north along the West Coast of North America. Hendershott (1973) and Munk, Snodgrass, and Wimbush (1970) (hereafter referred to as MSW) both contain figures comparing the M_2 cophase and corange lines for several of these solutions. The M_2 tidal elevation amplitude along northern California is predicted to be on the order of 50 cm. These general results have been confirmed observationally, with sea level and bottom pressure data indicating an apparent northward phase speed of 140 m/s.

MSW sought to interpret the tides locally off California as the sum of Kelvin, Poincare and forced waves over a step-shelf topography. By fitting the unknown amplitudes and phases of the two free waves to a coastal sea level record at La Jolla and an offshore bottom pressure record, they calculated the amplitudes of the Kelvin, Poincare and forced waves at the coast to be 54, 16 and 4 cm, respectively (for a Poincare wave of length 9780 km propagating towards the south). Using this model, MSW found the barotropic current ellipses off southern and central California to be aligned primarily alongshore with semi-major axes on the order of 3 cm/s. Battisti and Clarke (1982a, hereafter referred to as BC), using a quadratic fit to coastal sea level measurements to calculate a complex alongshore wavenumber, predicted

alongshore tidal currents of the same amplitude for northern California. Both of these models are consistent with the idea that the semidiurnal tide along the West Coast is dominated by a Kelvin wave, although a Kelvin wave alone can not account for the observed phase speed or the gradual increase in the M_2 surface tide amplitude to the north. In a normal mode calculation for a barotropic model of the world ocean, Platzman (1979) also found that a Kelvin wave accounts for much of the semidiurnal tide off California.

The alongshore scale of variability for the Kelvin wave, or for that matter, any of the possible free barotropic hydrostatic linear waves at the M_2 frequency in this area, is thousands of kilometers. Past estimates of barotropic semidiurnal tidal currents from shelf and slope data off the U.S. West Coast are 2-3 cm/s (see Bratkovich, 1985; Noble et al., 1986; Torgrimson and Hickey, 1979; and Denbo and Allen, 1984). These estimates are widely separated in the alongshore direction however, and do not allow determination of the scale of variability in that direction.

In this paper, current measurements separated by only 25 to 30 km in the alongshore direction on the northern California shelf are examined. Significant variability in the semidiurnal barotropic tidal currents on these short spatial scales is seen for the first time. A comparison made between the BC model and a more sophisticated version of the MSW model using more realistic cross-shelf topography indicates that both models, while agreeing closely with each other, fail to predict the observed spatial variation in current over the shelf. A simple model is then proposed to explain this small-scale variability as the direct effect of short-scale bumps in the coastal boundary.

Since the perturbations in the current field caused by this boundary bumpiness decay offshore with the same alongshore scale characterizing the boundary bumpiness, the new model predicts that the real current field should approach the BC and MSW model current field far offshore. This result is consistent with the Noble et al. (1987) description of tidal currents over the continental slope and deep sea fan off northern California.

The data discussed here were obtained on the continental shelf north of San Francisco during the Coastal Ocean Dynamics Experiment (CODE), a multi-institutional effort which included two small-scale densely-instrumented moored array experiments conducted during the summers of 1981 and 1982 (called CODE-1 and CODE-2, respectively), and a more sparsely instrumented moored array experiment conducted during the winter between. In sections 2 and 3 of this paper, the data and method of analysis, respectively, are described. Section 4 presents the observations. In section 5, the results are presented and discussed in light of the MSW and BC models mentioned above. Section 6 presents a new very simple model to explain the short alongshore length scales observed. Conclusions are presented in section 7.

2. DATA

The data utilized in this paper consist of hourly-averaged sea level (adjusted for atmospheric pressure), bottom pressure, and current records. Instrument positions are shown in Figure 1 and presented together with start and stop dates for the time periods analyzed in Table 1. Time series of sea level spanning the entire period from the start of CODE-1 to the end of CODE-2 were provided for

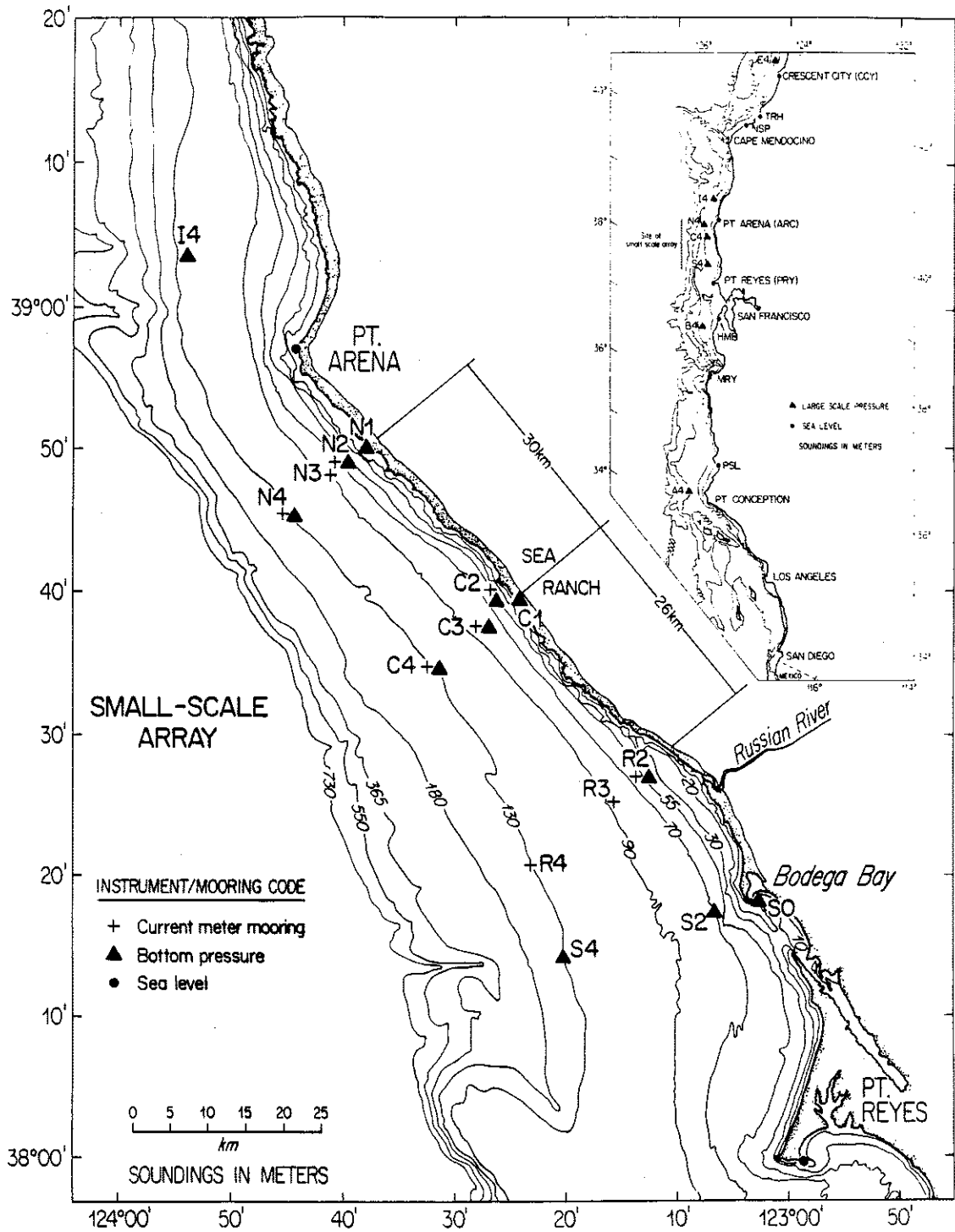


Figure 1. Bottom pressure, sea level and current measurement locations for the CODE small-scale array. The inset map shows the locations where the fifteen bottom pressure and sea level records used here were obtained.

Station		Latitude N	Longitude W	Start Date	Stop Date	No. of Days
SEA LEVEL						
Crescent City (CCY)		41.75	124.18	4/17/81	7/25/82	465
Trinidad Head (TRH)		41.05	124.15	4/17/81	7/25/82	465
North Spit (NSP)		40.75	124.23	4/17/81	7/25/82	465
Arena Cove (ARC)		38.92	123.72	4/17/81	7/25/82	465
Point Reyes (PRY)		38.00	122.97	4/17/81	7/25/82	465
Half Moon Bay (HMB)		37.50	122.48	4/17/81	7/25/82	465
Monterey (MRY)		36.60	121.88	4/17/81	7/25/82	465
Port San Luis (PSL)		35.17	120.75	4/17/81	7/25/82	465
BOTTOM PRESSURE						
	Depth (Nearest 10 m)					
E4	130	41.89	124.49	4/19/81	7/18/81	89
I4	130	39.05	123.92	3/27/82	8/03/82	129
N4	130	38.77	123.76	4/18/81	6/03/81	46
N2	60	38.83	123.67	4/18/81	7/18/81	91
				3/18/82	8/10/82	145
N1	40	38.83	123.66	4/18/81	7/18/81	91
C4	130	38.57	123.54	4/21/81	7/19/81	88
				7/20/81	1/01/82	165
				3/23/82	8/03/82	133
				3/25/82	8/03/82	131
C3	90	38.61	123.46	3/30/81	5/18/81	49
				3/12/82	8/09/82	150
				6/01/82	7/29/82	58
C2	60	38.65	123.42	4/01/81	7/24/81	114
				3/23/82	8/04/82	133
C1	30	38.66	123.41	4/01/81	7/10/81	100
				7/20/81	1/30/82	194
R2	60	38.45	123.23	3/12/82	8/09/82	150
S4	130	38.24	123.33	4/23/81	7/16/81	84
				7/20/81	3/03/82	226
				3/26/82	8/05/82	132
S2	60	38.29	123.10	4/06/81	7/31/81	116
S0	4	38.31	123.05	4/01/81	7/26/81	117
B4	130	37.29	122.79	4/08/81	7/16/81	99
				7/29/81	3/03/82	217
				4/02/82	6/12/82	70
A4	130	34.72	120.84	4/07/81	7/28/81	112

Table 1. Instrument locations and measurement dates

Stn	Depth (near- est 10 m)	Lati- tude °N	Longi- tude °W	Start Date	Stop Date	No. of Days	Instrument Depths (m)
DEPTH-AVERAGED CURRENTS							
N2	60	38.83	123.67	3/13/82	8/05/82	145	10,20,35
N3	90	38.80	123.69	3/12/82	8/05/82	146	10,35,53, 70,83
N4	130	38.76	123.76	3/25/82	8/20/82	148	10,20,35,55, 70,90,110,121
C2	60	38.64	123.42	3/12/82	8/05/82	146	10,20,35,53
C3	90	38.61	123.46	3/24/82	7/28/82	126	5,10,15,20,35, 53,70,83
C4	130	38.56	123.53	4/01/82	8/17/82	138	10,20,35,55,70, 90,121
R2	60	38.45	123.23	3/13/82	8/05/82	145	20,35,53
R3	90	38.42	123.27	3/13/82	8/05/82	145	20,35,53,70
R4	130	38.35	123.38	4/02/82	8/14/82	134	10,20,35,55,70, 90,110

Table 1. (Continued)

eight positions along the coast of California from Port San Luis in the south to Crescent City in the north by G. Halliwell and J. Allen of Oregon State University. Bottom pressure records from twelve sites within the small-scale CODE array and three more locations to the north and south of it for various time periods were provided by J. Irish and W. Brown of University of New Hampshire. Records from current meters maintained by C. Winant and R. Davis of Scripps Institution of Oceanography and R. Beardsley of Woods Hole Oceanographic Institution from nine sites arranged in three cross-shelf lines with moorings at the 60, 90, and 130 meter isobaths were used (Figure 1). Only the CODE-2 current records are included in the present analysis because the vertical resolution was best during this time period. The four month time series available from this part of the experiment are long enough to resolve the major tidal constituents. The reader is referred to the CODE-1 (Rosenfeld, 1983) and CODE-2 (Limeburner, 1985) moored array data reports for more details concerning the CODE field experiments and all the above data.

3. METHOD OF ANALYSIS

Time series of hourly adjusted sea level, bottom pressure and depth-averaged alongshore (positive towards 317°T) and cross-shore (positive towards 47°T) current were analyzed for the amplitude and phase estimates of the major tidal constituents. Under the assumption of a rigid lid (which is approximately true for baroclinic modes) and a uniformly sloping bottom with a subcritical bottom slope which allows internal waves to propagate onshore (Wunsch, 1969), the vertical integral of the horizontal velocity components for the

baroclinic tides (i.e., internal waves at tidal frequencies) is zero. Given adequate vertical resolution, depth-averaging of the observed currents should eliminate most of the baroclinic components and result in a time series representative of the barotropic flow field. For each of the nine current meter mooring sites shown in Figure 1, the depth-averaged time series of cross- and alongshore velocity components were obtained by trapezoidal integration over depth. Table 1 shows which instruments were included in the depth-average at each station for the given time periods.

The success of this method at eliminating baroclinic tidal energy from the barotropic current time series can be assessed in the following three ways. (1) Comparison of the spectra of the current at a given depth with that of the depth-averaged current shows a narrowing of the semidiurnal peak resulting from a reduction in the internal wave energy. Spectra from the mid-shelf C3 site shown in Figure 2 offer an example of this. The semidiurnal peak in the 9 m current spectrum is much broader ($Q \sim 5$) than in the depth-averaged current spectrum ($Q > 14$) or in the bottom pressure spectrum ($Q > 14$), where $Q = \frac{\omega_M}{\Delta\omega}$ with $\Delta\omega$ the band width between the half-power points of the semidiurnal peak. (2) The bottom pressure signal is influenced very little by baroclinic effects so that a high coherence between the depth-averaged current and local bottom pressure at tidal frequencies indicates that the depth-averaging has effectively filtered out baroclinic components in the depth-averaged current record. Table 2 gives these coherences which are generally well above the 95% confidence level for zero coherence. The computed coherence was not usually high across a wide range of frequencies, but instead peaked at

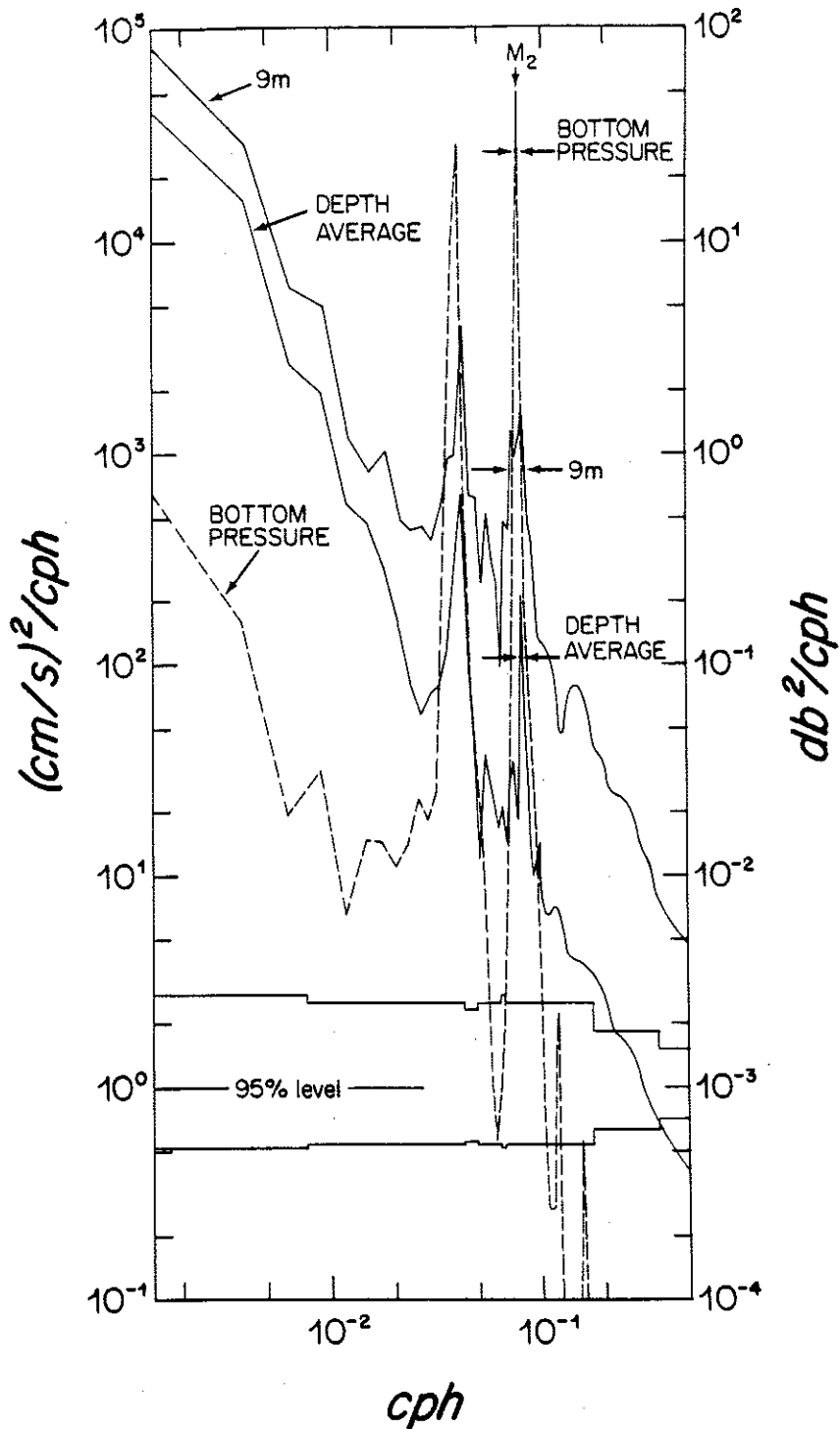


Figure 2. Power spectra for the 9 m and depth-averaged currents and bottom pressure measured at station C3 for the 99 day period starting April 13, 1982. A 24-hour cosine taper was applied to each end of the time series before Fourier transforming. 95% confidence limits are shown. The horizontal arrows around each M_2 peak indicate $\Delta\omega$ at the half-power points. Q is calculated as $\omega_{M_2} / \Delta\omega$.

Station	BP - u		BP - v	
	Coherence	Phase	Coherence	Phase
N2	0.53	-137	0.99	48 ± 8
C4	0.97	87 ± 13	0.68	87
C3	0.97	88 ± 12	0.85	69 ± 31
C2	0.86	89 ± 29	0.87	60 ± 28
R2	0.71	120	0.95	-15 ± 15

Table 2. Coherence between bottom pressure and depth-averaged currents. BP = bottom pressure, u = depth averaged cross-shore velocity, v = depth-averaged alongshore velocity. Time series from 4/2/82 - 7/21/82 (110 days) were used for this computation. Coherences for the frequency band 0.0801 - 0.0816 cph are reported. The M₂ frequency is 0.0805 cph. Error bars for phase are given only for those cases where the coherence is greater than 0.73, which is the 95% significance level.

the tidal frequencies. Not presented are coherences between bottom pressure and currents at a particular depth, which are lower than those for the depth-averaged currents. For instance, coherences between bottom pressure and the depth-averaged cross- and alongshore velocity components at C3 are 0.97 and 0.85, respectively, while corresponding coherences with the 5 m currents are 0.44 and 0.42, respectively, and the 70 m currents, 0.85 and 0.74. (3) The M_2 tidal constants derived from long bottom pressure or sea level records are time-invariant (once corrections for very low frequency variations in the astronomical tides have been made). Presumably the true barotropic semidiurnal tidal currents, which are due to the sloping sea surface, are also invariant. Comparison of the tidal analysis of the depth-averaged currents from the CODE-1 and winter time periods with that from the CODE-2 time period, shows that the scatter in the harmonic constants is smaller than the differences that will be emphasized here.

A least squares method of tidal analysis was used to calculate all the tidal constants reported here. This method is easily adaptable to time series of arbitrary length and does not require the use of a reference series. Comparisons made with the Fourier harmonic and response methods show that the results would be nearly identical had either of these been employed instead. The least-squares tidal analysis procedure followed here is described in Boon and Kiley (1978), with some minor modifications and corrections. For record lengths less than 4383 hours (182 days), tidal constants are calculated directly for ten primary constituents: M_2 , S_2 , N_2 , K_1 , O_1 , M_4 , S_4 , M_6 , S_6 , and M_8 . Fifteen other constituents are inferred

according to the equations in Schureman (1941), among them P_1 , T_2 , and K_2 which are then subtracted from the original time series, and the ten primary constituents listed above are recalculated so as to eliminate the effects of P_1 on K_1 and T_2 and K_2 on S_2 . For series of length 4384 to 8767 hours (365 days), P_1 and K_2 are also calculated directly and for series longer than 8767 hours, T_2 is added to those constituents directly calculated. These record lengths were chosen in accordance with the criteria described by Foreman (1977).

Error brackets given for the amplitude and phase are the 95% confidence limits, calculated as two times the quantity Δ which is analogous to a standard deviation. Δ is calculated following formulas presented in Godin (1972) and discussed in Tee (1982), with the modification that white noise is assumed across the semidiurnal band only, not the entire spectrum. $\Delta_{\text{amplitude}}$ equals the square root of the average noise variance in the semidiurnal band, where the noise is found by subtracting the tidal record predicted from the calculated harmonic constants from the original record, and the semidiurnal band is defined as 0.073-0.087 cycles/hr. Δ_{phase} in radians, equals $\Delta_{\text{amplitude}}$ divided by the amplitude.

4. OBSERVATIONS

The amplitude and Greenwich phase of the three largest semidiurnal constituents (M_2 , S_2 , and N_2) for the eight adjusted sea level records considered here are listed in the upper part of Table 3. Because the M_2 (principal lunar) is always the largest semidiurnal constituent in the sea level, bottom pressure, and depth-averaged velocity records, the discussion here will be limited to a description

	M_2 (12.42 h)		S_2 (12.00 h)		N_2 (12.66 h)		% Vari- ance in M_2	% Vari- ance in all Tides
	A(db)	G(deg)	A(db)	G(deg)	A(db)	G(deg)		
ADJUSTED SEA LEVEL								
CCY	0.715	211.3	0.185	230.8	0.155	183.8	63	96
TRH	0.688	209.6	0.175	228.3	0.149	183.0	63	97
NSP	0.680	218.3	0.172	240.0	0.147	193.5	62	97
ARC	0.571	196.3	0.143	205.3	0.126	169.9	57	96
PRY	0.549	190.2	0.141	195.2	0.124	163.5	54	96
HMB	0.545	184.6	0.144	186.9	0.126	158.6	57	97
MRY	0.496	181.7	0.136	180.7	0.115	155.7	51	97
PSL	0.493	168.8	0.157	164.2	0.116	144.4	52	97

The 95% confidence limits for the semidiurnal tidal constants are ± 0.004 db for amplitude and $\pm 0.4^\circ$ for phase.

BOTTOM PRESSURE								
E4	0.72	213	0.18	233	0.17	181	64	97
I4	0.58	201	0.14	211	0.14	178	56	97
N4*	0.56	195	0.14	205	0.14	165	--	--
N2	0.56	198	0.14	206	0.13	171	57	97
N1	0.56	199	0.14	208	0.14	166	58	95
C4	0.55	193	0.14	199	0.13	168	56	97
C3	0.55	199	0.14	207	0.12	174	56	99
C2	0.55	198	0.14	205	0.13	171	55	96
C1	0.55	196	0.14	202	0.13	169	55	96
R2	0.54	198	0.14	204	0.13	175	56	99
S4	0.55	195	0.14	200	0.13	167	55	98
S2*	0.55	195	0.14	202	0.13	165	54	95
S0*	0.53	193	0.13	200	0.15	170	53	95
B4	0.52	186	0.14	187	0.12	161	55	98
A4	0.47	165	0.16	160	0.12	138	52	97

Where more than one deployment was done at a particular site, the results have been averaged together. The 95% confidence limits for the semidiurnal tidal constants are less than or equal to ± 0.01 db for amplitude and $\pm 1^\circ$ for phase, except for those stations indicated by an asterisk, for which the error brackets are ± 0.02 db and $\pm 2^\circ$. Estimates of the % variance are unreliable for station N4 due to the short record length.

Table 3. Semidiurnal tidal constants for adjusted sea level and bottom pressure

of the sea surface and barotropic velocity fluctuations at the M_2 period of 12.42 hours. Bottom pressure records, while not free from effects of internal density variability, do primarily reflect changes in sea surface elevation at tidal periods, as evidenced by the consistency between bottom pressure records and nearby tide gage records. The semidiurnal tidal constants for all bottom pressure records obtained in CODE are listed in the lower part of Table 3. These are almost identical, as expected, to the tidal constants reported by Brown et al., (1983) and Brown (1985) for bottom pressure records from the CODE-1 and CODE-2 periods separately. The M_2 tide accounts for 50 to 65% of the total variance in the sea level and bottom pressure records. The sum of N_2 and S_2 adds another 4 to 8%. The diurnal constituents make up most of the rest, so that the tides in total account for over 95% of the variance in adjusted sea level and bottom pressure. Figure 3 shows how the amplitude and phase of the M_2 surface tide (from both bottom pressure and sea level data) varies with alongshore location. The pronounced increase in both amplitude and phase toward the north has been noted previously by MSW and others.

The tidal currents account for only 1 to 10% of the total variance in the barotropic currents, of which the M_2 constituent makes up 20 to 70%. The barotropic tidal currents comprise a larger proportion of the variance at greater distances from the coast. This trend is confirmed by Noble et al. (1987) who report that tides may account for as much as 50% of the current variance over the slope and deep sea fan off northern California. The computed M_2 amplitude and phase for the observed depth-averaged along- and cross-shore velocity components are

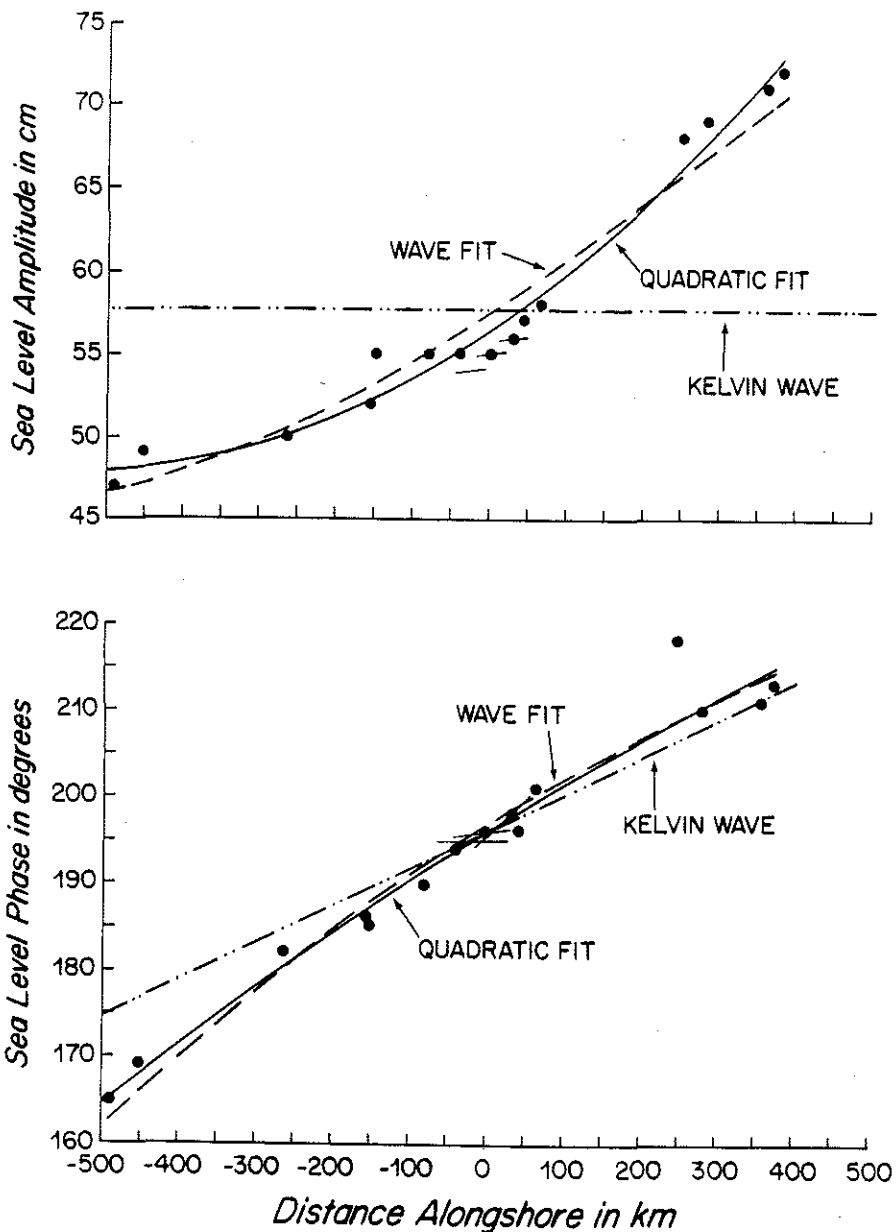


Figure 3. The dots indicate amplitude and phase for the seven bottom pressure and eight sea level stations listed in Table 5. The CODE C-line corresponds to the origin of the x-axis. The dashed lines show amplitude and phase versus distance alongshore for the fit to the sum of a Kelvin, Poincaré and forced wave. The dot-dashed lines are for a Kelvin wave alone. The solid lines show the quadratic fit used in calculating the complex alongshore wavenumber used in the BC model. The three short lines at -26, 0, and 30 km alongshore indicate η_y calculated as $(-fu + i\omega v)/g$ from the velocities at R3, C3, and N3, respectively.

listed in Table 4. It is shown in Figure 4 that most of the M_2 ellipses rotate in a counter-clockwise (CCW) manner, are oriented nearly alongshore, and are very nearly in phase with each other. The cause of the deviations from alongshore orientation is unknown, but is not believed to be an effect of the baroclinic tidal currents which are discussed in Chapter IV of this thesis. Perhaps surprisingly however, the ellipse major axes range from about 1 cm/s at the southern (R) and central (C) lines to over 5 cm/s at the northern (N) line. Since the 95% confidence limits range from ± 0.2 to ± 0.4 cm/s, these differences are statistically significant. The S_2 and N_2 constituents show this same trend of much larger alongshore components at the N-line than at the other two mooring transects.

5. DISCUSSION

Two models for the barotropic semidiurnal tides off California have been proposed by previous investigators. Both are based on the linear hydrostatic equations for a homogeneous fluid on an f-plane. MSW sought to interpret the observations as the sum of a Kelvin, Poincaré and forced wave propagating along a straight coast. To facilitate an analytic solution to the problem, they modelled the topography as a 600 m deep, 155 km wide shelf, abutting a "deep-sea" of 3600 m depth. This resulted in a Kelvin wave of 7925 km length. MSW tried several different Poincaré waves, and chose an equatorward propagating one of length 9780 km as giving what they thought were the most physically reasonable amplitude estimates. With this choice, they found the amplitudes at the coast for the Kelvin and Poincaré waves to be 54 and 16 cm, respectively, based on a fit to bottom

Stn	Cross-shore		% Var in		Alongshore		% Var in		Ellipse Parameters		Orientation (°)	Phase (°)
	Amplitude (cm/sec)	Greenwich Phase (°)	M2	All Tides	Amplitude (cm/sec)	Greenwich Phase (°)	M2	All Tides	Semi-Major Axis (cm/sec)	Semi-Minor Axis (cm/sec)		
N2	0.2±.2	11±47	0.3	2	5.5±.4	151± 4	4	7	5.5±.4	0.1±.2	-2±2	151± 4
N3	0.9±.1	154± 9	3	8	5.5±.3	151± 3	5	7	5.6±.3	-0.0±.1	9±2	151± 3
N4	1.6±.2	172± 7	6	13	5.0±.3	148± 3	7	9	5.2±.3	-0.6±.2	17±2	150± 3
C2	0.5±.2	112±17	2	5	1.1±.3	133±14	0.4	3	1.2±.3	0.2±.2	27±9	129±13
C3	0.9±.1	109± 8	3	5	0.9±.3	125±16	0.2	2	1.3±.2	0.2±.2	45±9	117± 9
C4	1.9±.2	99± 5	7	10	0.5±.3	105±32	0.1	2	2.0±.2	0.1±.3	74±9	100± 5
R2	0.3±.2	83±30	0.7	2	1.4±.2	214± 9	1	5	1.5±.2	0.2±.2	-9±7	-145± 9
R3	0.6±.2	98±17	1	3	1.4±.2	212± 8	0.6	3	1.4±.2	0.5±.2	-11±8	-144± 9
R4	1.1±.2	73±11	1	3	1.4±.2	217± 9	1	6	1.7±.2	0.5±.2	-36±8	-130± 8

Table 4. Depth-averaged M₂ tidal currents for CODE-2. 95% confidence limits are shown. A negative value for the semi-minor axis indicates clockwise rotation. Positive ellipse orientation is measured clockwise from the alongshore direction (317°T). Positive phase is measured along the ellipse in the direction of rotation from the reference point (t = 0) to the point of orientation (which is a point of maximum velocity).

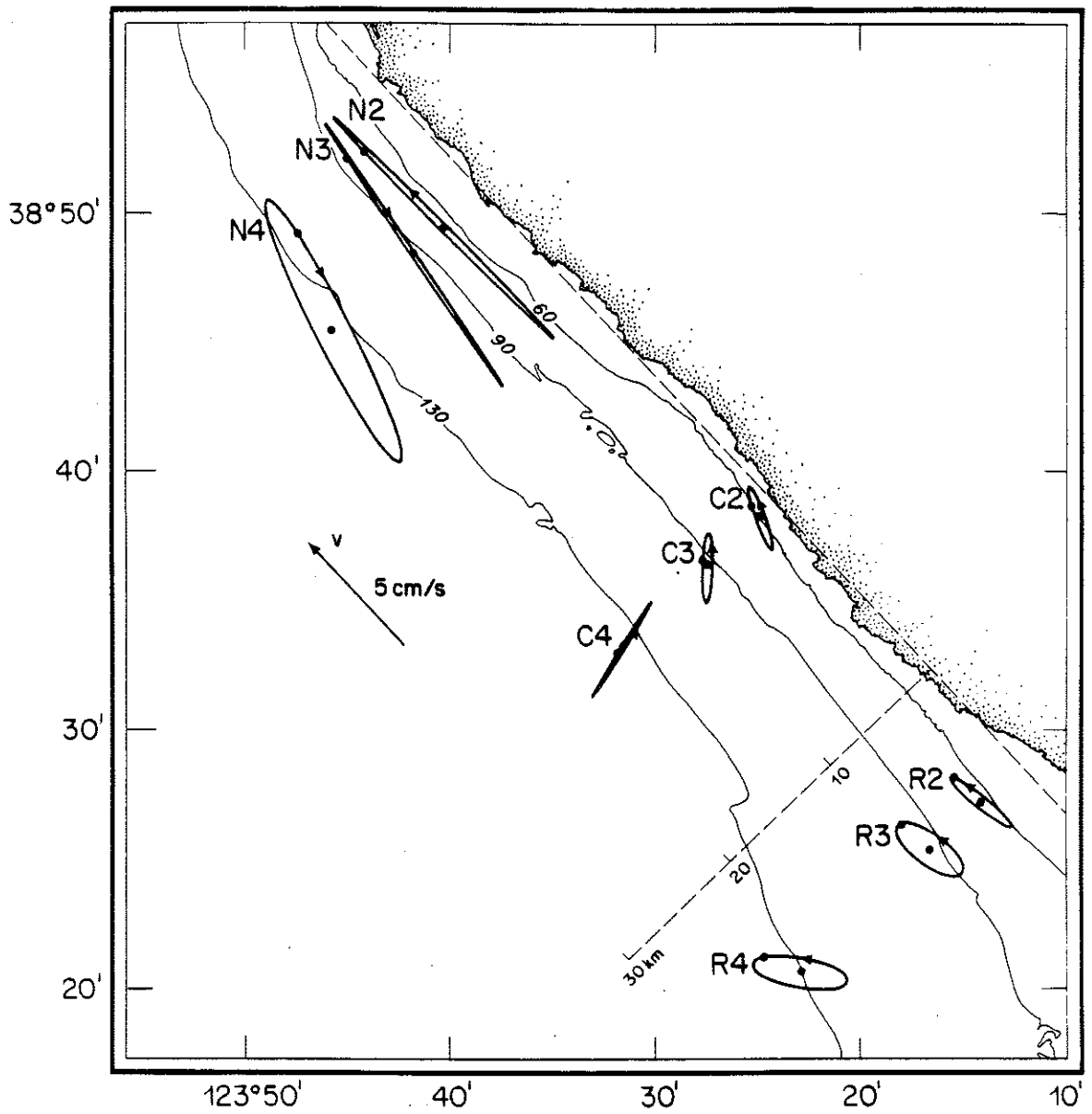


Figure 4. The depth-averaged velocity ellipses for the M₂ frequency. Arrows indicate direction of rotation of the velocity vector. The dots in the ellipse centers indicate mooring location. The dots on the ellipses mark the tip of the velocity vector at the time of high tide at the C-line.

pressure records at La Jolla and a position 900 km offshore. Figure 3 in MSW shows the comparison between observed and model predictions of tidal constants for coastal sea level. Their predictions agree reasonably well with the observations for southern California (where their stations used to determine the constants are located), but clearly disagree in amplitude and phase north of San Francisco. By their own admission, the MSW model predictions of observed tidal currents are less than satisfactory. They attribute this partially to the poor signal-to-noise ratio in the observations making it difficult to determine accurately the barotropic tidal velocity signal, and partially to the inclusion of only one Poincaré wave in the model (Irish, Munk, and Snodgrass, 1971).

Given the more accurate estimates of the barotropic tidal currents made possible by the CODE data, we decided to redo the MSW model with some modifications to see if the fit could be improved. The model is based on the following momentum and continuity equations:

$$u_t - fv + g\eta_x = g\eta_{Ex} \quad , \quad (1)$$

$$v_t + fu + g\eta_y = g\eta_{Ey} \quad , \quad (2)$$

$$(uh)_x + (vh)_y + \eta_t = 0 \quad , \quad (3)$$

where u and v are the cross- and alongshore components of depth-averaged velocity (with positive x directed onshore and positive y directed towards $317^\circ T$ for the coast of northern California), η is the sea surface elevation, f the inertial frequency, g the gravitational acceleration, and subscripts denote partial differentiation. The astronomical forcing, η_E , equals $.69 V/g$, where V is the tidal

potential. η_E may be written as $H_E e^{i(\alpha x + \lambda y + G - \omega t)}$, where $\alpha = \alpha_E \cos \phi$, $\lambda = -\alpha_E \sin \phi$, $\alpha_E = -2/(r \cos \theta)$, r is the radius of the earth, θ the latitude, and ϕ the angle the coastline makes with true north.

If the depth h is a function of x only and the difference between the sea surface elevation and the forcing is assumed to have the form $\eta - \eta_E = \text{Re}[F(x)e^{i(\gamma y - \omega t + G)}]$, a single equation for $F(x)$ can be obtained from (1) - (3):

$$(hF_x)_x + \left[\frac{\omega^2 - f^2}{g} - h\gamma^2 - \frac{f\gamma}{\omega} h_x \right] F = - \frac{\omega^2 - f^2}{g} H_E e^{i\alpha x} . \quad (4)$$

This equation together with a boundary condition of no normal flow at the coast was solved numerically (using a centered finite difference scheme) on a uniform grid in x with .5 km spacing. For each cross-shelf transect where computations were made, the topography was digitized from bathymetry charts and interpolated to the grid spacing. A flat bottom at 3750 m depth was assumed for offshore distances greater than 100 km. For the forced solution, γ was determined by the wavelength of the forcing ($\gamma = -\alpha_E \sin \phi$). For the free solutions, η_E was set to zero, and γ is an eigenvalue of the system (found here by a shooting technique) for waves decaying in the offshore direction, or is arbitrary within the Poincaré continuum, for waves sinusoidal in the x direction. Each wave individually satisfies the coastal boundary condition. The horizontal components of velocity were then calculated using numerical approximations to the polarization equations,

$$u = \frac{g}{\omega^2 - f^2} [(\eta - \eta_E)_{xt} + f(\eta - \eta_E)_y] , \quad (5a)$$

$$v = \frac{g}{\omega^2 - f^2} [(\eta - \eta_E)_{yt} - f(\eta - \eta_E)_x] \quad , \quad (5b)$$

with $\eta_E = 0$ for the free waves. In this way the cross-shelf structure for the forced wave and all possible free waves may be calculated. For the cross-shelf topography at the C-line off Sea Ranch (where $y = 0$), the free Kelvin wave (which is the mode zero edge wave propagating to the north) was found to have a wavenumber of $7.47 \times 10^{-7} \text{ m}^{-1}$ (wavelength 8400 km). No other edge waves were distinguishable, and as the inertial frequency at this latitude is less than the M_2 frequency, no other trapped modes exist.

The sum of this Kelvin wave, the forced response, and a Poincaré wave was then fit in a least squares sense to the fifteen sea level and bottom pressure stations listed in Table 5 to determine the amplitude and phase for the two free waves (Appendix I). The Poincaré wave giving the best fit has a wavenumber of $5.59 \times 10^{-7} \text{ m}^{-1}$ (wavelength 11240 km) and this is the shortest possible southward propagating Poincaré wave at the M_2 frequency. These three waves alone account for 99.6% of the variance in the M_2 sea level and bottom pressure observations. The amplitudes at the coast were found to be 69.8, 26.9, and 4.6 cm for the Kelvin, Poincaré, and forced waves, respectively. The addition of another Poincaré wave does little to improve this fit. A Kelvin wave alone (amplitude 57.7 cm), or a Kelvin wave (amplitude 53.3 cm) plus the forced wave accounts for 97.5% of the pressure variance. Figure 3 shows the observations and model fit. M_2 current ellipses were calculated at a given location by summing the currents due to each wave using the calculated coastal amplitudes and phases and appropriate cross-shelf structure for the

Station	Variable	Alongshore Position (km)	Amp (db)	Greenwich Phase (deg)
E4	BP	375	0.72	213
CCY	SL	356	0.71	211
TRH	SL	278	0.69	210
NSP	SL	247	0.68	218
I4	BP	63	0.58	201
ARC	SL	41	0.57	196
N4	BP	29	0.56	198
C4	BP	0	0.55	196
S4	BP	-41	0.55	194
PRY	SL	-81	0.55	190
HMB	SL	-151	0.55	185
B4	BP	-157	0.52	186
MRY	SL	-264	0.50	182
PSL	SL	-453	0.49	169
A4	BP	-491	0.47	165

Table 5. M_2 tidal constants for sea level (SL) and bottom pressure (BP) data used in models. For bottom pressure, the amplitude and phase represent an average over all deployments (in time and in x) on a given cross-shelf transect.

	Ellipse Characteristics							
	Cross-shore Amp (cm/s)	Phase (°)	Alongshore Amp (cm/s)	Phase (°)	Semi- Major (cm/s)	Semi- Minor (cm/s)	Orien- tation (°)	Phase (°)
<u>N3</u>								
Wave Model	0.4	103	4.3	165	4.3	0.4	3	165
BC Model	0.6	108	4.2	163	4.2	0.5	5	162
Observed	0.9	154	5.5	151	5.6	0.0	9	151
<u>C3</u>								
Wave Model	0.5	98	4.2	164	4.2	0.5	3	164
BC Model	0.6	106	4.1	164	4.1	0.5	5	163
Observed	0.9	109	0.9	125	1.3	0.2	45	117

Table 6. Comparison of observed and modelled currents at C3 and N3. Ellipse orientation is measured CW from 317°T (the positive alongshore direction). Phase is measured along the ellipse from the reference point (t = 0) to the point of orientation.

topography at that cross-section. Velocity components and ellipse characteristics for currents at C3 and N3 are listed in Table 6. It should be noted that in this discussion, the amplitudes of the Kelvin and other free waves have been assumed to be constant and independent of y . Miles (1972, 1973) has pointed out that the amplitude of a free Kelvin wave propagating without energy loss along a simple continental margin should change as a function of latitude (proportional to \sqrt{f}) and offshore depth (proportional to $1/\sqrt{h}$). While both effects act to increase the M_2 sea level amplitude to the north along the California coast, the observed amplitude variation is in fact significantly larger than predicted by $\sqrt{f/h}$, and these considerations can not account for the observed phase speed, so that we have chosen to use the three-wave model as the best fit to the observations.

The observed barotropic semidiurnal tidal currents and those predicted by the wave model just described, may be compared with predictions from the BC model. Battisti and Clarke, in a series of three papers (Clarke and Battisti, 1981; Battisti and Clarke, 1982a, 1982b), develop a method for estimating barotropic tidal currents from coastal sea level measurements taking into account changes in both the amplitude and phase speed along the coast. This is done by letting γ , the alongshore wavenumber, be a complex number that is a function of y . γ is defined by

$$i \gamma(x,y) = \frac{1}{n} \eta_y, \quad (6)$$

or equivalently, $\eta = \eta(0) e^{i(\int \gamma dy + \omega t)}$ (where we change to $e^{+i\omega t}$ for time dependence in keeping with BC). The sea level at any location can also be expressed in terms of its tidal constants (A, G) as

$\eta = Ae^{i(\omega t - G)}$. Taking the y derivative of these two expressions for η and setting them equal yields a second definition of γ as

$$\gamma = -G_y - i \frac{1}{A} A_y . \quad (7)$$

We used (7) to calculate γ , following the method described in Appendix B of Clarke and Battisti (1981). Amplitude and phase for the same sea level and bottom pressure data set used in the wave fit (Table 5 and Figure 3) were each fit to a quadratic in y , and then γ was calculated from A , A_y , and G_y for the alongshore positions of the R, C, and N mooring lines from

$$A(\text{db}) = 0.565 + 3.19 \times 10^{-4}y + 2.98 \times 10^{-7}y^2 ,$$

$$G(\text{deg}) = 196.1 + 5.58 \times 10^{-2}y - 1.44 \times 10^{-5}y^2 ,$$

where y is the distance alongshore in km from the C-line. These quadratic fits explain 97.7% and 96.5% of the variance in amplitude and phase, respectively. The cross-shelf velocity, u , is found by integrating the continuity equation (3) out from the coast and assuming $(hu)_x \gg (hv)_y$, so that

$$\int_0^x (hu)_x dx \approx - \int_0^x \eta_t dx .$$

Applying the coastal boundary condition, assuming η is constant with x over the shelf, and substituting $i\omega$ for $(\partial/\partial t)$ results in

$$u = -i\omega \frac{x}{h} \eta(0) . \quad (8)$$

This is equivalent to saying that the change in sea level during a tidal cycle is due solely to the cross-shore velocity during that time, and is a consequence of the assumed very long ($0(10^4)$ km) along-shore length scale of the tide in comparison to the cross-shelf scale of the continental margin. Petrie (1975) and Bratkovich (1985) found that (8) gave good predictions for the cross-shelf velocity on the Scotian shelf and southern California shelf, respectively. The along-shelf velocity, v , is then found by substituting (6) and (8) into the homogeneous form of (2) to get

$$v = \left(f \frac{x}{h} - g \frac{y}{\omega} \right) \eta(0) . \quad (9)$$

The upper part of Table 7 shows how the real and imaginary parts of γ are calculated from (8) and the lower part gives the amplitude and phase for u and v for the nine current meter sites listed in Table 1. The predicted velocity ellipses are shown in Figure 5. They agree very closely with the results of the wave model (Table 6), but are distinctly different from the observations (Figure 4). Although the BC and wave models correctly predict the alongshore orientation and CCW sense of rotation of the current ellipses, they are unable to predict the correct alongshore variability of the alongshore component of velocity. The two models may under- or over-estimate the true velocities by as much as 30-200%.

We should note that all the relevant assumptions made in the derivation of the BC model are satisfied in the CODE area. $|\gamma| x \ll 1$, where x is the offshore distance at which predictions are to be made. $|\mu| x \ll 1$, where $\mu = (\omega^2 - f^2)/(g\alpha) + (f\gamma/\omega)$ and α is the average

	y (km)	f (10^{-5} s $^{-1}$)	A (db)	G (deg)	A _y (10^{-4} db/km)	$\gamma_r = -G_y$ (10^{-4} km $^{-1}$)	$\gamma_i = (-1/A) A_y$ (10^{-4} db/km $^{-1}$)
N	+30	9.11	0.575	197.8	3.4	-9.6	-5.91
C	0	9.08	0.565	196.1	3.2	-9.7	-5.66
R	-26	9.03	0.557	194.6	3.0	-9.9	-5.39

Stn	x (km)	H (m)	u (cm/s)	Phase of u (deg)	v _r (s $^{-1}$)	v _i (s $^{-1}$)	v (cm/s)	Phase of v (deg)
N2	-3.3	60	0.44	108	0.062	0.041	4.27	164
N3	-6.6	90	0.59	108	0.060	0.041	4.18	163
N4	-15.5	130	0.96	108	0.056	0.041	3.99	162
C2	-2.2	60	0.29	106	0.067	0.039	4.38	166
C3	-7.0	90	0.62	106	0.061	0.039	4.09	164
C4	-15.1	130	0.92	106	0.057	0.039	3.90	162
R2	-5.4	60	0.72	105	0.061	0.038	3.99	163
R3	-10.6	90	0.92	105	0.058	0.038	3.85	161
R4	-23.2	130	1.40	105	0.053	0.038	3.62	159

Table 7. Calculation of the barotropic M₂ currents with the BC model.

A, G, A_y, G_y are calculated using

$$A = 0.565 + 3.19 \times 10^{-4} y + 2.98 \times 10^{-7} y^2,$$

$$G = 196.1 + 5.58 \times 10^{-2} y - 1.44 \times 10^{-5} y^2.$$

The velocity components u and v are calculated using

$$u = -i\omega\eta(0)x/H,$$

$$v = (fx/H - g\gamma/\omega)\eta(0).$$

$$v_r = fx/H - g\gamma_r/\omega$$

$$v_i = -g\gamma_i/\omega$$

$$|v| = \sqrt{v_r^2 + v_i^2} |\eta(0)|$$

$$\text{Phase of } v = -[\tan^{-1}(v_i/v_r) - \text{phase of } \eta(0)]$$

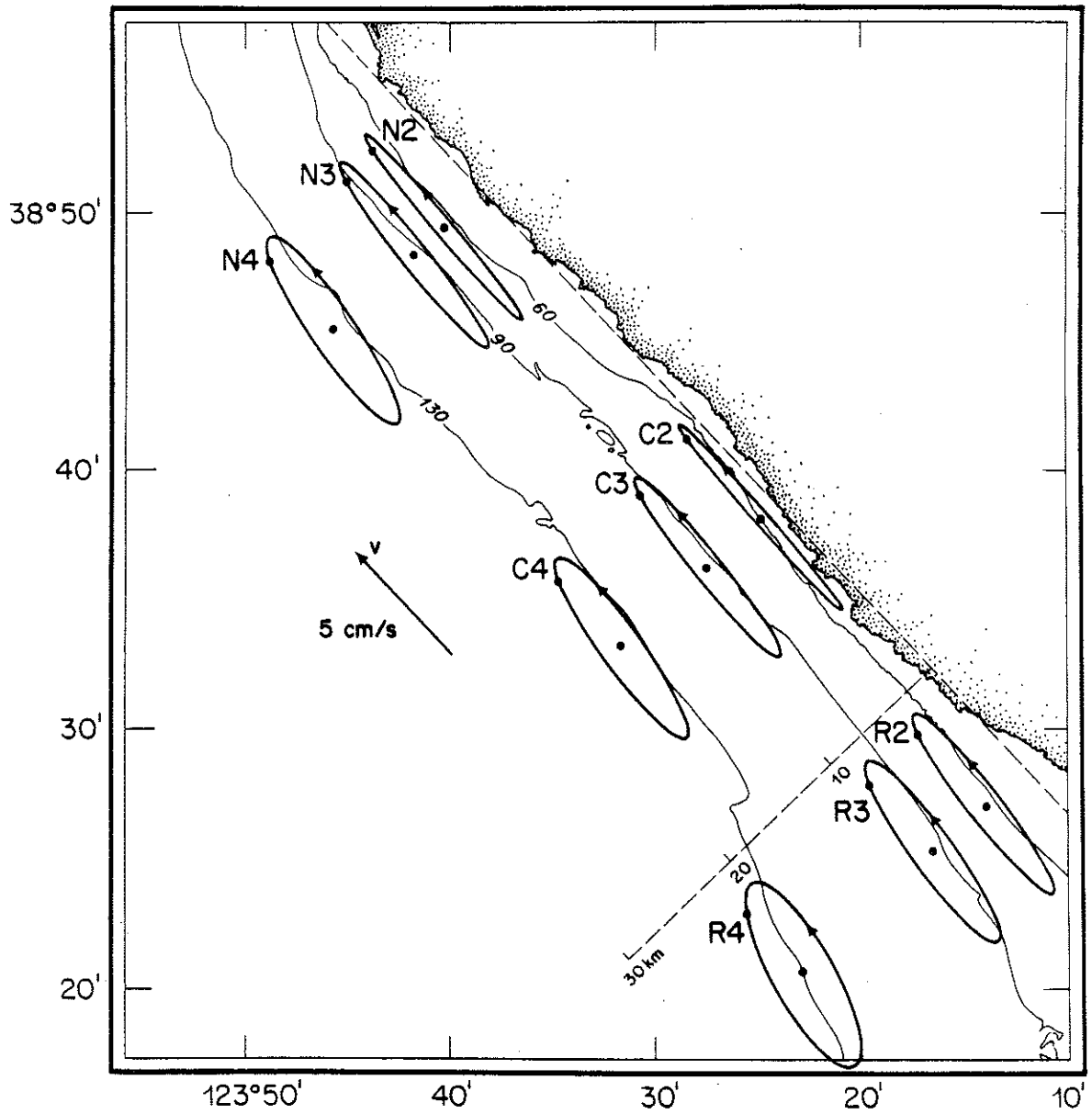


Figure 5. Barotropic velocity ellipses for the M_2 frequency as predicted by the BC method. Markings are as described for Figure 4.

bottom slope, so η is approximately constant across the shelf as is verified from the pressure data at the coast and 130 m isobath. The addition of linear friction based on an rms velocity of 5 cm/s, estimated from observed near-bottom currents, and a drag coefficient of 3×10^{-3} causes less than a 1% change in the calculated alongshore velocities at even the shallowest depths considered here.

Both the BC model and the wave model are consistent with the earlier findings of MSW and Platzman (1979) that the semidiurnal surface tide along the coast of California is dominated by a Kelvin-wave-like response. The large alongshore length scales that seem appropriate to the description of the pressure field are clearly not adequate to predict the velocity field, which depends on the spatial derivatives of pressure. When v at C3 and N3 is predicted from (9) using values of η_y based on just the two closest sea level measurements (Arena Cove and Pt. Reyes for C3, North Spit and Arena Cove for N3), the amplitudes are found to be 3.5 and 7.8 cm/s, respectively. While these results do show more alongshore variability in the correct sense, they are still not satisfactory predictors of the observed velocities. The principal drawback to the use of the BC method is that in any given situation it is difficult to know a priori the appropriate length scale to use in calculating η_y . In Figure 3, A_y and G_y , calculated by substituting the observed u and v into $\eta_y = (-fu + i\omega v)/g$ and making use of (6) and (7), are shown for the positions of the R-, C-, and N-lines. While all of these correspond to values of γ and μ for which $|\gamma| \ll 1$ and $|\mu| \ll 1$ and therefore satisfy the assumptions of the BC theory, it is easy to see the problems one would have in extracting these values from the sea level

and bottom pressure data. Holloway (1983) also points out the strong dependency of v on γ and discusses the difficulty in evaluating the latter.

6. THEORY FOR A KELVIN WAVE ALONG A BUMPY BOUNDARY

A Kelvin-like wave propagating along a straight boundary accounts for much of the semidiurnal variance in the sea level and bottom pressure records measured along the coast of California. The wavelength of the Kelvin wave, which is the shortest of the suite of possible barotropic waves at this frequency, is on the order of 8000 km, and thus can not explain the short scales of variability observed in the velocity field. Here we propose a mechanism that could cause these short scale variations in the velocity field, while altering the pressure field only slightly.

The coastline of California is characterized by bumps (e.g., capes and headlands) with alongshore scales much less than the external Rossby radius of deformation (of order 2000 km). A Fourier decomposition of the coast from Pt. Conception to Cape Mendocino, a straight-line distance of roughly 760 km, reveals deviations of magnitude one to four kilometers for wavelengths from 75 to 760 km. The amplitude of the bumps is smaller for shorter wavelengths. During the decade from 1968 to 1977, numerous papers appeared dealing with the scattering of Kelvin, Poincaré, edge and continental shelf waves by sharp bends in the coastline, discontinuities in depth, large-scale coastline curvature, and random small amplitude coastal irregularities. In general, these papers were concerned with the reflection and scattering of these waves and how the energy flux, phase speed, and

dispersion relation were changed by these varying geometries. Although a great deal can be learned about the effects of an irregular coastline on wave propagation from these studies, none of the previous work directly addresses the question of how the presence of small amplitude bumps with length scales much smaller than the Rossby radius of deformation affects the nearshore velocity field¹. To obtain an answer to this question, we adopt a perturbation approach similar to that used by Pinsent (1972) in his work on the propagation of Kelvin waves along a coastline with large radius of curvature.

For simplicity, we consider a free Kelvin wave propagating along a bumpy coastline over a flat bottom ocean as shown schematically in Figure 6. The equation for the sea surface elevation η is then given by

$$\eta_{xx} + \eta_{yy} + \frac{(\omega^2 - f^2)}{gh} \eta = 0 \quad , \quad (10)$$

where an $e^{-i\omega t}$ time dependence has been assumed. The boundary condition is no normal flow at the coast: $\vec{u} \cdot \hat{n} = 0$ at $x = b(y)$ where \hat{n} is the unit vector normal to the coast. This may be rewritten as

¹ Mysak, in a series of three papers (Howe and Mysak, 1973; Mysak and Tang, 1974; and Fuller and Mysak, 1977), looked at the scattering of Poincaré waves, Kelvin waves, and edge waves from an infinitely long straight coast with small deviations regarded as a stationary random function of position along the coast. These papers employed a stochastic approach to the problem. Mysak and Tang (1974) concluded that for $\omega/f > 1$, the phase speed of a Kelvin wave will be reduced, but only by 1% for the coast of California. They predicted that energy would be scattered by large scale irregularities into Poincaré and Kelvin modes, and that this would cause a decrease in amplitude in the direction of propagation. Obviously this effect is small, since the observations show an increase in amplitude in the direction of propagation. Miles (1972) derived the first order correction to sea level due to a sustained displacement of the coast, and also the correction far downstream of an isolated bump.

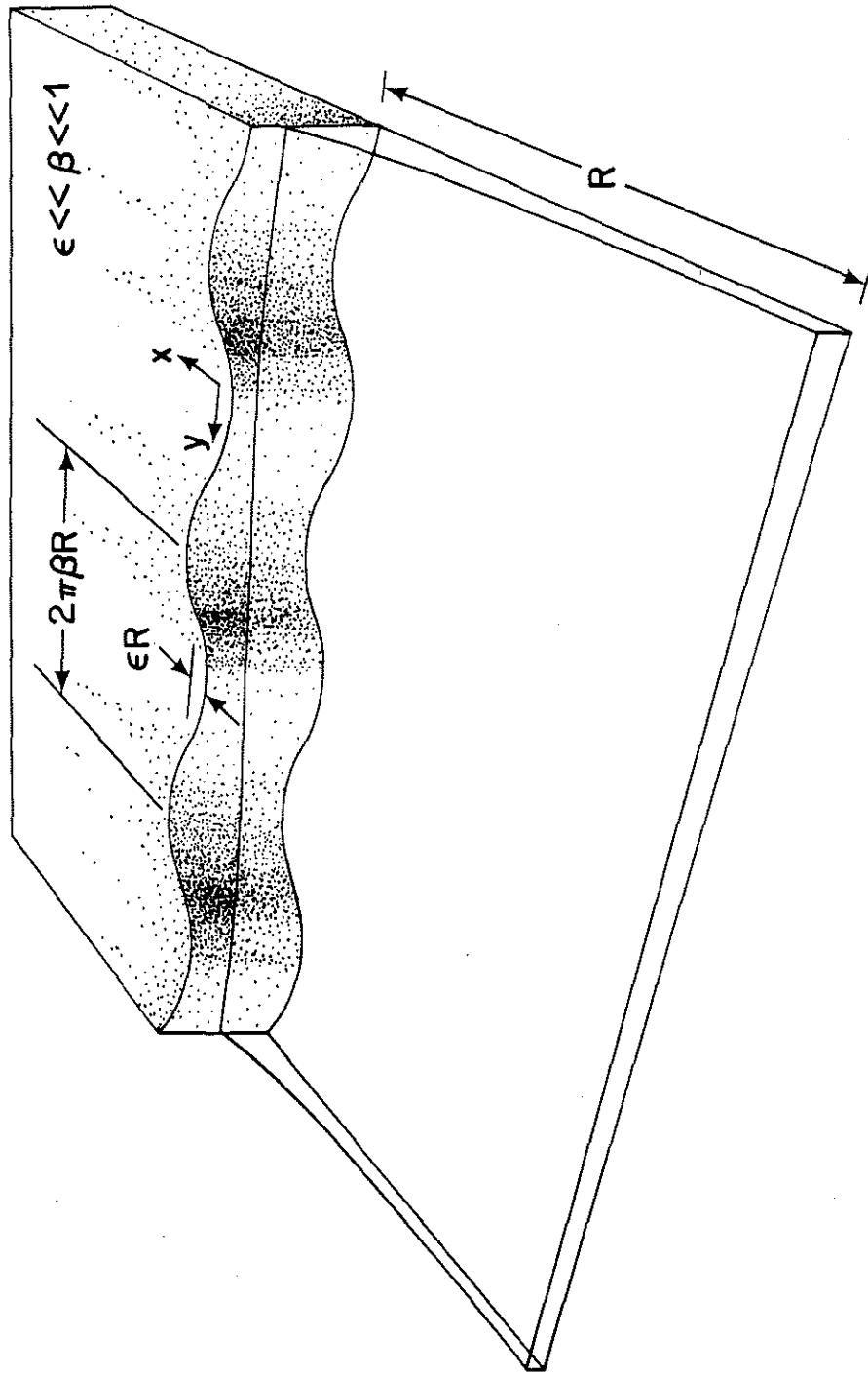


Figure 6. Coordinate system and scaling for bumps in the coastline are shown in schematic drawing of a Kelvin wave propagating along a bumpy boundary.

$$u - b_y v = -i\omega\eta_x + f\eta_y + b_y (i\omega\eta_y + f\eta_x) = 0 \quad \text{at } x = b(y) .$$

Let x and y be scaled by the Rossby radius $R = \sqrt{gh}/f$ everywhere except near the coastal boundary itself where the characteristic cross-shore and alongshore length scales, ϵR and βR , respectively, are set by the geometry of the boundary defined by $b(y)$. Sea level is scaled by C , the surface elevation amplitude at the coast. Thus

$$\eta = C\eta', \quad x = Rx', \quad y = Ry', \quad b = \epsilon R b'(y'), \quad b_y = \epsilon/\beta b'_{y'},$$

where the primes indicate non-dimensional variables. We chose $\epsilon \ll \beta \ll 1$, so that the magnitude of the bumps is much less than their alongshore scale which is in turn much less than the Rossby radius of deformation.

The governing equation for η written in the non-dimensional variables (without the primes) is then

$$(\eta_{xx} + \eta_{yy}) + (\sigma^2 - 1)\eta = 0 \quad , \quad (11)$$

with $\sigma = \omega/f$ and the boundary condition at the coast reducing to

$$-i\sigma\eta_x + \eta_y + \epsilon/\beta b_y (i\sigma\eta_y + \eta_x) = 0 \quad \text{at } x = \epsilon b \quad . \quad (12)$$

Equations (11) and (12), together with the condition that the solution becomes the classical straight boundary Kelvin wave far offshore, constitute a closed problem. After an expansion of η in powers of the small parameter ϵ/β and a Taylor series expansion of η around $x = 0$ for the boundary condition, the zeroth or lowest order problem for η

becomes

$$\eta_{0xx} + \eta_{0yy} + (\sigma^2 - 1)\eta_0 = 0, \text{ for } x < 0, \quad (13)$$

$$-i\sigma\eta_{0x} + \eta_{0y} = 0 \text{ at } x = 0.$$

The solution to (13) is just the Kelvin wave on a straight coast,

$\eta_0 = e^x e^{i(\sigma y - \omega t)}$, which, in dimensional form, is

$$\eta_0 = C e^{\frac{xf}{\sqrt{gh}}} e^{i\omega\left(\frac{y}{\sqrt{gh}} - t\right)},$$

with $u_0 = 0$ and $v_0 = \sqrt{\frac{g}{h}} \eta_0$.

The perturbation problem to first order in ϵ/β is

$$\eta_{1xx} + \eta_{1yy} + (\sigma^2 - 1)\eta_1 = 0, \text{ for } x < 0, \quad (14)$$

$$-i\sigma\eta_{1x} + \eta_{1y} + b_y (i\sigma\eta_{0y} + \eta_{0x}) = 0 \text{ at } x = 0.$$

Up to this point, the form of the boundary b has been arbitrary. We will now choose a sinusoidal form for b to facilitate the rest of the analysis. In dimensional form, $b(y) = \epsilon R \sin(y/\beta R)$ and $b_y = (\epsilon/\beta) \cos(y/\beta R)$: in non-dimensional form, $b_y = \cos my$ where $m = 1/\beta \gg 1$.

The solution to (14) that decays away from the coast is then

$$\frac{\epsilon}{\beta} \eta_1 = \frac{\epsilon m}{2i} \left[\frac{\sigma^2 - 1}{-\sigma k_1 + m + \sigma} e^{k_1 x} e^{i(m+\sigma)y} + \frac{\sigma^2 - 1}{-\sigma k_2 - m + \sigma} e^{k_2 x} e^{-i(m-\sigma)y} \right], \quad (15)$$

where $k_1 \equiv \sqrt{m^2 + 2m\sigma + 1} \doteq m + \sigma + O(1/m)$, and $k_2 \equiv \sqrt{m^2 - 2m\sigma + 1} \doteq m - \sigma + O(1/m)$. When the above expression is expanded in powers of $1/m$, we discover that η_1 is actually of order ϵ . There is no order ϵ/β term in the expansion of η . Thus the first order perturbation solution is

$$\begin{aligned} \frac{\epsilon}{\beta} \eta_1 &= i \frac{\epsilon}{2} e^{mx} [(\sigma + 1) e^{i(m+\sigma)y} + (\sigma - 1) e^{-i(m-\sigma)y}] , \\ \frac{\epsilon}{\beta} v_1 &= i \frac{\epsilon m}{2} e^{mx} [e^{i(m+\sigma)y} - e^{-i(m-\sigma)y}] , \\ \frac{\epsilon}{\beta} u_1 &= \frac{\epsilon m}{2} e^{mx} [e^{i(m+\sigma)y} + e^{-i(m-\sigma)y}] . \end{aligned} \tag{16}$$

The perturbations in the coastline have more effect on the velocity field than on the pressure field. Also, larger values of m (corresponding to smaller alongshore length scales) will result in larger corrections to the velocity field, but cause no change in the amplitude of the pressure correction. This is because the lowest order velocity corrections, u_1 and v_1 , are order $\epsilon m (= \epsilon/\beta)$ whereas the lowest order sea level correction is only of order ϵ and independent of m . Both velocity and surface elevation correction fields decay away from the coast with the dimensional length scale βR .

Multiplying by $e^{-i\omega t}$, taking the real parts, and combining with the zeroth order solution, yields the total non-dimensional velocities

$$\begin{aligned} v_{\text{tot}} &= \cos(\sigma y - \omega t) [e^x - \epsilon m e^{mx} \sin my] , \\ u_{\text{tot}} &= \epsilon m e^{mx} \cos my \cos(\sigma y - \omega t) . \end{aligned} \tag{17}$$

In dimensional terms, the amplitudes of u and v at the coast are

$$v_{\text{amp}} = \sqrt{g/h} C \{1 - \epsilon/\beta \sin [fy/(\beta\sqrt{gh})]\} ,$$

$$u_{\text{amp}} = \sqrt{g/h} C \epsilon/\beta \cos [fy/(\beta\sqrt{gh})] .$$
(18)

Figure 7 shows the coastline configuration to the right and the amplitudes of u and v at the coast to the left for the following model parameters: $h = 3750$ m, $\omega = 1.4 \times 10^{-4} \text{ s}^{-1}$, $f = 0.9 \times 10^{-4} \text{ s}^{-1}$, $R = \sqrt{gh}/f = 2130$ km, coastal bump magnitude $\epsilon R = 2.7$ km, coastal bump wavelength $2\pi\beta R = 110$ km, $\epsilon = 1.3 \times 10^{-3}$, $\beta = 8.2 \times 10^{-3}$, $\epsilon/\beta = 0.16$, and sea level amplitude at the coast $C = 0.55$ m. Figure 8 shows the velocity ellipses at the coast (which are rectilinear due to the constraint of no flow through the boundary) for the same parameters. The alongshore velocity amplitude is found to vary $\pm 15\%$ from the value for a straight coast. The velocities are greatest near the promontories (considered here to crudely represent Pt. Reyes and Pt. Arena) and smaller in between. The reason for this is that the flow far offshore is constrained to match the value for a Kelvin wave along a straight boundary. This effectively causes the flow to speed up as it goes through a constriction represented here by a bump in the coastline. This simple perturbation analysis for a flat bottom ocean indicates that small sinusoidal perturbations in the coastline of scaled amplitude ϵ and alongshore wavelength β cause differences in alongshore velocity amplitude of $2\epsilon/\beta$ (which is $\sim 30\%$ for the parameters used here). A more realistic prediction of the tidal flow field will depend on a full Fourier representation of the coast as well as the addition of shelf topography.

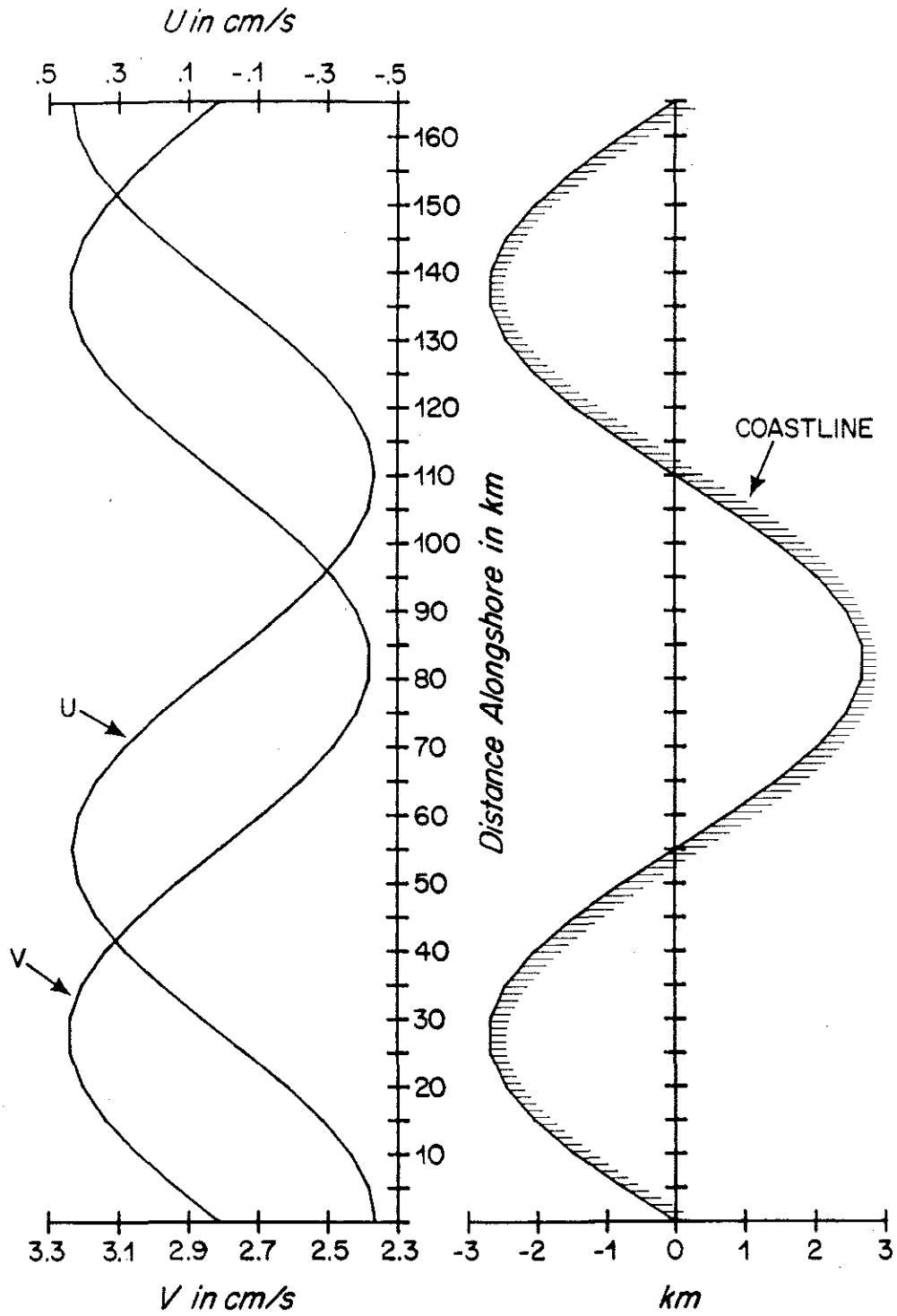


Figure 7. Alongshore, v , and cross-shore, u , velocity components at the coast for a Kelvin wave with coastal amplitude of 55 cm on a flat bottom of 3750 m depth.

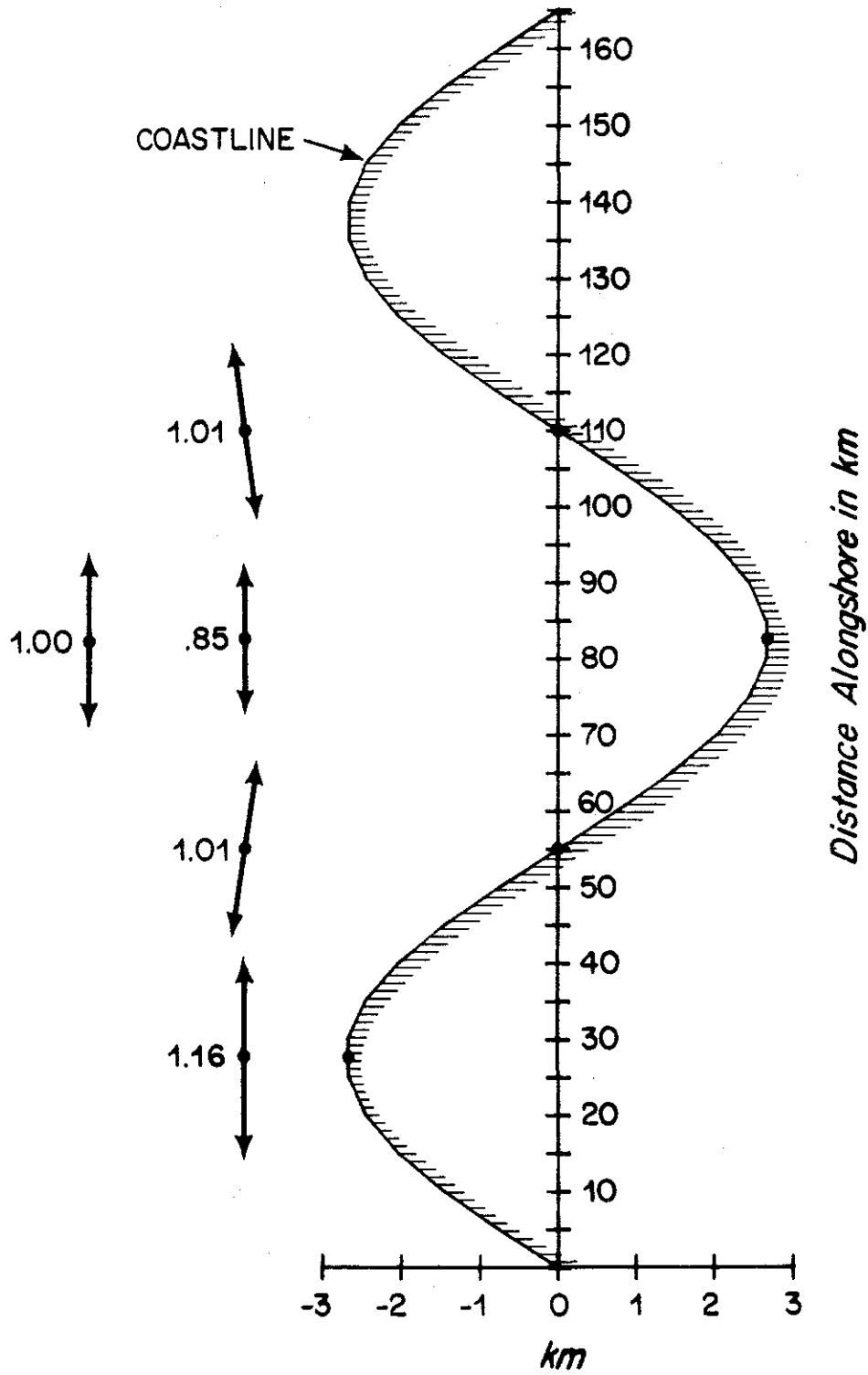


Figure 8. Velocity ellipses at four points along the coast for a Kelvin wave with coastal amplitude of 55 cm on a flat bottom of 3750 m depth.

7. CONCLUSIONS

The semidiurnal surface tide off northern California is characterized by amplitude and phase which increase from south to north. Sea level and bottom pressure measurements indicate an apparent northward phase speed of about 140 m/s. The barotropic tidal currents on the shelf are aligned primarily in the alongshore direction, have CCW rotation and show little variation in the cross-shore direction. They show alongshore variability on scales less than 100 km, with ellipse major axes ranging from 1 to 6 cm/s. No single free barotropic wave can account for the observed pressure signal because no wave with the proper wavelength and phase speed exists for this topography at this frequency. The sum of a Kelvin, forced and one Poincaré wave can account for many of the characteristics of the observed pressure and current fields, including the phase speed, direction of rotation, and orientation of currents. These waves can not describe the observed small-scale variability, however, because these waves have wavelengths which are much greater than the observed length scales in the current field. The BC model applied to the CODE region predicts barotropic tidal currents over the shelf and slope from coastal sea level observations, which compare favorably with the wave model, but it also fails to predict the differences in velocity over short distances due to the difficulty in choosing the appropriate alongshore wavenumber.

Perturbation analysis of a Kelvin wave propagating along a boundary with small bumps with a characteristic alongshore length much less than the Rossby radius of deformation shows effects on the nearshore velocity field which are larger than the effects on the pressure field by the ratio of the Rossby radius to the alongshore scale of the bumps.

The perturbations in both velocity and pressure induced by the bumps decay away from the coast with the same scale as the alongshore length scale of the bumps. Evidence for this is presented in Noble et al. (1987) who find that the magnitude of observed barotropic tidal currents at sites 25, 50 and 300 km from the coast of northern California agree well with predictions made according to the BC model. Although variations in velocity of the magnitude observed in CODE can not be attained through the very simple first order perturbation analysis presented here, the predicted amplification of alongshore velocity near points in the coastline is in accord with the CODE observations. We suggest then that small coastal deviations with short alongshore length scales induce short scale variations in the tidal current field that are reflected in the CODE velocity measurements.

APPENDIX

The amplitudes (A_α) and phases (θ_α) for the free waves are found by minimizing the residual expressed as

$$\text{Res} = \sum_{j=1}^J R_j^* R_j \quad , \quad (\text{A1})$$

where J is the number of stations in the fit and the residual at the j^{th} station is given by

$$R_j = H_j e^{iG_j} - F_j e^{i\beta_j} - \sum_{\alpha} A_{\alpha} \exp(i\theta_{\alpha} - i\gamma_{\alpha} y_j) \quad . \quad (\text{A2})$$

The first term in R_j is the observed tidal constant. The second term is the calculated forced response. The last term is the sum of the responses due to the free waves. The percent of variance accounted for by the model is calculated as

$$\% \text{var} = \left(1 - \frac{\text{Res}}{\sum_j (H_j)^2} \right) \times 100 \quad . \quad (\text{A3})$$

ACKNOWLEDGMENTS

The authors wish to thank Ken Brink and Dave Chapman for helpful discussions during the course of this work. We also thank Carol Alessi for assistance with the data processing and Yeta Green for typing the manuscript and Anne-Marie Michael for preparing this chapter in the thesis format. This work was supported by National Science Foundation under grant numbers OCE 80-14941 and OCE 84-17769.

References

- Battisti, D. S., and A. J. Clarke, A simple method for estimating barotropic tidal currents on continental margins with specific application to the M_2 tide off the Atlantic and Pacific Coasts of the United States. Journal of Physical Oceanography, 12, 8-16, 1982a.
- Battisti, D. S., and A. J. Clarke, Estimation of nearshore tidal currents on nonsmooth continental shelves. Journal of Geophysical Research, 87, 7873-7878, 1982b.
- Boon, J. D., and K. P. Kiley, Harmonic analysis and tidal prediction by the method of least squares. Applied Marine Science and Ocean Engineering of Virginia Institute of Marine Science, Special Report No. 186, 49 pp, 1978.
- Bratkovich, A., Aspects of tidal variability observed on the southern California continental shelf. Journal of Physical Oceanography, 15, 225-239, 1985.
- Brown, W. S., J. D. Irish, and M. R. Erdman, CODE-1: Bottom pressure observations, in CODE-1: Moored Array and Large-Scale Data Report. L. K. Rosenfeld, ed., WHOI Technical Report 83-23, CODE Technical Report No. 21, 117-138, 1983.
- Brown, W. S., CODE-2: Bottom pressure observations, in CODE-2: Moored Array and Large-Scale Data Report. R. Limeburner, ed., WHOI Technical Report 85-35, CODE Technical Report No. 38, 165-178, 1985.
- Clarke, A. J. and D. S. Battisti, The effect of continental shelves on tides. Deep-Sea Research, 28, 665-682, 1981.
- Denbo, D. W. and J. S. Allen, Rotary empirical orthogonal function analysis of currents near the Oregon coast. Journal of Physical Oceanography, 14, 35-46, 1984.
- Foreman, M. G. G., Manual for tidal heights analysis and prediction, Institute of Ocean Sciences. Patricia Bay Pacific Marine Science Report. 77-10, 97 pp, 1977.
- Fuller, J. D. and L. A. Mysak, Edge waves in the presence of an irregular coastline. Journal of Physical Oceanography, 7, 846-855, 1977.
- Godin, G. The Analysis of Tides. Univ. of Toronto Press, 269 pp, 1972.
- Hendershott, M. C., Ocean tides. EOS, 54, 76-86, 1973.
- Holloway, P. E., Tides on the Australian northwest shelf. Australian Journal of Marine and Freshwater Research, 34, 213-230, 1983.
- Howe, M. S. and L. A. Mysak, Scattering of Poincaré waves by an irregular coastline. Journal of Fluid Mechanics, 57, 111-128, 1973.

- Irish, J., W. Munk and F. Snodgrass, M_2 amphidrome in the northeast Pacific. Geophysical Fluid Dynamics, 2, 355-360, 1971.
- Limeburner, R., ed. Code-2: Moored Array and Large-Scale Data Report. WHOI Technical Report 85-35, CODE Technical Report No. 38, 234 pp, 1985.
- Miles, J. W., Kelvin waves on oceanic boundaries. Journal of Fluid Mechanics, 55, 113-127, 1972.
- Miles, J. W., Kelvin-wave diffraction by changes in depth. Journal of Fluid Mechanics, 57, 401-413, 1973.
- Munk, W., F. Snodgrass and M. Wimbush, Tides off-shore: transition from California coastal to deep-sea waters. Geophysical Fluid Dynamics, 1, 161-235, 1970.
- Mysak, L. A. and C. L. Tang, Kelvin wave propagation along an irregular coastline. Journal of Fluid Mechanics, 64, 241-261, 1974.
- Noble, M., L. K. Rosenfeld, R. Smith, J. V. Gardner, and R. C. Beardsley, Tidal currents seaward of the northern California continental shelf. Journal of Geophysical Research, 92, (1987), in press.
- Petrie, B., M_2 surface and internal tides on the Scotian shelf and slope. Journal of Marine Research, 33, 303-325, 1975.
- Pinsent, H. G., Kelvin wave attenuation along nearly straight boundaries. Journal of Fluid Mechanics, 53, 273-286, 1972.
- Platzman, G. W., A Kelvin wave in the eastern North Pacific Ocean. Journal of Geophysical Research, 85, 2525-2528, 1979.
- Rosenfeld, L. K., ed., CODE-1: Moored Array and Large-Scale Data Report, WHOI Technical Report 83-23, CODE Technical Report No. 21, 186 pp, 1983.
- Schureman, P., Manual of harmonic analysis and prediction of tides. U.S. Dept. of Commerce Special Publication No. 98, 1941.
- Tee, K.-T., The structure of three-dimensional tide-generating currents: experimental verification of theoretical model. Estuarine, Coastal and Shelf Science, 14, 27-48, 1982.
- Torgrimson, G. M. and B. M. Hickey, Barotropic and baroclinic tides over the continental slope and shelf off Oregon. Journal of Physical Oceanography, 9, 945-961, 1979.
- Wunsch, C., Progressive internal waves on slopes. Journal of Fluid Mechanics, 35, 131-144, 1969.

CHAPTER IV

BAROCLINIC SEMIDIURNAL TIDAL CURRENTS OVER THE CONTINENTAL SHELF
OFF NORTHERN CALIFORNIA

ABSTRACT

Time-varying depth-dependent currents of semidiurnal frequency are identified in data collected over the northern California continental shelf during the 1982 upwelling season as part of the Coastal Ocean Dynamics Experiment (CODE). Semidiurnal band kinetic energy is seen to increase with increasing stratification over the shelf and upper slope. Comparison with internal wave theory shows the vertical and horizontal structure of the semi-diurnal band horizontal currents to be consistent with a first baroclinic mode internal wave with a horizontal wavelength of about 20 km. The vertical structure of the phase of the semidiurnal band temperature fluctuations shows evidence of the influence of the sub-critical bottom slope over the continental shelf. The bottom slope is super-critical over the upper continental slope, suggesting that generation of the semidiurnal internal waves observed over the shelf may take place near the shelf break.

List of Symbols

- α = bottom slope
- b = buoyancy $-g\rho/p_0$
- c = slope of characteristic in fluid with no horizontal density variation $[(w^2 - f^2)/(N^2 - w^2)]^{1/2}$
- c' = slope of characteristic in fluid with horizontal density variation $s \pm [s^2 + (w^2 - w_f^2)/N^2]^{1/2}$
- c_g = group velocity
- c_p = phase velocity
- d = mixed layer depth for Baines' model
- Δ = $(c + \alpha)/(c - \alpha)$
- f = inertial frequency
- g = gravitational acceleration
- G = vertical structure function
- h_L = shelf depth for Baines' model
- H = bottom depth
- η = sea surface elevation
- i = $(-1)^{1/2}$
- k = cross-shelf wavenumber

List of Symbols - 2

K = horizontal wavenumber

l = along-shelf wavenumber

λ_n^2 = eigenvalue

m = vertical wavenumber

M_2 = principal lunar semidiurnal tidal constituent

M^2 = horizontal analog to buoyancy frequency squared
 $-g\rho_x/\rho_0 = f\bar{v}_z$

n = mode number

N^2 = buoyancy frequency squared $-g\rho_z/\rho_0$

p = pressure

q = $2n\pi/ln(\Delta)$

ρ = perturbation density

ρ_0 = reference density

s = $-M^2/N^2$

t = time

T = temperature

u = cross-shelf velocity

v = along-shelf velocity

List of Symbols - 3

- θ = angle of bottom slope relative to horizontal $\tan^{-1}(\alpha)$
- w = vertical velocity
- W = horizontal structure function
- ω = frequency
- ω_f = effective inertial frequency $[f(f + \bar{v}_x)]^{1/2}$
- ω_L = low frequency cutoff for freely propagating internal waves
- ω_H = high frequency cutoff for freely propagating internal waves
- x = cross-shelf direction
- y = along-shelf direction
- z = vertical direction

1. INTRODUCTION

Analysis of currents measured over the continental shelf off northern California during the Coastal Ocean Dynamics Experiment (CODE) shows large temporal and spatial variability at the semidiurnal frequency. Previous work (Rosenfeld and Beardsley, 1987) has shown that the depth-averaged semidiurnal tidal currents may vary substantially over along-shelf distances as short as 25 km. The vertical structure and intermittent nature of the semidiurnal currents are examined here. Due to the beating effect between the principle tidal constituents, some variation in the amplitude of the currents is expected. Complex demodulation, however, shows that on several occasions during the period between January and August, 1982, the amplitude of the semidiurnal currents rose well above the background level. Internal waves of tidal frequency are believed to be responsible for these events. During one event, in February of 1982, near-surface semidiurnal current amplitudes reached 30 cm s^{-1} . Due to the sparse instrumentation deployed during the winter, an event which occurred in April of 1982, during the more intensive CODE-2 experiment, was examined in detail. The vertical and cross-shelf structure of the current and temperature fields during this event are consistent with the interpretation of a first baroclinic dynamical mode.

Evidence presented here suggests that during the 1982 upwelling season, the amplitude of the semidiurnal internal tide is controlled primarily by the strength of the stratification over the continental shelf and adjacent slope, with the largest internal wave events occurring during periods of wind relaxation when upwelling ceases and stratification increases. The theory of Baines (1982), while inadequate

for predicting the observed velocities, does provide a useful framework for understanding why the internal wave energy increases with increasing stratification.

In Section 2, other observations of internal tides over continental shelves are reviewed. Sections 3 and 4 present the data and analysis methods, respectively. The temporal variability and spatial structure of the internal tide is described in Section 5. In Section 6, certain properties of the observations are compared with linear internal wave theory for vertically standing modes on a flat bottom, and the effects of a sloping bottom are discussed. Ideas concerning the generation of internal tides and the effects of mean shear are discussed in Sections 7 and 8, respectively. Conclusions are given in Section 9.

2. OBSERVATIONS OF INTERNAL TIDES ON CONTINENTAL SHELVES

Internal waves of semidiurnal frequency have been observed on continental shelves in many parts of the world, and are usually seen to be intermittent in time. They are commonly thought to be generated by the interaction of the barotropic tide with topography, in particular the shelf break. Wunsch (1975) reviewed the state of knowledge up to that time concerning internal tides in the ocean, including some coastal observations. Winant (1979), in a brief review of coastal current observations, also touched on coastal internal tides. Baines (1986) offers an excellent summary in table form of internal tide observations on continental shelves. In almost all shelf cases, the baroclinic energy appears intermittently in time and is observed to be in the lowest mode, as opposed to the situation over the slope where

more beam-like structures have been observed. In order to place the CODE observations in perspective, observations of internal tides on continental shelves from five different areas of the world are summarized in this section. These sets of observations are categorized here by shelf width. First, internal tides on the wide shelves (order 100 km) off Nova Scotia and the northwest coast of Australia will be reviewed. Next, results of an experiment on the intermediate width shelf (50 km) off northwest Africa will be reviewed, and finally, observations on narrow shelves will be discussed. The shelf off Oregon is about 30 km wide, the closest to that in the CODE area. Southern California has a very narrow shelf (about 4 km).

Petrie (1975) described the M_2 tide on the Scotian shelf and slope from current meter and temperature measurements made in 1967, 1968, and 1973. He observed that the semidiurnal tidal currents were primarily barotropic over the shelf and baroclinic over the slope. He noted that by looking at only a particular frequency (the M_2 in his case), there was a risk of missing the internal tide signal if it had been Doppler-shifted. The shelf is about 175 km wide at the experimental site and the shelf moorings analyzed were about 35 km from the shelf break (200 m depth). The cross-shelf barotropic velocities are large, 11 to 14 cm s^{-1} , and consistent with $u = \omega \eta x / H$ where ω is the M_2 frequency, η is sea level amplitude, x is distance offshore and H is depth. From the slope observations, he estimated an e-folding scale for the internal wave energy to be 15 km (using a vertical eddy viscosity of $30 \text{ cm}^2 \text{ s}^{-1}$), thus internal waves generated at the shelf break would be dissipated before reaching the shelf moorings. He estimated the horizontal wavelength over the slope to be 42 km.

The horizontal wavelength over the shelf was calculated to be 14 km, using a depth of 100 m and an average N^2 profile.

Holloway (1983a), in an investigation of the tidal currents on the Australian northwest shelf, also determined that the semidiurnal tidal currents were primarily barotropic, with M_2 and S_2 speeds averaging about 25 and 20 cm s^{-1} respectively over the 100 km wide shelf. Barotropic tidal current ellipses were oriented in the cross-shelf direction. Near the shelf break (75 m depth), shoreward-propagating semidiurnal internal waves of length 20 km were observed (Holloway 1983b and 1984). These exhibited a first mode structure in the vertical. The amplitude of the cross-shelf baroclinic currents was as large as 20 cm s^{-1} near the shelf break, but decreased in the shoreward direction with a five-fold reduction in amplitude over a distance of one wavelength. Maximum baroclinic currents were about one-third the size of the maximum barotropic currents. Near the shelf break, 30 m vertical displacements of the isopycnals in 70 m water depth were observed. Holloway concluded that these waves did not propagate very far onto the shelf. No well-defined spring-neap cycle was observed in the baroclinic current or temperature records, despite the fact that the barotropic currents showed a strong fortnightly signal. The time variability of the internal tidal signal showed a correlation with the degree of stratification, with decreasing amplitude corresponding to smaller values of N^2 . Although no specific generation region could be identified, characteristics, along which energy propagates, were determined to be steeper than the bottom slope, and an attempt was made to apply Baines' (1982) model for that situation. It was found that this model predicted baroclinic tidal currents much smaller than those observed.

Holloway (1985) compared the baroclinic tidal currents at three locations on the Australian northwest shelf; one of which has bottom topography which is subcritical ($\alpha/c = 0.2$), one is near-critical ($\alpha/c = 1.2$) and one supercritical ($\alpha/c = 1.9$), where α is the bottom slope and $c = [(\omega^2 - f^2)/(N^2 - \omega^2)]^{1/2}$ is the slope of the characteristics. He found that the vertical structure most strongly resembled a first mode where $\alpha < c$, and that in these areas, the baroclinic currents were smaller than the barotropic. Where $\alpha > c$, the baroclinic currents were bottom-intensified and exceeded the barotropic currents. Bottom intensification was greatest for the site where $\alpha/c = 1.2$, consistent with the theory of Wunsch (1969).

The continental shelf off northwest Africa is 50 km wide, with the shelf break at 100 m depth. From analysis of current meter and temperature data gathered on the shelf during the JOINT-1 experiment of the Coastal Upwelling Ecosystems Analysis (CUEA) program, Gordon (1978) noted that internal waves with periods between 0.5 and 8 hours exhibited vertical structure consistent with a first baroclinic mode. In 400 m depth, where the bottom slope is super-critical for the semi-diurnal frequency, Gordon (1979) observed first mode internal waves of semidiurnal frequency propagating in the alongshore direction. Averaged over a 30-day period in March, 1974, the near-surface and near-bottom along-shelf tidal currents were about 6 and 8 cm s^{-1} respectively. Huthnance and Baines (1982) examined 28 days of current meter data collected from five moorings over the shelf and slope off the northwest coast of Africa during February, 1975. Bottom depth at the mooring locations ranged from 74 to 3000 m. The baroclinic semidiurnal

currents were strongest at the two moorings in 500 m depth, in fact much stronger than predicted by the model of Baines (1982) for steep topography. Their vertical structure suggests the lowest baroclinic mode. The semidiurnal tidal currents in 74, 2000 and 3000 m total depth were nearly barotropic. No explanation is offered for the lack of internal tidal energy at the 74 m depth.

One would expect the properties of the internal tide on the shelf off Oregon to be most similar to those in the CODE area, because of their similarity in topography and prevailing oceanographic conditions. Both shelves are 20 to 30 km wide with the shelf break at 150 to 200 m depth, and are characterized by upwelling in the summertime. Hayes and Halpern (1976), Torgrimson and Hickey (1979) and Denbo and Allen (1984) have all discussed the tidal currents measured by current meters deployed during CUE-2 in the summer of 1973 on the continental shelf off Oregon. Hayes and Halpern (1976) examined the time variability of the internal wave energy measured at two moorings on the shelf in 100 m water depth. They found that horizontal kinetic energy in the semidiurnal frequency band (0.073 - 0.094 cph) peaked during times of wind relaxation, when stratification over the shelf increased. They attempted to account for the change in energy as being due to changes in N^2 . They concluded that stratification over the shelf break, which was presumed to be the generation area, remained roughly constant and was probably not the source of the time variability observed at the moorings. By comparing the characteristics passing through the mooring site during periods of upwelling and relaxation, they concluded that the energy loss observed during upwelling was due to dissipation near the sea surface, which did not occur during relaxation

periods when the characteristics from the generation area passed through the moorings without any surface reflections.

Torgrimson and Hickey (1979) also sought to interpret the horizontal and vertical structure in the semidiurnal (0.074 - 0.087 cph) tidal currents in terms of characteristics. They identified the source of the internal tidal energy as a beam with vertical thickness of 80 m generated along the bottom between 474 and 1050 m where the slope is critical for the M_2 frequency. They identified the location of the beam in the current meter data by noting where signal-to-noise ratios in the tidal analysis were low (indicating the presence of internal tides incoherent with the surface tide) and located points of reflection by noting where the direction of vertical phase propagation (and hence energy propagation) switched. Currents in the beam had the largest amplitudes, with observed baroclinic currents as large or larger than the barotropic tidal currents which were clockwise-rotating and of order 5 cm s^{-1} . For any given mooring (there were moorings at 50, 100, 200, and 500 m depth), a relative maximum in amplitude occurred at only one depth, not two or more as would be evident if a simple modal structure dominated. Ellipse orientation for the baroclinic currents was primarily in the cross-shelf direction, indicating horizontal energy propagation in that direction.

Denbo and Allen (1984) used rotary empirical orthogonal function (EOF) analysis to analyze the same data used by Torgrimson and Hickey (1979). For the semidiurnal frequency band (0.077 - 0.083 cph), they found that the largest clockwise-rotating EOF was consistent with the general shape of a first dynamical baroclinic mode. Because of the 180° phase difference between displacement and surface velocity, they

equated the first EOF with an internal wave standing in the vertical and propagating shoreward with horizontal wavelength of 40 km. The node in the vertical was at a depth of 0.4 times the local water depth. The first counter-clockwise-rotating EOF had a relatively depth-independent structure and was interpreted as being representative of the barotropic tidal currents. Given this interpretation, there is no way to reconcile the results of Torgrimson and Hickey (as summarized in their Figure 11a) with Denbo and Allen's results (as summarized in their Figure 5). The problem arises from the fact that the barotropic tidal current, as resolved by Torgrimson and Hickey, was in fact rotating clockwise (CW), and because it was not incoherent with the baroclinic tide, Denbo and Allen's largest CW-rotating mode is really a combination of baroclinic and barotropic energy. The nodes in the mode are due to the destructive interference between the barotropic and baroclinic currents there. They are not necessarily nodes in the first baroclinic dynamical mode. Unfortunately (as was pointed out by Hsieh (1986) for the low frequency band), Denbo and Allen (1984) made the common error of equating EOFs with dynamical modes when interpreting their results.

The region off southern California offers an example of a very narrow, steep ($\alpha = 0.017$) shelf. It is only 4 km wide, with the shelf break at 60 to 80 m depth. Over a month-long period in the summer of 1974, Winant and Olson (1976), using four electromagnetic current meters mounted on a tower in 18 m water depth off La Jolla, observed baroclinic semidiurnal tidal currents with a first mode vertical structure. Cross-shelf current amplitudes were order 20 cm s^{-1} . The along-shelf velocity fluctuations at the semidiurnal frequency

were barotropic in nature. The internal tide was not phase-locked to the surface tide, even over as short a period as a week. Current and temperature data from three moorings at 15, 30, and 60 m depth in the same area also revealed the semidiurnal cross-shelf currents to have a first baroclinic mode structure in the vertical, while the along-shelf component was barotropic (Winant and Bratkovich, 1981). The phase relationship between temperature and cross-shelf currents in this data set indicated that the semidiurnal internal waves were standing in the cross-shelf as well as vertical direction. The energy associated with the internal tide was seen to decay with decreasing total water depth, and was also a strong function of season, with the least energy in winter when stratification is weakest. A more detailed analysis of the same data is given by Bratkovich (1985) who shows that the cross-shelf baroclinic motions were bottom-intensified.

To summarize this section, several conclusions regarding the nature of semidiurnal internal tides on continental shelves are drawn.

- 1) Energy is usually observed to be in the form of a first baroclinic mode.
- 2) Bottom-intensification is present when the bottom slope is near-critical for this frequency band.
- 3) Internal tides are intermittent in time, with increases in energy accompanying increasing stratification.
- 4) Dissipation takes place over distances on the order of one to two horizontal wavelengths, where the wavelength is about 20 km. Because the continental slope and shelf break are the primary generation sites, little baroclinic tidal energy is observed far from the shelf break on wide continental shelves.

3. DATA

The data used here were collected over the continental shelf and slope off northern California in the area between Pt. Reyes and Point Arena (Figure 1). The moored array component of CODE consisted of two heavily instrumented arrays deployed during the summers of 1981 (CODE-1) and 1982 (CODE-2), and a sparser array during the intervening winter. Only a subset of all the available data is used here. Hourly-averaged current and temperature data collected during CODE-2 along the Central (C-) line from moorings in 60, 90, and 130 m depths are the focus of this investigation. Comparisons are made with moorings at the same isobaths to the north (N-line) and south (R-line) of the C-line. The mooring locations are shown in Figure 1 and the instrument types, locations, depths and duration are given in Table 1. A brief description of the moorings and an evaluation of mooring motion is given in Chapter II. In addition, reference is made to measurements made at C3 during the winter. Currents were decomposed into along-shelf (positive towards 317°T) and cross-shelf (positive towards 47°T) components. Time is referred to Greenwich Mean Time (GMT). More information concerning CODE-2 current and temperature data can be found in Winant, Send, and Lentz (1985) and Irish (1985), respectively.

During three time periods within CODE-2, CTD measurements were made along the CODE or CODE-2 C-lines (separated by an along-shelf distance of 2 km). Fleischbein, Gilbert and Huyer (1983a) describe CTD data collected between April 20-24, Fleischbein, Gilbert and Huyer (1983b) describe CTD data from May 26 - June 2, and Huyer, Fleischbein and Schramm (1984) describe July 16-26 CTD data. Vertical profiles of buoyancy frequency squared (N^2) were computed from one meter averages

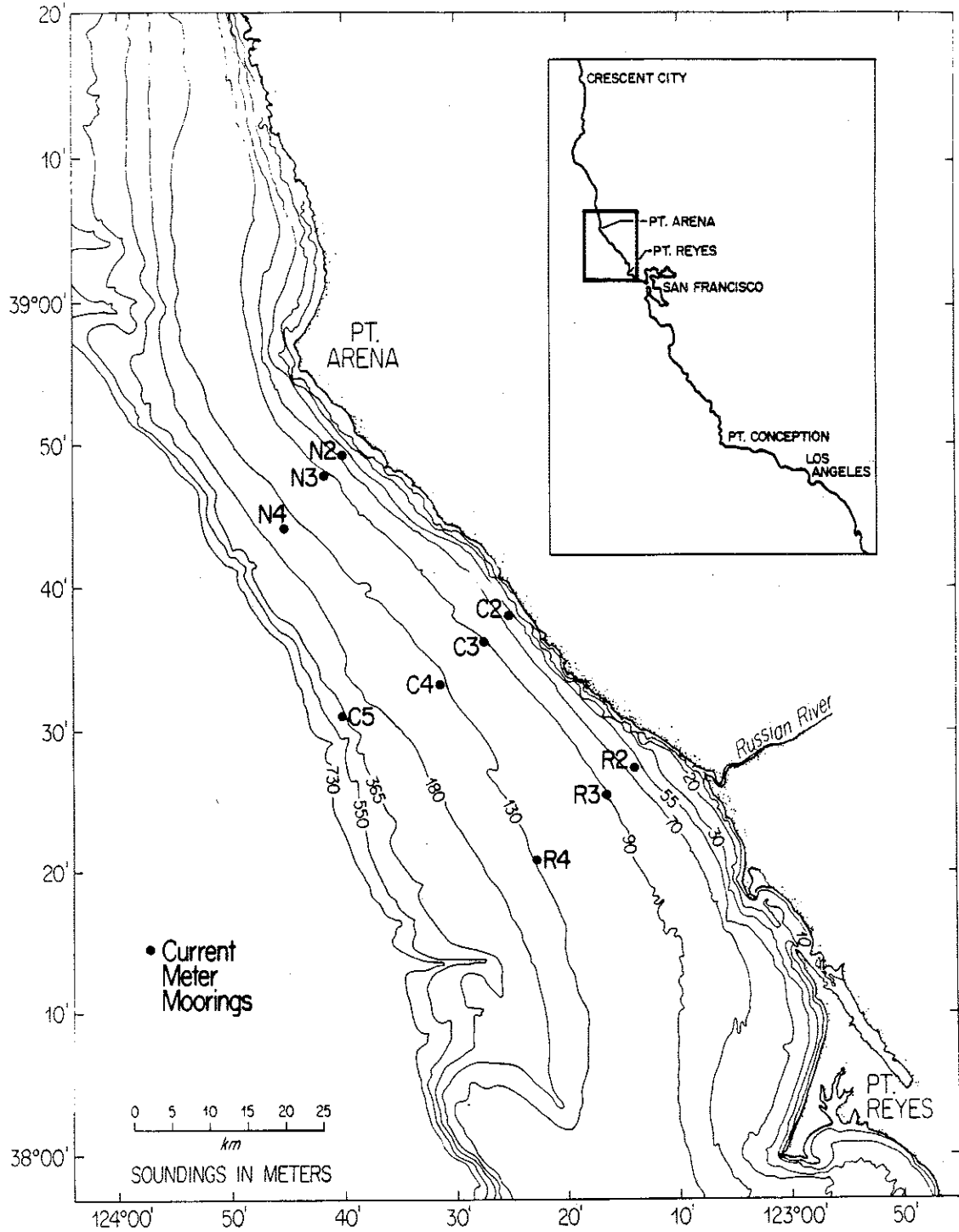


Figure 1. Positions of CODE-2 R-, C-, and N-line current meter moorings are shown.

<u>Stn</u>	<u>Water Depth (m)</u>	<u>Latitude North</u>	<u>Longitude West</u>	<u>Start</u>	<u>Stop</u>	<u>Instrument</u>	<u>Depth (m)</u>
C2	60	38°38.2'	123°25.3'	3/12/82	8/05/82	VMCM/T	10
				3/12/82	8/13/82	VMCM/T	20
				3/12/82	8/05/82	VMCM/T	35
				3/12/82	8/05/82	VMCM/T	53
C3	93	38°36.4'	123°27.7'	3/24/82	7/28/82	VMCM/T	5
				3/24/82	7/28/82	VACM/T	10
				3/24/82	7/28/82	VMCM/T	15
				3/12/82	8/09/82	VMCM/T	20
				3/12/82	8/05/82	VMCM/T	35
				3/12/82	8/09/82	VMCM/T	53
				3/12/82	8/05/82	VMCM/T	70
				3/12/82	8/09/82	VMCM/T	83
C4	130	38°33.3'	123°31.6'	4/01/82	8/17/82	VACM/T	10
				4/01/82	8/17/82	VMCM/T	20
				4/01/82	8/17/82	VMCM/T	35
				4/01/82	8/17/82	VMCM/T	55
				4/01/82	8/17/82	VMCM/T	70
				4/01/82	8/17/82	VMCM/T	90
				4/01/82	8/17/82	VACM/T	21
N2	60	38°49.5'	123°40.1'	3/11/82	8/05/82	VMCM/T	10
				3/11/82	8/11/82	VMCM/T	20
				3/12/82	8/05/82	VMCM/T	35
N3	91	38°48.1'	123°41.8'	3/11/82	8/11/82	VMCM/T	10
				3/12/82	8/05/82	VMCM/T	35
				3/11/82	8/10/82	VMCM/T	53
				3/12/82	8/05/82	VMCM/T	70
				3/11/82	8/10/82	VMCM/T	83

Abbreviations: VMCM/T - vector measuring current meter with temperature sensor, VACM/T - vector averaging current meter with temperature sensor.

Table 1a. Location, instrument type and depth are listed for the current and temperature data used in this paper. Start and stop dates (GMT) are for the full record length available, although the entire time series was not necessarily used in the analysis here.

<u>Stn</u>	<u>Water Depth (m)</u>	<u>Latitude North</u>	<u>Longitude West</u>	<u>Start</u>	<u>Stop</u>	<u>Instrument</u>	<u>Depth (m)</u>
N4	130	38°45.7'	123°45.6'	3/24/82	8/20/82	VACM/T	10
				3/24/82	8/20/82	VMCM/T	20
				3/25/82	8/20/82	VMCM/T	35
				3/25/82	8/20/82	VMCM/T	55
				3/25/82	8/20/82	VMCM/T	70
				3/25/82	8/20/82	VMCM/T	90
				3/25/82	8/20/82	VMCM/T	110
				3/25/82	8/20/82	VACM/T	121
R2	60	38°27.1'	123°14.0'	3/12/82	8/10/82	VMCM/T	20
				3/13/82	8/05/82	VMCM/T	35
				3/13/82	8/05/82	VMCM/T	53
R3	90	38°25.4'	123°16.4'	3/13/82	8/14/82	VMCM/T	20
				3/13/82	8/05/82	VMCM/T	35
				3/13/82	8/14/82	VMCM/T	53
				3/13/82	8/05/82	VMCM/T	70
R4	130	38°20.8'	123°23.0'	4/02/82	8/18/82	VACM/T	10
				4/02/82	8/18/82	VMCM/T	20
				3/26/82	8/14/82	VMCM/T	35
				3/26/82	8/14/82	VMCM/T	55
				3/26/82	8/14/82	VMCM/T	70
				3/26/82	8/14/82	VMCM/T	90
3/26/82	8/14/82	VMCM/T	110				

Abbreviations: VMCM/T - vector measuring current meter with temperature sensor, VACM/T - vector averaging current meter with temperature sensor.

Table 1b. Location, instrument type and depth are listed for the current and temperature data used in this paper. Start and stop dates (GMT) are for the full record length available, although the entire time series was not necessarily used in the analysis here.

of pressure, temperature, and salinity supplied by A. Huyer of Oregon State University.

4. METHODS OF ANALYSIS

The goal of this work is to describe the time variability and spatial structure of the baroclinic semidiurnal tidal currents observed over the shelf off northern California. Practically speaking, an exact separation of the barotropic and baroclinic components of flow is virtually impossible. In Rosenfeld and Beardsley (1987), the barotropic component of the tidal flow was operationally defined as that part which was depth-averaged and phase-invariant over the length of the record (4 months). Trying to extract the baroclinic tidal signal from a moored array of current and temperature sensors is a difficult task at best. The major problems involved stem from the non-stationarity of the phenomenon, the presence of noise, and the fact that the internal tide may be partially phase-locked to the surface tide. As discussed in Noble et al. (1987), the length of time over which the phase-locked part is calculated will affect how much of the baroclinic component is included in it. When the baroclinic and barotropic components are comparable in size, the task of separating them is that much harder, so the choice was made to concentrate here on a description of those time periods when the baroclinic energy levels are well above the background.

To aid in identifying periods with large semidiurnal energy, a complex demodulation technique similar to that described in Appendix A of Chapter II was used to examine the time variability of the signal. The hourly data (temperature and velocity components) were high-pass

filtered (Appendix B of Chapter II), and then 48 hour periods (starting every 6 hours) were fit to the sum of a mean and sine wave with the M_2 period (12.42 hours). Due to the presence of noise and the fact that only one frequency was used in the fit, the calculated amplitude and phase are representative of a band of frequencies around the principal lunar constituent, as evidenced by the fact that the time series of 12 and 12.42 hour amplitudes are virtually indistinguishable. Time series of the semidiurnal amplitude extracted from a bottom pressure record (Figure 2) (in which over 95% of the energy is tidal) clearly shows a fortnightly modulation, again indicating that the sum of the semidiurnal constituents (rather than any individual one) is being resolved. Phases are referred to 0000 GMT on April 4, 1982.

Once the time intervals of interest were identified, two methods were used to quantify the average semidiurnal variance in them. The first, EOF analysis in the frequency domain, extracts the coherent part of the current and temperature variance in the whole semidiurnal frequency band, defined here as 0.072 to 0.086 cph. The advantage of looking at the energy in the whole band, rather than at a single frequency, is that the internal tidal energy may be spread out in a band around the tidal lines due to Doppler-shifting by the low frequency flow (Wunsch, 1975). The fortnightly beating that is evident in bottom pressure records is not distinguishable in the current records, which is evidence of this smearing. Currents in cm s^{-1} were weighted by 1 and temperature in $^{\circ}\text{C}$ by 20 so that they contributed approximately equally to the total variance. In choosing the record length over which to analyze for properties of a signal intermittent in time, two considerations must be balanced. A short time period is

C4 BOTTOM PRESSURE

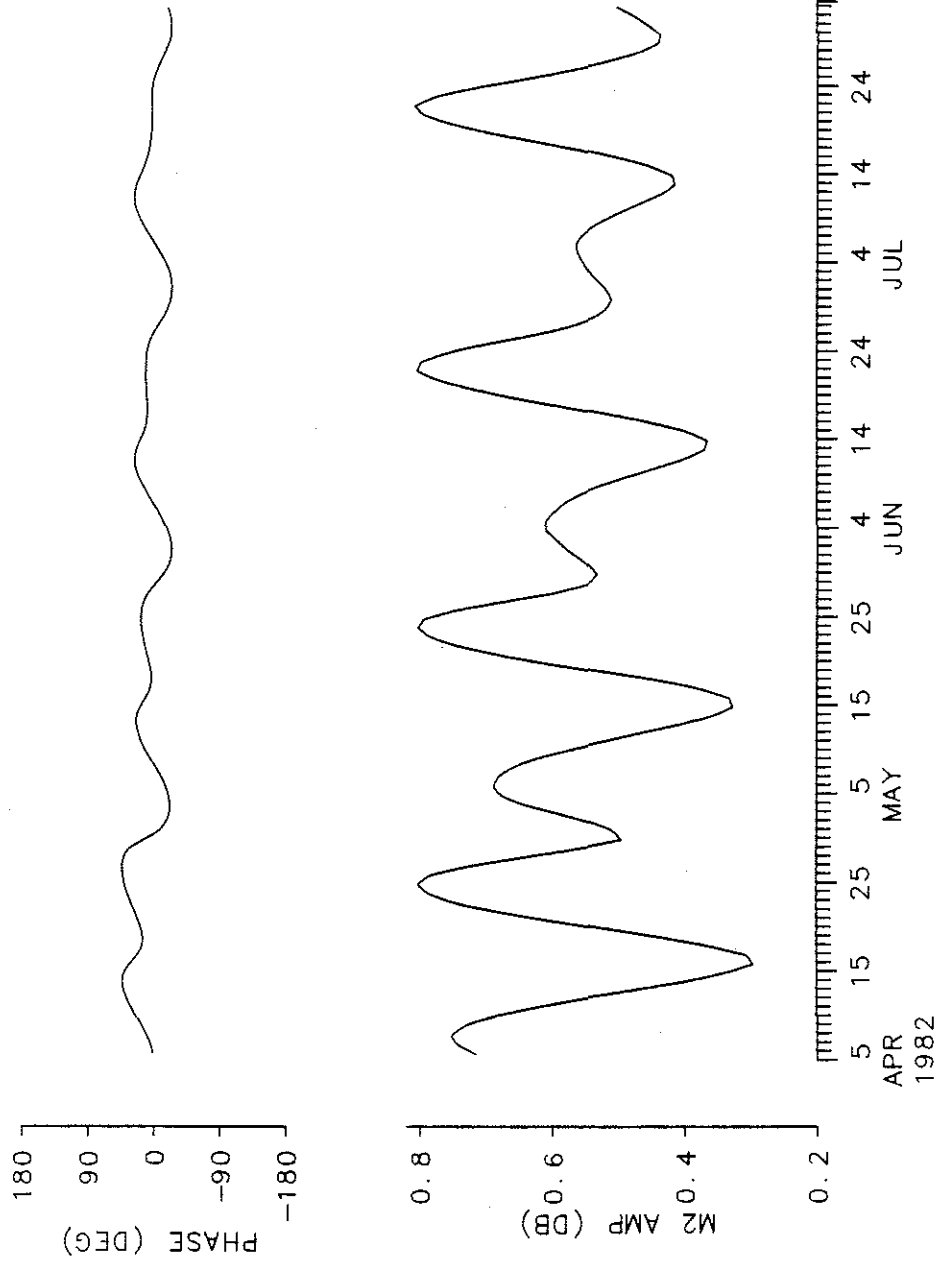


Figure 2. Amplitude and phase of C4 bottom pressure as determined from complex demodulation.

desirable because the properties are changing rapidly, but statistical reliability is increased if the analysis period is lengthened. The EOF analysis was carried out over 15 day periods, resulting in 12 degrees of freedom.

In the second method, amplitude and Greenwich phase were estimated separately for each component of velocity for ten tidal constituents, using least squares tidal analysis (Boon and Kiley, 1978) over 29 days. The barotropic M_2 ellipses determined from a similar analysis of the depth-averaged currents over the whole CODE-2 time period (Rosenfeld and Beardsley, 1987) were then subtracted from the M_2 ellipses calculated over the shorter time period, resulting in what shall be referred to as the residual currents.

Vertical profiles of N^2 were derived from least squares estimates of the specific volume anomaly gradient calculated over 4 m intervals. The specific volume anomalies were calculated from CTD data according to the equations of state given in Fofonoff and Millard (1983). The dynamical modes in a flat bottom ocean (at $z = -H$) with free surface boundary condition (at $z = 0$) were calculated using a computer program developed by M. Blumenthal of the Massachusetts Institute of Technology. The vertical structure equation for the vertical velocity,

$$N^2(z) - 1 G_{zz} + \lambda_n^2 G = 0 \quad ,$$

is solved using a finite difference scheme subject to the boundary conditions,

$$-g^{-1} G_z + \lambda_n^2 G = 0 \quad \text{at } z = 0 \quad \text{and} \quad G = 0 \quad \text{at } z = -H \quad ,$$

where g is the gravitational acceleration. The eigenvalues λ_n^2 and corresponding eigenvectors G_n , which are independent of frequency under the hydrostatic approximation, are calculated from the tridiagonal coefficient matrix. They are related to the horizontal wavenumbers K_n , frequency ω , and inertial frequency f , by the horizontal structure equation,

$$\lambda_n^2 = K_n^2 / (\omega^2 - f^2) .$$

The vertical structure of the horizontal velocity components and pressure is calculated as the z -derivative of G . G is normalized such that

$$\int_{-H}^0 G_z^i G_z^j dz = \delta_{ij} H ,$$

where i, j are mode numbers.

5. OBSERVATIONS

Complex demodulation at the M_2 frequency of the current and temperature time series from the C-line in CODE-2 show the amplitude and phase to be quite variable in time. Some of this variation is due to beating in the semidiurnal band, as seen for bottom pressure in Figure 2. However, two events occur between the spring transition (April 15) and the end of CODE-2 which are of sufficient amplitude and duration to stand out above the background. The size and duration of these two events varies somewhat with cross-shelf location and substantially with depth, but they always fall between April 16 - May 8 (with most of the variance between April 19 and May 3) and June 22 - July 6. Two examples for temperature and cross-shelf velocity are shown in Figure 3. The along-shelf component of velocity is highly correlated

with, and similar in amplitude to, the cross-shelf component. A maximum amplitude of over 25 cm s^{-1} occurs in the along-shelf velocity component at 5 m depth at C3 on April 26. Complex demodulation of the depth-averaged currents shows amplitudes that are always less than 4 cm s^{-1} (Figure 4). The amplitude modulation of one or both of the depth-averaged current components is correlated with the amplitude modulation of the bottom pressure at some locations, with the baroclinic currents at other locations, and with neither at still other locations. This correlation, or the lack of it, may be due to how energy is transferred from the barotropic to the baroclinic component.

Examination of plots of the hourly temperature data at C2, C3, and C4 in Irish (1985) shows visibly increased semidiurnal variability during the time periods cited above, which is also seen in the complex demodulation time series in Figure 3. The low-passed temperature data shown in Figure 5 reveal that these were times of strong stratification which occurred when the winds relaxed and upwelling weakened (Send, Beardsley, and Winant, 1987). The onset of the increase in semidiurnal energy in June lags the beginning of the warming (and increased stratification) trend by a few days. Note that no increase in semidiurnal energy accompanies the relaxation at the end of May, during which the stratification is nearly as large as in the April and June relaxations. The correlation (calculated for a 353 day period from the end of CODE-1 to the end of CODE-2) between the stratification at C3 (represented by the temperature difference between the 10 and 75 m temperatures) and the amplitude of the along-shelf semidiurnal velocity at C3 10 m is only marginally significant ($r = 0.15$) at the 90% confidence level. Over the 111-day period from April 4 - July 25, 1982, the semidiurnal

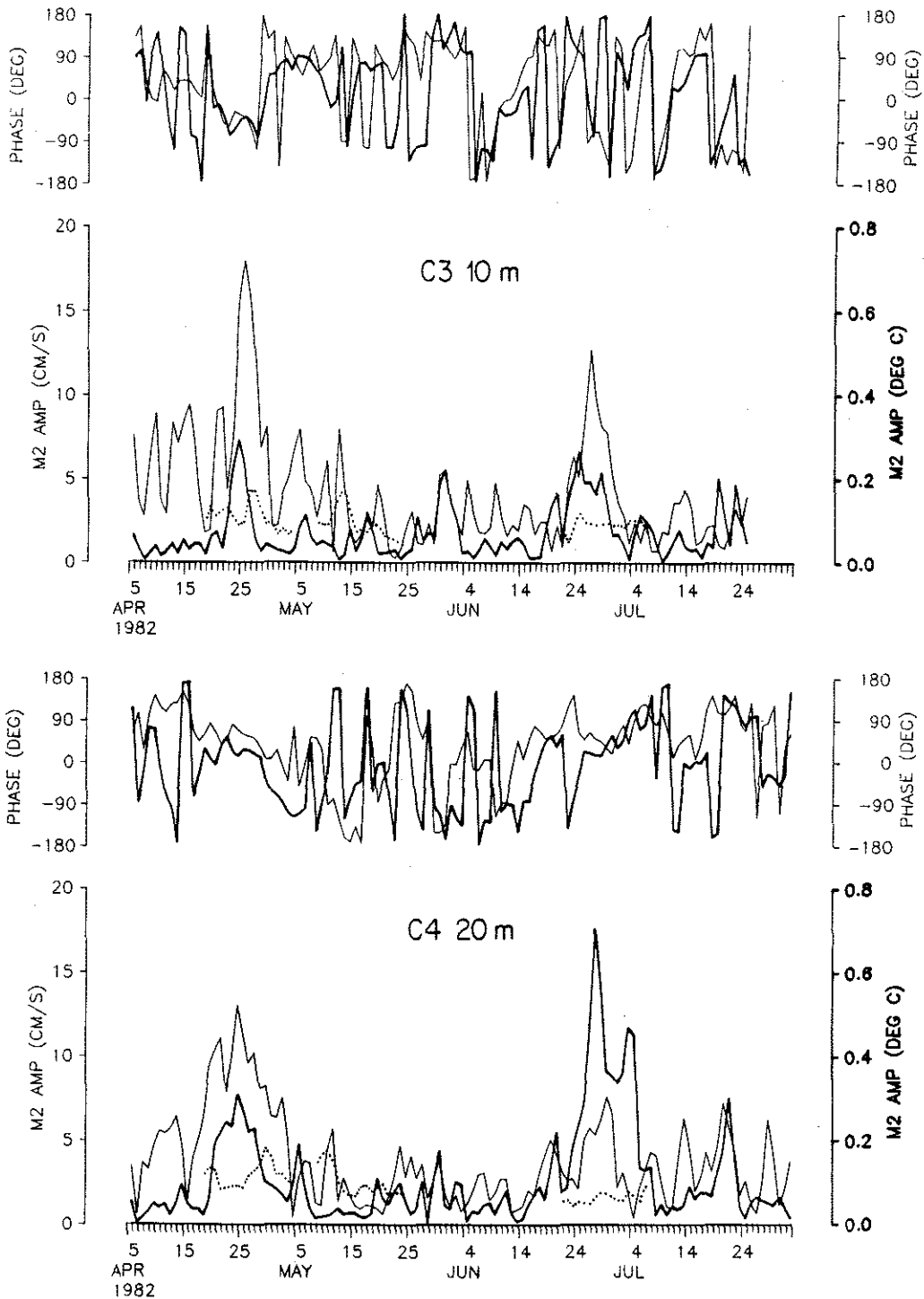


Figure 3. Amplitude and phase of the semidiurnal period cross-shelf (u) velocity (light line) and temperature (heavy line) fluctuations at C3 10 m depth and C4 20 m depth, as determined from complex demodulation. Dotted line indicates estimate of two times the standard error (defined in Appendix A of Chapter II) on the amplitude of u during three 15-day periods.

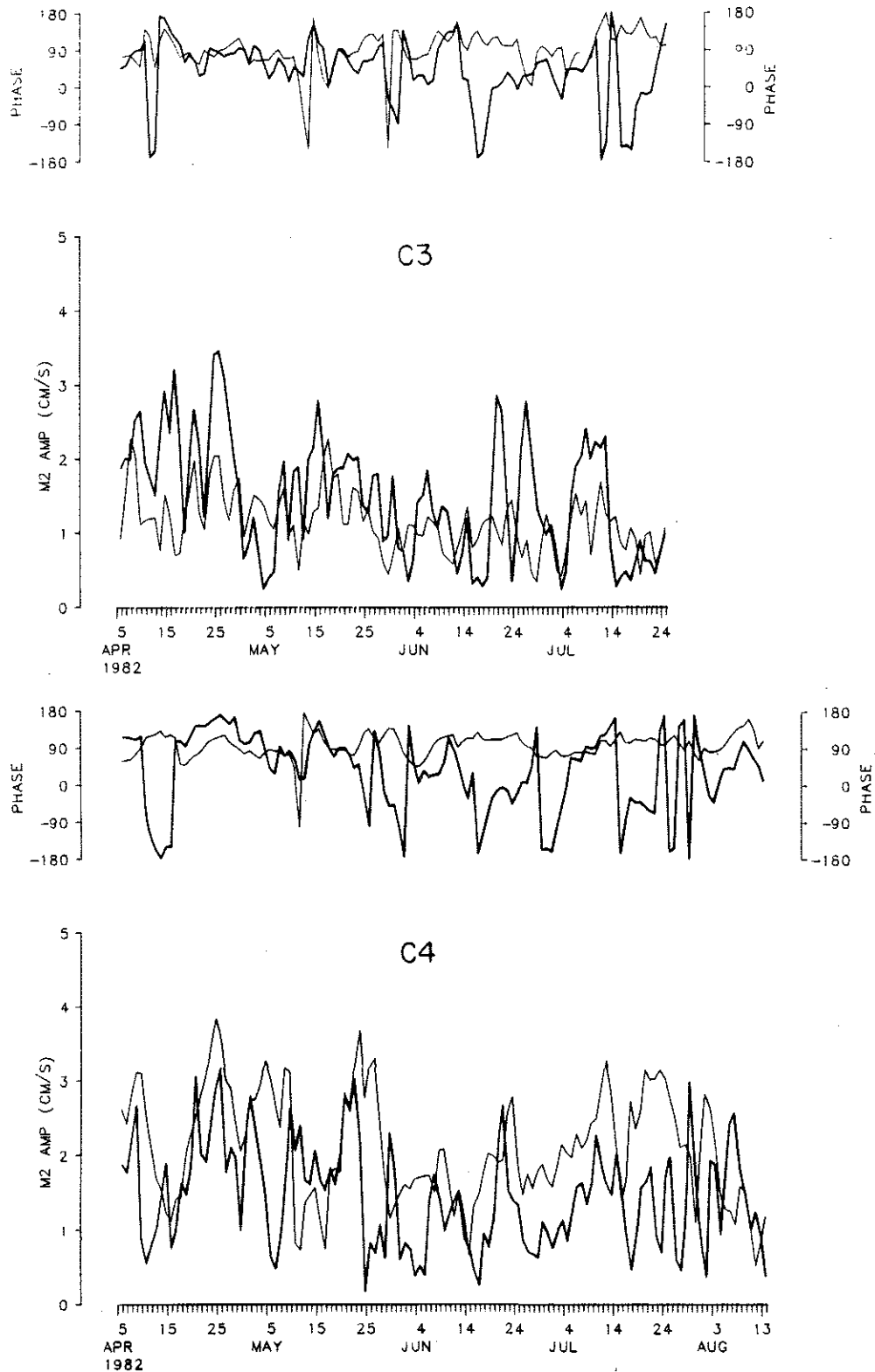


Figure 4. Amplitude and phase of the semidiurnal period depth-averaged cross-shelf (light line) and along-shelf velocity (heavy line) at C3 and C4, as determined from complex demodulation.

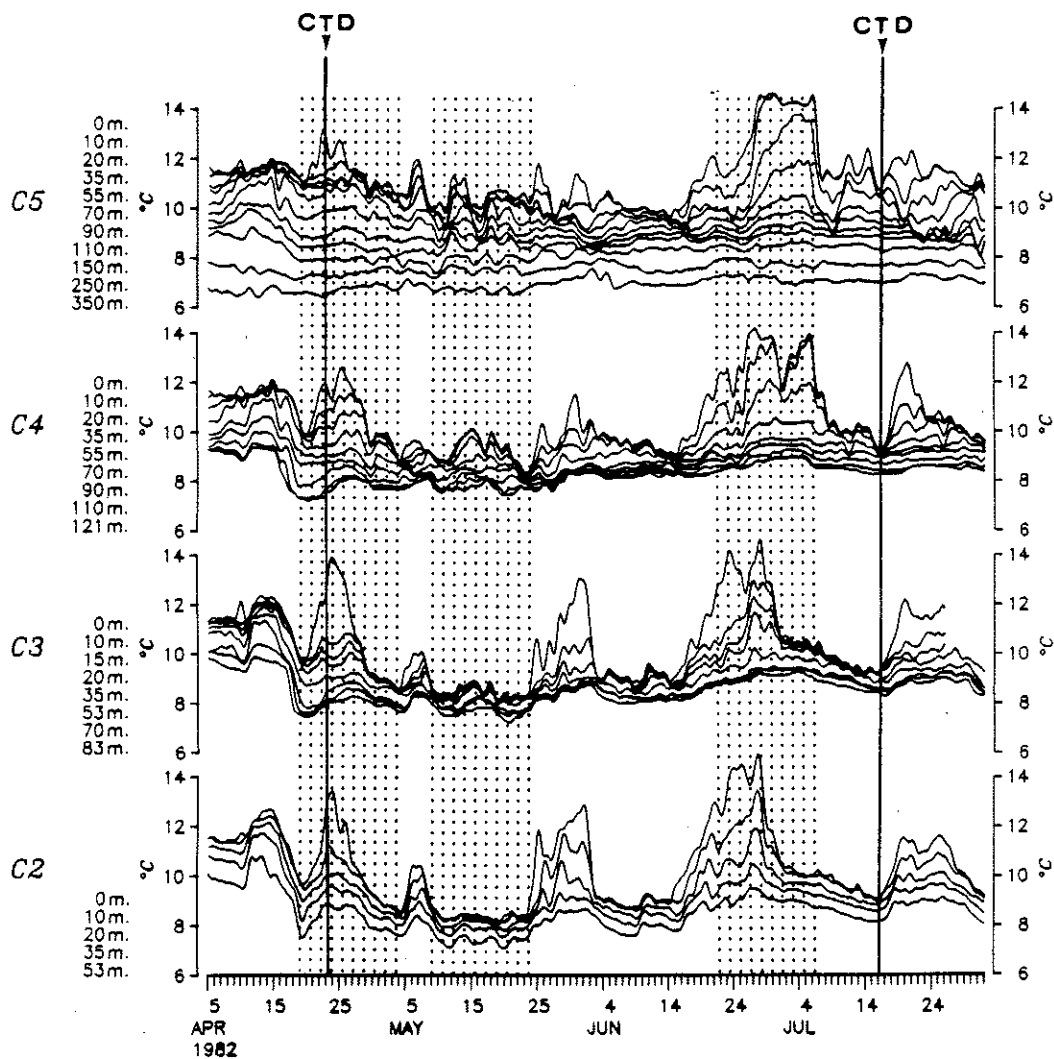


Figure 5. Low-pass filtered (half power point at 38 hours) temperature measured by the current meter thermistors at four locations along the C-line. Instrument depths are indicated to the left. The three 15-day periods used for EOF analysis are shaded. Dates of CTD sections shown in Figure 16 are indicated.

amplitudes of temperature and both components of velocity at C3 10 m were significantly correlated at zero time lag at the 99.9% confidence level* with the 10-75 m temperature difference ΔT . The scatter plot shown in Figure 6 indicates that the amplitude of the along-shelf semidiurnal component of velocity at C3 at 10 m usually exceeds 6 cm s^{-1} only when ΔT is greater than 1.5°C .

EOF analysis for the 0.072-0.086 cph frequency band was performed for the two 15 day periods previously mentioned (April 19 - May 3 and June 22 - July 6), a third 15 day "control" period (May 9-23), during which the semidiurnal variance was not unusually large, and the whole CODE-2 time period (April 2 - July 28). Along-shelf and cross-shelf currents, as well as temperature, for each of the instruments at C2, C3, and C4 (Table 1) was included. The resulting current ellipses for the first and second modes are shown in Figure 7. It is seen that the largest velocities occur during the April and June periods and the first mode during these periods accounts for a large percentage (71% in April) of the semidiurnal current and temperature variance. The velocity ellipses rotate CW and show, at least in the April case, a distinct minimum in mid-water. The currents in the upper and lower parts of the water column are out of phase with each other. During the May control period, the velocities are much smaller and the variance is spread out over more modes. The first mode has predominantly CCW-rotating ellipses and no distinct phase shift is apparent over the water column. Note the cross-shelf orientation of the ellipses in the lower water column at C4 which give rise to the cross-shelf orientation

*Every eighth 6-hourly point was considered to be independent, resulting in 56 degrees of freedom for the 111-day period, and 176 for the 353-day period.

C3 CODE-2

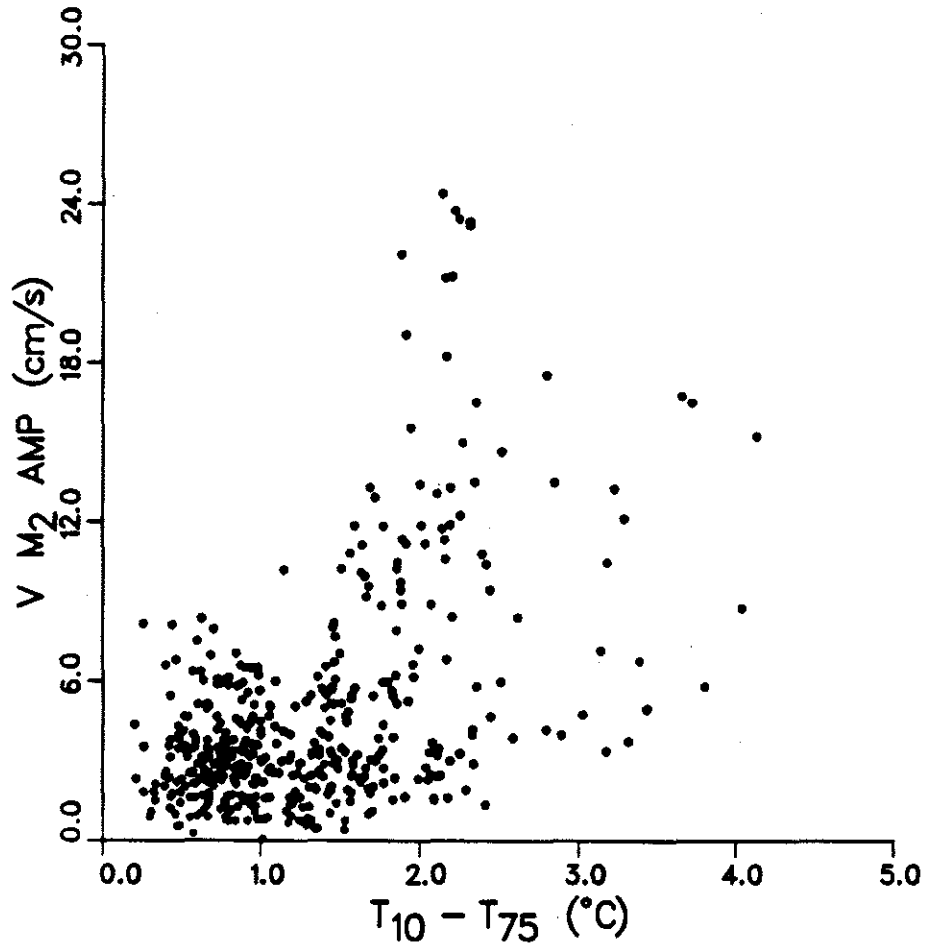
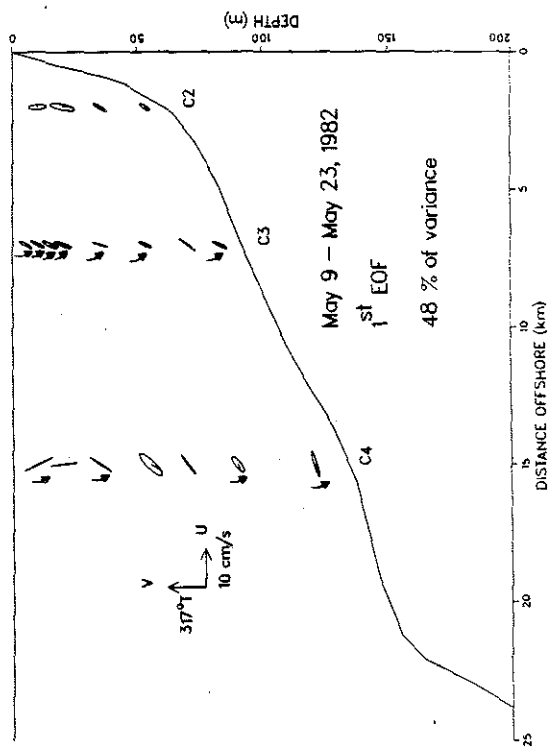
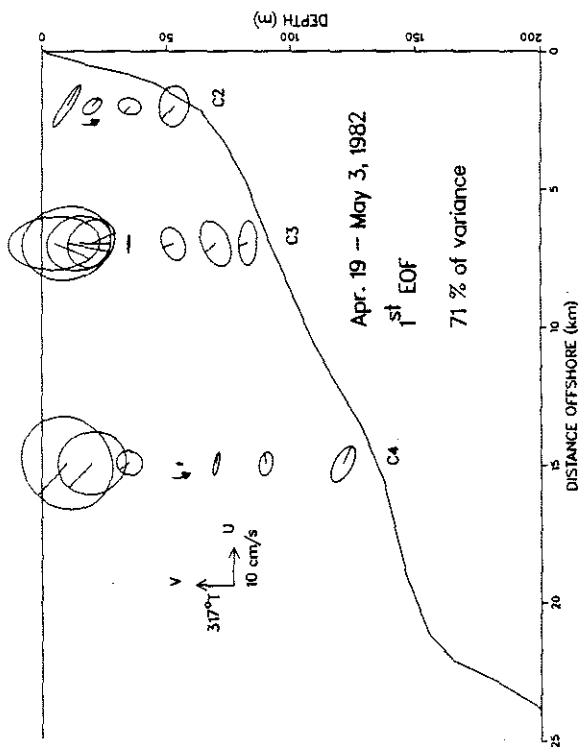
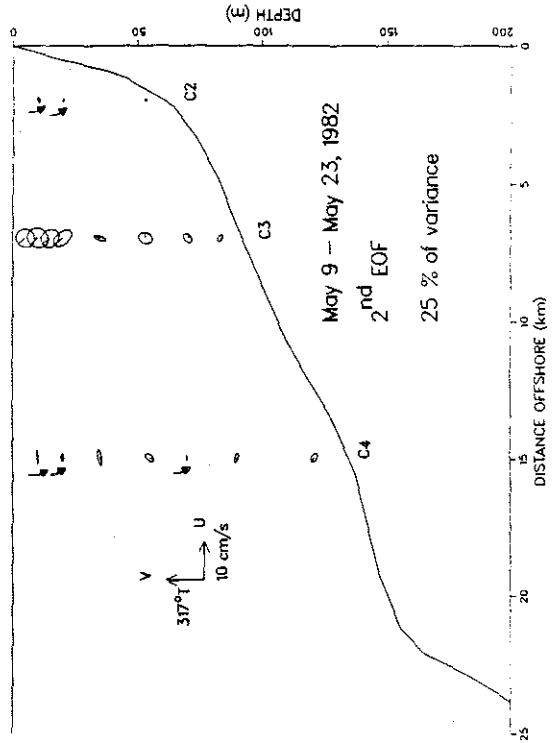
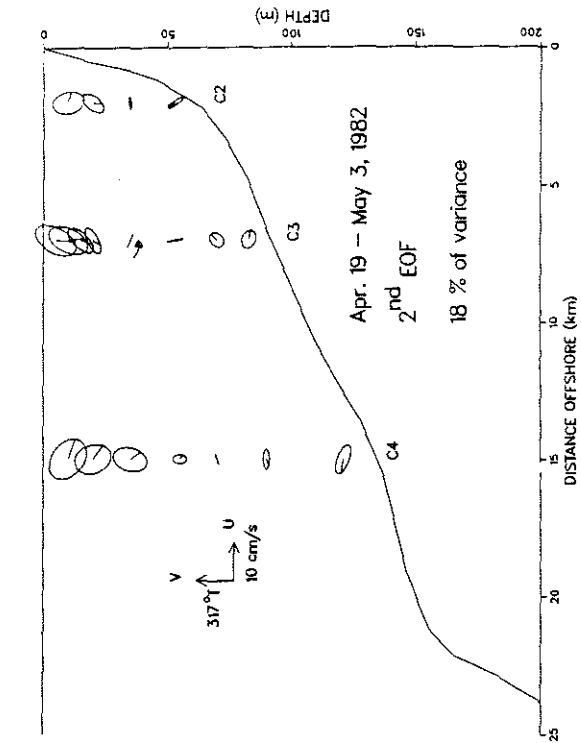
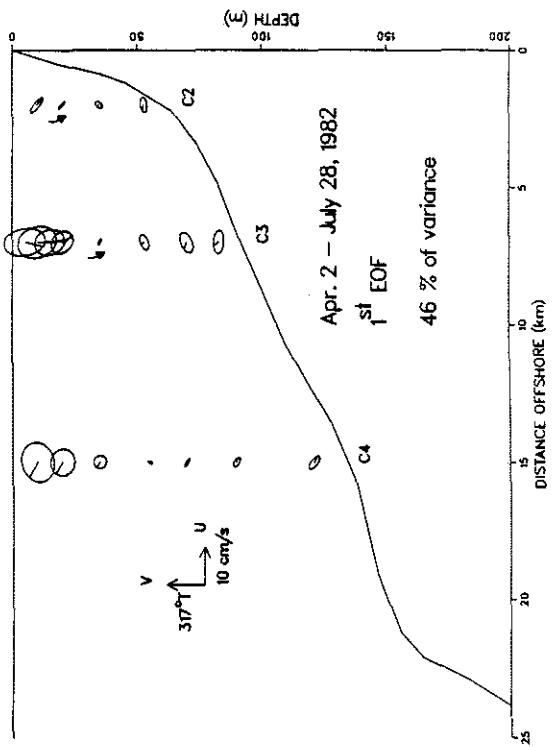
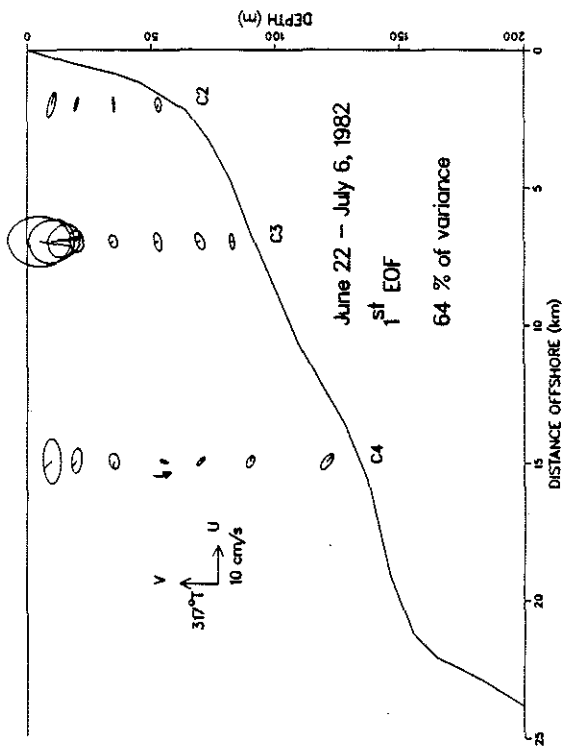
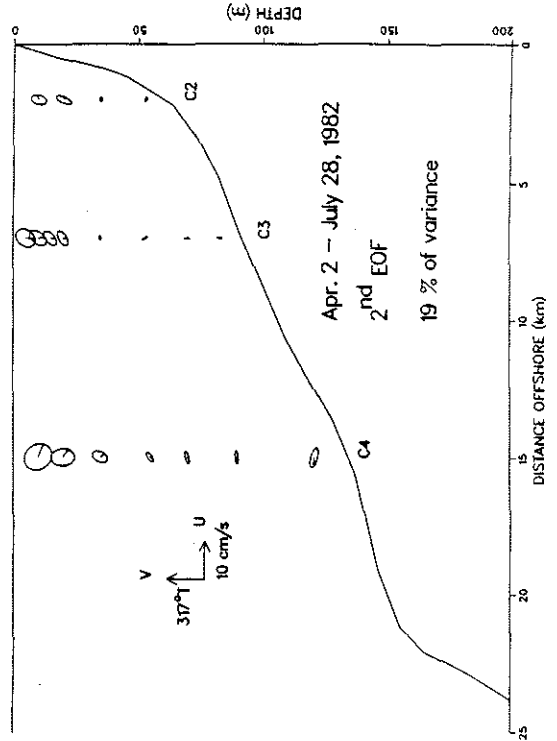
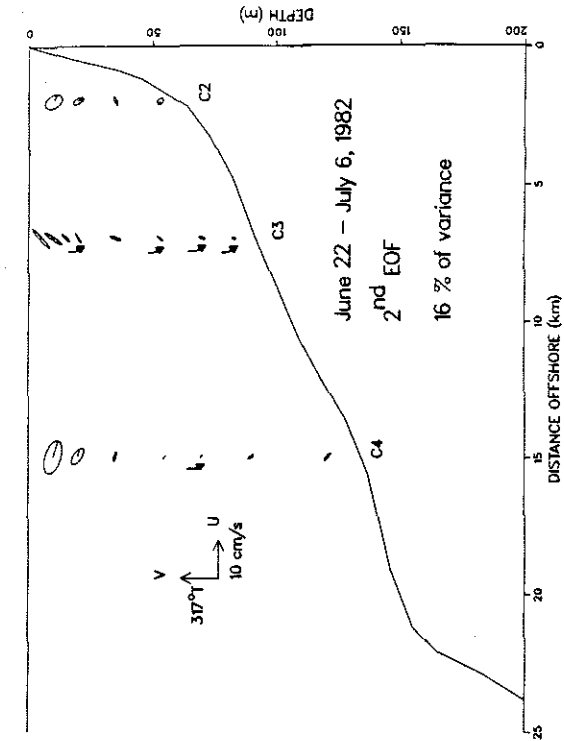


Figure 6. Scatter plot of 6-hourly values of amplitude of semidiurnal period along-shelf velocity component at 10 m versus 10 m - 75 m temperature difference at C3 for April 3 - July 25, 1982.

Figures 7a and 7b

Horizontal current ellipses for first and second C-line EOFs for four time periods during CODE-2. Current vectors rotate CW unless otherwise indicated. Phases relative to cross-shelf velocity at uppermost current meter nearest to the coast are marked. The percentage of total variance accounted for by each EOF is given.





of the depth-average ellipse at that location shown in Figure 4 of Rosenfeld and Beardsley (1987). The cause for this is not known, but does not appear to be related to the baroclinic flow since it is evident during the time of smallest internal tides.

The first mode temperature amplitudes and phases for the April and June periods are shown in Figure 8. During May 9-23, the average semidiurnal temperature amplitude, as calculated from the first mode, was less than 0.03°C along the C-line, and so is not shown. It should be emphasized that the currents and temperatures, although presented in two separate figures here for ease of viewing, were used together in the EOF calculation. Figure 8 shows that the maximum temperature variability generally occurred near 20 m and the amplitude was close to zero at the bottom, except at C2. The phase is fairly constant with depth over the middle part of the water column, but shows an increase with depth over the bottom part at C3 and C4 and a jump near the surface at C3. An estimate for the barotropic tide's contribution to the temperature fluctuations can be made by assuming $T_t = w\bar{T}_z$, with $w = uh_x$ at the bottom and η_t at the surface. Using the barotropic tidal results of Rosenfeld and Beardsley (1987), the amplitude of η_t and uh_x were both estimated to be $5 \times 10^{-3} \text{ cm s}^{-1}$. Based on the mean temperatures during April 19 - May 3, when T_z is largest, T_z near the surface is $6 \times 10^{-4}^{\circ}\text{C cm}^{-1}$, and near the bottom, it is one third as large. Therefore the amplitude of the near-surface temperature fluctuations due to the barotropic tide is about 0.03°C , and near-bottom about 0.01°C . Thus, the temperature fluctuations due to the barotropic tide are about an order of magnitude less than the maximum fluctuations observed in the April event, and are consistent with those observed

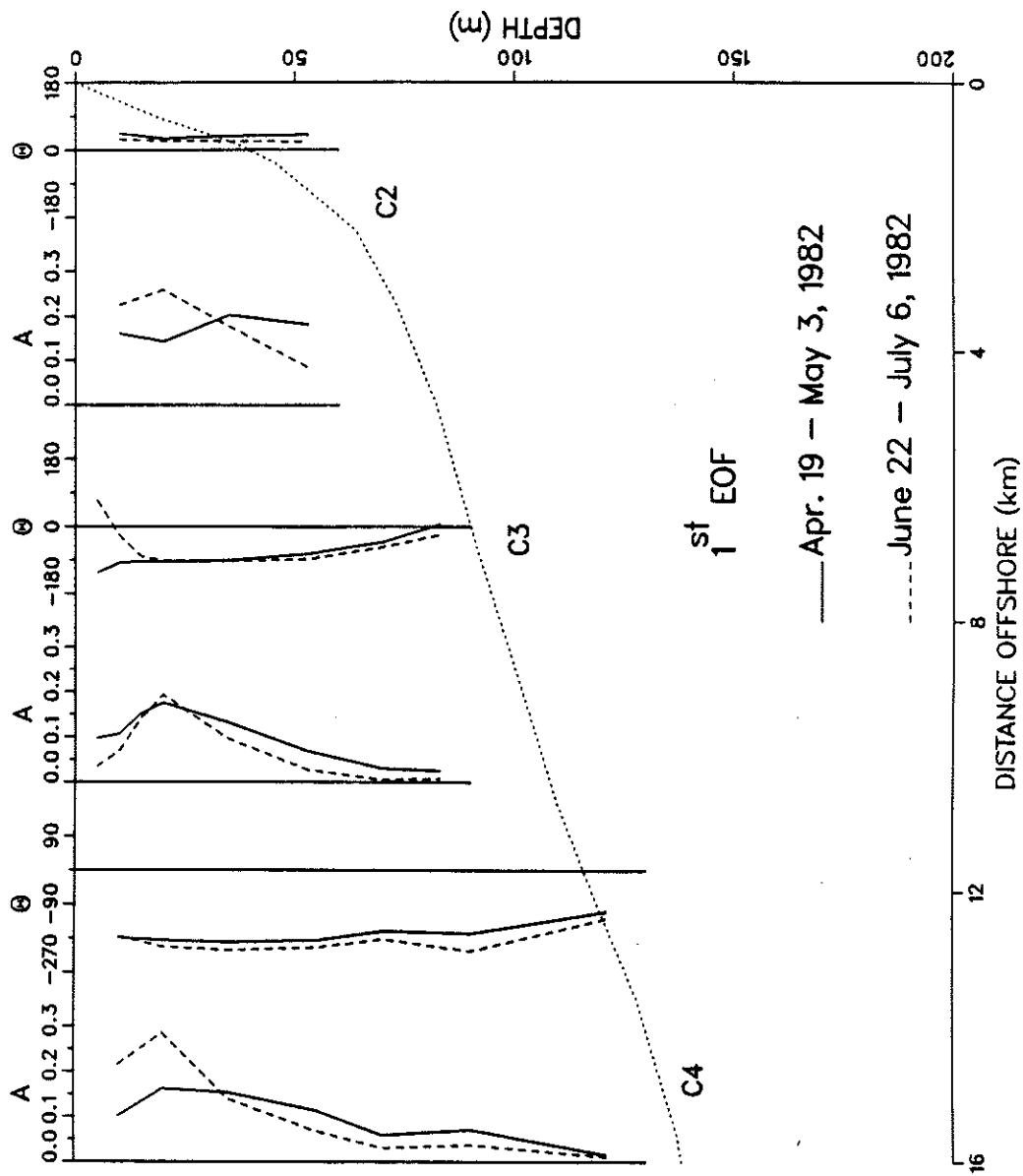


Figure 8. Amplitude (in °C) and phase (in degrees) of temperature fluctuations from C-line first EOFs for April 19 - May 3 and June 22 - July 6, 1982. Phases are relative to cross-shelf velocity at C2 10 m.

during the May control period. The first mode at the C-line calculated over the entire 4 month period, April 2 - July 28, during which all 19 instruments were in the water and working, accounts for 46% of the current and temperature variance, and is almost identical in structure with that for the two week period in April, but with about half the amplitude (Figure 7). This shows that the internal wave events, although of brief duration, make a large contribution to the variance over the whole CODE-2 time period.

The structure of the largest mode at the N-line during the two-week periods in April and May and over the whole four months are similar to each other (Figure 9). The current ellipses are very elongated, are oriented along-shelf, and are nearly depth-independent both in amplitude and phase. They are also in phase across the shelf. At N2 and N3, the currents at some depths rotate CW and some CCW, but at N4, where the ellipses are more circular, all are CW-rotating. The second modes (Figure 9) have CW-rotating ellipses almost everywhere and the cross-shelf and vertical structures are very similar to the first mode at the C-line.

The EOF analysis results reflect the coherent variance in the whole semidiurnal band. In contrast, the velocity ellipses shown in Figure 10 represent the residual M_2 currents at the R-, C-, and N-lines over the 29-day period from April 13 - May 11, 1982. As described in Section 4, these were arrived at by subtracting the depth-averaged M_2 currents. The residual ellipses at the C-line show essentially the same vertical and cross-shelf structure as the first mode EOF's, thus indicating that the variance at the M_2 frequency is representative of the whole semidiurnal band, and that

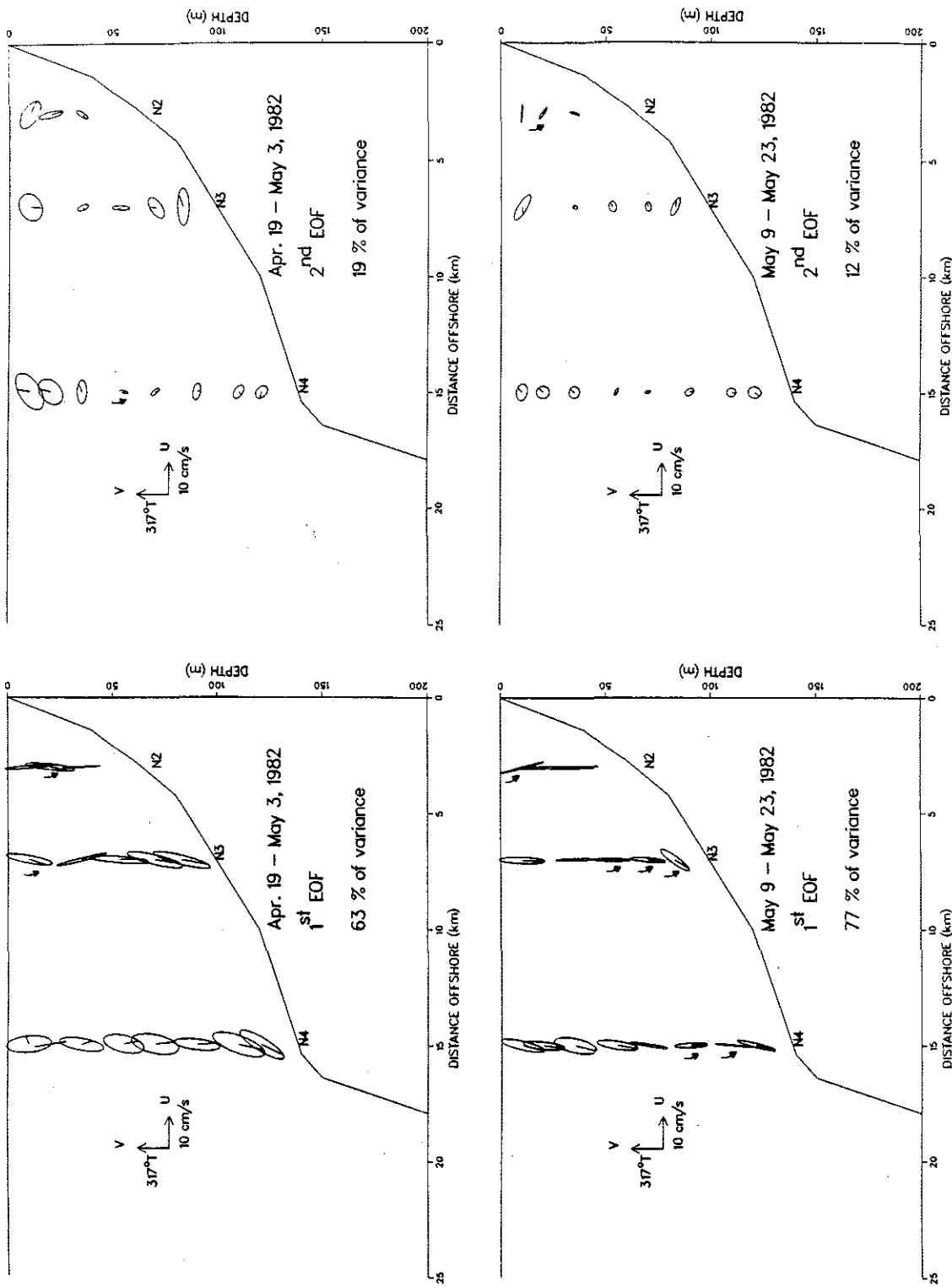


Figure 9a.

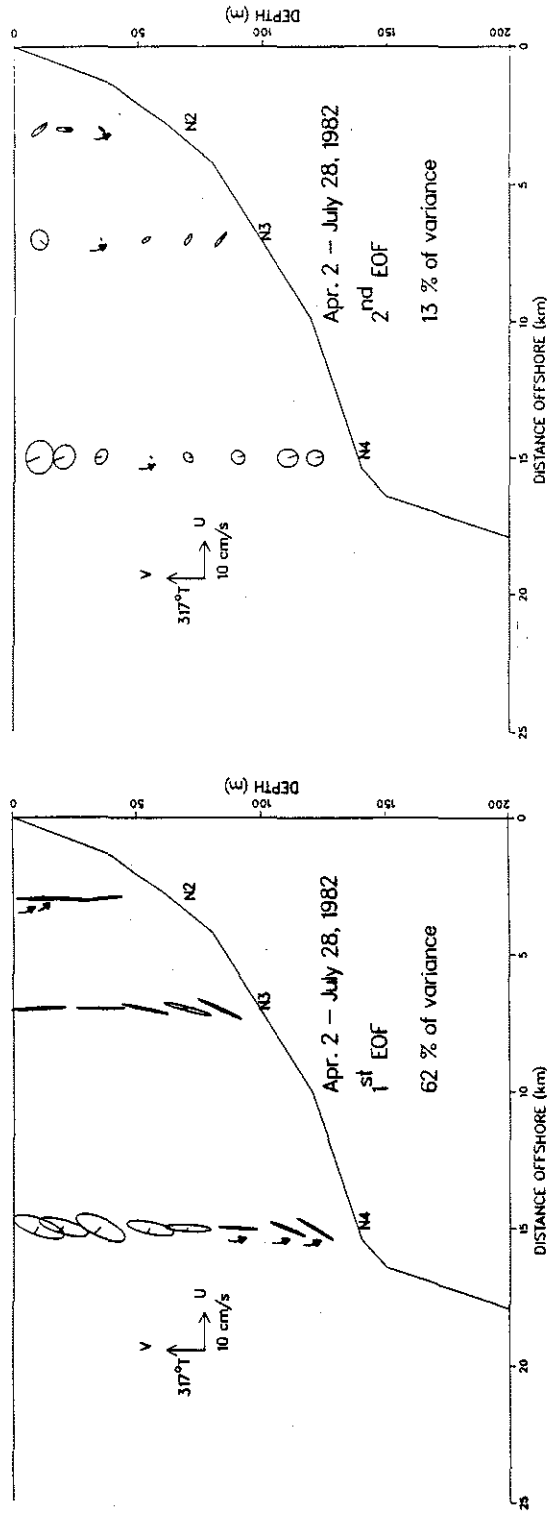


Figure 9b. Horizontal current ellipses for first and second N-line EOFs for three time periods during CODE-2. Current vectors rotate CW unless otherwise indicated. Phases relative to cross-shelf velocity at uppermost current meter nearest to the coast are marked. The percentage of total variance accounted for by each EOF is given.

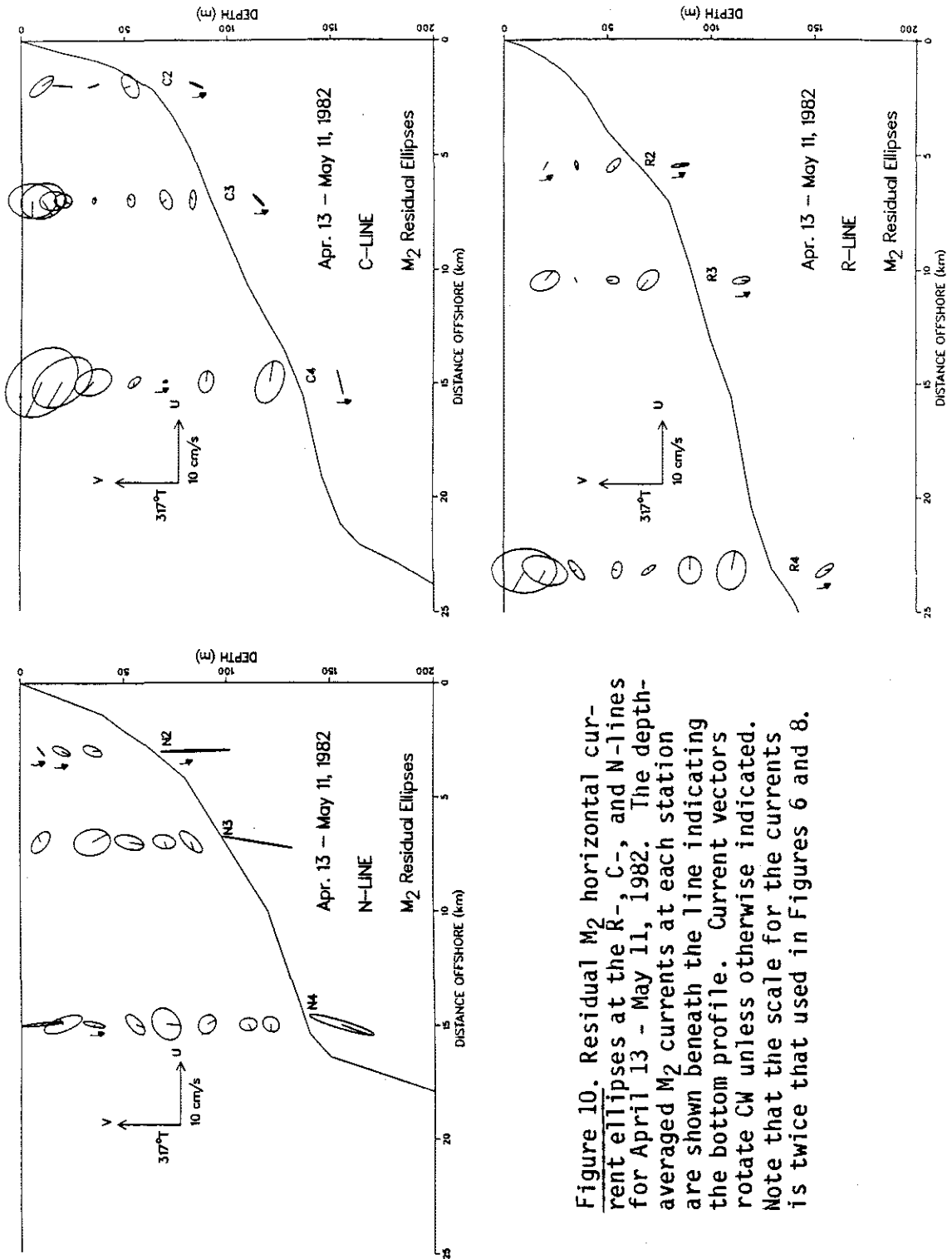


Figure 10. Residual M₂ horizontal current ellipses at the R-, C-, and N-lines for April 13 - May 11, 1982. The depth-averaged M₂ currents at each station are shown beneath the line indicating the bottom profile. Current vectors rotate CW unless otherwise indicated. Note that the scale for the currents is twice that used in Figures 6 and 8.

the structure extracted by the tidal analysis done separately at each location is the same as the coherent variance picked out by the EOF analysis. The R-line structure is very similar to the C-line. The residual currents at the N-line, which has larger depth-averaged tidal currents, do not show the same type of structure as either the first or second N-line EOF, thus indicating that the M_2 variance identified by the tidal analysis is not very coherent among the instruments in this cross-section. There is no simple structure to the N-line M_2 residual currents, as there is at the R- and C-lines.

6. COMPARISON WITH INTERNAL WAVE THEORY

In considering the propagation of internal waves in the ocean, one of two dynamical frameworks is often used; vertical modes and propagation along characteristics. Vertical modes represent the sum of waves with upward and downward propagating components that cancel each other to form waves which are standing in the vertical direction. A vertical mode representation requires a separation of variables in the horizontal and vertical directions. Characteristics represent the direction of the group velocity vector along which energy propagates, and their slopes vary continuously in a nonhomogeneous medium. At a given position in the horizontal plane, any vertical structure can be made up by the superposition of either a number of modes or a number of beams centered on the characteristics. At different points in the horizontal, the composition of modes or beams needed to describe the vertical structure may vary. In any given situation, it may be more useful to envision the internal waves in terms of one or the other of these frameworks. The nature of the vertical structure to be described

and the degree to which the medium and the boundary conditions vary in the horizontal will help to determine this. In the case of the observed velocity structure at the C-line, where all across the shelf there is a distinct mid-depth minimum in horizontal velocity with a 180° phase reversal in the vertical across this minimum, a description in terms of modes seems more appropriate. The separation of variables needed to define vertically standing modes is only valid, strictly speaking, for a flat bottom. It has been shown, however, that when the bottom slope is gentle (i.e. much less than the slope of the characteristics), the horizontal wavelength is locally the same as what would be predicted for a flat bottom (Wunsch, 1969). The observations in the CODE area, as on most other continental shelves (Torgrimson and Hickey (1979) is a notable exception), show the semidiurnal baroclinic tidal energy to be predominantly in the lowest mode (Baines, 1986). The reasons for this are discussed in the next section.

In the remainder of this section, a description of the internal tide in terms of vertical modes on a flat bottom is developed and compared with the observations. Then modifications due to the sloping bottom are discussed. The linearized, hydrostatic, inviscid, Boussinesq equations of motions on an f-plane are taken as a starting point:

$$u_t - fv = -p_x , \quad (1)$$

$$v_t + fu = -p_y , \quad (2)$$

$$u_x + v_y + w_z = 0 , \quad (3)$$

$$p_z = b , \quad (4)$$

$$b_t = -N^2 w \quad , \quad (5)$$

where u , v , w are the components of velocity in the cross-shelf (x), along-shelf (y), and vertical (z) directions, respectively. p is the perturbation pressure divided by the reference density ρ_0 , b is the buoyancy equal to $-g\rho/\rho_0$, f is the inertial frequency, N^2 is the buoyancy frequency squared equal to $-g\rho_z/\rho_0$, and subscripts denote partial differentiation. These five equations may be combined into one equation in any of the five variables. The choice of a governing equation for the vertical velocity makes application of the boundary conditions on a flat bottom particularly easy.

$$\left(f^2 + \frac{\partial^2}{\partial t^2} \right) w_{zz} + N^2 \left(\frac{\partial^2}{\partial x^2} + \frac{\partial^2}{\partial y^2} \right) w = 0 \quad . \quad (6)$$

Assuming that all variables behave as $e^{i(kx+ly+mz-\omega t)}$ leads to the familiar dispersion relation for hydrostatic internal waves,

$$\frac{m^2}{k^2 + l^2} = \frac{N^2}{\omega^2 - f^2} \quad , \quad (7)$$

from which the group and phase velocities, which are perpendicular to each other, may be derived.

(1) and (2) may be combined to give expressions for u and v in terms of p ,

$$u = \frac{\omega k + ifl}{\omega^2 - f^2} p \quad \text{and} \quad v = \frac{\omega l - ifk}{\omega^2 - f^2} p \quad , \quad (8)$$

from which it can be seen that for a wave propagating in the x-direction only ($l = 0$), $u/v = i\omega/f$. This can be generalized to the statement that the ratio between the horizontal velocity components parallel and perpendicular to the horizontal wavenumber vector is $i\omega/f$ (Gill, 1982). This means that in practice the horizontal direction of propagation should be determinable by looking at the orientation of the horizontal current ellipse, since in any ellipse the component of velocity along the major axis (which points in the direction of orientation) is 90° out of phase with that along the minor axis. Theoretically the absolute value of the ratio of major to minor axis should be ω/f (1.6 for the semidiurnal frequency at the CODE latitude). In reality however, the two criteria, the velocity components being 90° out of phase and in the ratio ω/f , are rarely met simultaneously, making a determination of the direction of propagation somewhat ambiguous. Frictional and nonlinear effects, which are not included in the above equations, may be responsible for the discrepancy between these two criteria.

Examination of the residual ellipses shown in Figure 10 and the coherent depth-dependent ellipses from the EOF analysis, shows that the ellipse orientations vary in space, as do the ratios of major to minor axes. These orientations and ratios for the residual ellipses and the first EOFs for the April event are listed in Table 2 for the C- and N-lines. It is seen that over much of the water column at the C-line the ratio of major to minor axis is close to the theoretical value of 1.6, but the orientation varies between $\pm 90^\circ$, where 0° is the cross-shelf direction. Previous observations of internal tides on continental shelves indicate that their direction of propagation is

Station	Depth	First EOF		M ₂ Residual	
		Major/Minor	Orientation (deg)	Major/Minor	Orientation (deg)
C2	10	-5.7	-33	-2.9	-48
	20	1.9	-54	-40.5	86
	35	-1.4	77	-11.5	-73
	53	-1.4	-8	-1.8	28
C3	5	-1.7	-86	-1.4	89
	10	-1.2	-78	-1.3	-74
	15	-1.2	-71	-1.4	-82
	20	-1.2	-43	-1.3	87
	35	-9.3	-4	-2.2	-9
	53	-1.6	23	-1.8	0
	70	-1.7	24	-1.8	24
83	-2.4	-2	-3.3	-3	
C4	10	-1.1	39	-1.4	-48
	20	-1.1	-69	-1.6	-57
	35	-1.1	87	-1.6	-69
	55	5.2	85	-2.4	-50
	70	-5.0	-14	2.9	-81
	90	-1.8	-13	-1.5	-13
121	-2.2	-31	-1.7	-23	
N2	10	-16.9	-85	10.0	40
	20	8.5	84	2.6	65
	35	-75.2	-86	-2.2	68
N3	10	6.2	80	-1.9	-38
	35	-16.9	-76	-1.5	-79
	53	-9.4	86	-2.3	77
	70	-5.9	77	-1.8	81
	83	-6.4	76	-2.6	48
N4	10	-2.8	-85	-15.1	-84
	20	-261.4	-80	-2.9	-69
	35	-3.8	80	4.6	79
	55	-3.4	78	-2.3	42
	70	-2.6	78	-1.3	36
	90	-4.4	84	-1.3	-33
	110	-3.2	70	-1.5	-90
	121	-3.9	59	-1.2	58

Table 2. The ratios of the major to minor axes (negative values mean rotation is CW) and the orientations (measured positive CCW from the cross-shelf direction of 47°T) of the semidiurnal band current ellipses from the largest EOF calculated over the period April 19 - May 3, 1982 are listed for the C- and N-lines. The C-line ellipses are shown in Figure 6, the N-line ones in Figure 8. Also listed are the ratios and orientations for the C- and N-line residual M₂ ellipses shown in Figure 9.

primarily onshore. That is not inconsistent with the observations at the C-line, but unfortunately it is impossible to determine accurately the direction of horizontal propagation from this velocity data. The velocity ellipses do rotate in a CW manner as predicted by theory.

Some information on the horizontal propagation characteristics of the internal tide can be gained by examining the phase relationship between temperature and velocity fluctuations. The T-u phase differences for the first EOF during April 19 - May 3 are listed in Table 3. Given that the error bars for 95% confidence are roughly $\pm 20-30^\circ$, it is difficult to draw any concrete conclusions from these results. Excluding the bottom-most instruments, since the phase of temperature there is strongly affected by bottom slope (Table 5), there is some suggestion that at C3 and C4 the wave is progressing in the shoreward direction (for which case the theoretical T-u phase difference is 0° in the upper layer and $\pm 180^\circ$ in the lower layer). At C2, where reflection from the coast might be expected to play a more important role, the phase difference at 35 m is closer to the theoretical value for a wave standing in the cross-shelf direction. Unlike the situation over the narrow shelf off the coast of southern California, where Winant and Bratkovich (1981) found that the coherent semidiurnal-band cross-shelf velocity and temperature fluctuations had a 90° phase difference in the upper water column and a -90° phase difference in the lower water column (consistent with an internal wave standing in both the vertical and cross-shelf directions), it is inappropriate to characterize the wave here as either purely propagating or purely standing in the cross-shelf direction. Most probably, the reflection coefficient at the coast is intermediate between 0 and 1.

<u>C2</u>		<u>C3</u>		<u>C4</u>	
Depth	$\theta_T - \theta_u$	Depth	$\theta_T - \theta_u$	Depth	$\theta_T - \theta_u$
(m)	(deg)	(m)	(deg)	(m)	(deg)
10	44	5	2	10	47
20	15	10	6	20	33
35	-103	15	-3	35	43
53	-91	20	-29	55	118
		35	-135	70	178
		53	-174	90	170
		70	-155	121	-104
		83	-90		

Table 3. Phase differences between the temperature (T) and cross-shelf component of velocity (u) are shown for the largest C-line EOF calculated over the period April 19 - May 3, 1982.

The internal tide is clearly not propagating seaward however, since this would require a T-u phase difference of $\pm 180^\circ$ in the upper layer and 0° in the lower layer, which are well outside even the most conservative error brackets for the estimates in Table 3.

The coherent structure represented by the largest EOF at the N-line during all the time periods examined, shows currents that are oriented nearly along-shelf everywhere in the cross-section. The narrowness of these ellipses, and the fact that they are nearly in phase both vertically and horizontally is inconsistent with interpretation as internal waves. The second EOFs at the N-line show more vertical structure, but they contain only a small percentage of the variance. The larger amount of variance in the depth-independent currents at the N-line, relative to the C-line, makes description of the baroclinic part harder, so the remainder of this section will deal with interpretation of the baroclinic tidal currents at the C-line. The similarities between the residual ellipses at the R- and C-lines (Figure 10) suggest that any conclusions drawn for the C-line may also be applicable for the R-line.

If N^2 is assumed to be a function of z only, (6) can be separated into horizontal and vertical structure equations,

$$W_{xx} + W_{yy} - \lambda_n^2 \left(f^2 + \frac{\partial^2}{\partial t^2} \right) W = 0 \quad , \quad (9)$$

$$G_{zz} + N^2(z) \lambda_n^2 G = 0 \quad , \quad (10)$$

where the substitution $w = W(x,y,t) G(z)$ has been made and λ_n^2 is a separation constant. Application of a free surface boundary

condition ($w = p_t/g$) at $z = 0$ and a no normal flow condition ($w = 0$) at the flat bottom ($z = -H$) results in a system of equations that can be solved numerically to obtain the dynamical modes for arbitrary $N(z)$ as described in Section 4.

The horizontal wavenumber $K = (k^2 + l^2)^{1/2}$ and the horizontal phase speed $c_p = \omega/K$ are then found from (9),

$$K^2 = \lambda_n^2 (\omega^2 - f^2) \quad \text{and} \quad c_p^2 = \frac{\omega^2}{\lambda_n^2 (\omega^2 - f^2)}. \quad (11)$$

The horizontal group velocity $c_g = \partial\omega/\partial K$ is given by

$$c_g = (c_p \lambda_n^2)^{-1}, \quad (12)$$

where n is the mode number.

The vertical structure for the horizontal and vertical velocities was calculated in the manner just described, using N^2 profiles derived from the CTD stations taken along the CODE-2 C-line during April 23-24, 1982. The first baroclinic dynamical mode (Figure 11), characterized by one zero crossing in the horizontal velocity, is relatively insensitive to the details of the N^2 profile. Features such as the surface intensification, vertical position of the minimum in horizontal velocity, and 180° phase shift across that minimum, compare favorably with the observations. To facilitate this comparison, Figure 7a is reproduced in Figure 12 with the same depth and distance scales as Figure 11. The current data show the zero crossing in horizontal velocity to be at 0.4 to 0.5 times the water depth at the 60, 90, and 130 m isobaths (Figures 10 and 12). The hydrographic data

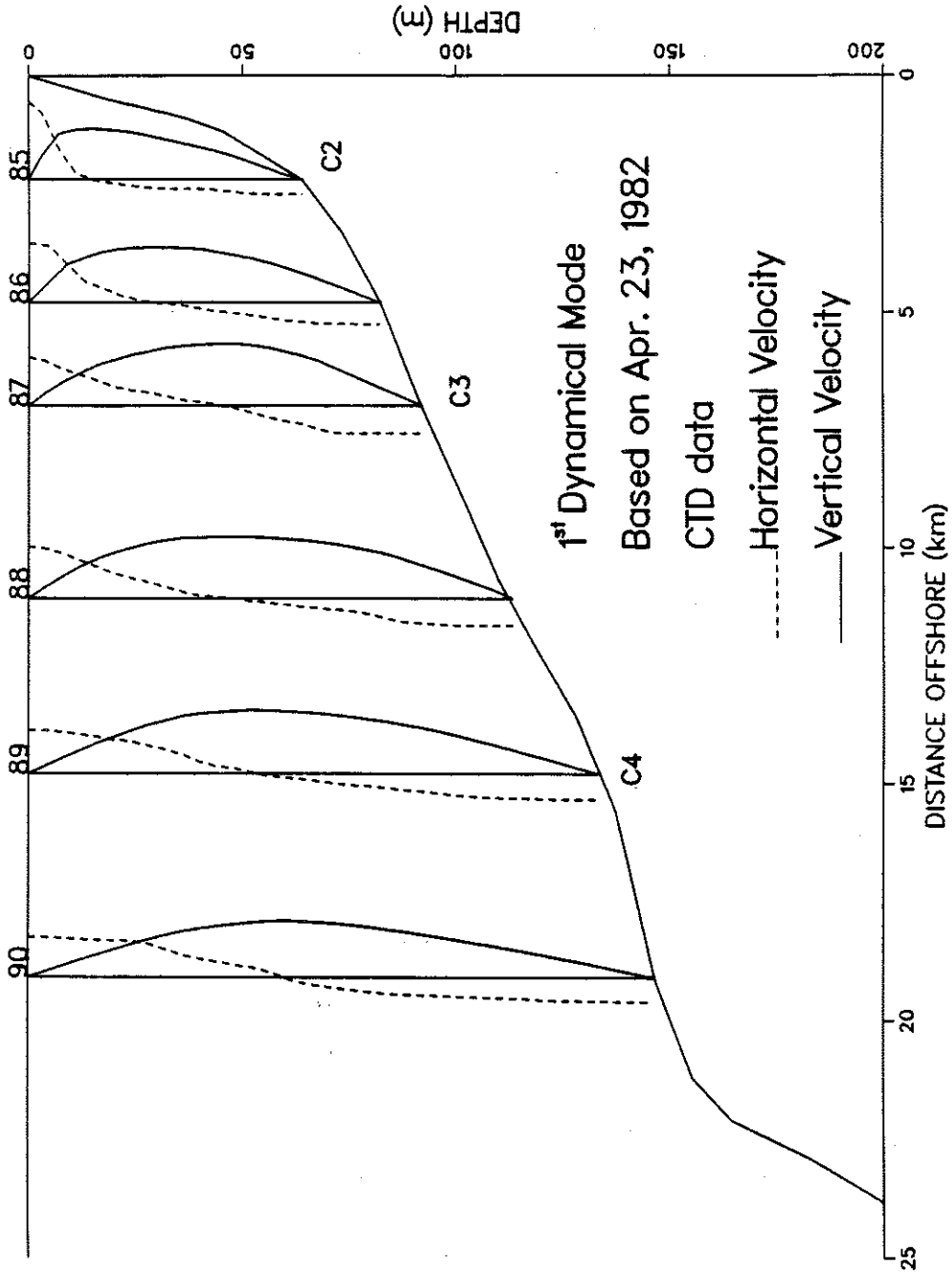


Figure 11. First baroclinic dynamical mode horizontal and vertical velocity structure calculated for C-line CTD stations 85-90. Amplitude is arbitrary. Flat bottom was assumed locally at each station. Position of C-line moorings is indicated for reference.

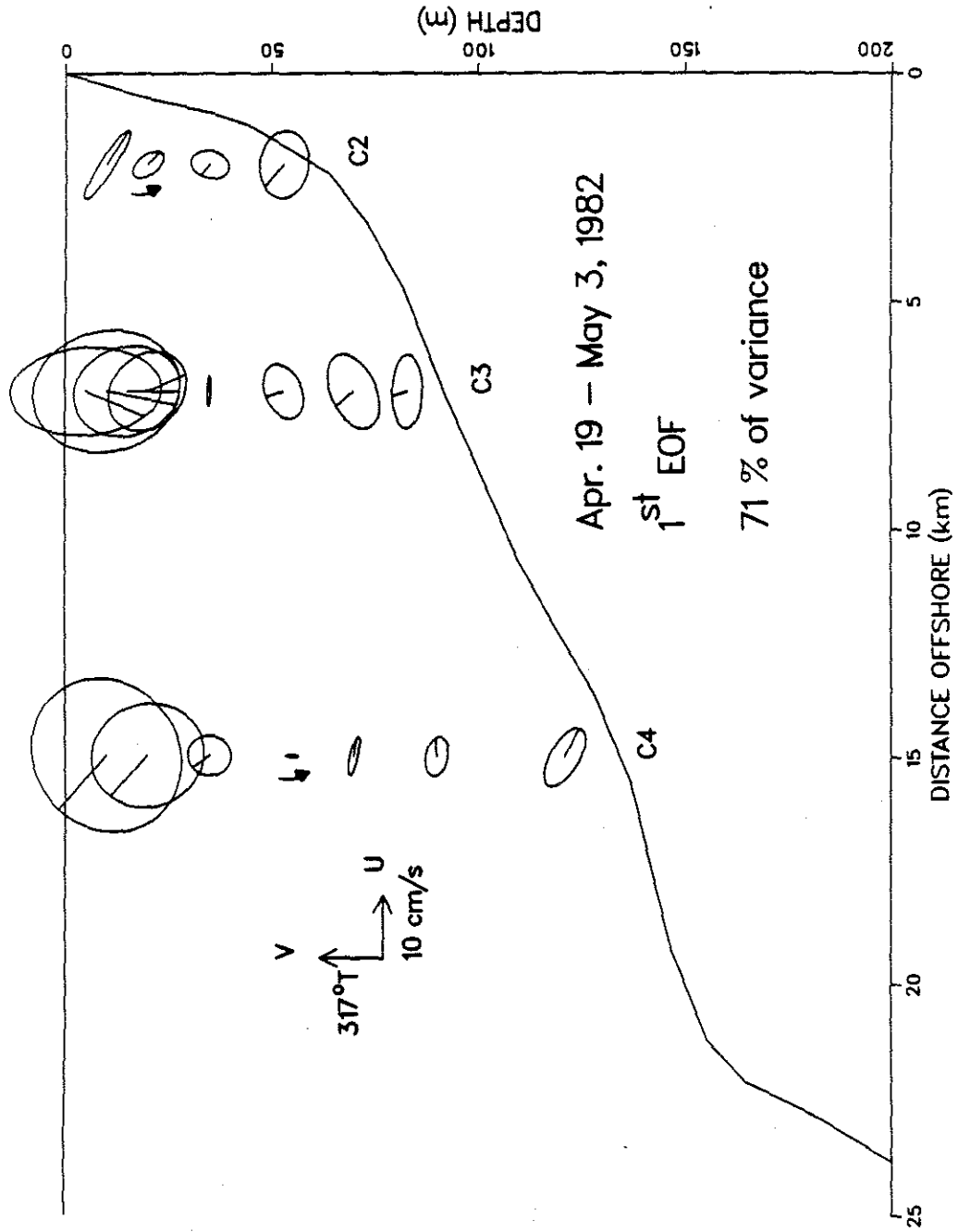


Figure 12. C-line horizontal current ellipses from first EOF for April 19 - May 3, 1982. This is an enlargement of the upper left panel of Figure 6a.

also predict a zero crossing at these depths over the outer and mid-shelf, but a shallower crossing at the two CTD stations closest to shore (Figure 11). The steep bottom slope just shoreward of C2 makes the flat-bottom approximation, used in predicting the modal structures, less valid there than at C3 and C4. It should be remembered when making these comparisons that the hydrographic data with which the dynamical modes are calculated are a snapshot in time, whereas the EOFs and residual current ellipses represent an average over 15 and 29 days, respectively.

Comparison of the vertical structure of the amplitude of the vertical velocity with data is more difficult. If horizontal advection is assumed to be small and w is calculated as T_t/T_z , where T_t is found from the EOFs (Figure 8) and T_z is calculated from the mean temperature over the 15 days, then the vertical position of the maximum in w at C3 and C4 is at 20 or 35 m. This is the same as, or one instrument lower than, the maximum in temperature. The maximum predicted from the N^2 profiles at CTD stations 87 and 89 (Figure 11) is at 44 and 52 m, respectively. In an attempt to allow a more direct comparison between the temperature results from the EOF and the dynamical modes, the first dynamical mode for vertical velocity at each CTD station was multiplied by T_z calculated from the CTD data over the same 4 m intervals used to determine N^2 . Unfortunately, these temperature modes (Figure 13) are highly sensitive to the details of the vertical structure of temperature.

Comparison of the first dynamical mode vertical velocity phase with the EOF results is easier because the correspondence in phase between temperature and vertical velocity is less ambiguous than the amplitude relationship. T and w are 90° out of phase with each other

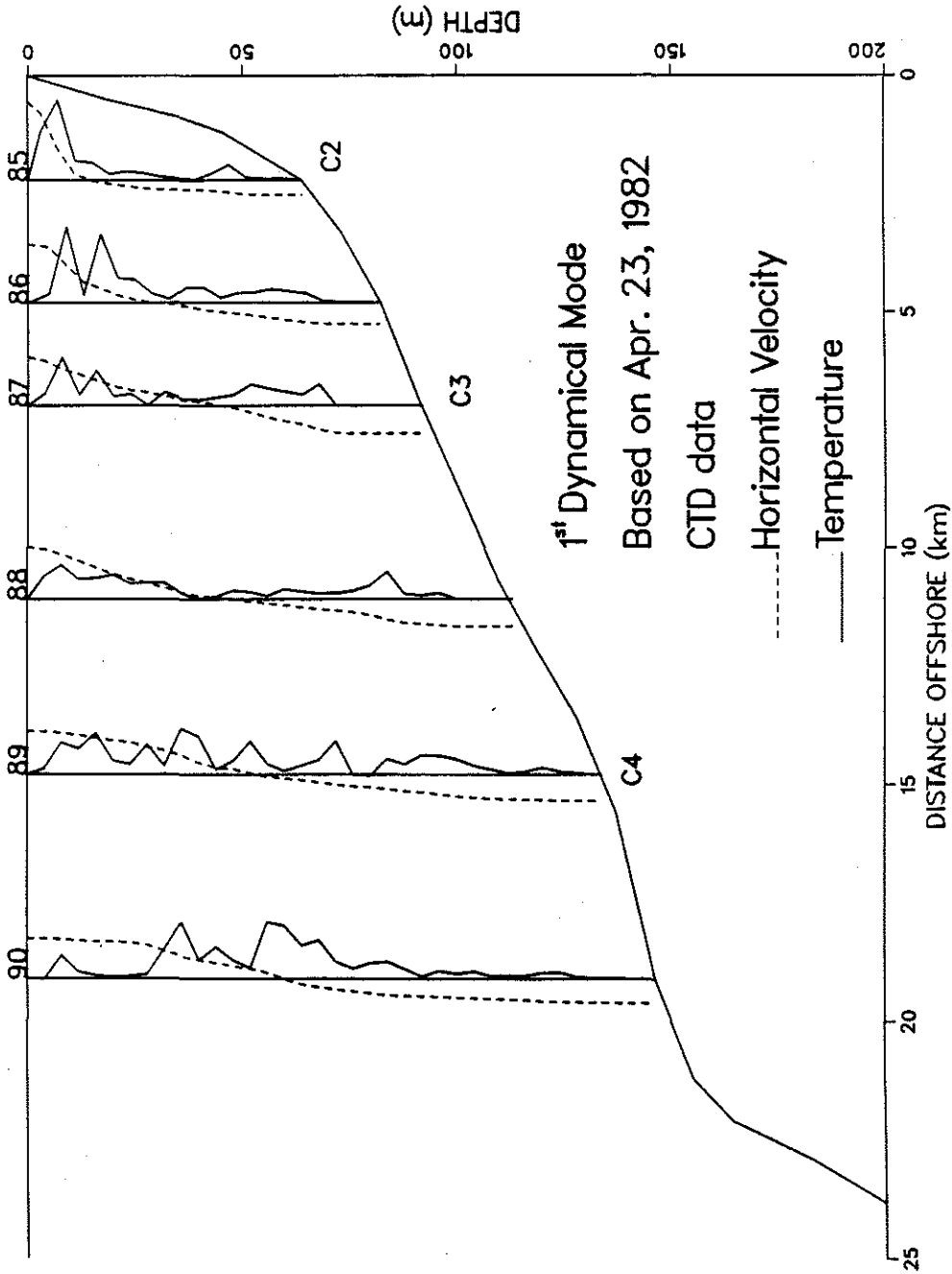


Figure 13. First baroclinic dynamical mode horizontal velocity and temperature structure for C-line CTD stations 85-90. Temperature structure was calculated by multiplying vertical velocity (Figure 10) by vertical temperature gradient. Amplitude is arbitrary.

in time, but both have phase constant with depth. The temperature phases from the EOF (Figure 8) are relatively constant with depth over most of the water column. Possible explanations for the deviations of the phase near the bottom are discussed later in this section.

Table 4 lists the horizontal phase speed, group speed, wavenumber, and wavelength predicted for the lowest baroclinic mode at each CTD station shown in Figure 11. These were calculated according to (11) and (12), using the eigenvalues found by assuming a flat bottom locally at each cross-shelf location. The group velocity for the first baroclinic mode is about 0.25 m s^{-1} , which means that energy takes approximately a day to cross the shelf.

The horizontal wavelength over the shelf predicted by this method is about 20 km. This is compared to the wavelength calculated from the phases of the temperature fluctuations in the largest EOF. Examination of Figure 8 shows the difference in the phase of the temperature signal between C2 and C4 (a distance of 13 km) to be 220° , resulting in a maximum wavelength of 21 km, if it is assumed that the wave is propagating in the cross-shelf direction. Of course if more than one wave fits between C2 and C4, the wavelength would be much shorter. Velocity was not used in this calculation because the ellipse phases are relative to their orientations, which have already been shown to be quite variable in depth.

Allowing for a sloping, instead of a flat, bottom introduces new considerations into the problem. Bottom-trapped waves as defined by Rhines (1970) become a possibility, and the vertical structure and horizontal wavelength and phase speed of vertically propagating and standing internal waves are modified in the presence of a sloping

CTD Station	Distance Offshore	Depth	Eigenvalue	Horizontal Wavenumber	Horizontal Wavelength	Horizontal Phase Speed	Horizontal Group Speed
			λ_1^2 ($s^2 m^{-2}$)	$K_H = \lambda_1 \sqrt{(\omega^2 - f^2)}$ ($10^{-4} m^{-1}$)	$2\pi/K_H$ (km)	$c_p = \omega/K_H$ ($m s^{-1}$)	$c_g = 1/(c_p \lambda_1^2)$ ($m s^{-1}$)
85	2.2	64	8.4	3.1	20.3	0.45	0.26
86	4.8	82	9.5	3.3	19.0	0.42	0.25
87	7.0	92	12.4	3.8	16.5	0.37	0.22
88	11.1	113	9.7	3.3	19.0	0.42	0.25
89	14.8	133	6.0	2.6	24.2	0.54	0.31
90	19.1	146	3.9	2.1	29.9	0.67	0.38

Table 4. The eigenvalue and horizontal wavenumber, wavelength, phase, and group speeds are listed for the first baroclinic flat-bottom mode calculated for each shelf CTD station taken along the CODE-2 C-line during April 23-24, 1982. Values of $\omega = 1.4 \times 10^{-4} s^{-1}$ and $f = 0.9 \times 10^{-4} s^{-1}$ were used.

bottom. Additionally, interaction between topography and the barotropic component of flow in a stratified fluid is a generating mechanism for internal waves, but discussion of that issue is deferred to the following section. Rhines (1970) showed that in a rotating stratified fluid bounded by a single rigid wall oriented at angle ϕ to the horizontal, edge waves may occur at all frequencies up to $N \sin(\phi)$. These waves are trapped at the wall, decaying in the direction perpendicular to it. The average bottom slope along the C-line between the 60 and 130 m isobaths is 0.005, which means that ϕ is also 0.005. Depth-averaged N values typically do not exceed 10^{-2} s^{-1} , even during the periods of largest stratification, although near-surface values may be somewhat larger. Using these values for N and ϕ , the maximum allowable frequency for bottom-trapped waves is $5 \times 10^{-5} \text{ s}^{-1}$, which is below the semidiurnal frequency of $1.4 \times 10^{-4} \text{ s}^{-1}$. Thus, the continental shelf in the CODE region slopes too gently to allow bottom trapping of waves of semidiurnal frequency.

Wunsch (1969) considered the problem of internal waves propagating in a constant N ocean with a uniformly sloping bottom. He showed that as the internal waves approach shallower water they are refracted such that the crests become parallel to shore. He also showed that far from the apex over a gentle slope, the solution reduces to that for the flat bottom. The slope of the mid-shelf region in the CODE area is subcritical with respect to internal waves of semidiurnal frequency (i.e. the bottom slope is less than the slope of the characteristic c , defined below). In an effort to assess the changes in vertical structure due to the sloping bottom, Wunsch's solution for internal waves propagating upslope in a subcritical wedge are evaluated here

using parameters appropriate to the mid-shelf in the CODE area. Expressions for the cross-slope (u) and vertical (w) velocities derived from equation (9) of Wunsch (1969) are:

$$u = \text{Re} \left\{ -iqA \left[\frac{e^{-iq \ln(cx-z)}}{cx-z} + \frac{e^{-iq \ln(cx+z)}}{cx+z} \right] e^{-i\omega t} \right\}, \quad (13a)$$

$$w = \text{Re} \left\{ -iqcA \left[\frac{e^{-iq \ln(cx-z)}}{cx-z} - \frac{e^{-iq \ln(cx+z)}}{cx+z} \right] e^{-i\omega t} \right\}, \quad (13b)$$

where $q = \frac{2n\pi}{\ln(\Delta)}$, $\Delta = \frac{c+\alpha}{c-\alpha}$; $c = \sqrt{\frac{\omega^2 - f^2}{N^2 - \omega^2}}$, n is an integer equal to the mode number, and A is an arbitrary amplitude. Equations (13a) and (13b) were evaluated at $x = 18$ km for values of z from the surface down to the bottom at 90 m with $\alpha = 0.005$, $\omega = 1.4 \times 10^{-4} \text{ s}^{-1}$, $f = 0.9 \times 10^{-4} \text{ s}^{-1}$, and $n = 1$. Table 5 compares how the phase of u and w and the amplitude of u vary with depth for solutions in a wedge with two different values of N^2 , the solutions on a flat bottom with constant N^2 and with real $N^2(z)$, and the observations. Phases and amplitudes are referenced to 83 m, the depth of the bottom instrument on the C3 mooring. Figure 14 is a visual representation of some of the information that is listed in Table 5.

The effects of the sloping bottom are to cause a slight bottom-intensification and phase shift in the horizontal velocity and a larger phase shift in the vertical velocity, relative to the flat-bottom solutions. All of these effects increase with increasing stratification. For $N^2 = 5 \times 10^{-5} \text{ s}^{-2}$, the vertical velocity at the bottom lags that near the surface by 126° . This is a possible explanation for at least some of the increase in phase with depth of the temperature

Depth (m)	Phase w(83) - Phase w(z)				u(z) / u(83)				Phase u(83) - Phase u(z)					
	Wedge		Flat-Bottom		Wedge		Flat-Bottom		Wedge		Flat-Bottom			
	$N^2 = 5 \times 10^{-5} s^{-2}$	$N^2 = 1 \times 10^{-5} s^{-2}$	Constant N^2	Real $N^2(z)$	Observed	$N^2 = 5 \times 10^{-5} s^{-2}$	$N^2 = 1 \times 10^{-5} s^{-2}$	Constant N^2	Real $N^2(z)$	Observed	$N^2 = 5 \times 10^{-5} s^{-2}$	$N^2 = 1 \times 10^{-5} s^{-2}$	Constant N^2	Real $N^2(z)$
0	a	a	a	a	a	0.94	1.01	1.03	1.75	b	-200.9	-189.4	-180	-180
5	80.2	42.2	0	0	130.1	0.93	1.00	1.01	1.61	2.08	-200.7	-189.3	-180	-180
10	79.8	42.0	0	0	103.4	0.88	0.95	0.97	1.23	2.00	-199.8	-188.9	-180	-180
15	79.0	41.7	0	0	100.1	0.83	0.88	0.90	0.92	1.47	-198.4	-188.2	-180	-180
20	78.0	41.2	0	0	101.5	0.74	0.78	0.79	0.69	1.18	-196.2	-187.2	-180	-180
35	72.8	38.8	0	0	96.6	0.38	0.36	0.35	0.20	0.41	-179.1	-178.6	-180	0
53	61.4	33.6	0	0	78.8	0.29	0.28	0.29	0.25	0.77	-50.1	-22.2	0	0
70	40.4	23.9	0	0	47.4	0.76	0.79	0.79	0.93	1.08	-16.1	-6.9	0	0
83	0	0	0	0	0	1.00	1.00	1.00	1.00	1.00	0.0	0.0	0	0
90	-46.1	-63.7	a	a	b	1.05	1.03	1.03	1.00	b	9.4	4.0	0	0

a: w = 0
b: No Data

Table 5. Three measures of the vertical structure for the first baroclinic mode; the phase of the vertical and horizontal velocities at 83 m relative to those at depth z, and the ratio of the horizontal velocity at depth z to that at 83 m, are listed for:

- (1) solutions in a wedge (Munsch, 1969) with bottom slope $\alpha = 0.005$, $N^2 = 5 \times 10^{-5} s^{-2}$, and $\alpha/c = 0.33$. Distance from coast is 18 km, corresponding to a depth of 90 m.
- (2) same as (1), but with $N^2 = 1 \times 10^{-5} s^{-2}$ and $\alpha/c = 0.15$.
- (3) solutions in a flat-bottom ocean of 90 m depth. Vertical structure is independent of N^2 .
- (4) same as (3) but with $N^2(z)$ determined from CTD station 87.

For comparison, the ratios of the ellipse major axes and the temperature phase differences at C3 from the largest C-line EOF, calculated over April 19 - May 3, are also listed. Phase differences for the horizontal currents are not listed because they are difficult to interpret due to the change in orientation of the ellipses with depth.

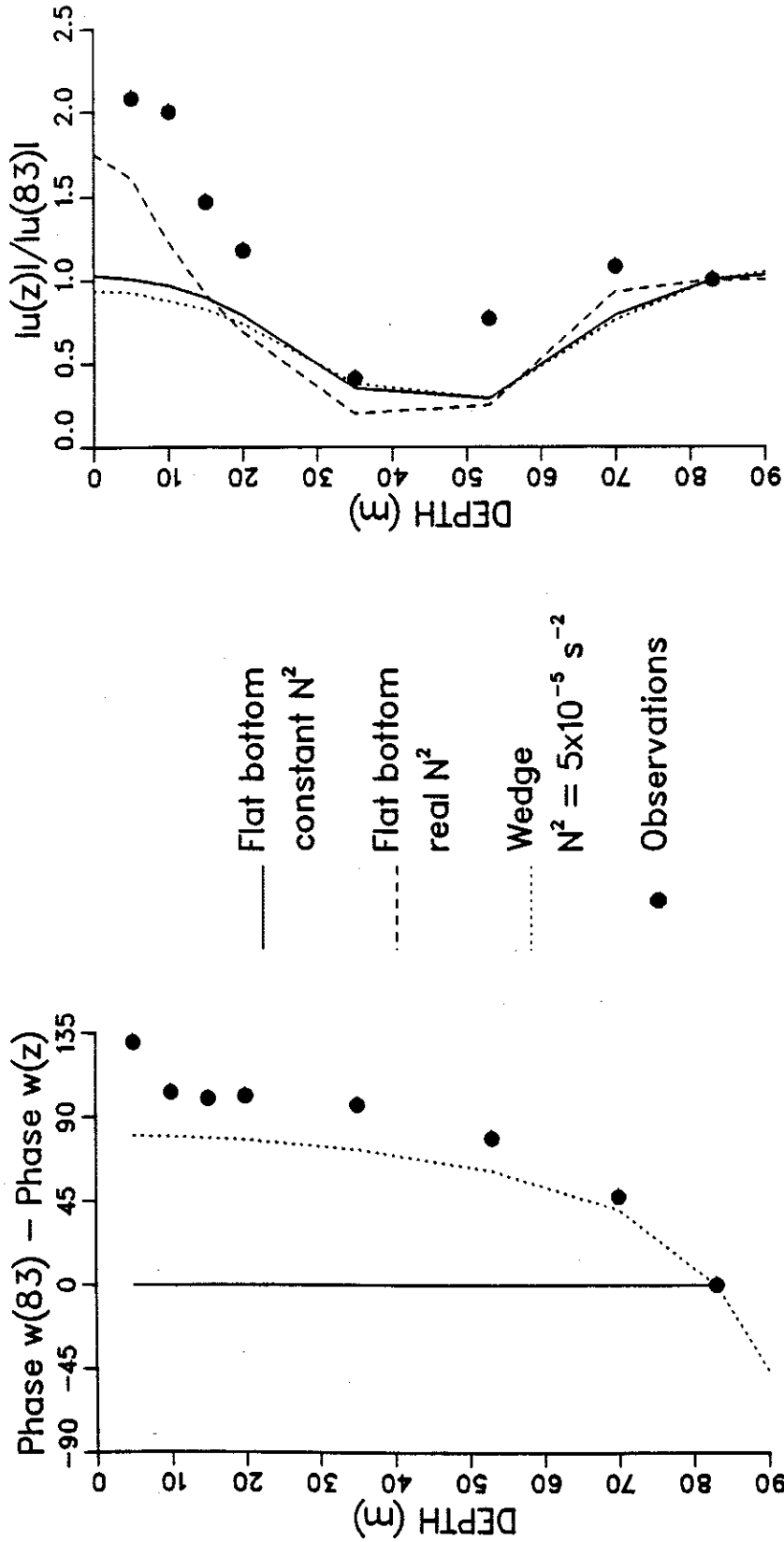


Figure 14. Phase of vertical velocity (or temperature) relative to that at 83 m (left panel), and the ratio of the amplitude of the cross-shelf velocity to that at 83 m (right panel), are shown for the first baroclinic mode calculated by three different methods, and compared with that from the largest C-line EOF for April 19 - May 3, 1982. The solid and dashed lines overlay each other in the left panel.

fluctuations seen in Figure 8. The addition of bottom friction based on a linear drag law can also cause a considerable phase shift in the vertical velocity (and temperature fluctuations) in the same sense as the bottom slope does (Brink, personal communication), which may account for the underprediction of the observed phase shift based on bottom slope alone. The amount of the friction-induced phase shift is independent of the strength of the stratification for uniform N^2 . The phase shift in the horizontal velocity across the water column is 210° with $\alpha = 0.005$ and $N^2 = 5 \times 10^{-5}$, as opposed to 180° with a flat bottom. Because of the change in orientation with depth of the current ellipses, a valid comparison of this information with the data is not possible. The ratio of surface to bottom cross-slope velocity for the above values of α and N^2 is 0.89. The 5 m to 83 m ratio is 0.93. The effect on the horizontal velocity amplitude vertical structure of using realistic $N^2(z)$ far outweighs the effect of the sloping bottom, as seen by the fact that the observed 5 m currents are twice as large as the 83 m ones, as compared to a ratio of 1.6 predicted from the dynamical modal structure on a flat bottom.

7. GENERATION

This section discusses how internal tides come to be present on the continental shelf, why their energy generally appears in the lowest baroclinic mode, and why that energy increases with increasing stratification. It is generally accepted that internal tides in the ocean are the result of barotropic tidal currents in a stratified fluid flowing over topography which causes displacement of the isopycnals. Internal tides found on the shelf may be generated locally

(most probably at the shelf break), or may propagate onto the shelf from the deep sea. Chapman and Hendershott (1981) have shown that for all deep-sea modes up to number $1.5/\gamma$, where γ is the ratio between the shelf and offshore depths, the first baroclinic mode will dominate on the shelf. This means that even if the internal tide off the shelf has a very complicated vertical structure, the lowest baroclinic mode will be preferentially excited as it propagates onto the shelf.

Generation of internal tides at the shelf break, modelled by a sharp corner, was first considered by Rattray (1960) for a two-layer fluid. Total reflection at the coast was assumed, resulting in standing waves over the shelf. In the inviscid case, this leads to quarter wave resonances. Rattray, Dworski, and Kovala (1969) extended the problem to continuous stratification. In order to satisfy matching conditions at the step, a large number of modes, with amplitude approximately inversely proportional to mode number, is needed to describe the characteristic emanating from the shelf break.

Subsequent continuously stratified models (Baines, 1974 and Sandstrom, 1976) for generation of internal waves at steep topography also predict a beam-like structure, made up of many modes, near the generation site. However, the vast majority of observations of internal tides in the ocean show the energy to be predominantly in very low modes. Four factors which could contribute to broadening of the beam have been identified. (1) Internal waves are dispersive, with the lowest vertical mode having the greatest horizontal group velocity. When generation is a discontinuous process, an observer at a point removed from the generation site will see the different modes arrive at different times. This mechanism operates even in a uniform

medium with no dissipation. (2) Schott (1977) pointed out that the modes making up the beam, which are phase-locked at the generation site, will uncouple as they propagate through a randomly varying density field. In addition, non-uniformity in the low frequency flow will cause variable Doppler-shifting, contributing to the phase unlocking which causes the beam to broaden. Again, no dissipation is required for this process. (3) The addition of a simple Rayleigh type friction term, producing damping proportional to time, introduces a mechanism favoring the low modes. Because high modes will take longer to travel from the generation to the observation site, they will be more severely damped upon arrival. (4) LeBlond (1966) and Prinsenberg, Wilmot and Rattray (1974) showed that the low modes are also favored by the preferential internal dissipation of the higher modes, due to their increased vertical shear. As a result of a combination of these mechanisms, the lowest modes will be dominant even in areas only a short distance away from the generation site.

Baines, in a series of papers, considered the problem of the generation of internal tides by flow over realistic topography. In his 1982 paper, he summarizes his previous work in this area and presents simplified methods for application of his generation theory to several oceanographic situations. The model, as it applies to a coastal region with a flat shelf adjoining a continental slope with an assumption of no reflection at the coast, is restated in his 1986 paper. The density structure is modelled as a surface mixed layer above a linearly stratified deep layer. This corresponds to an N^2 profile with a value of zero in the surface layer separated from the constant N^2 deep layer by a delta function (Figure 15). Depth vari-

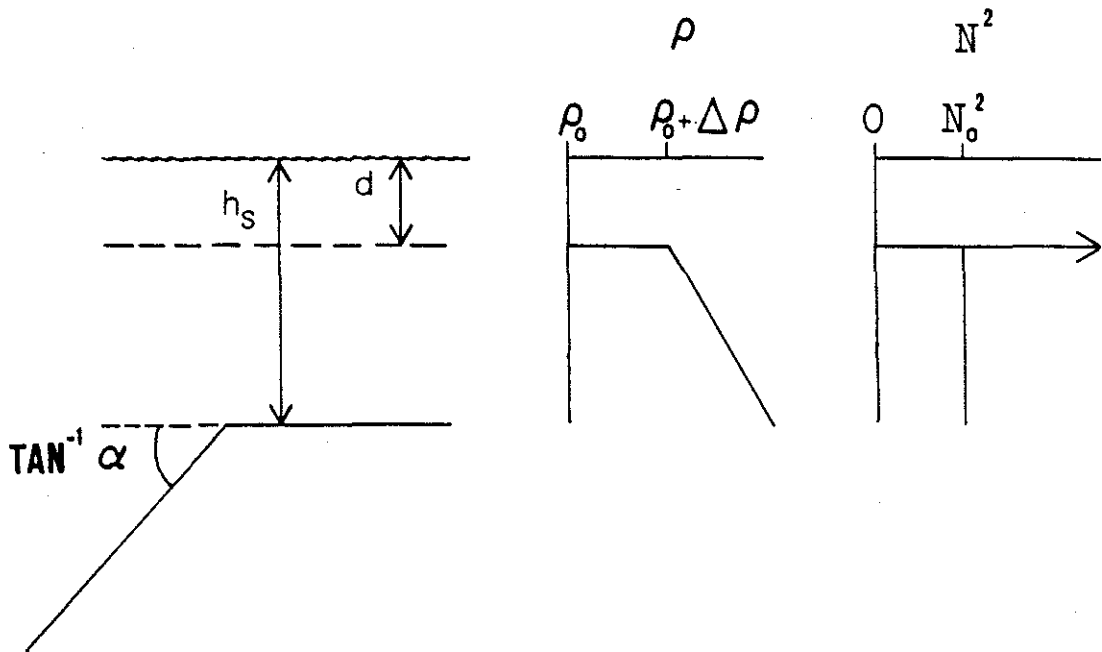


Figure 15. Parameters used in Baines (1982) model for the generation of internal tides are defined. The value of N^2 at the base of the mixed layer (depth d) is infinite.

ations are treated more easily using ray theory, but ray theory cannot handle the effects of the interface and surface mixed layer very well. Consequently, Baines considers separately situations in which the effects of the upper mixed layer and interface on the motions below may be ignored, and situations where the mode due to the interface may be isolated and then the interface held rigid in evaluating by ray theory the contribution due to the constant N^2 deeper layer. He shows that the internal tides on the shelf are largely due to the contribution from the interfacial mode, regardless of whether the continental slope is sub- or supercritical. The parameters $R = d/h_s$ and $S = g\Delta\rho/(d\rho_0 N_0^2)$ (where the variables are defined in Figure 15) were evaluated using CTD stations 92 and 93 (Figure 16) taken on April 23, 1982 near the shelf break. It is found that the conditions for which independent solution of the interfacial mode is a good approximation are met. The cross-shelf velocity over the shelf due to the interfacial mode is evaluated in the Appendix and is shown to be very much less than the observed velocities. Huthnance and Baines (1982), working off the northwest coast of Africa, and Holloway (1983b), off the northwest coast of Australia, also found that the theory underpredicted the observed velocities.

Baines' theory does offer some insight into the causes of the time variability of the internal tidal energy over the continental shelf. His analysis shows that the forcing function for the internal tide is proportional to the bottom slope, barotropic cross-shelf velocity, and stratification (N^2). The stratification comes in through the density perturbation caused by the topographically-induced vertical velocity advecting the basic state density field. An implicit assumption is

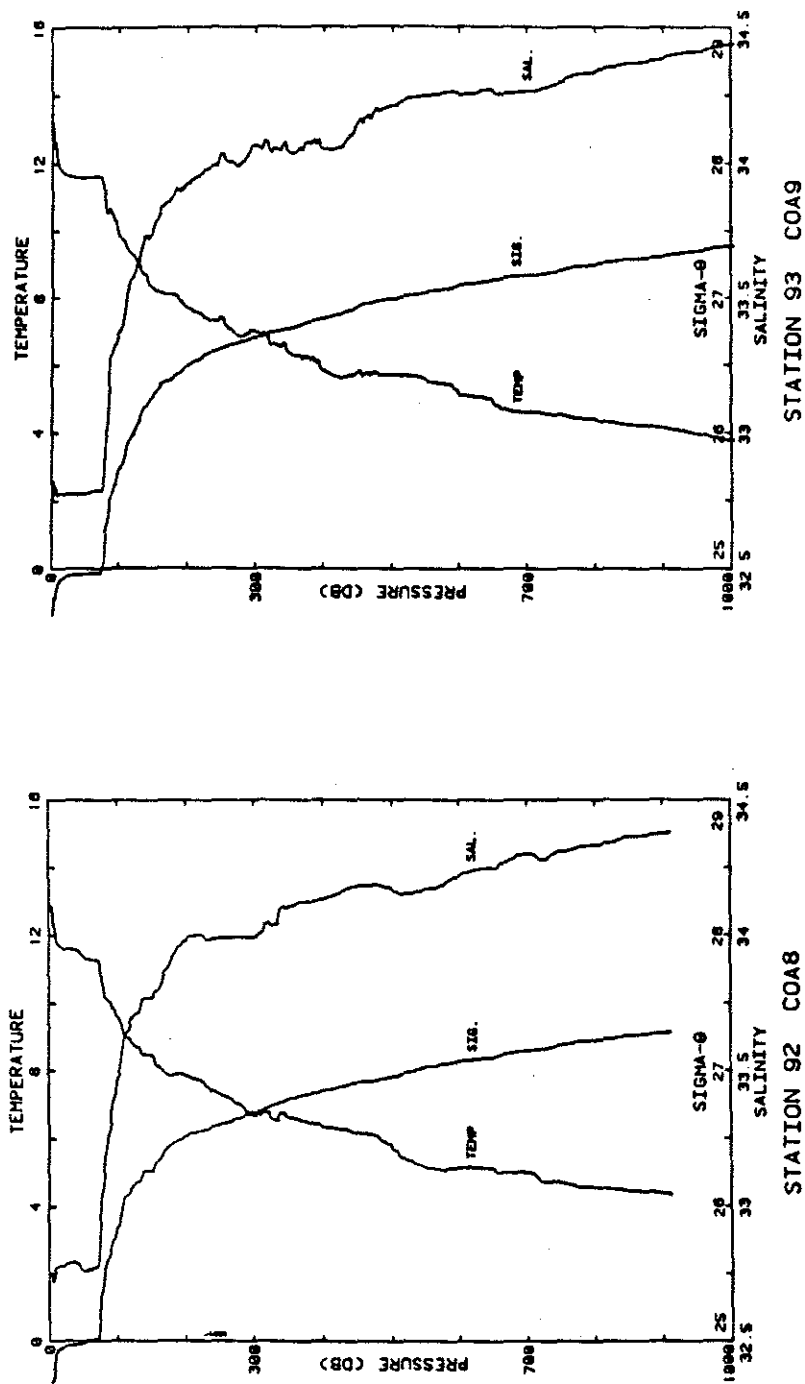


Figure 16. Temperature, salinity and sigma-t profiles for CTD stations 92 and 93 (from Fleischbein et al., 1983a).

made that the barotropic cross-shelf and vertical velocities are independent of the stratification. However, since the strength of the internal tide is dependent on the stratification, and it draws energy from the barotropic tide, this is not exactly true. In Baines' theory, time variability in internal tides over the shelf is mostly due to the changes in stratification at the shelf break. To show that the stratification over the slope and shelf break does indeed vary in time, the C-line density cross-sections measured on April 23-24 during a relaxation event and on July 16 during typical upwelling conditions are compared (Figure 17). The increased stratification over both the shelf and slope in the April transect is evident. This is also seen in the low-passed temperature records over the shelf and to a lesser extent over the slope at mooring C5 (Figure 5).

In Figure 18, the slope, $c = [(\omega^2 - f^2)/(N^2 - \omega^2)]^{1/2}$, of the characteristics near the bottom over the upper continental slope and outer shelf are shown in relation to the bottom slope. The values of N^2 that were used in calculating c are shown in the figure. They were determined from the April CTD data, and are representative of the few meters above the bottom mixed layer (if one existed). It is seen that the bottom slope switches from being sub- ($\alpha < c$) to supercritical ($\alpha > c$) between stations 90 and 91 which bracket the shelf break, thus identifying that area as the probable generation region. The deep stratification over the continental slope is nearly the same during the relaxation and upwelling periods, as is seen more clearly in Figure 19, which shows the N^2 profiles calculated from the slope CTD stations 92 and 18 taken during April and June, respectively. Although the exact part of the continental slope that is critical changes some-

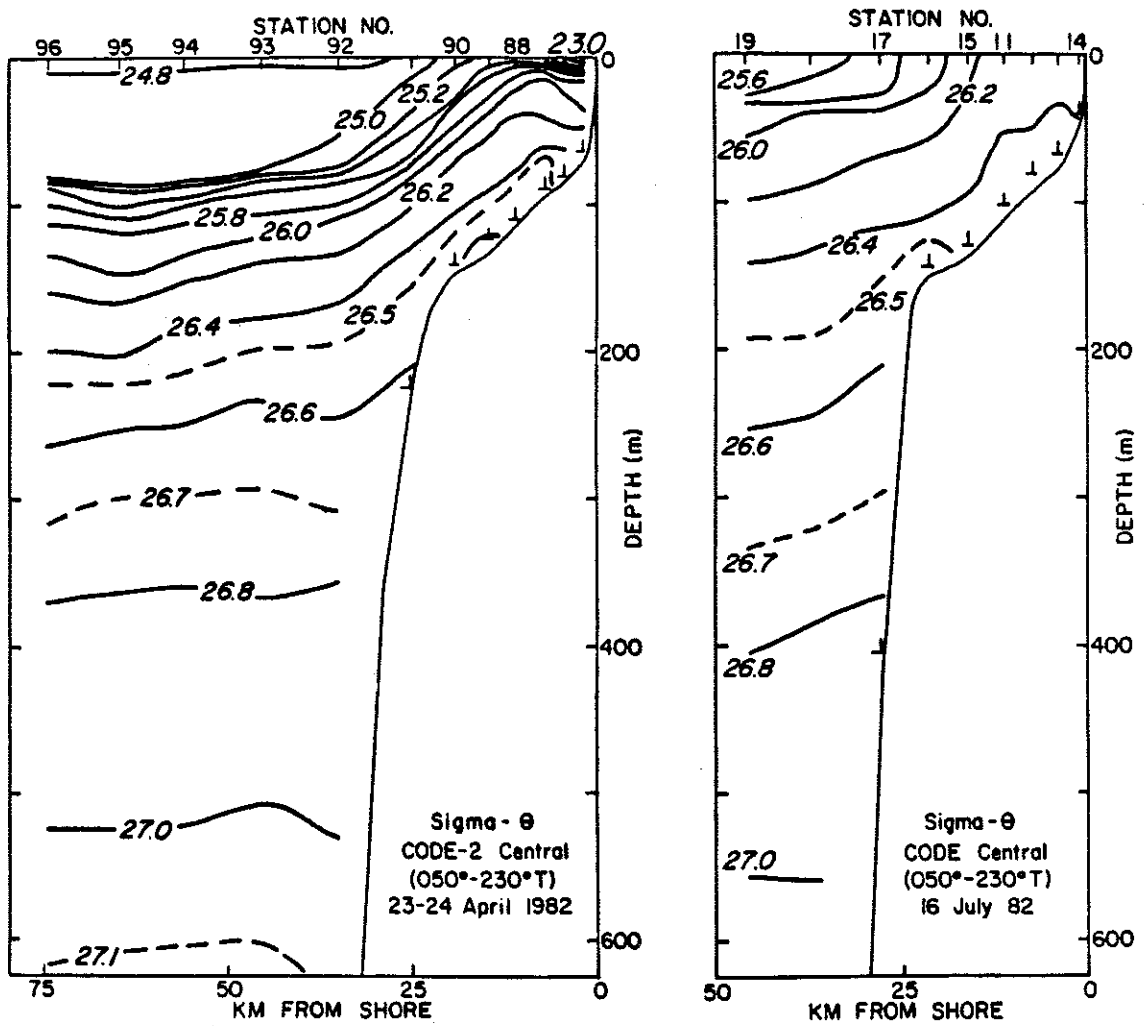


Figure 17. Sigma- θ cross-sections from CODE-2 C-line CTD stations taken on April 23-24, 1982 (Fleischbein et al., 1983a) and July 16, 1982 (Huyer et al., 1984).

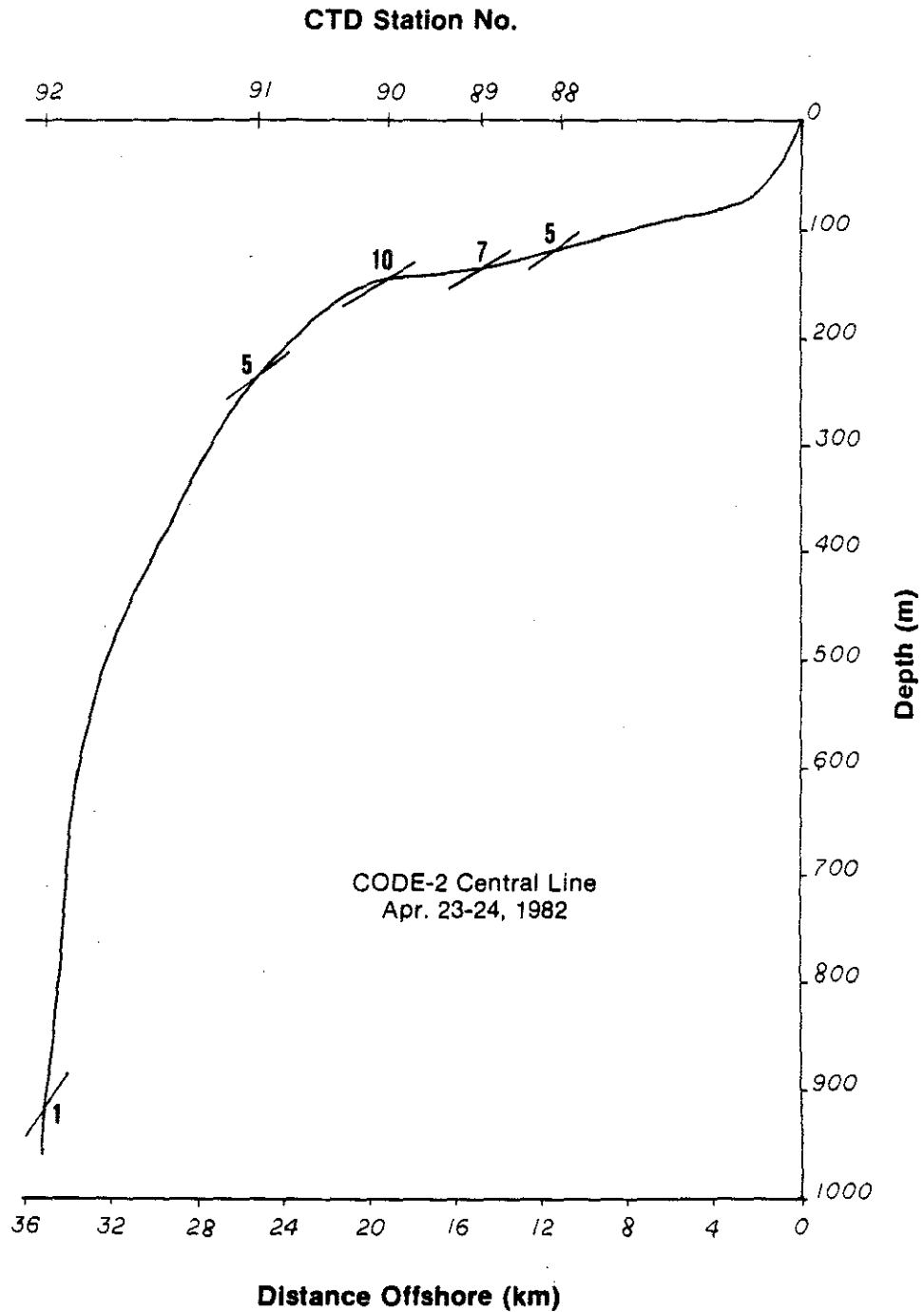
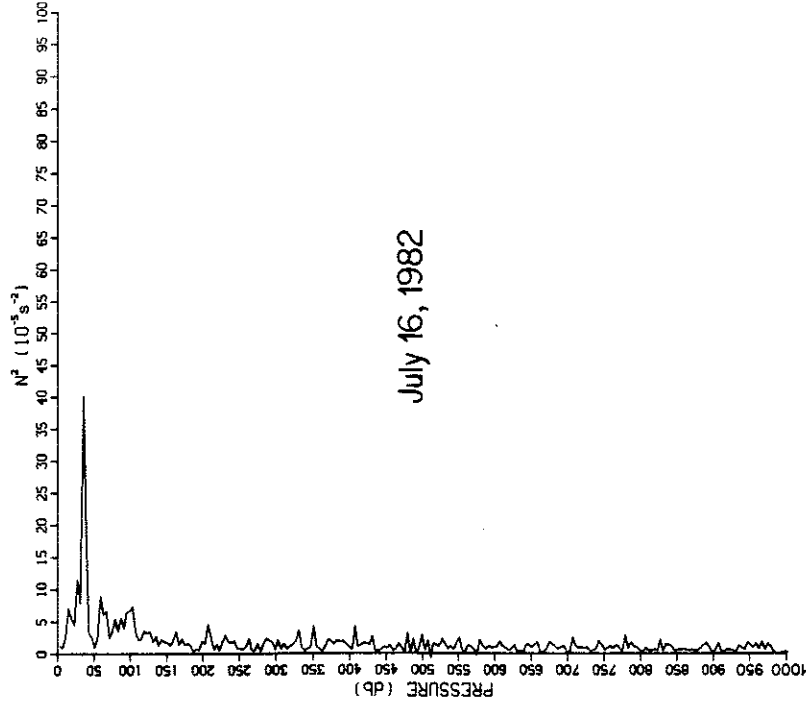


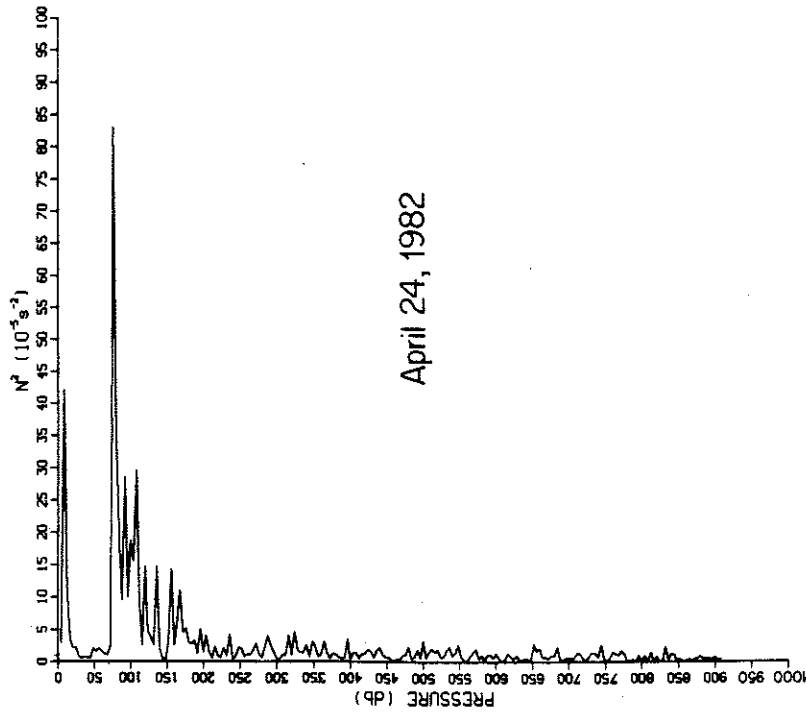
Figure 18. Slope of characteristics for semidiurnal frequency internal waves are shown in relation to bottom slope over outer shelf and upper continental slope. Values of N^2 (in 10^{-5} s^{-2}) used in calculating $c = [(\omega^2 - f^2)/(N^2 - \omega^2)]^{1/2}$ are shown next to lines indicating characteristic slope.

STN 18



July 16, 1982

STN 92



April 24, 1982

Figure 19. N^2 profiles calculated from CTD data taken over continental slope on April 24, 1982 and July 16, 1982 are shown.

what in time, the bottom goes from being subcritical over the shelf to supercritical over some part of the upper slope during both time periods. The upper level stratification is clearly different during the two periods, however (Figure 19), which supports the contention of Baines (1982, 1986) that it is the stratification changes in the upper 150 m over the generation region that are responsible for the time variability of the semidiurnal energy over the shelf. Whether increased stratification over the shelf itself also plays a role in amplification of the internal tidal energy there is uncertain. More work is needed to identify the mechanisms by which this could occur. It has been shown that the horizontal length scale over which internal tides are damped, due to both internal turbulence (LeBlond, 1966) and bottom drag (Brink, personal communication), increases with increasing stratification.

8. EFFECTS OF SHEAR IN THE LOW FREQUENCY FLOW

In this section, the effects of mean horizontal and vertical shear on the propagation of internal tides are considered. The objective is to determine whether the low frequency flow contributes significantly to the time variability of the internal tidal energy observed over the shelf. The questions of how these shears affect the upper and lower bounds of the passband for freely-propagating internal waves, and what effect they have on the slope of the characteristics are addressed. Since the low frequency flow is predominantly in the along-shelf direction (Winant, Beardsley, and Davis, 1987), and the internal tide is presumed to be generated at the shelf break, the problem can be conceptualized as an internal wave propagating perpendicularly to a

baroclinic current, thus eliminating the possibility of Doppler-shifting. As discussed in Mooers (1975), the upper and lower bounds for the internal wave passband are

$$\omega_U^2 \approx N^2 (1 + s^2) \quad \text{and} \quad \omega_L^2 \approx \omega_f^2 - s^2 N^2 \quad (14)$$

The slopes of the characteristics are given by

$$c'_{\pm} = s \pm \frac{\sqrt{(s^2 + \omega^2 - \omega_f^2)}}{N^2} \quad (15)$$

where it has been assumed that $(\omega_f/N^2) \ll 1$ and $s^2 = (-M^2/N^2)^2 \ll 1$. The effective inertial frequency ω_f equals $[f(f + \bar{v}_x)]^{1/2}$. M^2 is defined as $-g\rho_x/\rho_0$, in analogy with N^2 . Overbars are used to denote low frequency flow. Note that if $\omega_f = f$ and $M^2 = 0$, c' reduces to c as defined in the previous sections, with the assumption that $\omega \ll N$.

Effects of the mean vorticity, approximated here by \bar{v}_x , are considered first. Examination of the low-passed current and wind vectors, shown in Beardsley and Alessi (1985), reveal that the largest horizontal shears occur near the start of the relaxation periods (Send et al., 1987). The maximum horizontal shear resolved by the array occurs on April 21, 1982. The near-surface low-passed currents at C4 are equatorward at about 55 cm s^{-1} , and 8 km nearer to shore at C3, the currents are poleward at 20 cm s^{-1} . This results in $\bar{v}_x = 9.4 \times 10^{-5} \text{ s}^{-1}$. The effective inertial frequency ω_f is then $1.3 \times 10^{-4} \text{ s}^{-1}$, which is just slightly below the semidiurnal frequency. Therefore, the semidiurnal frequency always exceeds the lower bound for freely propagating

internal waves. To determine whether the shelf is transmissive to semidiurnal internal tides, the ratio c'/α must be evaluated. If s is taken to be constant, then (15) shows that as \bar{v}_x increases, ω_f moves toward ω and c' gets smaller. For $\omega_f = 1.3 \times 10^{-4} \text{ s}^{-1}$ and $N^2 = 10^{-4} \text{ s}^{-2}$, $c' = 0.005$, the same as the bottom slope over the shelf. Based on consideration of the horizontal shear alone, it appears that for short periods (order 1 day) at the start of a wind relaxation, the current shears over the shelf are large enough such that the slope of the characteristics for the semidiurnal internal tide approach criticality with respect to the bottom slope over the shelf. Under these conditions, generation might take place over the shelf itself. The effects of the horizontal variations in density, which are considered next, are seen to moderate somewhat the effect of the horizontal shear.

Winant et al. (1987) have shown that the horizontal variations in density in the CODE area are related to the low frequency vertical shear by the thermal wind equation, so that M^2 may be expressed as $f\bar{v}_z$. As is seen from (14) and the definition of s^2 , a non-zero value of M^2 , regardless of its sign, acts to decrease ω_L and increase ω_U . However, the sign of M^2 introduces an asymmetry between the seaward- (c'_-) and shoreward-propagating (c'_+) characteristics (eqn. 15). Mooers (1975) points out that the slope of the isopycnals significantly affects the slope of the characteristics, when the two are of the same order. Thus, when $\omega_f \approx f$, $s \ll [(\omega^2 - \omega_f^2)/N^2]^{1/2}$ and contributes very little to c' , but when ω_f approaches ω , s plays a more important role. It acts to steepen the shoreward-propagating ray, while flattening the seaward-going one. Based on an average value of the along-shelf velocity vertical shear in the upper 40 m at C3 (Winant et al., 1987), and

on ρ_x calculated from the April 23-24 C-line density cross-section (Figure 17), M^2 is found to be in the range -4 to $-7 \times 10^{-7} \text{ s}^{-2}$. For $M^2 = -5 \times 10^{-7}$, $\omega = 1.4 \times 10^{-4} \text{ s}^{-1}$ and N^2 and ω_f as in the previous paragraph, $c'_+ = 0.012$, which is steeper than the bottom slope. Since the effects of the vertical and horizontal shear in the mean flow act to compensate each other, they probably do not have a large impact on the internal tides over the continental shelf in the CODE area.

9. CONCLUSIONS

As on other narrow continental shelves, internal tidal currents of amplitude equal to, or greater than, the barotropic tidal currents are observed over the continental shelf off northern California. During CODE-2, the shelf is always subcritical with respect to internal waves of semidiurnal frequency, and there is always sufficient stratification over the shelf to allow these waves to propagate, even if only along the interface between nearly mixed surface and bottom layers. In spite of these facts, which show that during CODE-2 the conditions necessary to support semidiurnal internal tides on the shelf are always present, large internal wave events are seen only intermittently in time. As on the continental shelves off Oregon, southern California, and northwest Australia (Hayes and Halpern, 1976, Winant and Bratkovich, 1981, and Holloway, 1984), the currents associated with the internal tide tend to increase with increasing stratification. The deep stratification over the slope is relatively constant throughout the CODE-2 experiment, but changes in the upper layer stratification near the shelf break may be responsible for the time variability in the internal tides over the shelf, as suggested by Baines (1982, 1986).

The strength of the internal tidal currents over the shelf is under-predicted by Baines' theory. How the time variability of the stratification over the shelf itself contributes to the variability of the internal tidal energy over the shelf is unresolved.

The cross-shelf and vertical structure of the semidiurnal current and temperature fluctuations along the C-line is examined in detail for a 15-day period from April 19 - May 3, 1982, when the internal tide is especially large. Comparisons were made with the first baroclinic mode calculated using the actual N^2 profile, but assuming a flat bottom, and with a first baroclinic mode in a wedge with constant N^2 . Both the coherent horizontal velocity fluctuations in the semidiurnal band, and the residual horizontal M_2 currents calculated separately for each instrument, have vertical structure consistent with the lowest baroclinic mode calculated for a flat bottom. This mode has a horizontal wavelength of approximately 20 km, in good agreement with that estimated from the temperature data. Evidence for the phase shift in the vertical velocity predicted by the wedge model is seen in the temperature data.

APPENDIX: Application of Baines' Theory of Internal Tide Generation

To use the theory of Baines (1982), the continental shelf and adjacent slope are modelled as shown in Figure 15 with the shelf depth h_L equal to 125 m and the slope $\alpha = 0.061$. Based on CTD stations 91-93, the mixed layer depth d is taken to be 70 m with a density jump $\Delta\rho$ at the base from 1.02496 to 1.02650 g cm^{-3} . The latter is chosen as being the density below which N^2 has an approximately constant value N_0^2 of 10^{-5} s^{-2} (Figure 19). ρ_0 is a reference density equal to 1.025 g cm^{-3} and g is the gravitational acceleration. Thus,

$$R = \frac{d}{h_L} = 0.56 \quad , \quad (\text{A1})$$

$$S = \frac{g \Delta\rho}{\rho_0 d N_0^2} = 21 \quad , \quad (\text{A2})$$

$$\frac{1}{1 + \frac{\pi}{2} \sqrt{S}} = 0.12 < R = 0.56 \quad . \quad (\text{A3})$$

The preceding inequality satisfies Baines' condition for approximating the modes by a two-layer form. Over the shelf, the upper and lower layer cross-shelf velocities due to the interfacial mode are found by,

$$\begin{aligned} u_U &= R e \left[\frac{Q D_0}{d} e^{-i(\theta + \omega t)} \right] \quad , \\ u_L &= R e \left[\frac{-Q D_0}{h_L - d} e^{-i(\theta + \omega t)} \right] \quad , \end{aligned} \quad (\text{A4})$$

where Q is the cross-shelf volume flux, equal to the barotropic cross-shelf tidal velocity (u_B) times the depth at the shelf break. Based

on the estimates in Rosenfeld and Beardsley (1987), u_B for the M_2 constituent is about 2 cm s^{-1} , so that

$$Q = 2.5 \times 10^4 \text{ cm}^2 \text{ s}^{-1} ,$$

$$D_0 = - \frac{R \gamma(R,T)}{1 + \frac{1}{\sqrt{1-R}}} = - 0.19 e^{i0.1\pi} ,$$

$$T = - \frac{h_L \sqrt{w^2 - f^2}}{\sqrt{\frac{d g \Delta \rho}{\rho}} \alpha} = 0.216 ,$$

where the amplitude and phase of $\gamma(R,T)$ found from graphs in Figure 5 of Baines (1986) or Figure 3 of Baines (1982) are

$$|\gamma(R,T)| = 0.85 , \quad \arg \gamma(R,T) = 0.1\pi .$$

Plugging the above values for Q , D_0 , h_L and d into (A4) results in

$$|u_U| = 0.68 \text{ cm s}^{-1} ,$$

$$|u_L| = 0.86 \text{ cm s}^{-1} .$$

Even if Q were doubled, due to the constructive interference between semidiurnal constituents, the predicted velocities would still be much smaller than the observed ones which have amplitudes of $6-12 \text{ cm s}^{-1}$ averaged over April 19 - May 3. Note that an increase in $\Delta \rho$ causes an increase in u_U and u_L because γ is inversely proportional to T .

ACKNOWLEDGMENTS

The author is indebted to M. Blumenthal for kindly making available his program to calculate vertical structure for the dynamical modes. The author's understanding of many of the ideas discussed here was enhanced by discussions with E. Kunze, D. Kelley, K. Helfrich, and T. Wood. The author also wishes to acknowledge R. Beardsley for overseeing this work and Anne-Marie Michael for helping with the typing. S. Lentz supplied the low-passed version of the temperature data shown in Figure 4. This work was supported by the National Science Foundation under grant numbers OCE 80-14941 and OCE 84-17769.

References

- Baines, P. G., The generation of internal tides over steep continental slopes. Philosophical Transactions of the Royal Society of London, A277, 27-58, 1974.
- Baines, P. G., On internal tide generation models. Deep-Sea Research, 29, 307-338, 1982.
- Baines, P. G., Internal tides, internal waves and near-inertial motions In: Baroclinic Processes on Continental Shelves, C. N. K. Mooers, ed., Published by AGU, 19-31, 1986.
- Beardsley, R. C. and C. A. Alessi, CODE-2: An array description of the surface wind and near-surface currents, in CODE-2: Moored Array and Large-Scale Data Report. R. Limeburner, ed., Woods Hole Oceanographic Institution Technical Report WHOI-85-35, CODE Technical Report No. 38, 109-132, 1985.
- Boon, J. D. and K. P. Kiley, Harmonic analysis and tidal prediction by the method of least squares. Applied Marine Science and Ocean Engineering of Virginia Institute of Marine Science, Special Report No. 186, 49 pp., 1978.
- Bratkovich, A., Aspects of the tidal variability observed on the southern California continental shelf. Journal of Physical Oceanography, 15, 225-239, 1985.
- Chapman, D. C. and M. C. Hendershott, Scattering of internal waves obliquely incident upon a step change in bottom relief. Deep-Sea Research, 28A: 1323-1338, 1981.
- Denbo, D. W. and J. S. Allen, Rotary empirical orthogonal function analysis of currents near the Oregon coast. Journal of Physical Oceanography, 14, 35-46, 1984.
- Fleischbein, J., W. E. Gilbert, and A. Huyer, Hydrographic data from the second Coastal Ocean Dynamics Experiment: R/V Wecoma, Leg 6, 18-24 April 1982. Oregon State University, School of Oceanography, OSU Reference No. 83-4, CODE Technical Report No. 11, 86 pp., 1983a.
- Fleischbein, J., W. E. Gilbert, and A. Huyer, CTD observations off Oregon and California: R/V Wecoma, W8205A and Code 2 Leg 8, 18 May - 4 June 1982. Oregon State University, School of Oceanography, OSU Reference No. 83-10, CODE Technical Report No. 16, 149 pp., 1983b.
- Fofonoff, N. P. and R. C. Millard, Jr., Algorithms for computation of fundamental properties of seawater. Unesco Technical Papers in Marine Science, No. 44, 53 pp., 1983.

- Gill, A. E., Atmosphere-Ocean Dynamics, Academic Press, 662 pp., 1982.
- Gordon, R. L., Internal wave climate near the coast of northwest Africa during JOINT-1. Deep-Sea Research, 25, 625-643, 1978.
- Gordon, R. L., Tidal interactions in a region of large bottom slope near northwest Africa during JOINT-1. Deep-Sea Research, 26, 199-210, 1979.
- Hayes, S. P. and D. Halpern, Observations of internal waves and coastal upwelling off the Oregon coast. Journal of Marine Research, 34, 247-267, 1976.
- Holloway, P. E., Tides on the Australian North West Shelf. Australian Journal of Marine and Freshwater Research, 34, 213-230, 1983a.
- Holloway, P. E., Internal tides on the Australian North West Shelf: A preliminary investigation. Journal of Physical Oceanography, 13, 1357-1370, 1983b.
- Holloway, P. E., On the semidiurnal internal tide at a shelf-break region on the Australian North West Shelf. Journal of Physical Oceanography, 14, 1787-1799, 1984.
- Holloway, P. E., A comparison of semidiurnal internal tides from different bathymetric locations on the Australian North West Shelf. Journal of Physical Oceanography, 15, 240-251, 1985.
- Hsieh, W. W., 1986, Comments on "Rotary Empirical Orthogonal Function Analysis of Currents near the Oregon Coast." Journal of Physical Oceanography, 16, 791-792, 1986.
- Huthnance, J. M. and P. G. Baines, Tidal currents in the northwest African upwelling region. Deep-Sea Research, 29, 285-306, 1982.
- Huyer, A., J. Fleischbein and R. Schramm, Hydrographic data from the second Coastal Ocean Dynamics Experiment: R/V Wecoma, Leg 9, 6-27 July 1982. Oregon State University, School of Oceanography, OSU Reference No. 84-7, CODE Technical Report No. 25, 130 pp., 1984.
- Irish, J. D., CODE-2 moored temperature and conductivity observations, in CODE-2: Moored Array and Large-Scale Data Report, R. Limeburner, ed., Woods Hole Oceanographic Institution Technical Report WHOI 85-35, CODE Technical Report No. 38, 133-164, 1985.
- LeBlond, P. H., On the damping of internal gravity waves in a continuously stratified ocean. Journal of Fluid Mechanics, 25, 121-142, 1966.
- Mooers, C. N. K., Several effects of a baroclinic current on the cross-stream propagation of inertial-internal waves. Geophysical Fluid Dynamics, 6, 245-275, 1975.

- Noble, M., L. K. Rosenfeld, R. L. Smith, J. V. Gardner and R. C. Beardsley, Tidal currents seaward of the northern California continental shelf. Journal of Geophysical Research, 92 (1987), in press.
- Petrie, B., M2 surface and internal tides on the Scotian shelf and slope. Journal of Marine Research, 33, 303-323, 1975.
- Prinsenbergh, S. J., W. L. Wilmot and M. Rattray, Jr., Generation and dissipation of coastal internal tides. Deep-Sea Research, 21, 263-281, 1974.
- Rattray, M., Jr., On the coastal generation of internal tides. Tellus, 12, 54-62, 1960.
- Rattray, M., Jr., J. G. Dworski, P. E. Kovala, Generation of long internal waves at the continental slope. Deep-Sea Research, 16(Suppl.), 179-195, 1969.
- Rhines, P., Edge-, bottom-, and Rossby waves in a rotating stratified fluid. Geophysical Fluid Dynamics, 1, 273-302, 1970.
- Rosenfeld, L. K. and R. C. Beardsley, Barotropic semidiurnal tidal currents off northern California during the Coastal Ocean Dynamics Experiment (CODE). Journal of Geophysical Research, 92 (1987), in press.
- Sandstrom, H., On topographic generation and coupling of internal waves. Geophysical Fluid Dynamics, 7, 231-270, 1976.
- Schott, F., On the energetics of baroclinic tides in the North Atlantic. Annales de Geophysique, 33, 41-62, 1977.
- Send, U., R. C. Beardsley, and C. D. Winant, Relaxation from upwelling in CODE. Journal of Geophysical Research, 92 (1987), in press.
- Torgrimson, G. M. and B. M. Hickey, Barotropic and baroclinic tides over the continental slope and shelf off Oregon. Journal of Physical Oceanography, 9, 945-961, 1979.
- Winant, C. D. and J. R. Olson, The vertical structure of coastal currents. Deep-Sea Research, 23, 925-936, 1976.
- Winant, C. D., Coastal current observations. Reviews of Geophysics and Space Physics, 17, 89-98, 1979.
- Winant, C. D. and A. W. Bratkovich, Temperature and currents on the southern California shelf: a description of the variability. Journal of Physical Oceanography, 11, 71-86, 1981.

Winant, C. D., U. Send, and S. J. Lentz, CODE-2: Moored current observations, in CODE-2: Moored Array and Large-Scale Data Report, R. Limeburner, ed., Woods Hole Oceanographic Institution Technical Report WHOI-85-35, CODE Technical Report No. 38, 133-164, 1985.

Winant, C. D., R. C. Beardsley, and R. E. Davis, Moored wind, temperature, and current observations made during CODE-1 and CODE-2 over the northern California shelf and upper slope. Journal of Geophysical Research, 92 (1987), in press.

Wunsch, C., Progressive internal waves on slopes. Journal of Fluid Mechanics, 35, 131-144, 1969.

Wunsch, C., Internal tides in the ocean. Reviews of Geophysics and Space Physics, 13, 167-182, 1975.

CHAPTER V

CONCLUSIONS

Current measurements made during the summer upwelling seasons of 1981 and 1982 over the continental shelf off northern California during the Coastal Ocean Dynamics Experiment reveal that, second only to the synoptic band, the most energetic part of the frequency spectrum is the tidal band (diurnal to semidiurnal frequencies). Although tides and tidal currents have been studied for many years, the prediction of the tidal frequency currents in any given location at any given time is still quite difficult. Many processes besides the astronomical tide-generating force are at work in producing currents in the tidal band. In this thesis, the temporal variability and spatial structure of the diurnal and semidiurnal band currents observed during CODE are described in considerable detail, and it has been shown that the currents associated with the surface tide account for only a fraction of the kinetic energy at tidal frequencies. Each chapter focuses on a non-astronomical mechanism responsible for generating or altering tidal period current fluctuations. The processes discussed here are only some of those that can cause the observed tidal band currents to deviate from what would be predicted based solely on sea level measurements.

Chapter II discusses the diurnal period current fluctuations. They are strongly surface-intensified and intermittent in time. The case is made that these currents are the direct result of forcing by the local diurnal wind stress, the strength of which is correlated with the low frequency equatorward wind stress. Currents generated by a one-dimensional mixed layer model forced with diurnal and mean wind stress and diurnal surface heat flux confirm that the observed diurnal currents in the upper water column may in fact be due in large part to

local atmospheric forcing. The failure of the model to duplicate more exactly the observed currents is probably a result of the absence of three-dimensional effects. Evidence that a one-dimensional model is not totally adequate for describing the diurnal variability in this area is given by the fact that the observed diurnal temperature variations in the upper water column are greater than can be accounted for by local surface heat flux, and the near-surface diurnal currents over the outer shelf and upper slope are disproportionately large in comparison with the diurnal wind stress there. A fully three-dimensional model including realistic coast and shelf geometry, nonlinear terms, and bottom friction may be necessary to more accurately predict the diurnal current variability.

In Chapter III, the horizontal structure of the depth-averaged semidiurnal currents is described. Comparisons are made with two existing models for the prediction of the barotropic tidal currents from sea level measurements. More alongshore variability is observed than is predicted by these models. A simple flat-bottom model for one possible source of this spatial variability - small-scale structure in the geometry of the coastline - is presented. While this mechanism does not account for all of the observed structure, it does explain the following important features of the observations: the maximum velocities occur near capes in the coastline, the effect of coastline geometry on the velocity field is much greater than on the pressure field, and the effect of the coastline decays offshore over a short distance set by the alongshore scale of the coastline geometry. The addition of shelf topography to this may improve the model-data comparison, and should be investigated in the future.

Chapter IV deals with the baroclinic semidiurnal tidal currents. During periods when the wind relaxed and the stratification over the shelf increased, the baroclinic semidiurnal tidal currents increased in amplitude. The vertical and horizontal structure of the semidiurnal current and temperature fluctuations during these approximately two week time periods is consistent with first mode internal waves propagating with shoreward components of phase and group velocity. There is evidence for the modification of the vertical structure by the sloping bottom and/or bottom friction. Application of existing theory is inadequate to explain the generation of internal tidal currents as large as those observed here. This is an important problem which needs to be addressed in the future.

The stated goal of CODE was to examine the dynamics governing the synoptic band (2 - 10 day periods) wind-driven flow over the continental shelf in an area of relatively simple topography and strong wind forcing. This thesis points out that even small variations in the alongshore geometry can affect the tidal band flow measurably. In addition, it has been shown here that atmospheric forcing can have significant direct effects on the diurnal currents through forcing by the diurnal wind stress and heating, and indirect effects on the semidiurnal currents through restructuring of the density field.

BIOGRAPHICAL NOTE

Leslie Karen Rosenfeld was born on Oct. 4, 1955 in New York City. She lived in Chappaqua, New York until graduating from high school in 1972. She studied photography in Denmark before attending Tufts University for one semester. She then sailed aboard the Westward, before returning to school at Florida Institute of Technology's School of Marine and Environmental Technology in Jensen Beach, Florida, from which she received an A.S. degree in 1976. She gained experience in other aspects of oceanography as a summer intern with the late Dr. Bruce Heezen at Lamont-Doherty Geological Observatory, and with Mr. John Thompson at the Harbor Branch Foundation, before deciding to concentrate on physical oceanography. She went on to major in that discipline at the University of Washington, from which she received her B.S. degree in 1978. Before entering the Joint Program in Oceanography in 1980, she worked for the U.S. Naval Oceanographic Office, the Chesapeake Bay Institute of The Johns Hopkins University, and the Martin Marietta Environmental Center. She has accepted a post-doctoral fellowship at the Cooperative Institute for Marine and Atmospheric Studies in Miami, Florida.

Publications and Technical Reports

- Rosenfeld, L. K. and R. C. Beardsley, 1987, Barotropic semidiurnal tidal currents off northern California during the Coastal Ocean Dynamics Experiment (CODE). Journal of Geophysical Research, 92, in press.
- Noble, M., L. K. Rosenfeld, R. L. Smith, J. V. Gardner, and R. C. Beardsley, 1987, Tidal currents seaward of the northern California continental shelf. Journal of Geophysical Research, 92, in press.
- Beardsley, R. C., C. E. Dorman, C. A. Friehe, L. K. Rosenfeld, and C. D. Winant, 1987, Local atmospheric forcing during CODE-1 and CODE-2. Part I: A description of the marine boundary layer and atmospheric conditions over a northern California upwelling region. Journal of Geophysical Research, 92, in press.
- Beardsley, R. C., R. Limeburner, and L. K. Rosenfeld, 1985, Introduction to the CODE-2 moored array and large-scale data report. In CODE-2: Moored Array and Large-Scale Data Report, R. Limeburner, ed. Woods Hole Oceanographic Institution Technical Report WHOI-85-35, 1-22.
- Rosenfeld, L. K., R. P. Signell, and G. G. Gawarkiewicz, 1984, Hydrographic Study of Buzzards Bay, 1982-1983. Woods Hole Oceanographic Institution Technical Report WHOI-84-5, 134 pp.
- Beardsley, R. C. and L. K. Rosenfeld, 1983. Introduction to the CODE-1 moored array and large-scale data report. In CODE-1: Moored Array and Large-Scale Data Report, L. K. Rosenfeld, ed. Woods Hole Oceanographic Institution Technical Report WHOI-83-23, 1-16.
- Thompson, M. J., L. E. Gilliland, and L. K. Rosenfeld, 1979, Light scattering and extinction in a highly turbid coastal inlet. Estuaries, 2: 164-171.